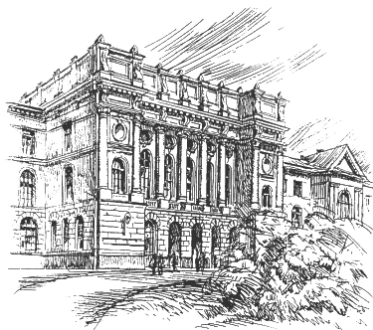


3(249)/2016



Научно-технические ведомости СПбГУ

St. Petersburg Polytechnic University Journal
of Engineering Sciences and Technology

Санкт-Петербург. Издательство Политехнического университета

Министерство образования и науки РФ

Санкт-Петербургский политехнический университет Петра Великого

НАУЧНО-ТЕХНИЧЕСКИЕ ВЕДОМОСТИ СПбПУ ST. PETERSBURG POLYTECHNIC UNIVERSITY JOURNAL OF ENGINEERING SCIENCES AND TECHNOLOGY

РЕДАКЦИОННЫЙ СОВЕТ ЖУРНАЛА

Васильев Ю.С. – председатель редакционного совета, научный руководитель СПбПУ академик РАН

Алфёров Ж.И. – академик РАН

Згуровский М.З. – ин. член РАН, академик НАН Украины

Костюк В.В. – академик РАН

Лагарьков А.Н. – академик РАН

Окрепилов В.В. – академик РАН

Патон Б.Е. – академик НАН Украины и РАН

Рудской А.И. – чл.-корр. РАН

Тендлер М.Б. – ин. член РАН (Швеция)

Федоров М.П. – президент СПбПУ, академик РАН

РЕДАКЦИОННАЯ КОЛЛЕГИЯ ЖУРНАЛА

Васильев Ю.С. – главный редактор, научный руководитель СПбПУ, академик РАН

Кондратьев С.Ю. – зам. главного редактора, д-р техн. наук, профессор СПбПУ

Аксёнов Л.Б. – д-р техн. наук, профессор СПбПУ

Башкарёв А.А. – д-р техн. наук, профессор СПбПУ

Боронин В.Н. – д-р техн. наук, профессор СПбПУ

Гордеев С.К. – д-р техн. наук, ст. научн. сотр. ЦНИИМ

Гуменюк В.И. – д-р техн. наук, профессор СПбПУ

Дегтярева Р.В. – д-р ист. наук, профессор СПбПУ

Иванов А.В. – д-р техн. наук; СПбПУ

Кириллов А.И. – д-р техн. наук, профессор СПбПУ

Титков В.В. – д-р техн. наук, профессор СПбПУ

Толочко О.В. – д-р техн. наук, профессор СПбПУ

Журнал с 1995 года издается под научно-методическим руководством Российской академии наук.

Журнал с 2001 года входит в Перечень ведущих рецензируемых научных журналов и изданий, в которых должны быть опубликованы основные результаты диссертаций на соискание ученой степени доктора и кандидата наук.

Сведения о публикациях представлены в Реферативном журнале ВИНТИ РАН, в базе Russian Science Citation Index на платформе Web of Science, международной библиографической и реферативной базе данных ProQuest, в международной наукометрической базе Index Copernicus, в международной системе по периодическим изданиям "Ulrich's Periodicals Directory".

Журнал зарегистрирован в Федеральной службе по надзору за соблюдением законодательства в сфере массовых коммуникаций и охране культурного наследия (свидетельство ПИ № ФС77-25981 от 13 октября 2006 г.)

Подписной индекс **18390** в объединенном каталоге «Пресса России».

The journal is published under the scientific and methodical guidance of the Russian Academy of Sciences since 1995.

The journal has been included in the List of leading peer-reviewed scientific journals and other editions to publish major findings of theses for the research degrees of Doctor of Sciences and Candidate of Sciences since 2001.

The publications are presented in the VINITI RAS Abstract Journal, Russian Science Citation Index on the platform Web of Science, ProQuest, Index Copernicus, Ulrich's Periodicals Directory and Russian Science Citation Index databases.

The journal is registered with the Federal Service for Supervision in the Sphere of Telecom, Information Technologies and Mass Communications (ROSKOMNADZOR). Certificate ПИ № ФС77-25981 issued October 13, 2006.

The journal is distributed through the CIS countries catalogue, the «Press of Russia» joint catalogue and the «Press by subscription» Internet catalogue. The subscription index is **18390**.

EDITORIAL COUNCIL

Vasiliev Yu.S. — head of the editorial council, Scientific director of the Peter the Great St. Petersburg Polytechnic University, full member of the Russian Academy of Sciences.

Alferov Zh.I. — full member of the Russian Academy of Sciences

Zgurovskiy M.Z. — foreign member of the Russian Academy of Sciences, full member of the National Academy of Sciences of Ukraine

Kostiuk V.V. — full member of the Russian Academy of Sciences

Lagar'kov A.N. — full member of the Russian Academy of Sciences

Okrepilov V.A. — full member of the Russian Academy of Sciences

Paton B.E. — full member of the Russian Academy of Sciences and the National Academy of Sciences of Ukraine

Rudskoy A.I. — corresponding member of the Russian Academy of Sciences

Tendler M.B. — foreign member of the Russian Academy of Sciences (Sweden)

Fedorov M.P. — President of the SPbPU, full member of the Russian Academy of Sciences

JOURNAL EDITORIAL BOARD

Vasiliev Yu.S. — editor-in-chief, full member of the Russian Academy of Sciences, Scientific director of the Peter the Great St. Petersburg Polytechnic University

Kondrat'ev S.Yu. — deputy editor-in-chief, Dr.Sc. (tech.), prof. SPbPU

Aksyonov L.B. — Dr.Sc. (tech.), prof. SPbPU

Bashkarev A.A. — Dr.Sc. (tech.), prof. SPbPU

Boronin V.N. — Dr.Sc. (tech.), prof. SPbPU

Gordeev S.K. — Dr.Sc. (tech.), prof. CNIIM

Gumenyuk V.I. — Dr.Sc. (tech.), prof. SPbPU

Degtyareva R.V. — Dr.Sc. (history), prof. SPbPU

Ivanov A.V. — Dr.Sc. (tech.), SPbPU

Kirillov A.I. — Dr.Sc. (tech.), prof. SPbPU

Titkov V.V. — Dr.Sc. (tech.), prof. SPbPU

Tolochko O.V. — Dr.Sc. (tech.), prof. SPbPU

С 2005 года журнал включен в базу данных «Российский индекс научного цитирования» (РИНЦ), размещенную на платформе Научной электронной библиотеки на сайте <http://www.elibrary.ru>

При перепечатке материалов ссылка на журнал обязательна.

Точка зрения редакции может не совпадать с мнением авторов статей.

Адрес редакции и издательства: Россия, 195251, Санкт-Петербург, ул. Политехническая, д. 29.

Тел. редакции (812) 294-47-72.

© Санкт-Петербургский политехнический университет Петра Великого, 2016

The journal has been included in the Russian Science Citation Index (RSCI) database since 2005 © Scientific Electronic Library (<http://elibrary.ru/>).

No part of this publication may be reproduced without clear reference to the source.

The views of the authors may not represent the views of the Editorial Board.

Address: 29 Politekhnicheskaya St., St. Petersburg, 195251, Russia.

© Peter the Great St. Petersburg Polytechnic University, 2016

Contents

Power engineering

Zabelin N.A., Saychenko A.S. <i>Development of an environmentally friendly steam turbine working on organic fluid for waste heat utilization</i>	5
Shabanov A.U., Zaitsev A.B., Metelev A.A., Pystovalov U.P. <i>Simulation parameters of friction and wear conjugation in the friction cylinder</i>	15
Matrosov A.V., Isaev Yu.M., Sunarchin R.A. <i>Mathematical modeling of an electrohydraulic drive for a hydraulic turbine</i>	22
Sebelev A.A., Saychenko A.S., Zabelin N.A., Smirnov M.V. <i>Numerical analysis of the expansion process in a two-stage axial turbine operating with MDM siloxane</i>	29
Borishanskiy K.N. <i>Increasing the accuracy of measuring the flutter of steam turbine blades in service</i>	39

Electrical engineering

Shakirov M.A. <i>2nT-shaped equivalent circuit of a transformer comprising n windings</i>	49
Solovyev Yu.V., Nazarythev A.N., Tadzhibaev A.I. <i>Development of the method for assessing the covered conductors state due to electrical ageing in moist and highly pollution environment</i>	64

Metallurgy and Materials technology

Kondrat'ev S.Yu., Anastasiadi G.P., Ptashnik A.V. <i>Microstructural evolution of heat – resistant HP alloys under long-time operation at high temperatures</i>	72
Tonitzki A., Skvortsova A.N., Koltsova T.S., Ganin S. V., Danilova M.A., Shamshurin A.I. <i>Aluminum - Carbon Nanofibers Composite Coating Produced by Cold Spraying</i>	81
Krylov N.A., Skotnikova M.A., Tsvetkova G.V., Ivanova G.V. <i>Influence of structure and phase composition of the material of steam turbine blades from titanium alloys on their resistance to erosive destruction</i>	89
Bogdanov E.A., Chupakhin E.G., Sotnikov E.B., Vasilyeva E.S., Bulanov S.S., Patrushev M.V., Shusharina N.N., Goikhman A.Yu. <i>New Materials for DNA isolation</i>	97

Mechanical engineering

Kuschenko A.V., Bashkarev A.Ya. <i>Control of Friction Properties in Polyamide Coatings in Tension Joints</i>	105
Mamutov V.S., Mamutov A.V., Kunkin S.N., Arsenyeva X.S. <i>Method of obtaining FLD for using in simulation of metal forming by movable media</i>	111
Hoodorozhkov S.I. <i>The mechanical stepless impulse type transmission for advanced small-sized transport</i>	118
Gavrilov P.A. <i>Seismic analysis of cranes regarding geometric and physical nonlinearities</i>	128

Содержание

Энергетика

Забелин Н.А., Сайченко А.С. Разработка экологически чистой паровой турбины на органическом рабочем теле для утилизации вторичной тепловой энергии	5
Шабанов А.Ю., Зайцев А.Б., Метелев А.А., Пустовалов Ю.П. Моделирование параметров трения и износа сопряжений трения ЦПГ поршневого двигателя.....	15
Матросов А.В., Исаев Ю.М., Сунарчин Р.А. Математическое моделирование многомашинного следящего электрогидропривода кольцевого затвора гидротурбины	22
Себелев А.А., Сайченко А.С., Забелин Н.А., Смирнов М.В. Численный анализ процесса расширения в двухступенчатой осевой турбине, работающей с MDM силоксаном.....	29
Боришанский К. Н. Повышение точности регистрации автоколебаний лопаток паровых турбин в условиях эксплуатации	39

Электротехника

Шакиров М.А. 2nT-образная схема замещения трансформатора, содержащего n обмоток	49
Соловьев Ю.В., Назарычев А.Н., Таджикибаев А.И. Метод оценки состояния защищенных проводов при электрическом старении в условиях повышенных загрязнений и увлажнений	64

Металлургия и материаловедение

Кондратьев С.Ю., Анастасиади Г.П., Пташник А.В. Эволюция микроструктуры жаропрочных НР сплавов при длительной высокотемпературной эксплуатации	72
Тониитзки А., Скворцова А.Н., Кольцова Т.С., Ганин С.В., Данилова М.А., Шамшурин А.И. Холодное газодинамическое напыление покрытий системы алюминий – углеродные нановолокна..	81
Крылов Н.А., Скотникова М.А., Цветкова Г.В., Иванова Г.В. Влияние структуры и фазового состава материала лопаток паровых турбин из титановых сплавов на их устойчивость к эрозионному разрушению	89
Богданов Е.А., Чупахин Е.Г., Сотников Е.Б., Васильева Е.С., Буланов С.С., Патрушев М.В., Шушарина Н.Н., Гойхман А.Ю. Новые материалы для выделения ДНК	97

Машиностроение

Куценко А.В., Башкарев А.Я. Контроль свойств трения в полиамидных покрытиях напряженных соединений	105
Мамутов В.С., Мамутов А.В., Кункин С.Н., Арсентьева К.С. Диаграммы предельных деформаций тонколистового металла при формовке подвижными средами	111
Худорожков С.И. Механическая бесступенчатая импульсная передача для современной малогабаритной транспортной техники	118
Гаврилов П.А. Учет физической и геометрической нелинейностей при расчете сейсмостойкости крановых металлических конструкций	128

DOI 10.5862/JEST.249.1

УДК 621.165

N.A. Zabelin, A.S. Saychenko

DEVELOPMENT OF AN ENVIRONMENTALLY FRIENDLY STEAM TURBINE WORKING ON ORGANIC FLUID FOR WASTE HEAT UTILIZATION

Н.А. Забелин, А.С. Сайченко

РАЗРАБОТКА ЭКОЛОГИЧЕСКИ ЧИСТОЙ ПАРОВОЙ ТУРБИНЫ НА ОРГАНИЧЕСКОМ РАБОЧЕМ ТЕЛЕ ДЛЯ УТИЛИЗАЦИИ ВТОРИЧНОЙ ТЕПЛОВОЙ ЭНЕРГИИ

This article discusses the waste heat utilization technology of various industries, by steam-turbine installations working by an organic Rankin cycle. Application of this technology allows making the electric power without any fuel expenses which allows to decrease the relative emission of production pollution, to decrease the environmental heat pollution and to increase the efficiency of fuel usage in the main production. As an example, the study presents a calculation of the potential of waste heat utilization for the PAO «Gazprom» gas transmission network, which amounts to 3,9 GW, allowing to reduce the relative emission of production pollution by 25 %. The article also offers information about the 560 kW organic turbine design and the problems of experimental research.

STEAM TURBINE; ORGANIC RANKINE CYCLE; HEAT UTILIZATION; EMISSION; HARMFUL EMISSIONS; ENERGY EFFICIENCY; ORGANIC FLUID; HEXAMETHYLDISILOXANE.

В представленной статье рассматривается технология утилизации теплоты выхлопных газов термических агрегатов различных отраслей промышленности с использованием паротурбинных установок, работающих по органическому циклу Ренкина. Применение подобной технологии позволяет вырабатывать электроэнергию без дополнительных топливных затрат, что приводит к снижению относительной эмиссии вредных веществ основного производства, уменьшает тепловое загрязнение окружающей среды и, таким образом, приводит к росту эффективности использования внутренней энергии топлива, потребляемого на основном производстве. В качестве примера выполнен расчет использования потенциала теплоты уходящих газов газоперекачивающих агрегатов газотранспортной сети ПАО «Газпром», суммарная мощность которых составляет 3,9 ГВт. Показано, что возможно сократить удельную эмиссию вредных веществ на 25 %. В статье также представлена информация о разрабатываемой утилизационной органической паровой турбине натурной мощностью 560 кВт и проблемах экспериментальных исследований данной турбины.

ПАРОВАЯ ТУРБИНА; ОРГАНИЧЕСКИЙ ЦИКЛ РЕНКИНА; УТИЛИЗАЦИЯ ТЕПЛОТЫ; ЭМИССИЯ; ВРЕДНЫЕ ВЫБРОСЫ; ЭНЕРГОЭФФЕКТИВНОСТЬ; ОРГАНИЧЕСКАЯ ЖИДКОСТЬ; ГЕКСАМЕТИЛДИСИЛОКСАН.

Introduction

The intensive growth of modern industry, which using as the main energy source hydrocarbon fuel, leads to a direct increasing of pollution by exhaust gases. This article narrates conversion technology of medium and low-potential waste heat of gas transport industry to electricity. Technology provides full electricity autonomy of gas compressor stations, gas distribution stations and points of shields, reducing the specific value of emission of harmful substances.

Secondary heat sources overview

The main sources of medium and low-potential waste heat are industrial production with unused thermal potential in the future irrevocably discharged into the environment with outgoing exhaust gases or coolant. This leads to thermal environmental pollution and to reduce the competitiveness of finished products associated with the energy lost in view of the cost of these products. Current productions of this kind are:

- ferrous metallurgy;
- the chemical industry;
- manufacture of glass;
- ceramics production;
- manufacture of cement;
- high power diesel generators;
- gas transportation industry (gas turbine engines).

Since the 2000s, the world began active implementation in the above industries utilizing steam power plants operating on organic Rankine cycle (ORC). ORC utilization units provide conversion of waste heat with 8 to 18 % absolute electrical efficiency without any extra fuel consumption, decreasing the specific value of the emission of harmful substances.

The principle of organic Rankine cycle

ORC is a classical steam closed cycle and consists of (fig. 1): *waste heat vaporizer* (4-1), where the heat of exhaust gas transfers to a liquid organic working fluid transforming it into superheated steam; *steam turbine* (1-2), which converts the potential energy of the working fluid into rotational energy of the rotor; *condenser* (2-3), where the organic steam cools, passes into the liquid phase; *feed pump* (3-4), which increases the fluid pressure to the required value before the steam turbine.

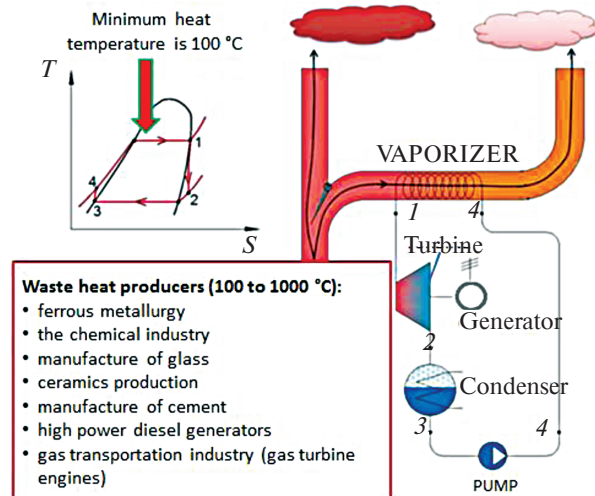


Fig. 1. Structural schema and $T(S)$ diagram of ORC utilization unit [1]

Historical distribution of ORC units have been started at 1890s, when the company “Gas Engine & Power Company” (USA) has sold 500 units (Fig. 2), based on steam piston engine with a working fluid naphtha (flammable hydrocarbon liquid), patented by Franck W. Ofeldt [2].

Next development of ORC was based on researches of new low-boiling organic fluid and have been used in the fields of solar energy (the first solar installation working by ORC with etheric 2,6 kW capacity, was designed by Frank Schumann in 1907 [3]), geothermal power units (the world’s first geothermal power unit Paratunskaya with ORC net power of 500 kW, was built in the USSR in 1967 (Kamchatka) [4]), waste heat recovery units and special purpose machinery (autonomous space energy units of 1,5 and 6 kW electricity power of USSR [5]).

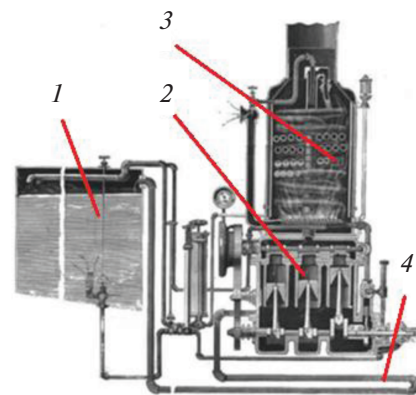


Fig. 2. ORC unit patented by Franck W. Ofeldt in 1897 [2]:
1 – fuel tank; 2 – vaporizer; 3 – steam piston engine;
4 – condenser

Statistics of ORC usage in Europe

Research of the University of Liege (Belgium) in 2009 showed [6] that the main fields of ORC application are next: the utilization of biomass (wood processing and recycling plants, biogas producers) 48 %; geothermal electro stations 31 %; industrial waste heat utilization 20 %; solar systems 1 %.

There are leading manufacturers of commercial ORC units in table 1 [7]. General difference between units is usage of different organic working fluids which have individual chemical and thermodynamic properties what influence deeply at unit's construction. The most dangerous point of some organic working fluid is toxicity what requires a careful unit's seals design.

ORC usage at natural gas transmission infrastructure of Russia

PAO "Gazprom" - the world's largest gas company, owner of the most extensive gas transmission system (more than 160 000 km), the operator about 3800 gas turbine engines (GTE) with total power of 44,3 GW [9].

Further in an article will be considered ORC usage for exhaust gas waste heat recovery of turbine driven gas compressor stations (GCS), characterized by high temperature (350 to 550 °C, depends on GTE efficiency) and large mass flow. This ORC utilization units allow to provide electro autonomy of turbine driven GCS without fuel consumption and to reduce a relative emission of production pollution by 25 % (at maximum recovery of waste heat).

Electricity consumption research of Ltd "Gazprom transgas St.Petersburg" shows that electricity consumption of one GCS is from 200 to 500 kW. In case of necessity of air cooling fans working, the electricity consumption increasing for 500 to 1500 kW, depending on natural gas mass flow and pressure in

gas pipeline, environment and earth temperature. This research shows the necessary power of ORC utilization unit, which was selected as 560 kW.

According to European research of 2013 [9], overall exhaust gas waste heat recovery potential of PAO «Gazprom» GCS using ORC utilization units is 3,9 GW at single unit power from 1,2 to 15 MW. The calculation took into account next nuances: reserve GTE power is not taken into account (one reserve GTE for two working GTE, $k_1 = 0,65$); efficiency of ORC unit is around 30 % of GTE efficiency and equals to 10 % ($k_2 = 0,3$), total annual operating time of GTE is around 4000 hours ($k_3 = 0,45$).

Positive exploitation experience of ORC utilization units is presented in the report of the American Association of natural gas for 2009 [10]. Report says that at GCS of North America (USA and Canada) since 1999 have been operated 15 ORC utilization units with total power of 75,5 MW (fig. 3 [11]). All units are made by ORMAT company (USA) and have a power range from 4 to 6 MW. An important fact is that the weight and size characteristics of the organic turbine is several times less than the heat transfer equipment (heat recovery boiler, economizer, evaporator, condenser).



Fig. 3. ORC utilization unit 6MW power working at gas compressor station in Loreburn (Canada) [11]

Table 1

Leading manufacturers of commercial ORC units [7]

Producer	Unit power, kW	Working fluid	Fluid parameters at turbine inlet		Number of working units, pc.
			$T, ^\circ\text{C}$	P, MPa	
General Electric Energy (USA)	125	R245fa	121	1,72	>100
Ormat (USA)	400-15000	<i>n</i> -Pentane	105-180	–	>200
Turboden (Italy)	200-15000	<i>n/a</i>	100-200	–	>260

Emission of production pollution of Russian's gas transmission network

PAO "Gazprom" gas transmission network is accompanied by large volumes of emission of harmful substances contained in the exhaust gas of GTU. Evaluation of the annual volume of pollutants is shown at figure 4 [12]. Integration of ORC utilization units to PAO "Gazprom" gas transmission network will provide the reducing of a relative emission of production pollution by 25 %. Reducing specific emissions is achieved by converting the heat capacity of exhaust gases in the exhaust gas turbine engine into electrical energy, without additional combustion of fuel.

Electricity production (3,9 GW) without necessity of fuel consumption allows to estimate saving of natural fuel resources. The estimation is done by two ways: classical electricity production using GTU (efficiency 35 %) and combined cycle with GTU and steam turbine (efficiency 45 %). The savings are 11,990 and 9330 thousand ton of conventional fuel per year respectively.

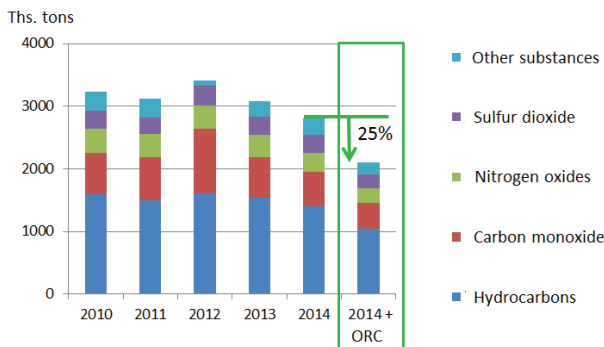


Fig. 4. Annual volume of pollutants of PAO "Gazprom" gas transmission network and potential of its decreasing using ORC utilization units [12]

Experimental stand for organic turbine research

Today at the Russian market of ORC utilization units presented only Turboden company, which has installed at oil refining factory of Lukoil-Perm company the ORC utilization unit (1,8 MW power) running on the heat from the burning of associated petroleum gas. The need for such units is increasing from year to year.

In 2012 the department of «Turbines, hydromachines and aircraft engines» of Peter the Great Saint-Petersburg Polytechnic University has started the development of environmentally friendly ORC utilization unit electrical power of 560 kW (fig. 5) [13], with

a non-toxic and ozone-safe working fluid, hexamethyldisiloxane. The unit is able to utilize the industrial waste heat with minimum temperature of 200 °C.

At the present time performed cycle variant calculations, organic turbine design, designed and built an experimental stand for organic turbine model research using air like a working fluid.

The model geometry is equal to designed organic turbine. It means that similarity factor equals to one (fig. 2).

At experimental stand will be researched two turbine types:

high enthalpy drop turbine stage of Peter the Great Saint-Petersburg Polytechnic University construction, which is designed for two-loop organic turbine with working fluid hexamethyldisiloxane;

organic turbine with axial symmetry nozzles.

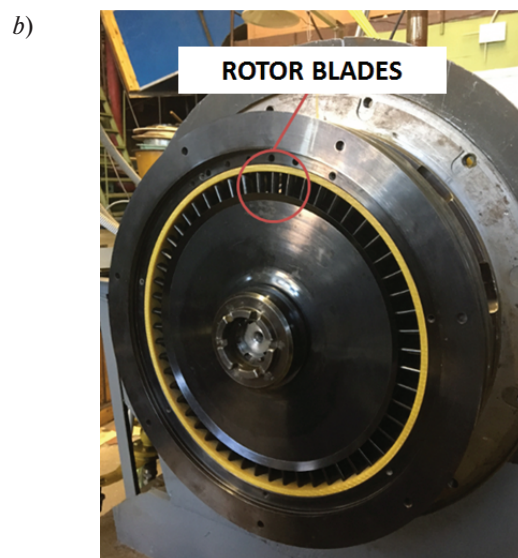
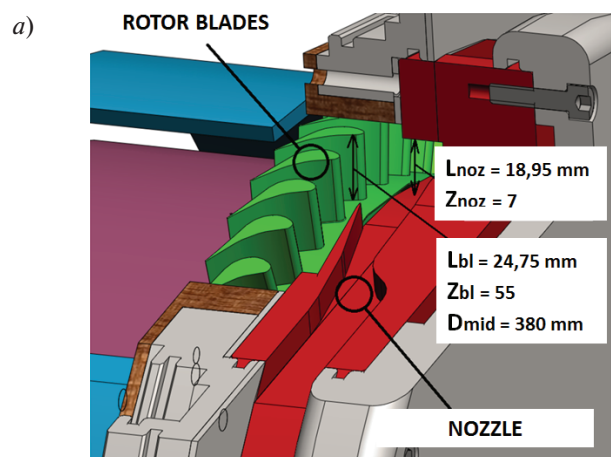


Fig. 5. Construction (a) and experimental stand (b) of organic turbine air model [13]: L – height; Z – quantity; D – diameter

Problems of organic turbine design and further experimental research at air experimental stand

The complexity of the organic turbine design is linked to a strong change of the working fluid’s thermal parameters during flow expansion in turbine’s channel. This feature requires the development of nonclassical complex approach to the turbine design comprising a numerical calculation and experimental physical research.

Experimental research of classical models of steam (water vapor) and gas turbines are carried out at experimental air stands using the theory of similarity, and dimensionless turbine criterions. Theory of similarity such turbines involves providing of geometric, kinematic and dynamic similarity.

For correct turbine similarity under condition of turbine geometry preservation, enough to withstand next parameters:

characteristic turbine number U/C_0 , where U – rotor blade velocity; C_0 – isentropic spouting velocity;

Mach criterion behind the nozzles M_{C1} and rotor blades M_{W2} , M_{C2} calculated from the relationship $k_m M_m = k_n M_n$, where $k = C_p/C_v$ – specific heat ratio; M – mach number; C_1 – absolute velocity at nozzle outlet; C_2 and W_2 – absolute and relative velocities at rotor blades outlet; “ m ” and “ n ” – model and natural turbine stages.

In case of using organic working fluids, the value of the parameter k is strongly dependent on pressure and temperature, making it difficult to direct use the classical theory of modeling for the study of expansion process of hexamethyldisiloxane using air as the working fluid.

The most simple, from a physical point of view, method of organic turbine experimental research is creating an experimental stand with natural (organic) working fluid. However, this method approach leads to a whole range of difficult obstacles.

The complexity of creating a full-scale experimental stand with organic working fluid is that the various working fluids (with different thermal characteristics) may have very different mass flow through the stand, what will require the development, manufacture and application of massive sectional constructions of the steam generator, condenser and different housing parts for placement nozzle diaphragms and impellers. The second complexity is high pressure inside the stand, which may run higher than 1 MPa. It means that the rules need to perform the safe operation of the device and vessels operating under pressure. Finally, some of the used ORC working fluids are toxic or dangerous that requires increased attention to sealing and security systems. Aforesaid says that the experimental stand for organic turbines research cannot be made universal and manufacture with operation of it are expensive.

The way out is to develop new approaches in the framework of similarity theory, allowing to simulate workflows in organic turbines, using experimental air stands. A special feature of this approach is the difficulty or impossibility of the simultaneous holding of similarity criteria of natural and air model turbine stages.

In case of air modeling of designed 560 kW organic (hexamethyldisiloxane) turbine (fig. 5), possible to withstand similarity criterions U/C_0 and M_{C1} , but it is impossible to simultaneously withstand criterion M_{C2} (table 2). It can be explained by high difference between specific heat ratio (k) and gas constant (R) values of hexamethyldisiloxane and air, what leads to significant difference of sound velocity, enthalpy drop and incompatibility of velocity triangles (table 3 and fig. 6).

This particularly applies to the rotor blades outlet triangle velocities – is not achieved axial outlet flow in the model stage, what greatly reduces the efficiency of the model turbine stage.

Table 2

Parameters of natural (hexamethyldisiloxane) and air model turbine stages

Parameter	Dimension	Natural parameters	Model parameters
Mach criterion for nozzle outlet absolute velocity, M_{C1}	–	1,640	1,467
Total inlet pressure, P_0^*	MPa	1,0	0,469
Total inlet temperature, T_0^*	K	477,1	353,16

Ending table 2

Parameter	Dimension	Natural parameters	Model parameters
Static outlet pressure, P_2	MPa	0,04	0,11
Total outlet temperature, T_2^*	K	380,6	291,0
Mach criterion for rotor blades outlet absolute velocity, M_{C_2}	—	0,814	0,624
Working fluid	—	Hexamethyl-disiloxane, $C_6H_{18}OSi_2$	Air
Mass flow, G	kg/s	6,513	1,615
Characteristic turbine number, U/C_0	—	0,654	0,645
Rotor blade velocity, U	m/s	238,8	316,4
Absolute velocity at rotor blade outlet, C_2	m/s	111,6	211,5
Rotational speed, n	rpm	12000	15900
Turbine power, N	kW	285,0	97,7
Degree of reaction	—	0,541	0,123

Table 3

Physical parameters of hexamethyldisiloxane and air

Parameter	Dimension	Air	Hexamethyl-disiloxane
R – gas constant	kJ/(kg · K)	287	51,3
$k = C_p/C_v$ – specific heat ratio	—	1,4	1...1,3 = $f(P; T)$
C_p – heat capacity at 100 °C and 0,5 MPa	J/(kg · K)	1015	2099
a – sound speed at 100 °C and 0,5 MPa	m/s	387,8	549,5

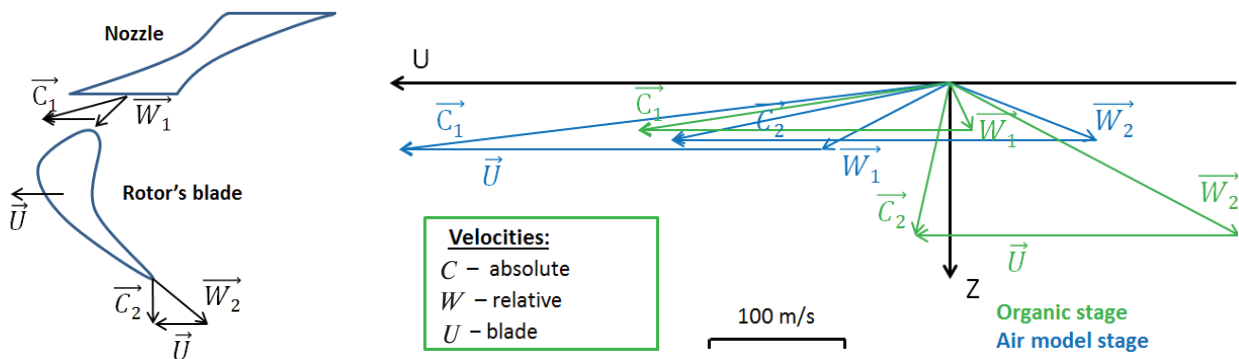


Fig. 6. Velocity triangles of natural (green) and model (blue) turbine stages

A physical modeling to ensure full accordance all the criteria of similarity is impossible. Therefore, as already mentioned, formulated a new approach to modeling of organic working fluids expansion process at experimental air stand.

The approach is based on complex research of the expansion process in the turbine by methods of numerical experiment, and methods of physical experiment.

Such a study is currently in progress at the laboratory of the department of «Turbines, hydromachines and aircraft engines» of Peter the Great Saint-Peters-

burg Polytechnic University and consists of three phases.

The first phase involves the analysis of flow characteristics of working fluid (air) through air model of designed organic turbine. Performing the model in scale 1:1 allows to exclude from the flow analysis the effect of the size factor. This phases includes numerical research (flow’s parameters calculation has been completed) (fig. 7) and physical research on the exact geometric model of turbine stage (fig. 5). The design of experimental stand and methodology of physical research are detailed in [13].

Analysis of the results of the first phase will assess, for a given geometry of the turbine stage, the deviation of the numerical research, compared with the physical research. Achieved deviation will be used at the second phase of study.

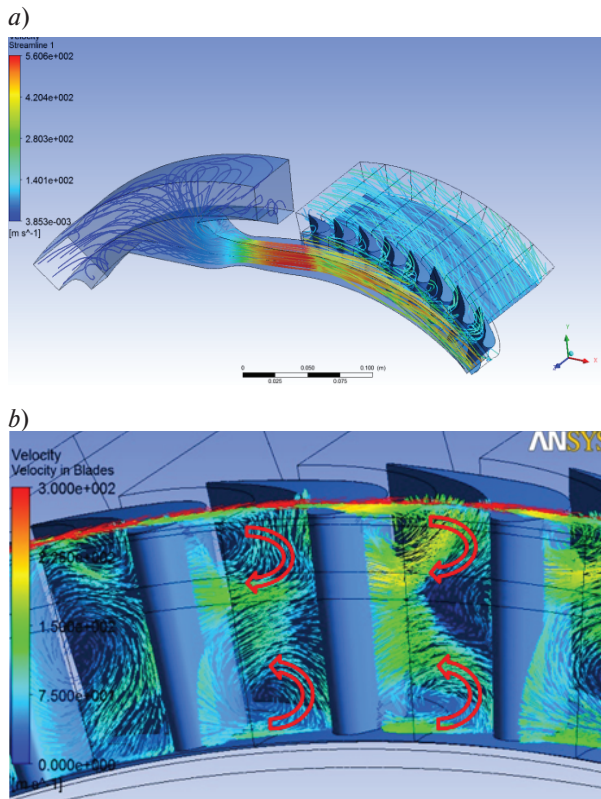


Fig. 7. Results of numerical research of air model of organic turbine stage: a) Streamlines through the turbine stage; b) The formation of horseshoe vortices in channels between the rotor blades

The second phase consists of carrying out a numerical experiment of organic (hexamethyldisiloxane) working fluid on the same computational mesh (from first phase), based on achieved deviation at the first phase. Computational mesh, as well as the stage geometry, is unchanged.

The third phase consists of comparing and analyzing the results of natural (organic working fluid) and model (air working fluid) turbine researches and confirm the new approach to the theory of computational and experimental modeling of organic working fluids using air as the working fluid.

The final research will be conducted using ORC utilization unit with designed organic turbine. The ORC unit will be installed at GCS “Severnaya” of Ltd “Gazprom transgas St.Petersburg”. At the present the ORC unit is under manufacturing and instal-

lation (filling of foundation). The launch is scheduled for autumn 2017.

Hexamethyldisiloxane wet steam modeling aspects

A feature of thermo-physical properties of hexamethyldisiloxane is that during the flow expansion in turbine channels from the saturation line to the condenser the diagram wet should be absolutely dry.

However, even if hexamethyldisiloxane enters to the first turbine stage at zero diagram wet, possible the falling out of condensed moisture at the beginning of expansion what may be the reason of gap and drop erosion first of all of nozzles and rotor blades. The process of evaporation of drops is very inertial, requires a lot of time and may not be able to complete until turbine outlet.

Questions of hexamethyldisiloxane moisture-formation, wet phase transformation and it’s evaporating during expansion in turbine stage have not been studied and are not reflected in world literature.

To solve the problem of the possibility of a two-phase hexamethyldisiloxane flow simulation assumes the using of air experimental turbine stand with artificial flow moisture by injection the liquid phase.

To complete transfer model test results on natural conditions, except of geometric similarity, it is necessary to provide a range of coincidence of the dimensionless parameters, the number of which is so large that their simultaneous and strict coincidence is impossible in most cases. At the same time empirically established that many of the criteria of similarity within a certain range of their changes have only a minor influence on the final result [14].

Most significant in modeling of two-phase flow are gas-dynamic similarity criteria. As already mentioned, to achieve a full coincidence of similarity criteria is impossible. Therefore, we can only talk about a partial simulation, based on experience and theoretical analysis of the processes chosen system of similarity criteria, the most detailed process describing the study of movement and evaporation of the droplets.

As is known from [14–17], with the partial simulation of the interaction processes of liquid particles with vapor streams and part surfaces, the following points are gas-dynamic similarity criteria: Reynolds Re , Froude Fr , Weber We , Euler Eu , Stokes St , Mach M , Strouhal Sh , the mass and expenditure level of humidity. These parameters are presented for natural (hexamethyldisiloxane) and air model of designed organic turbine stage in table 4.

Table 4

Similarity criteria of natural (hexamethyldisiloxane) and air model of designed turbine stage

Dimensionless flow criterion		Hexamethyl-disiloxane	Air (with water injection)
Reynolds	Re_{C1}	4,3E+0,6	5,1E+05
	Re_{C2}	5,9E+06	7,4E+05
Strouhal	$Sh = U/C_0$	0,654	0,654
Euler	Eu_{nozzle}	1,142	1,169
	Eu_{blades}	7,963	0,374
Froude	Fr_{nozzle}	4,18E+05	1,37E+06
	Fr_{blades}	3,67E+04	1,32E+05
Mach	M_{C1}	1,640	1,467
	M_{C2}	0,814	0,624
Average diameter of the droplet, m We critical = 14	$d1_{nozzle}$	0,0015	0,0301
	$d2_{blades}$	0,0186	0,0699

There is a satisfactory agreement between the main criteria: Reynolds, Mach, Strouhal and Euler at nozzle outlet.

Results analysis allows concluding that it is possible to simulate the wet-steam flow of hexamethyl-disiloxane at air experimental stand. The requirement of the simulation is providing a necessary droplet size, which depends on critical Weber criterion. Unfortunately unable to find data on the critical value of the Weber criterion for hexamethyldisiloxane, for calculations as a first approximation is set to 14, that is typical for water and steam.

Conclusion

1. The gas transportation network in Russia produces huge amounts of air pollutants, the specific amount of which can be reduced by 25% by using

ORC utilization units. The specific pollution decrease achieves by waste heat converting to electricity without burning additional fuel.

2. ORC utilization units allow to provide the electricity autonomous of gas compressor stations, gas distribution stations and points of shields and other objects of Russian gas transport system without additional fuel costs.

3. New approach of ORC design is under creation. It includes methodology of organic turbine research at experimental air stands, what will significantly reduce the time and cost of the development in comparison with the full-scale research at experimental organic stand.

4. It is shown that is possible to model the flow of wet hexamethyldisiloxane vapor, providing a necessary droplet size.

REFERENCES

1. Saychenko A.S. Razrabotka parogazovoy ustanovki moshchnostyu 250 kVt dlya utilizatsii teploty ukho-dyashchikh gazov gazoperekachivayushchikh agregatov. *Otkrytaya nauchno-prakticheskaya konferentsiya molodykh rabotnikov. "Vnedreniye peredovykh tekhnologiy i tekhnicheskikh resheniy, razrabotannykh s uchastiyem molodezhi – neotyemlemaya sostavlyayushchaya razvitiya Obshchestva". Sbornik dokladov.* Gazprom transgaz Sankt-Peterburg. 2012. T. 1.
2. American patent US611792 A. Engine / Frank W. Ofeldt. 1898.
3. Pytilinski J.T. Solar energy installations for pumping irrigation water. *Solar Energy*, 1978. № 21(4). P. 255 – 262.
4. Tomarov G.N., Nikolskiy A.I., Semenov V.N., Shipkov A.A. Geotermalnaya energetika: Spravochno-metodicheskoye izdaniye / Pod redaktsiyey P.P. Bezrukikh. M.: "Intertekhenergo-Izdat", "Teplenergetik", 2015. 304 s (rus).
5. Grishutin M.M. Paroturbinnyye ustanovki s organicheskimi rabochimi telami. Leningrad: Mashinostroyeniye, 1988. 219 s. (rus.)
6. Quoilin S., Lemort V. Technological and Economical Survey of Small-Scale Organic Rankine Cycle Systems. *Fifth European conference, Economics and management of energy in industries*. 2009. Access mode: <http://www.eolss.net/sample-chapters/c05/E6-35-43-00.pdf> (date of access: 29.04.2016).

7. **Emiliano I.M.** Casati New concepts for Organic Rankine Cycle Power Systems. Milan, 2014.

8. **Van den Broek M., Chys M., Vanslambrouck B., De Paepe M.** Increasing the efficiency and generated electricity of organic rankine cycles by using zeotropic mixtures as working fluids. *9th International Conference on Heat Transfer, Fluid Mechanics and Thermodynamics* 16 – 18 July, 2012. Malta.

9. **Campana F., Bianchi M., Branchini L., Pascale A. De., Peretto A., Baresi M., Fermi A., Rossetti N., Vescovo R.** ORC waste heat recovery in European energy intensive industries: *Energy and GHG savings. 2013.* Access mode: <http://www.sciencedirect.com/science/article/pii/S0196890413004123> (date of access: 29.04.2016).

10. Status of Waste Heat to Power Projects on Natural Gas Pipelines. *Interstate Natural Gas Association of America.* November 2009. Access mode: <http://www.ingaa.org/file.aspx?id=9373> (date of access: 29.04.2016).

11. ORMAT web site. Available: <http://www.ormat.com/case-studies/loreburn> (Accessed: 20.05.2016).

12. *Ekologicheskiy otchet OAO «Gazprom» za 2014 god* (Date of access: 29.04.2016). (rus.)

13. **Zabelin N.A., Olennikov S.Yu., Saychenko A.S., Sivokon V.N., Smirnov Ye.T., Smirnov M.V.** Eksperimentalnyy stand dlya issledovaniya vysokooborotnoy vozduшной модели odnostupenchatoy maloraskhodnoy turbiny konstruksii LPI moshchnostyu 260 kVt. *Nauchno-tekhnicheskiy zhurnal «Nauka i tekhnika v gazovoy promyshlennosti»*. 2015. № 3. S. 33–39. (rus.)

14. **Filippov G.A., Povarov O.A., Pryakhin V.V.** Issledovaniya i raschety turbin vlazhnogo para. M.: Energiya, 1973. 232 s.

15. **Deych M.Ye., Filippov G.A.** Gazodinamika dvukhfaznykh sred. 2-ye izd., pererab. i dop. M.: Energoizdat, 1981. 472 s. (rus)

16. **Kirillov I.I., Yablonik P.M.** Osnovy teorii vlahnoparovykh turbin. L.: Mashinostroyeniye, 1968. 264 s. (rus.)

17. **Zabelin N.A.** Issledovaniye separatsii vlagi v podvodyashchikh i perepusknykh patrubkakh parovykh turbin: Diss. ... kand. tekhn. nauk. L., 1982. (rus.)

СПИСОК ЛИТЕРАТУРЫ

1. **Сайченко А.С.** Разработка парогазовой установки мощностью 250 кВт для утилизации теплоты уходящих газов газоперекачивающих агрегатов // Открытая научно-практическая конференция молодых работников "Внедрение передовых технологий и технических решений, разработанных с участием молодежи – неотъемлемая составляющая развития общества": Сборник докладов. Газпром трансгаз Санкт-Петербург. 2012. Т. 1. С.

2. **American patent US611792 A.** Engine / Frank W. Ofeldt. 1898.

3. **Pytilinski J.T.** Solar energy installations for pumping irrigation water // *Solar Energy.* № 21(4). 1978. P. 255 – 262.

4. **Томаров Г.Н., Никольский А.И., Семенов В.Н., Шипков А.А.** Геотермальная энергетика: Справочно-методическое издание / Под. ред. П.П. Безруких. М.: "Интертехэнерго-Издат", "Теплоэнергетик", 2015. 304 с.

5. **Гришутин М.М.** Паротурбинные установки с органическими рабочими телами. Ленинград: Машиностроение, 1988. 219 с.

6. **Quoilin S., Lemort V.** Technological and Economical Survey of Small-Scale Organic Rankine Cycle Systems // *Fifth European conference, Economics and management of energy in industries.* 2009. Access mode: <http://www.eolss.net/sample-chapters/c05/E6-35-43-00.pdf> (date of access: 29.04.2016).

7. **Emiliano I.M. Casati** New concepts for Organic Rankine Cycle // *Power Systems.* Milan, 2014.

8. **Van den Broek M., Chys M., Vanslambrouck B., De Paepe M.** Increasing the efficiency and generated

electricity of organic rankine cycles by using zeotropic mixtures as working fluids // *9th International Conference on Heat Transfer, Fluid Mechanics and Thermodynamics* 16–18 July 2012. Malta.

9. **Campana F., Bianchi M., Branchini L., Pascale A. De., Peretto A., Baresi M., Fermi A., Rossetti N., Vescovo R.** ORC waste heat recovery in European energy intensive industries: *Energy and GHG savings. 2013.* Access mode: <http://www.sciencedirect.com/science/article/pii/S0196890413004123> (date of access: 29.04.2016).

10. Status of Waste Heat to Power Projects on Natural Gas Pipelines. *Interstate Natural Gas Association of America.* November 2009. Access mode: <http://www.ingaa.org/file.aspx?id=9373> (date of access: 29.04.2016).

11. ORMAT web site. Available: <http://www.ormat.com/case-studies/loreburn> (Accessed: 20.05.2016).

12. *Экологический отчет ОАО «Газпром» за 2014 год.* (Дата обращения: 29.04.2016).

13. **Забелин Н.А., Оленников С.Ю., Сайченко А.С., Сивоконь В.Н., Смирнов Е.Т., Смирнов М.В.** Экспериментальный стенд для исследования высокооборотной воздушной модели одноступенчатой малорасходной турбины конструкции ЛПИ мощностью 260 кВт // *Наука и техника в газовой промышленности.* 2015. № 3. С. 33–39.

14. **Филиппов Г.А., Поваров О.А., Пряхин В.В.** Исследования и расчеты турбин влажного пара. М.: Энергия, 1973. 232 с.

15. **Дейч М.Е., Филиппов Г.А.** Газодинамика двухфазных сред. 2-е изд., перераб. и доп. М.: Энергоиздат, 1981. 472 с.

16. Кириллов И.И., Яблоник Р.М. Основы теории влажнопаровых турбин. Л.: Машиностроение, 1968. 264 с.

17. Забелин Н.А. Исследование сепарации влаги в подводящих и перепускных патрубках паровых турбин : Дисс. ... канд. техн. наук. Л., 1982.

СВЕДЕНИЯ ОБ АВТОРАХ/AUTHORS

ZABELIN Nikolai A. – Peter the Great St. Petersburg Polytechnic University.
29 Politechnicheskaya St., St. Petersburg, 195251, Russia.
E-mail: n. zabelin.turbo@mail.ru

ЗАБЕЛИН Николай Алексеевич – кандидат технических наук директор института энергетики и транспортных систем Санкт-Петербургского политехнического университета Петра Великого. 195251, Россия, г. Санкт-Петербург, Политехническая ул., 29.
E-mail: n. zabelin.turbo@mail.ru

SAYCHENKO Aleksandr S. – Peter the Great St. Petersburg Polytechnic University.
29 Politechnicheskaya St., St. Petersburg, 195251, Russia.
E-mail: Saychen@yandex.ru

САЙЧЕНКО Александр Сергеевич – аспирант Санкт-Петербургского политехнического университета Петра Великого. 195251, Россия, г. Санкт-Петербург, Политехническая ул., 29.
E-mail: Saychen@yandex.ru



DOI 10.5862/JEST.249.2

УДК 621.31

A.U. Shabanov, A.B. Zaitsev, A.A. Metelev, Y.P. Pystovalov

SIMULATION PARAMETERS OF FRICTION AND WEAR CONJUGATION IN THE FRICTION CYLINDER

А.Ю. Шабанов, А.Б. Зайцев, А.А. Метелев, Ю.П. Пустовалов

МОДЕЛИРОВАНИЕ ПАРАМЕТРОВ ТРЕНИЯ И ИЗНОСА СОПРЯЖЕНИЙ ТРЕНИЯ ЦПГ ПОРШНЕВОГО ДВИГАТЕЛЯ

The article presents the results of research which aims to develop a model of the friction units of the cylinder-piston group, i.e., the “piston ring — cylinder liner” and “piston trunk — cylinder liner” couples taking into account the change in the real state of the working surfaces of the mating parts and lubricating oil. We have examined the factors that have a progressive impact on the operation of the engine friction units during their wear life. The impact of these factors on the wear and forecasting it has been assessed. We propose the method for predicting the operation life and the real state of the engine. An experimental study to validate the developed method to the particular engine has been conducted.

WEAR; INTERNAL COMBUSTION ENGINE; LIFE PREDICTION; ENGINE OIL; TRIBOUNIT.

В статье представлены результаты научно-исследовательской работы, цель которой — разработать модель узлов трения цилиндропоршневой группы, а именно пар «поршневое кольцо — втулка цилиндра» и «тронк поршня — втулка цилиндра». Модель учитывает изменение реального состояния рабочих поверхностей сопрягаемых деталей (тронк поршня, первое и второе поршневое кольцо, масляное кольцо, зеркало цилиндра, коренные и шатунные шейки и вкладыши коленчатого вала) и смазочного масла. Рассматриваются факторы, оказывающие прогрессирующее влияние на работу узлов трения двигателя по мере их износа. Оценена степень влияния этих факторов на износ и его прогнозирование. Предложен метод для прогнозирования ресурса и реального состояния двигателя. Проведено экспериментальное исследование для подтверждения правильности разработанной методики на конкретном двигателе.

ИЗНОС; ДВИГАТЕЛЬ ВНУТРЕННЕГО СГОРАНИЯ; ПРОГНОЗИРОВАНИЕ РЕСУРСА; МОТОРНОЕ МАСЛО; ТРИБОСОПРЯЖЕНИЯ.

Introduction

Change of technical and economic parameters of the engine during the service life (from the beginning of operation to write-off) in many respects is defined by dependence on real condition of its friction units, first of all — the cylinder-piston group (CPG). However the existing models describing the frictional processes in an internal combustion engine (ICE) do not consider the change dynamics of the key design data during the deterioration of the friction couples.

Research objective is to propose the model of work of the cylinder-piston group friction units (couples «piston ring-cylinder liner» and «piston trunk-cylinder liner») considering change of real condition of the working surfaces of mating parts and lubricating oil.

Method of achieving this goal. We will emphasize the following from the factors having essential impact on work of CPG friction units and changing itself during operation:

1) change the gap values in CPG friction mating caused by processes of wear of cylinder liner working surfaces, pistons, and piston rings. As practice shows, the basic wear is occurred in the forming cylinder liner leading to formation the difficult conical and oval profile of its working surface. Tracking of this profile with elastic piston rings leads to continuous change of expansion gap values in the piston ring joints, and the average values of the gaps tends to increase in the process of wear. Losses of working medium in the combustion chamber are defined generally by leakages through the ring expansion gaps [1, 2] therefore

the current state of the forming cylinder liner significantly influences on the course of the indicator process in the engine cylinders and on the piston ring gas loads. The mechanism of rising force formation in the gaps under the rings and the piston allows us to neglect the cylinder working surface deplanation caused by wear and thereby not to consider this factor at the change of the form of the gaps and impinging angles of the flat bearing formed in these couplings. At the same time it is necessary to consider the change of the form for the friction surfaces of the piston rings and piston trunk caused by wear;

2) change the current state of the working surfaces of the CPG parts caused by accumulation the friction defects on them in use. In spite of this factor is especially casual, it has essential impact on work of the CPG flat bearings, changing the value and nature of distribution in them the rising force hydrodynamic pressure;

3) change the physical and chemical parameters of lubricating oil in the course of its long work, first of all the change of kinematic viscosity and the composition of the antiwear additives complex influencing friction coefficients in the couplings at disturbances of the friction hydrodynamic regime.

The first two factors are constant operating ones; their influence gradually increases in the process of the engine operating time during the period from the beginning of operation (the end of the break-in period) till capital repairs when there is a restoration of the friction units. The third factor is cyclic, acting between maintenance of the engine with change of engine oil.

As a result of the complex of theoretical and experimental studies conducted by the authors for the last years the approaches allowing to enter into classical model the description of the frictional processes in ICE CPG [1, 3, 4] the majority of the above influence factors of engine current state on the indicators of friction and wear have been formulated.

The factor of change the gaps in CPG friction mating is considered as follows.

Taking into account the leakage values of working medium from the combustion chamber on the indicator process in ICE cylinders is realized by the joint solution of the equations of the first law of thermodynamics for the combustion chamber and beyond ring volumes formed by lateral surfaces of the piston rings and the piston with cylinder walls [6, 7].

Calculated and Experimental Assessment

The system of the differential equations describing the mentioned thermodynamic process has the following appearance:

$$\partial Q_T - \partial Q_W = \partial U + \partial A + \sum i_k \partial M_k + i_{pr} \partial M_{pr}.$$

Where $\partial T = g_c Q_T \partial x$ — heat released during combustion of fuel; g_c — cyclic fuel feed, kg/cycle; Q_T — fuel net calorific value, J/kg; x — relative heat; $\partial Q_W = \alpha_G F_W (T - T_w) dt$ — heat loss due to heat exchange with the combustion chamber walls; α_G — medium over the surface instantaneous heat transfer coefficient from working medium, W/m · K; F_W — heat exchange surface area; T, T_w — temperatures of working medium and the combustion chamber surface, respectively, K; $\partial U = \partial (M C_V T) dt$ — change in internal energy of the thermodynamic system; M — mass, C_V — isochoric heat capacity of working medium; $\partial A = \Pi \partial V$ — work instantaneous value; P — working medium pressure, ∂V — cylinder volume change; $i_k, \partial M_k$ — respectively enthalpies and working medium mass flows through the valves and piston ring joints of CPG; $i_{pr}, \partial M_{pr}$ — respectively enthalpies and working medium mass flows through gappings of the first piston ring to the cylinder liner surface.

The masses of leakages of working medium from the combustion chamber in the engine case depend on piston rings set gas tightness, and consequently, on degree of the cylinder wear [8-10]. The real condition of the cylinder liner is considered by use in the calculation the profile of the deformed and worn out cylinder generatrix, gained by direct measurement, or by modeling of cylinder wear, for example by means of the technique [6]. Taking into account the local deformation and wear of the cylinder liner the current gap in the piston ring joint changes:

$$\Delta_k(z) = \Delta_{ko}(T_k) + 2\pi\Delta(z, T_G),$$

where $\Delta_k(z)$ — current gap in the piston ring joint; $\Delta_{ko}(T_k)$ — expansion gap in the joint at the ring temperature T_k ; $\Delta(z, T_G)$ — cylinder generatrix radial deformation at the operating temperature of the sleeve T_G taking into account its wear.

Figure 1 shows the results of gas load modeling at the first and second ring of the piston for the forced diesel at different degrees of the engine wear. These

results indicate that in the process of wear because of increase the leakages from the combustion chamber the gas load of the first piston ring decreases, but of the second one — increases. Influence of growth of leakages on the indicator showings of the engine in general is insignificant and is shown generally in a zone of small rotation frequencies of the crank shaft. Such redistribution of the gas load influences the power of friction losses and extent of wear zones.

Taking note of the real condition of the friction surfaces on formation of the bearing ability of the piston rings and piston trunks is carried out in the following way: the parameter which is conditionally called the “damage surface factor” is entered into the mathematical model for calculation the thickness of a lubricant layer in these couplings. It is calculated on the following dependence:

$$\Omega = \frac{P_{rf \text{ real}}}{P_{rf \text{ id}}}$$

where $P_{rf \text{ real}}$ — pressure of the hydrodynamic rising force for the real worn bearing, having certain amount of friction defects; $P_{rf \text{ id}}$ — pressure of the hydrodynamic rising force for the bearing with an ideal surface on the same design conditions.

To determine the values of damage surface factor there was the special calculated experiment at which

the numerical modeling of the hydrodynamic processes in the flat bearing with different types, sizes and amount of conditional friction defects in comparison to the ideal bearing under identical conditions of loading was carried out. In figures 2 and 3 the typical pictures of distribution of the hydrodynamic pressure in the bearings having a certain amount of friction defects are presented.

Taking into account this refinement, the final systems of the differential equations for the description the processes of formation of the hydrodynamic lubricant layers look as follows:

for the piston rings

$$\begin{aligned} \partial C_k / \partial \varphi = \pi Dh \left[(P_i - P_{i-1}) / 2 - P_y - \right. \\ \left. - 1,01 \mu(M) \Omega_i h_i^2 (C_k - C_p (\alpha_i + \delta / 2 h_i)) / \delta^3 \right] / 6 n m_k ; \\ \partial C_k / \partial \varphi = C_k / 6 n, \end{aligned}$$

where C_k — radial movement speed of the piston ring; α_i, h_i — parameters describing the working profile of the piston ring; m_k — ring mass; $\mu(M)$ — medium viscosity where tgh piston ring works; Ω_i — damage surface factor, considering existence on a working surface of the friction couple the defects caused by wear process; it is defined on the basis of the analysis of a profilogram of the worn-out rin;

Changing the gas load when worn

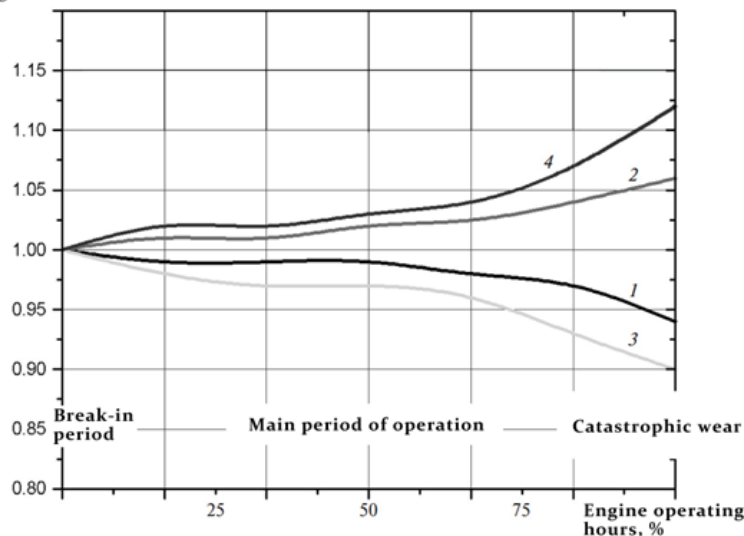


Fig. 1. The relative change in gas load at the first and second piston ring of the forced diesel various modes of operation depending on the engine wear factor (relative to the initial state): 1 — first ring, crank shaft high speed mode; 2 — second ring, crank shaft high speed mode; 3 — first ring, crank shaft low speed mode; 4 — second ring, crank shaft low speed mode

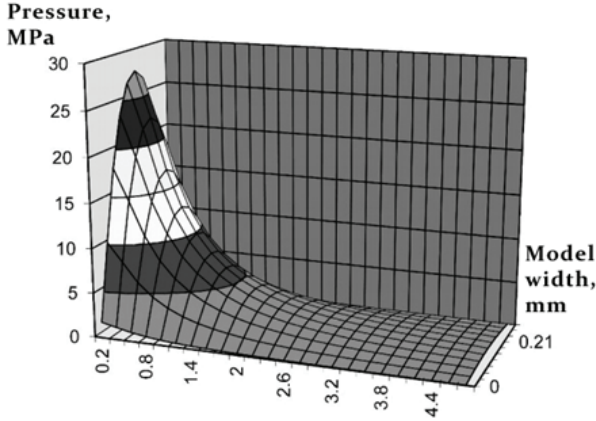


Fig. 2. Diagram of the hydrodynamic pressure in the ideal bearing

for the oil scraper ring this system of equations can be written as

$$\begin{aligned} \partial C_k / \partial \varphi &= \pi D h_{ic} \left[\rho_M C_p^2 / \pi^2 - P_y - \right. \\ &\left. - 1,01 \mu \Omega_4 h_{ic}^2 (C_K - C_p (\delta / 2 h_{ic})) / \delta^3 / 6 n m_k \right]; \\ \partial \delta / \partial \varphi &= C_k / 6 n, \end{aligned}$$

where ρ_M — oil density; h_{ic} — height of the scrapers work surfaces for the oil scraper ring;

for the piston trunk

$$\begin{cases} m_p \frac{dc_r}{d\varphi} = \frac{1}{6n} (\Omega P_{GD} - P_N); \\ J_p \frac{d\omega_p}{d\varphi} = \frac{1}{6n} (\Omega M_{GD} - M_N); \\ \frac{d\delta_{\min}}{d\varphi} = \frac{c_r}{6n}; \\ \frac{d\alpha}{d\varphi} = \frac{\omega_p}{6n}, \end{cases}$$

where P_N — normal force acting on the piston; M_N — longitudinal force moment relative to the piston pin axis; P_{GD} — hydrodynamic force acting on the piston,

$$\begin{aligned} P_{GD} &= 6\mu c_p \int_0^x dx \int_0^x \frac{dt}{(\delta_0 + \delta^*)} + 12\mu \frac{d\delta}{dt} \int_0^L dx \int_0^x \frac{t dt}{(\gamma_0 + \delta^*)^3} - \\ &- 6\mu c_p \Delta \varphi \left(1 + \frac{12B(\varphi)n}{A(\varphi)c_p} \frac{d\delta}{dt} \right) \int_0^x dx \int_0^x \frac{dt}{(\delta_0 + \delta^*)^3}; \end{aligned}$$

$$A(\varphi) = \int_0^L \frac{dx}{\delta^2} \Big/ \int_0^L \frac{dx}{\delta^3}; \quad B(\varphi) = \int_0^L \frac{xdx}{\delta^3} \Big/ \int_0^L \frac{dx}{\delta^3};$$

μ — dynamic oil viscosity; L — trunk length; M_{GD} — hydrodynamic force moment, acting on the piston relative to the piston pin axis,

$$M_{GD} = \int_{L_1}^{L_2} x dx \int_{-90}^{90} P(x, \varphi, \theta) \cos \theta d\theta;$$

m_p — piston mass; J_p — piston moment of inertia relative to the rotational axis (piston pin); c_r — radial movement speed of the piston forming an oil layer; ω_p — angular speed of the piston; φ — crank rotation angle; n — engine rotation speed; δ_{\min} — minimum gap in front of the trunk; α — angle of obliquity of the piston axis relative to the cylinder axis.

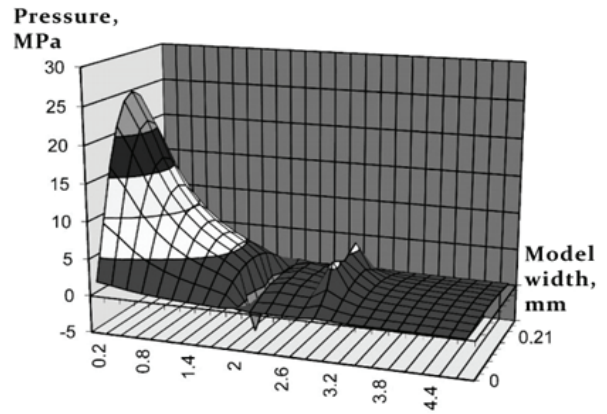


Fig. 3. Diagram of the hydrodynamic pressure in the ideal bearing with two friction defects

Figure 4 shows the calculation results of the relative change for lengths of the friction tracks (wear zones) on the walls of the cylinder liners of the forced diesel at different stages of its wear. Figure 5 shows the calculation results of power of mechanical losses in CPG for the same diesel during its work on the external speed characteristic at the same stages of wear.

Results of the Computational and Experimental Studies

The modeling results show that at small and average stages of wear the power of the mechanical losses in a set of the piston rings becomes slightly less than calculated power for the initial condition of the engine. The factor of some decrease in the gas load level of the first piston ring affects with a growth of

gaps, thus the damage factor value is still rather small and poorly influences the lubricant layer thickness. With a growth of the surface damage degree that is characteristic at high degrees of the engine wear, there is a noticeable falling of the oil layer bearing ability value leading to increase the boundary friction zone. At the same time the power of mechanical losses grows; and this factor starts influencing much more, than the gas loading change of the rings caused by the progressing wear.

Changing the gas load when worn

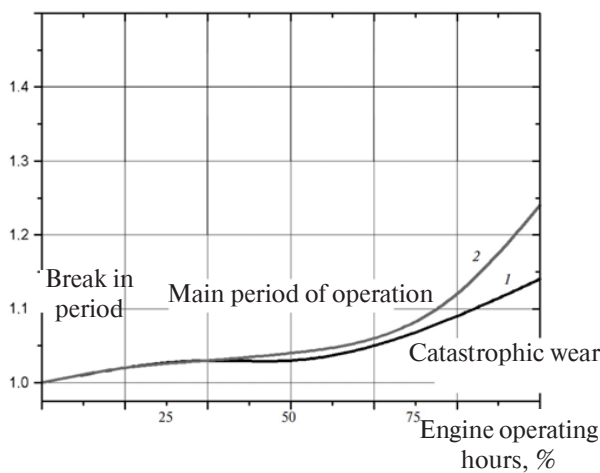


Fig. 4. Relative change of the lengths of the friction tracks on the working surface of the cylinder liners for the forced diesel at various modes of operation depending on the engine wear factor (relative to the initial state): 1 — crank shaft high speed mode; 2 — crank shaft low speed mode

Friction power in CPG, kW

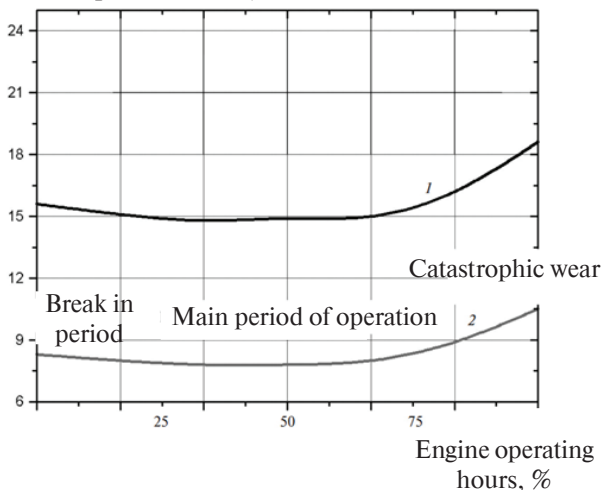


Fig. 5. Changing the friction power in the forced diesel CPG for various modes of operation depending on the engine wear factor: 1 — crank shaft high speed mode; 2 — crank shaft low speed mode

Oil kinematic viscosity, cSt

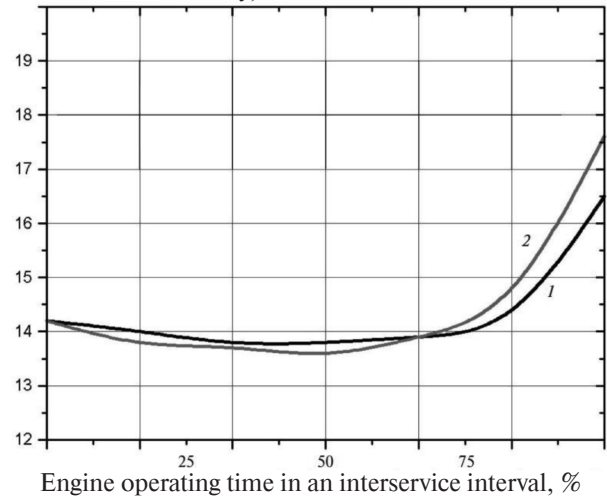


Fig. 6. Change the engine oil kinematic viscosity at different periods of its use: 1 — at the modes with crank shaft high speed; 2 — at the modes with crank shaft low speed

The factor of change of the physical and chemical parameters of the lubricating oil depending on lubrication operating time degree in the engine in an interservice interval is considered by use the dependence of the engine oil kinematic viscosity. It is calculated with the help of the Walter unified dependence [5]:

$$\lg \lg(n) = A(\tau) + B(\tau)t + C(\tau)t^2;$$

$$\lg \lg(v_t) = A(\tau) + B(\tau)t + C(\tau)t^2,$$

where v_t — desired value of the kinematic viscosity at the temperature t , cSt; t — temperature, °C; $A(\tau)$, $B(\tau)$, $C(\tau)$ — approximation coefficients taking into account oil operating time in an interservice interval.

Approximation coefficients of the oil viscosity change were determined for big sample group of marketable oils by the long resource tests according to the technique of the SPBPU DAiGM chair. Typical curve of viscosity changes for lubricating oil in the period of an interservice interval are shown in fig. 6.

Conclusion

Numerous calculated researches the work of the CPG friction units in the piston ICEs show that all three factors progressing in the process of engine wear have approximately equivalent impact on the engine outcome indicators and therefore have to be considered in forecasting of the ICE resource indicators. The offered technique realizes rather effective tool for solving this problem.

REFERENCES

1. **Petrichenko R. M., Baturin S.A., Isakov Yu.N. [i dr].** Elementy sistemy avtomatizirovannogo proyektirovaniya DVS: Algoritmy prikladnykh programm / Pod obshch. red. R.M. Petrichenko. L.: Mashinostroyeniye, 1990. 328 s. (rus.)
2. **Petrichenko R.M.** Fizicheskiye osnovy vnutritsilindrovyykh protsessov v dvigatelyakh vnutrennego sgoraniya. L.: Izd.-vo Leningr. un—ta, 1983. 244 s. (rus.)
3. **Petrichenko R.M., Shabanov A.Yu. [i dr].** Treniye i teploobmen v porshnevnykh koltsakh DVS. L.: Izd.-vo LGU, 1990. 320 s. (rus.)
4. **Shabanov A.Yu., Zaytsev A.B., Ryzenkov Yu.V.** Vliyaniye sostoyaniya poverkhnostey treniya dvigatelya vnutrennego sgoraniya na iznos detaley i kharakteristiki yego raboty. *Nauchno-tekhnicheskiye vedomosti SPbGPU. Osnovnoy vypusk.* 2008. № 2(54). S. 199–202.
5. **Shabanov A.Yu., Zaytsev A.B., Kudinov I.S.** O novykh metodakh approksimatsii vysokotemperaturnoy kinematicheskoy вязkosti motornykh masel. *Nauchnyye issledovaniya i innovatsionnaya deyatel'nost: Materialy nauch.-prakt. konf. SPb.: Izd.-vo Politekhn. un—ta, 2011. – S. 42–50.* (rus.)
6. **Galyshev Yu.V., Shabanov A.Yu., Zaytsev A.B., Metelev A. A.** Metodika uskorennykh ispytaniy motornykh masel na izmeneniye ikh svoystv v techeniye sroka ekspluatatsii. *Nauchno-tekhnicheskiye vedomosti SPbGPU.* 2012. № 1(147). S. 71–76. (rus.)
7. **Shabanov A.Yu., Zaytsev A.B., Kudinov I.S., Metelev A.A.,** Vliyaniye nekotorykh fiziko-khimicheskikh pokazateley motornogo masla na tekhniko-ekonomicheskkiye i resursnyye pokazateli porshnevnykh benzinovyykh dvigateley. *Dvigatelsestroyeniye.* 2011. № 1. S. 24–28. (rus.)
8. **Kolchin A.I., Demidov V.P.** Raschet avtomobilnykh i traktornykh dvigateley : Ucheb. Posobiye dlya vuzov. 3-ye izd. pererab. i dop. M.: Vyssh. shk., 2002. 496 s. (rus.)
9. **Dyachenko N.Kh., Kharitonov B.A., Petrov V.M. [i dr].** Konstruirovaniye i raschet dvigateley vnutrennego sgoraniya / Pod red. N.Kh. Dyachenko. L.: Mashinostroyeniye. 1979. 392 s. (rus.)
10. **Vasilyev B. N.** Zavisimost soprotivleniya treniya porshnevnykh kolets ot davleniya na ikh rabochuyu poverkhnost. *Izvestiya vuzov. Mashinostroyeniye.* 1967. № 7. S. 15–18. (rus.)

СПИСОК ЛИТЕРАТУРЫ

1. **Петриченко Р.М., Батури С.А., Исаков Ю.Н. [и др].** Элементы системы автоматизированного проектирования ДВС: Алгоритмы прикладных программ. / Под общ. ред. Р.М. Петриченко. Л.: Машиностроение, 1990. 328 с.
2. **Петриченко Р.М.** Физические основы внутрицилиндровых процессов в двигателях внутреннего сгорания. Л.: Изд—во Ленингр. ун—та, 1983. 244 с.
3. **Петриченко Р. М., Шабанов А. Ю. [и др].** Трение и теплообмен в поршневых кольцах ДВС. Л.: Изд.-во ЛГУ, 1990. 320 с.
4. **Шабанов А.Ю., Зайцев А.Б., Рыженков Ю.В.** Влияние состояния поверхностей трения двигателя внутреннего сгорания на износ деталей и характеристики его работы // Научно-технические ведомости СПбГПУ. Основной выпуск. 2008. № 2 (54). С. 199–202.
5. **Шабанов А.Ю., Зайцев А.Б., Кудинов И.С.** О новых методах аппроксимации высокотемпературной кинематической вязкости моторных масел // Научные исследования и инновационная деятельность: Материалы науч.-практ. конф. СПб.: Изд-во Политехн. ун-та, 2011. С. 42–50.
6. **Галышев Ю.В., Шабанов А.Ю., Зайцев А.Б., Метелев А.А.** Методика ускоренных испытаний моторных масел на изменение их свойств в течение срока эксплуатации // Научно-технические ведомости СПбГПУ. 2012. № 1(147). С. 71–76.
7. **Шабанов А.Ю., Зайцев А.Б., Кудинов И.С., Метелев А.А.** Влияние некоторых физико-химических показателей моторного масла на технико-экономические и ресурсные показатели поршневых бензиновых двигателей // Двигателестроение. 2011. № 1. С. 24–28.
8. **Колчин А.И., Демидов В.П.** Расчет автомобильных и тракторных двигателей: Учеб. Пособие для вузов. 3-е изд. перераб. и доп. М.: Высш. шк., 2002. 496 с.
9. **Дьяченко Н.Х., Харитонов Б.А, Петров В.М. [и др].** Конструирование и расчет двигателей внутреннего сгорания / Под ред. Н.Х. Дьяченко. Л.: Машиностроение, 1979. 392 с.
10. **Васильев Б. Н.** Зависимость сопротивления трения поршневых колец от давления на их рабочую поверхность // Известия вузов. Машиностроение. 1967. № 7. С. 15–18.

СВЕДЕНИЯ ОБ АВТОРАХ/AUTHORS

SHABANOV Aleksandr Yu. – Peter the Great St. Petersburg Polytechnic University.
29 Politechnicheskaya St., St. Petersburg, 195251, Russia.
E-mail: aush2003@mail.ru

ШАБАНОВ Александр Юрьевич – кандидат технических наук профессор Санкт-Петербургского политехнического университета Петра Великого.
195251, Россия, г. Санкт-Петербург, Политехническая ул., 29.
E-mail: aush2003@mail.ru

ZAITSEV Aleksei B. – Peter the Great St. Petersburg Polytechnic University.
29 Politechnicheskaya St., St. Petersburg, 195251, Russia.
E-mail: abzaytsev@mail.ru

ЗАЙЦЕВ Алексей Борисович – кандидат технических наук доцент Санкт-Петербургского политехнического университета Петра Великого.
195251, Россия, г. Санкт-Петербург, Политехническая ул., 29.
E-mail: abzaytsev@mail.ru

METELEV Andrei A. – Peter the Great St. Petersburg Polytechnic University.
29 Politechnicheskaya St., St. Petersburg, 195251, Russia.
E-mail: petmet@mail.ru

МЕТЕЛЕВ Андрей Александрович – аспирант Санкт-Петербургского политехнического университета Петра Великого.
195251, Россия, г. Санкт-Петербург, Политехническая ул., 29.
E-mail: petmet@mail.ru

PYSTOVALOV Yuri P. – Peter the Great St. Petersburg Polytechnic University.
29 Politechnicheskaya St., St. Petersburg, 195251, Russia.
E-mail: yurapust@mail.ru

ПУСТОВАЛОВ Юрий Петрович – аспирант Санкт-Петербургского политехнического университета Петра Великого.
195251, Россия, г. Санкт-Петербург, Политехническая ул., 29.
E-mail: yurapust@mail.ru

DOI 10.5862/JEST.249.3

УДК 621.225.2: 62.822

A.V. Matrosov, Yu.M. Isaev, R.A. Sunarchin

MATHEMATICAL MODELING OF AN ELECTROHYDRAULIC DRIVE FOR A HYDRAULIC TURBINE

A.B. Матросов, Ю.М. Исаев, Р.А. Сунарчин

МАТЕМАТИЧЕСКОЕ МОДЕЛИРОВАНИЕ МНОГОМАШИННОГО СЛЕДЯЩЕГО ЭЛЕКТРОГИДРОПРИВОДА КОЛЬЦЕВОГО ЗАТВОРА ГИДРОТУРБИНЫ

The results of a systematic study of two mathematical models of a multi-actuator electro-hydraulic drive designed for a ring gate of hydraulic turbine movement are presented in the work. We have investigated the main factors which have a negative impact on the synchronization of the servo cylinder movement, such as the load capacity, the external forces – additionally applied to the servo cylinders, and the manufacturing error of hydraulic cylinder pistons. Functional dependences of the synchronization error from these factors have been obtained. These dependences allow to develop reasonable recommendations for selecting the main parameters of the hydraulic drive and determine the operation regularities of this drive.

RING GATE OF HYDRAULIC TURBINE; MULTIACTUATOR HYDRAULIC DRIVE; SYNCHRONIZATION OF HYDRAULIC CYLINDER; MATHEMATICAL MODELING; MATLAB.

В статье приводятся результаты систематического исследования двух математических моделей многомашинных следящих гидроприводов, предназначенных для маневрирования кольцевым затвором гидротурбины. Исследованы основные факторы, оказывающие негативное влияние на синхронность работы исполнительных гидродвигателей, такие, как: масса перемещаемой нагрузки; внешние силы, дополнительно прикладываемые к сервоцилиндрам; разница эффективных площадей поршней гидродвигателей, вызванная технологической погрешностью изготовления. Исследование проведено на основе математического моделирования гидропривода в программном пакете MatLab. Получены зависимости относительной ошибки синхронизации перемещения поршней сервоцилиндров от указанных факторов, позволяющие выработать обоснованные рекомендации для выбора основных параметров гидропривода и определить закономерности работы данного привода, которые могут быть использованы в качестве основы для построения методики моделирования многомашинных гидроприводов кольцевых затворов.

КОЛЬЦЕВОЙ ЗАТВОР ГИДРОТУРБИНЫ; МНОГОМАШИННЫЙ СЛЕДЯЩИЙ ГИДРОПРИВОД; СИНХРОНИЗАЦИЯ ГИДРОЦИЛИНДРОВ; МАТЕМАТИЧЕСКОЕ МОДЕЛИРОВАНИЕ, MATLAB.

To shut-down the supply of water flow to hydraulic turbine in the case of an accident or if need for repair or maintenance work and to reduce leakages through closed guide vanes and prevent the development of a gap cavitation on blades of the guide vanes, pre-turbine gate valve are often set in the penstock. Their alternative are the ring gates, which have the form of annular shield is located between guide vanes and stay vanes. A characteristic feature the gate of this design is use of multi-actuator hydraulic drive for maneuvering of such shield. One of the main requirements for ring gate hydraulic drives is to pro-

vide in-phase synchronous motion of all servo motors (usually - cylinders) included in their structure.

The research results of ring gate multi-actuator hydraulic drive, consisting of 6 cylinders and electro-hydraulic servo control system are outlined below.

The main purpose of this study was to evaluate the influence of external forces acting on the ring gate and technological errors of pistons manufacturing on synchronicity and in-phase operation of electrohydraulic drive. This evaluate could be the basis for the calculation methodology of ring gates multi-actuator hydraulic drive.

The primary goals of the study were: obtaining dependencies of displacement pistons synchronization error on external factors: the mass of the movable load, external forces, additionally applied to the hydraulic cylinders, as well as the difference of effective area of the pistons, caused by technological errors of manufacturing; evaluation of influence the ring gate weight on synchronicity of servo actuators rods movement.

Two mathematical models were considered. In the first model, all rods of hydraulic cylinders connected with a common ring by spring linkage and the ring itself was considered absolutely rigid (fig. 1).

Hydraulic system for the first model consisted of six blocks of the same type, with a common control signal. Schematic diagram of such block is shown in fig.2.

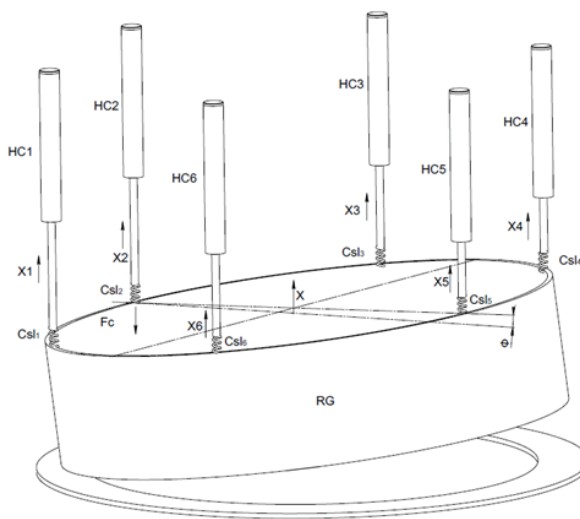


Fig. 1. Kinematic scheme of servodrive: RG – ring gate; HC1,...HC6 – hydraulic cylinder; X1,...X6 – instantaneous displacement of corresponding hydraulic cylinder; Csl1,...Csl6 – stiffness of corresponding spring linkage; X – instantaneous displacement of common ring; F_c – external forces

In describing mathematical drive model following assumptions were made: parameters are lumped; continuity condition of the working fluid is performed; elasticity modulus of working fluid is constant; throttling gaps flow coefficient of electrohydraulic amplifiers are constant; electrohydraulic

amplifiers design is ideal; in mathematical model do not take into account the action of guide supports, on which movement of the gate is performed. Displacements and velocities of hydraulic cylinders and pistons at the initial time were assumed equal to zero.

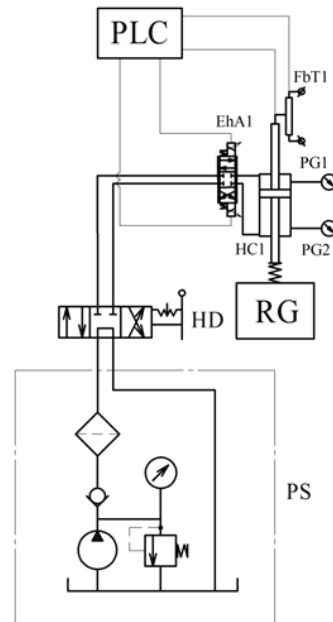


Fig.2. Fragment of hydraulic drive principle diagram: PS – pumping station; HD – hydraulic distributor; RG – ring gate; HC1 – hydraulic cylinder; PG1,PG2 – pressure gauge; EhA1 – electrohydraulic amplifier; FbT1 – feedback transducer; PLC – program logic controller

Each drive unit is described by four nonlinear differential equations: the motion equation of electrohydraulic amplifier, the motion equation of actuator movable part, the equation of flow continuity through the pressure gaps of the spool and lower cylinder chamber and the continuity equation through the top cylinder chamber and drain gaps of the spool.

Thus, the first mathematical model included six systems of equations for each of the blocks and, in addition, equations for common loading moving and its turning.

$$\left\{ \begin{aligned}
 m_{zi} \frac{d^2 z_i}{dt^2} &= K_{Fji} (J_i - K_{fbi} x_i) - K_{vzi} \frac{dz_i}{dt} - C_{emci} z_i; \\
 m_1 \frac{d^2 x_1}{dt^2} &= (p_{11} - p_{21}) S_1 - C_{sl1} (x_1 - X - 0,5R\varphi) - \\
 &- K_{vx1} \frac{dx_1}{dt} - m_1 g - F_{c1} \operatorname{sign} \left(\frac{dx_1}{dt} \right); \\
 m_2 \frac{d^2 x_2}{dt^2} &= (p_{12} - p_{22}) S_2 - C_{sl2} (x_2 - X - R\varphi) - \\
 &- K_{vx2} \frac{dx_2}{dt} - m_2 g - F_{c2} \operatorname{sign} \left(\frac{dx_2}{dt} \right); \\
 m_3 \frac{d^2 x_3}{dt^2} &= (p_{13} - p_{23}) S_3 - C_{sl3} (x_3 - X - 0,5R\varphi) - \\
 &- K_{vx3} \frac{dx_3}{dt} - m_3 g - F_{c3} \operatorname{sign} \left(\frac{dx_3}{dt} \right); \\
 m_4 \frac{d^2 x_4}{dt^2} &= (p_{14} - p_{24}) S_4 - C_{sl4} (x_4 - X + 0,5R\varphi) - \\
 &- K_{vx4} \frac{dx_4}{dt} - m_4 g - F_{c4} \operatorname{sign} \left(\frac{dx_4}{dt} \right); \\
 m_5 \frac{d^2 x_5}{dt^2} &= (p_{15} - p_{25}) S_5 - C_{sl5} (x_5 - X + R\varphi) - \\
 &- K_{vx5} \frac{dx_5}{dt} - m_5 g - F_{c5} \operatorname{sign} \left(\frac{dx_5}{dt} \right); \\
 m_6 \frac{d^2 x_6}{dt^2} &= (p_{16} - p_{26}) S_6 - C_{sl6} (x_6 - X + 0,5R\varphi) - \\
 &- K_{vx6} \frac{dx_6}{dt} - m_6 g - F_{c6} \operatorname{sign} \left(\frac{dx_6}{dt} \right); \\
 M \ddot{X} &= C_{sl1} (x_1 - X - 0,5R\varphi) + C_{sl2} (x_2 - X - R\varphi) + \\
 &+ C_{sl3} (x_3 - X - 0,5R\varphi) + C_{sl4} (x_4 - X + 0,5R\varphi) + \\
 &+ C_{sl5} (x_5 - X + R\varphi) + C_{sl6} (x_6 - X + 0,5R\varphi) - \\
 &- Mg - K_v \dot{X} - F_c; \\
 \mu_i \pi d_{zi} z_i \sqrt{\frac{2}{\rho} (P_s - p_{li})} &= S_i \frac{dx_i}{dt} + \frac{V_{1i}}{E} \frac{dp_{1i}}{dt}; \\
 S_i \frac{dx_i}{dt} &= \mu_i \pi d_{zi} z_i \sqrt{\frac{2}{\rho} (p_{2i} - p_{ci})} + \frac{V_{2i}}{E} \frac{dp_{2i}}{dt}; \\
 J_p \ddot{\varphi} &= F_c R - K_{M\omega} \dot{\varphi} - K_{M\omega} R \sum_{i=1}^6 C_{sli} \varphi,
 \end{aligned} \right.$$

where m_i – mass of the i -th spool; z_i – displacement of the i -th spool; K_{Fji} – electromagnetic converter gain of the i -th electrohydraulic amplifier; J_i – control signal strength of current for the i -th electrohydraulic

amplifier; K_{fbi} – feedback factor of the i -th electro-magnetic amplifier; x_i – stroke of the i -th piston; K_{vzi} – viscous friction coefficient of the i -th spool; C_{emci} – spring stiffness of the i -th electromechanical converter; $m_{1..6}$ – mass of the i -s pistons; $p_{11..16}$, $p_{21..26}$ – pressures in lower and top chambers of hydraulic cylinders respectively; $S_{1..6}$ – effective area of respective pistons; $K_{vx1..6}$ – viscous friction coefficient of respective pistons; $F_{c1..6}$ – dry friction forces, applied to respective pistons; μ_i – coefficient of flow for the i -th spool; P_s – supply pressure; V_{1i} , V_{2i} – values of initial volumes of the lower and top hydraulic cylinders chambers respectively; E – effective bulk modulus of working fluid; $C_{sl1..6}$ – spring linkages stiffness of respective hydraulic cylinders with the common load; X – displacement of the common load; R – radius of the ring gate shield; φ – rotation angle of the ring gate; M – mass of the ring gate; K_v – viscous friction coefficient of the gate; F_c – dry friction force, applied to the gate; J_p – polar moment of inertia for the ring gate shield; $K_{m\omega}$ – viscous friction load coefficient; $K_{M\varphi}$ – positional load coefficient.

The system of differential equations was solved in an integrated environment MATLAB using built-in functions ODE23s.

In the second model was considered hydraulic drive, working with ring gate, conventionally divided into six unrelated among themselves parts. Kinematic diagram of the second model is shown in fig.3.

It was assumed that such a simplified scheme may be useful in the practice of design, when it is necessary to fast (rapid) assessment of the design feature impact on the proposed design solution. Assumptions and initial conditions are taken the same to accepted in the case of model with common gate. Each of the drive, included in hydraulic system, is also described by four nonlinear differential equations: motion equation of electrohydraulic amplifier spool; motion equation of movable part of hydraulic drive; continuity equation through the pressure gaps of spool valve and a lower chamber of hydraulic cylinder and continuity equation through the top chamber of hydraulic cylinder and drain gaps of spool valve.

Thus, the second mathematical model includes 6 systems of equations of the following form:

$$\begin{cases} m_{zj} \frac{d^2 z_i}{dt^2} = K_{Fji}(J_i - K_{fbi} x_i) - K_{vzi} \frac{dz_i}{dt} - C_{emci} z_i; \\ m_i \frac{d^2 x_i}{dt^2} = (p_{1i} - p_{2i}) S_i - K_{vxi} \frac{dx_i}{dt} - m_i g - F_{ci} \text{sign} \left(\frac{dx_i}{dt} \right); \\ \mu_i \pi d_{zi} z_i \sqrt{\frac{2}{\rho} (p_p - p_{1i})} = S_i \frac{dx_i}{dt} + \frac{V_{1i}}{E} \frac{dp_{1i}}{dt}; \\ S_i \frac{dx_i}{dt} = \mu_i \pi d_{zi} z_i \sqrt{\frac{2}{\rho} (p_{2i} - p_{cl})} + \frac{V_{2i}}{E} \frac{dp_{2i}}{dt}. \end{cases}$$

$$\Delta_{rel} = \frac{\Delta}{\Delta_{max}},$$

where Δ – instantaneous synchronization error; Δ_{max} – permissible error.

From fig. 4,a can be seen, that dependence has a non-linear character and error value increases dramatically when approaching gravity force of the load to the maximum value, which can be achieved by hydraulic cylinder. However, in the values area, limited by permissible value of synchronization error (4 mm), characteristic is linear (fig. 4,b).

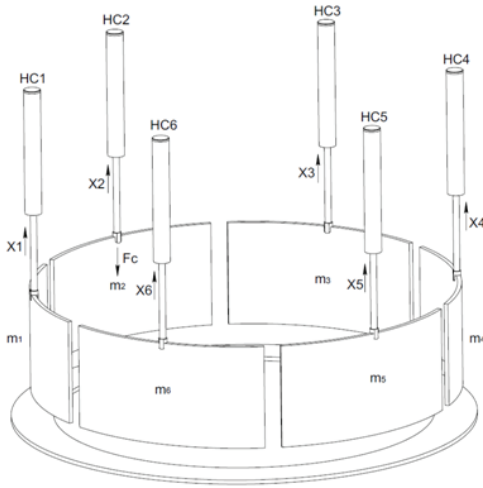


Fig. 3. Kinematic scheme of servodrive

The system of differential equations was solved in a similar way. Calculations showed that at a uniform distribution of the load, the mass attributed per each cylinder, will be equal to 10 t. With this load cylinders are moved synchronously, and synchronization error is absent. During carrying out the numerical experiment, deviation from nominal mass in the range of -100 to 387 % for one of the cylinders was set. Thus, in the final phase of experiment, gravity force of the load was comparable with maximum force, which can be achieved by hydraulic cylinder. According to the results of this numerical experiment, dependence has been built, as shown in fig. 4.

On the horizontal axis in fig. 4 value of relative load is plotted:

$$M_{rel} = \frac{mg}{P_s S_p},$$

where m – load mass, moving by hydraulic cylinder; g – acceleration of gravity; S_p – effective area of the piston;

On the vertical axis in fig. 4 relative synchronization error of piston displacement is plotted:

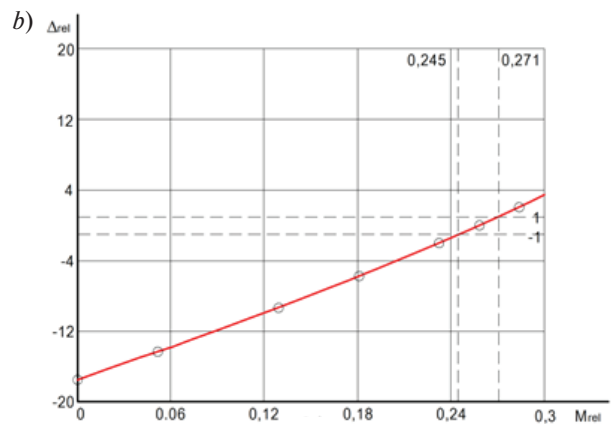
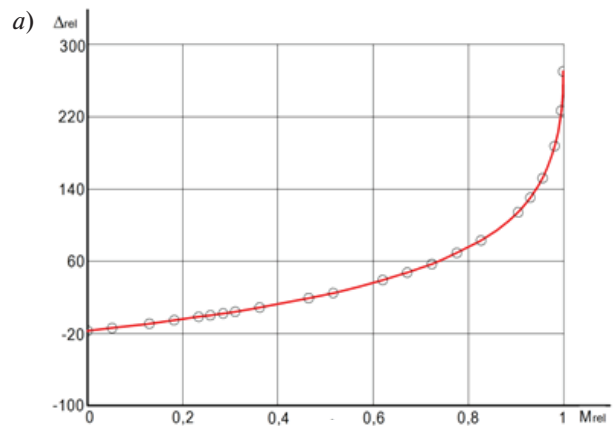


Fig. 4. Dependence of synchronization error of hydraulic cylinders displacement from mass deviation from nominal value in whole range of mass change (a) and in a range, limited by permissible error (b)

Analysis of fig. 4,b allows concluding that permissible value of synchronization error is limited by the ratio of the load weight to the maximum force equal to 27,5 %. Thus the deviation of load mass from the nominal value is 6,6 %.

During carrying out the numerical experiment, external load in the range from 0 to N was applied to one of the hydraulic cylinders additionally apart gravity

force. According to results of this numerical experiment, dependence has been built, as shown in fig. 5.

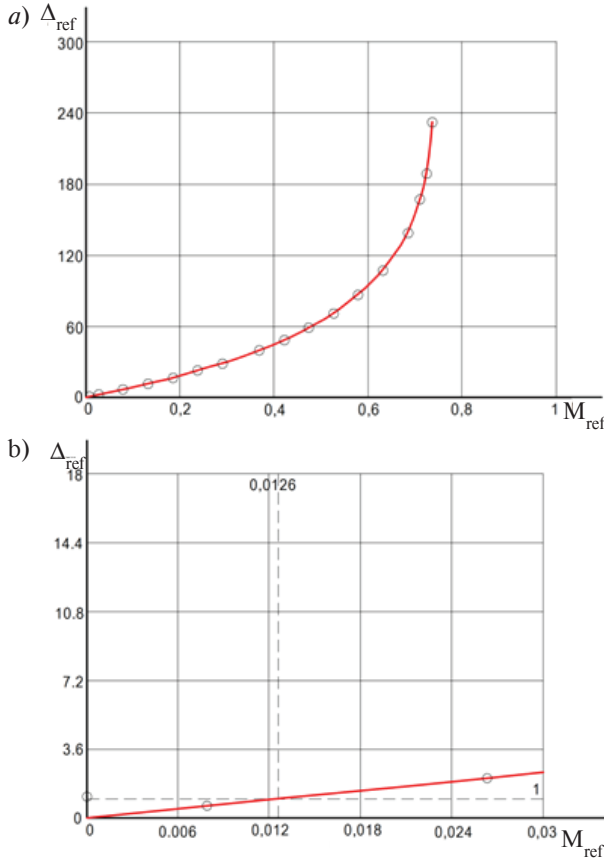


Fig. 5. Dependence of synchronization error of hydraulic cylinders displacement from external load, applied to one of the cylinder in whole range of mass change (a) and in a range, limited by permissible error (b)

On the horizontal axis in fig. 5 value of relative load is plotted:

$$M_{relF} = \frac{F_{ex}}{P_s S_p},$$

where F_{ex} – external force additionally applied to hydraulic cylinder.

On the vertical axis in fig. 5 relative synchronization error of piston displacement is plotted as in fig. 4.

From fig. 5,a it is evident that dependence of synchronization error from external load, applied to the cylinder, is also non-linear, but in range of values, limited by permissible synchronization error, is a linear function (fig. 5,b).

Analysis of fig.5b allows to conclude that permissible value of synchronization error is limited by the ratio of external force is additionally applied to hydrau-

lic cylinder to the maximum force equal to 1,26 %, i.e., maximum value of external load is 4792 N.

Impact of cylinders areas (diameter) difference, which was obtained in the course of numerical experiment, is shown in fig. 6. During calculations, diameter of the cylinder pistons was changed within tolerance, which in the manufacture of piston according to h8, is 89 mkm for 320 mm nominal diameter.

On the vertical axis in fig.6 parameter ΔD_{rel} is plotted:

$$\Delta D_{rel} = \frac{\Delta D}{\Delta D_{max}},$$

where ΔD – instantaneous value of diameter deviation from nominal; ΔD_{max} – maximum value of diameter deviation.

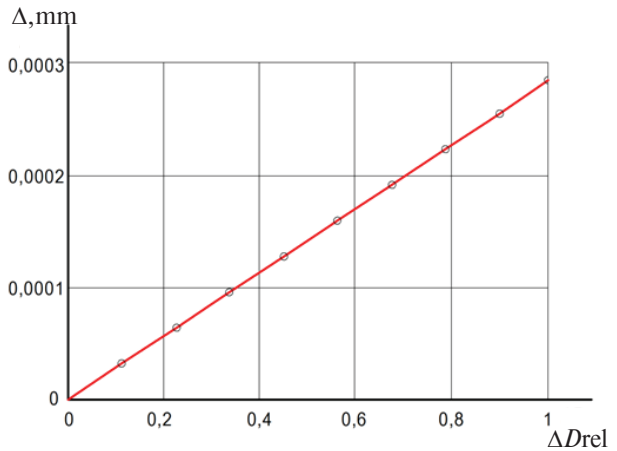


Fig. 6. Dependence of synchronization error from changing the diameter of one of the hydraulic cylinders

On the vertical axis in fig. 6 absolute value of synchronization error is plotted.

From fig.6 it is evident that the synchronization error caused by the change in the diameter of one of the hydraulic cylinders, relative to the nominal value is linear. Maximum synchronization error at a deviation of the piston diameter from the nominal value at 89 microns is 0,284 mm.

Thus, the study of mathematical model of multi-actuator drive with independent mass showed that:

maximum overload of the drive, caused by different values of moved mass, relative to maximum force of the drive, at which synchronization error is within acceptable limits, is not more than 27,5%, or 6,6% relative to the nominal value of the load.

external load, which are additionally applied to hydraulic cylinder, in addition to the current gravity force of the load, also has a significant impact on

synchronicity work of drives. Permissible value of external force to the maximum force is 1,26%.

synchronization error, which is caused by an error within the manufacturing tolerance is insignificant and does not exceed 7% of permissible synchronization error, but due to the action of other factors must be taken into account.

The study of multi-actuator drive mathematical model with a common load allows making the following conclusion:

the presence of common load substantially reduces synchronization error caused by the action of external forces applied directly to the cylinders, how-

ever, makes the drive more responsive to forces applied directly to the gate. The latter is due to the fact that these forces act on significant shoulders (up to 4,5 m), as a consequence, create considerable overturning moments.

The executed theoretical study of multi-actuator hydraulic drive of ring gate for hydraulic turbine, allows to determine common factors of this drive operation, to identify the most influencing factors, and to assess their negative impact on the synchronized movement of pistons and develop sound recommendations for choice of the main parameters of hydraulic drive.

REFERENCES

1. Navrotskiy K.L. Analiz dinamiki sinkhronnogo gidroprivoda koltseвого zatvora gidroturbiny. *Russian Engineering Research*. 2005. № 2. S. 3–8. (rus.)
2. Potetenko O.V., Shevchenko N.G., Koval Ie.S. Chislennoye modelirovaniye gidrodinamicheskogo usiliya, deystvuyushchego na koltsevoy zatvor v protsesse yego opuskaniya v protochnuyu chast radialno-osevoy gidroturbiny. *HPI publ. Kharkov*. 2012. № 54. S. 176–186. (rus.)
3. Shevchenko N.G., Koval E.C. Prognozirovaniye gidravlicheskoй sily vozdeystviya potoka vody na koltsevoy zatvor gidroturbiny.[Prediction of hydraulic power flow impact water annular valve turbines]. *Modern Directions of theoretical and applied researches*. 2013. № 2. S. 74–81. (rus.)
4. Deng Yingjian. Research on active synchronous control system of hydraulic press and its reliability analysis. *Second International Conference on Digital Manufacturing&Automation*. 2011. P. 940–943.
5. Dou Haibin, Wang Shaoping. Synchronization Control of Hydraulic Horizontal Regulation System. *6th IEEE Conference on Industrial Electronics and applications*. 2011. P. 1922–1927.
6. Guo Chunli, Guodong Wang, Juliang Xiao. Numerical Simulation for Hydraulic Characteristics of Cylindrical Valve in Runaway Protection Process. *Power and Energy Engineering Conference. APPEEC*. 2009. Asia – Pacific. – P. 201–205.
7. Guo Chunli, Li Zhifeng, Du Chenyang, Wang Fengyang. QFT Synchronous Control System of Ring gate for Hydraulic Turbine. *Power and Energy Engineering Conference. APPEEC*. 2009. Asia – Pacific. P. 221–225.
8. Jiangtao Tu, Minghui Huang. Simulation Research of a Synchronous Balancing System for Hydraulic Press Based on AME / Simulink. *International Conference on Measuring Technology and Mechatronics Automation*. 2009. P. 359–362.
9. Xiao Juliang, Wang Guodong, Song Weike. Electro-hydraulic proportional Synchronous Control System of Ring gate for Hydraulic Turbine. *Power and Energy Engineering Conference. APPEEC*. 2009. Asia-Pacific. 2009. P. 142–147.
10. Jiangtao Tu, Minghui Huang. Simulation Research of a Synchronous Balancing System for Hydraulic Press Based on AME / Simulink. *International Conference on Measuring Technology and Mechatronics Automation*. 2009. P. 359–362.

СПИСОК ЛИТЕРАТУРЫ

1. Навроцкий К. Л. Анализ динамики синхронного гидропривода кольцевого затвора гидротурбины // Вестник машиностроения. 2005. № 2. С.3–8.
2. Потетенко О.В., Шевченко Н.Г., Коваль Е.С. Численное моделирование гидродинамического усилия, действующего на кольцевой затвор в процессе его опускания в проточную часть радиально-осевой гидротурбины // Вісник НТУ “ХПІ”. 2012. № 54. С. 176–186.
3. Шевченко Н.Г., Коваль Е.С. Прогнозирование гидравлической силы воздействия потока воды на кольцевой затвор гидротурбины // Modern Directions of theoretical and applied researches. 2013. № 2. С. 74–81.
4. Deng Yingjian. Research on active synchronous control system of hydraulic press and its reliability analysis // Second International Conference on Digital Manufacturing&Automation. 2011. S. 940–943.
5. Dou Haibin, Wang Shaoping. Synchronization Control of Hydraulic Horizontal Regulation System// 6th IEEE Conference on Industrial Electronics and applications. 2011. S. 1922-1927.
6. Guo Chunli, Guodong Wang, Juliang Xiao. Numerical Simulation for Hydraulic Characteristics of Cylindrical Valve in Runaway Protection Process // Power and Energy Engineering Conference. APPEEC 2009. Asia – Pacific. S. 201–205.

7. **Guo Chunli, Li Zhifeng, Du Chenyang, Wang Fengyang.** QFT Synchronous Control System of Ring gate for Hydraulic Turbine. *Power and Energy Engineering Conference. APPEEC 2009. Asia – Pacific.* P. 221–225.

8. **Jiangtao Tu, Minghui Huang.** Simulation Research of a Synchronous Balancing System for Hydraulic Press Based on AME/Simulink. *International Conference on Measuring Technology and Mechatronics Automation.* P. 359–362.

9. **Xiao Juliang, Wang Guodong, Song Weike.** Electro-hydraulic proportional Synchronous Control System of Ring gate for Hydraulic Turbine. *Power and Energy Engineering Conference. APPEEC. 2009. Asia-Pacific.* P. 142–147.

10. **Jiangtao Tu, Minghui Huang.** Simulation Research of a Synchronous Balancing System for Hydraulic Press Based on AME/Simulink. *International Conference on Measuring Technology and Mechatronics Automation.* 2009. P. 359–362.

СВЕДЕНИЯ ОБ АВТОРАХ/AUTHORS

MATROSOV Artiom V. – Peter the Great St. Petersburg Polytechnic University.
29 Politechnicheskaya St., St. Petersburg, 195251, Russia.
E-mail: a.matrosov.hydro@mail.ru

МАТРОСОВ Артем Владимирович – аспирант Санкт-Петербургского политехнического университета Петра Великого.
195251, Россия, г. Санкт-Петербург, Политехническая ул., 29.
E-mail: a.matrosov.hydro@mail.ru

ISAEV Yurii M. – Peter the Great St. Petersburg Polytechnic University.
29 Politechnicheskaya St., St. Petersburg, 195251, Russia.
E-mail: ymi30@mail.ru

ИСАЕВ Юрий Митрофанович – кандидат технических наук профессор Санкт-Петербургского политехнического университета Петра Великого.
195251, Россия, г. Санкт-Петербург, Политехническая ул., 29.
E-mail: ymi30@mail.ru

SUNARCHIN Robert A. – Peter the Great St. Petersburg Polytechnic University.
29 Politechnicheskaya St., St. Petersburg, 195251, Russia.
E-mail: sunar1939@mail.ru

СУНАРЧИН Роберт Авалевич – кандидат технических наук доцент Санкт-Петербургского политехнического университета Петра Великого.
195251, Россия, г. Санкт-Петербург, Политехническая ул., 29.
E-mail: sunar1939@mail.ru



DOI 10.5862/JEST.249.4

УДК 621.165.1

*A.A. Sebelev, A.S. Saychenko, N.A. Zabelin, M.V. Smirnov***NUMERICAL ANALYSIS OF THE EXPANSION PROCESS
IN A TWO-STAGE AXIAL TURBINE OPERATING WITH MDM SILOXANE***A.A. Себелев, А.С. Сайченко, Н.А. Забелин, М.В. Смирнов***ЧИСЛЕННЫЙ АНАЛИЗ ПРОЦЕССА РАСШИРЕНИЯ
В ДВУХСТУПЕНЧАТОЙ ОСЕВОЙ ТУРБИНЕ,
РАБОТАЮЩЕЙ С MDM СИЛОКСАНОМ**

The problem of decreasing of fossil fuel consumption and energy efficiency is one of today's major conceptions in the field of energy economics. Waste heat recovery is one of the promising solutions for this problem. One of the ways to increase efficiency of the waste heat recovery process is using siloxanes as working fluids for organic Rankine cycles (ORC).

SPbPU scientists have analyzed peculiarities of the steady-state expansion process in the two-stage MDM siloxane turbine. The turbine is based on the principle of a classic velocity stage. First stage of the turbine was designed using the SPbPU high pitch-chord ratio supersonic design. The airfoils of the second stage are subsonic. A pressure ratio of the turbine is 37.2. Progressive steps of the initial temperature, pressure ratio and rotational velocity were used to obtain convergence of the solution process. The main factors, leading to the efficiency decreasing, were established and described.

The efficiency and power output of the investigated turbine stage were estimated as 67 – 68% and 544 kW respectively.

ORGANIC RANKINE CYCLE, AXIAL TURBINES, MDM SILOXANE, COMPUTATIONAL FLUID DYNAMIC

Необходимость снижения уровня потребления органического топлива и повышения энергоэффективности – в числе основных проблем в области современной энергетической экономики. Утилизация сбросной теплоты – одно из перспективных направлений в этой области. Использование силоксанов в качестве рабочих тел для органического цикла Ренкина (ORC) позволяет повысить эффективность утилизации сбросной теплоты.

Ученые СПбПУ проанализировали особенности стационарного процесса расширения MDM силоксана в силоксановой турбине. Турбина основана на принципе классической ступени скорости. Первая ступень турбины – высокоперепадная с большим относительным шагом лопаток рабочего колеса. Вторая ступень дозвуковая. Степень понижения давления 37.2. Для достижения сходимости процесса решения использовалось ступенчатое повышение начальных параметров. Установлены и описаны основные факторы, приводящие к уменьшению эффективности турбины. Эффективность и мощность турбины были оценены как 67-68% и 544 кВт соответственно.

ОРГАНИЧЕСКИЙ ЦИКЛ, АКЦИАЛЬНЫЕ ТУРБИНЫ, MDM СИЛОКСАН, ВЫЧИСЛИТЕЛЬНАЯ ДИНАМИКА ЖИДКОСТИ

Introduction

The problem of waste heat recovery is one of up-to-date problems in the energy efficiency field (Larjola [1], Vescovo [2]). Analysis of the Key World Energy Statistics [3] shows, that the highest volumes of waste heat resources take place at different thermal power plants, cement, metallurgical and chemical

productions. In Russia it is also the gas transport industry. The thermal power of waste heat at the all gas compressor stations of "Gazprom" is 87.9 GW by the estimation of Lykov et al. [4]. Rough estimations of waste heat thermal power at different productions in Russia, made on the base of Key World Energy Statistics [3], are:

3,9 GW in the cement industry;
 2,8 GW in the metallurgical industry;
 1,9 GW in the chemical industry.

The total waste heat thermal power in Russia is equal to 20 GW of electrical power by the most conservative estimate.

Nowadays in most cases the plants for waste heat recovery are based on Organic Rankine Cycle (ORC) because of higher cycle efficiency (Larjola [1], Hung et al. [5], Vescovo [2]). However, typically the efficiency of ORC recovery plants is less than 20% and strongly depends on the working fluid selection (Lecompte et al. [6]). Modern requirements for environment safety determine ozone depletion potential (ODP) and global warming potential (GWP) as main criteria for the selection process. It was shown that in this case the most promising alternatives to different hydrocarbons, freons and alcohols are zeotropic mixtures and siloxanes (Heberle et al. [7], Chys et al. [8], Weith et al. [9]) (fig. 1). Using of siloxanes in ORC allows increasing efficiency of the recovery units up to 23 – 25%. The aspects of siloxanes using in ORC were investigated by Lai et al. [10], Fernandez et al. [11], Uusitalo et al. [12].

The turbines for organic working fluids have essential differences in details of the expansion process in comparison with typical gas and steam turbines.

The special supersonic design is required for such turbines due to low speed of sound of different organic working fluids. Supersonic velocities in the turbine flow path and dense-gas effects have a significant influence on the turbine efficiency (Condego et al. [13], Guardone et al. [14]). The analysis of available experimental data shows that in case of axial turbines with mean diameter up to 500 mm the efficiency can dramatically drop down to 55% when the efficiency of traditional steam turbines is in the range 85-90% (see table 1).

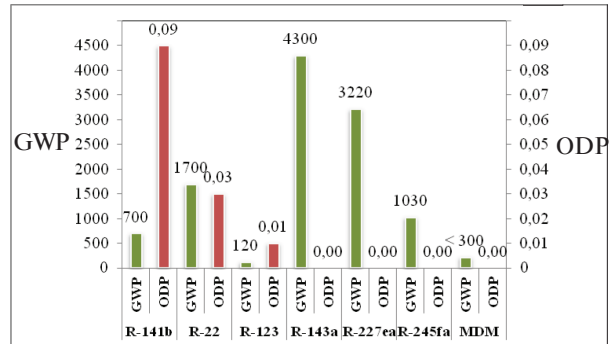


Fig. 1. Comparison of ODP and GWP of different working fluids

The design and performance of the siloxane axial turbines were investigated by Klonowicz et al. [22], Sebelev et al. [23]. However, relatively low level of efficiency of ORC axial turbines shows that details of the expansion process have to be investigated more clearly, especially in case of such a new class of working fluids as siloxanes. Thus, the scope of the present paper is to investigate the peculiarities of the MDM siloxane expansion process in the flow path of two-stage axial turbine.

Investigation object

Initial parameters of the expansion process. MDM siloxane was chosen as working fluid for the expansion process. The initial pressure p_0 was set as 0,75 MPa. The initial temperature T_0 was set as a vapor saturation temperature at chosen initial pressure. The turbine pressure ratio has been chosen as 37,2 to provide the required turbine enthalpy drop upon the condition of 500 kW power output of the turbine. Trans- and supercritical initial parameters were not considered. Positive slope of MDM vapor saturation curve provides inability of intersection between expansion process curve and two-phase region.

Table 1

Some available experimental data of ORC turbines efficiency

Authors	Working fluid	Turbine type	Turbine efficiency
Kang [15]	R-245fa	Radial-inflow turbine	0,822
Pei et al. [16]	R-123		0,625
Yamamoto et al. [17]	R-123	Centripetal turbine	0,500
Fu et al. [18]	R-245fa	Axial turbine	0,637
Klonowicz et al. [19]	R-227ea		0,530
Li et al. [20]	R-123		0,585
Ngyen et al. [21]	Pentane		0,498

The turbine. A two-stage axial turbine was chosen as the investigation object. This turbine is based on the principle of a classic velocity stage, where the main part of the enthalpy drop falls at the first stage as shown in fig. 2.

Table 2

The main geometric parameters of the turbine

Parameter	Dimensions	Value	
		1 st stage	2 nd stage
D_m	mm	550	
n	rev/min	3000	
H_0	kJ/kg	620,3	
u/C_{ax}	-	0,40	0,59
ε	-	0,89	1,00
Z_1	-	29	107
l_1	mm	30,4	82,5
α_1	grad.	5,0	20,0
ΔL_{ax}	mm	4,0	6,0
ΔL_{tc}	mm	1,0	1,0
β_1	grad.	12,0	56,0
Z_2	-	53	92
l_2	mm	60,4	88,5
β_2^*	grad.	12,0	30,0

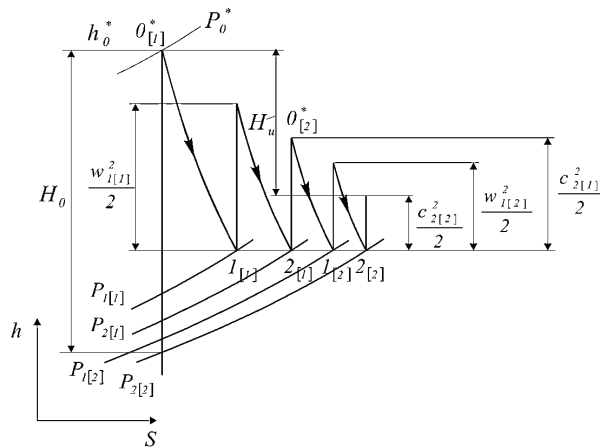


Fig. 2. Expansion process in a classic velocity stage (Lapshin [24])

The first stage was designed using the SPbPU high pitch-chord ratio supersonic design (Rassokhin [25]). The design of the 2nd stage is subsonic. The blade wheels of the turbine are shrouded. The nozzles and blade wheels design is shown in figure 3. The main geometric parameters of the turbine are presented in table 2.

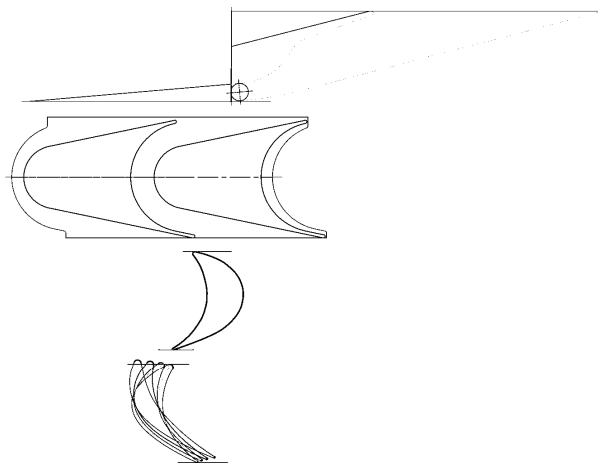


Fig. 3. The nozzles and blade wheels design

Numerical simulation method

The SPbPU method for numerical simulation of processes in supersonic turbines, described by Zabelin et al. [26], was used. ANSYS CFX was used to provide the numerical simulation.

The original relation between the number of nozzles and number of working blades is 29/53 for the first stage and 107/92 for the second stage. The relation 1/2/4/3 and periodic boundary conditions were used in the computational model. This assumption is correct to be used with Frozen Rotor interface between the nozzles and blade wheels areas because the relations between connecting areas in this case are 1:1,094, 1:0,991 and 1:0,872 respectively. The modeling of blade wheel tip shroud was also considered in numerical model in assumption of rotating motion of tip shroud domain. The computational model of the investigated turbine is presented in fig. 4.

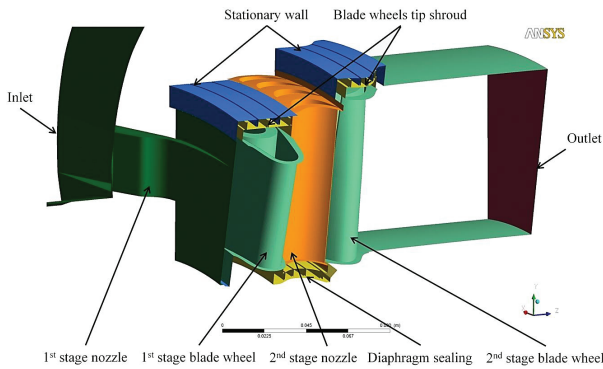


Fig. 4. Computational model of the investigated turbine

High-Reynolds version of the $k-\omega$ SST turbulence model was used. Steady-state Frozen rotor interface between the nozzles and blade wheels areas was used to model rotor-stator interactions. Flow parameters of the turbine were obtained by averaging of their values for 4 positions of the rotor relatively to the stator in the range of the 1st stage blade wheel pitch angle.

Aungier Redlich Kwong real gas equation of state was used to model thermodynamic properties of MDM during the expansion process. The main parameters have to be specified are: molar mass, critical temperature and pressure, acentric factor and boiling temperature. Zero pressure polynomial coefficients were obtained with using REFPROP databases to evaluate specific heat capacity of MDM. Kinetic Theory models were used to model transport properties of MDM. Rigid Non Interacting Sphere model was used to model MDM dynamic viscosity behavior.

Total parameters at the inlet ($p = 0,75$ MPa, $T = 523,15$ K) and static pressure at the outlet ($p = 0.02$ MPa) were specified as boundary conditions in the computational model. Progressive steps of the boundary conditions were used to obtain convergence of the solution process. The iteration steps between the changings of boundary conditions were different to decrease their negative influence on the convergence process. Monitoring of the RMS residuals, imbalances and turbine efficiency and power output were used to control convergence of the solution process. The criteria of the convergent solution in the present research were:

- drop of the RMS residuals more than 10^2 ;
- imbalances less than 0,5%;

fluctuation of the turbine efficiency and power output less than 5%.

The parameters of the computational domains discretization were chosen on the base of the grid independency study, presented by Sebelev et al. [23].

Discussion of the results

The values of the calculated thermodynamic and transport properties were compared with the values obtained with using REFPROP databases to estimate tolerance of the calculated results. Maximum deviation between CFX and REFPROP results was less than 5% for specific heat capacity and dynamic viscosity.

The turbine efficiency was estimated with consideration of the losses due to unsteady rotor-stator interaction with respect to equation:

$$\eta_{r-s} = \frac{M_{BW} \pi n}{30 G H_0} (1 - \zeta_{r-s}). \quad (1)$$

Te these losses were estimated as 0.13 (Natalevich [19]). Turbine power output was calculated with respect to equation:

$$N = \frac{M_{BW} \pi n}{30} (1 - \zeta_{r-s}). \quad (2)$$

Calculated turbine parameters are presented in table 3.

Table 3

Calculated turbine parameters				
Parameter	Dimensions	1 st stage	2 nd stage	Turbine
p_0^*	MPa	0,7725	0,0709	—
T_0^*	K	523,77	498,53	—
G	kg/s	13,915		—
c_1	m/s	219,75	127,68	—
α_1	deg.	18,37	-	—
p_1	MPa	0,1073	0,0367	—
w_1	m/s	147,03	61,06	—
w_2	m/s	206,53	153,23	—
c_2	m/s	128,75	97,09	—
p_2	MPa	0,0425	0,0199	—
T_2	K	-	488,87	—
H_N	kJ/kg	30,00	11,09	—
H_0	kJ/kg	45,58	21,38	58,34
π	-	18,16	3,57	38,91

Ending table 3

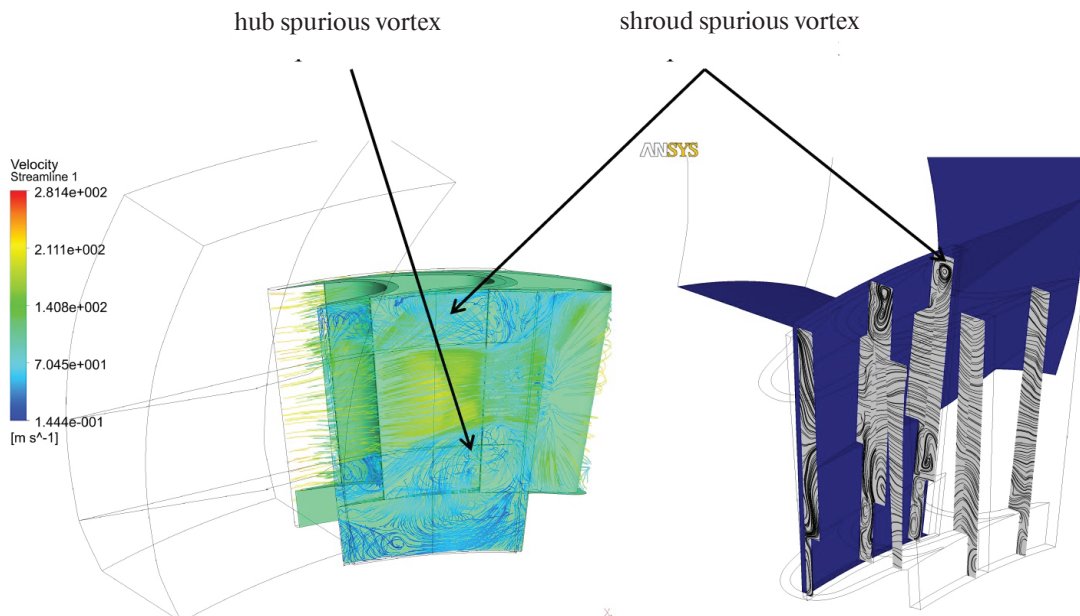
Parameter	Dimensions	1 st stage	2 nd stage	Turbine
$\overline{G_d}$	%	–	0,52	–
$\overline{G_{tsh}}$	%	3,90	1,05	–
u/C_{ax}	–	0,40	0,59	0,36
ρ_t	–	0,342	0,481	–
φ	–	0,897	0,857	–
M_{BW}	N·m	994,4	738,92	1733,33
F_{ax}	kN	10,52	2,39	12,92
η_{t-s}	–	–	–	0,671
η_{t-t}	–	–	–	0,730
N	kW	–	–	544,54

It is noteworthy that 1st stage has a significant value of reaction (0.34) despite its impulse design. Concurrently its u/C_{ax} value is 0,4 and velocity ratio φ is less than 0,9. These phenomena can take place due to the flow over-expanding in the 1st stage nozzle when the u/C_{ax} value is not optimal (Ras-sokhin [25]). It is important to emphasize that high value of the MDM density leads to the high value of the axial force acting to the rotor. More than 80% of the total axial force (10,52 kN) accrue to the 1st stage.

The 2nd stage fully performs its function. It decreases the flow velocity from 129 m/s to 97 m/s when the reaction value is 0,48 and pressure ratio is 3,57. It is important to emphasize that more than 42% of the total rotor torque accrue to the 2nd stage whereas its contribution to the total axial force is only 18,5%.

Analysis of the flow structure in the 1st stage shows negative influence of high values of hub and shroud overlaps on the flow characteristics due to spurious vortices formation. This process is illustrated in fig. 5. The influence of the hub and shroud overlaps on the efficiency of small-scaled turbines was investigated by Natalevich [27] and described in details by Zabelin et al. [26]. In case of the investigated turbine the negative influence of the hub and shroud overlaps is minimized by high speed of the MDM specific volume increasing after the nozzle. This leads to the stiff localization of the spurious vortices as shown in fig. 5.

It is also has to be emphasized that intensity of the oblique shock waves has its maximum at the nozzle hub and decreases towards to the shroud as illustrated in fig. 6. Another side of this phenomenon is that the mass-flow averaged nozzle outlet angle strongly differs from its geometrical value. These phenomena are the consequences of the flow linear motion in the axial clearance area as established by Kirillov [28] and Traupel [29].

Fig. 5. Flow structure in the 1st stage

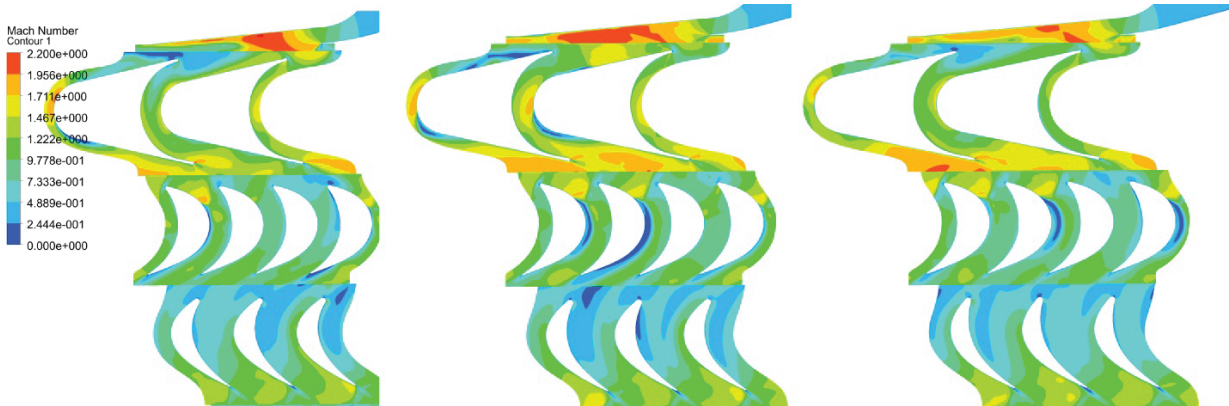


Fig. 6. Mach number fields on the cylindrical sections (left-to-right: $0,05l_1$, $0,5l_1$, $0,95l_1$)

Analysis of the flow structure in the axial cross section shows that flow tends to increase its “mean diameter” due to extreme increasing of its specific volume. This process is represented in fig. 7.

The occurrence of the normal shock wave after a turbine blade wheel was also described by Sebelev et al. [23]. Nonsufficient meridian fanning of the flow path leads to occurrence of additional losses on account of flow impinging on the tip shroud of the 2nd stage. This phenomenon leads to formation of the shroud vortex in 2nd stage nozzle. Hub overlap between 1st stage blade wheel and 2nd stage nozzle leads to formation of the hub vortex in the 2nd stage nozzle. These vortices occupy up to 50% of the nozzle cross sectional area. This situation is dramatized by the interaction of these vortices with secondary flows in the blade wheel. Filling of the cross sectional area by

the passive working fluid leads to local increasing of flow velocities up to supersonic values. Conversely, this leads to increasing of the profile losses because of their subsonic design. Thus, it can be assumed that neglect of extreme radial expansion of the flow is the main source of losses in the investigated case.

To sum up, the described phenomena lead to decreasing of the turbine efficiency down to 67–68% when its power output is 544 kW. Taking into account that other authors have described the same phenomena for the ORC axial turbines it is reasonably safe to suggest that the main factor, which leads to the low efficiency of axial ORC turbines, is extreme radial expansion of the working fluid. In this case it becomes significant to take into account strong radial expansion of the organic working fluids in the turbine design process.

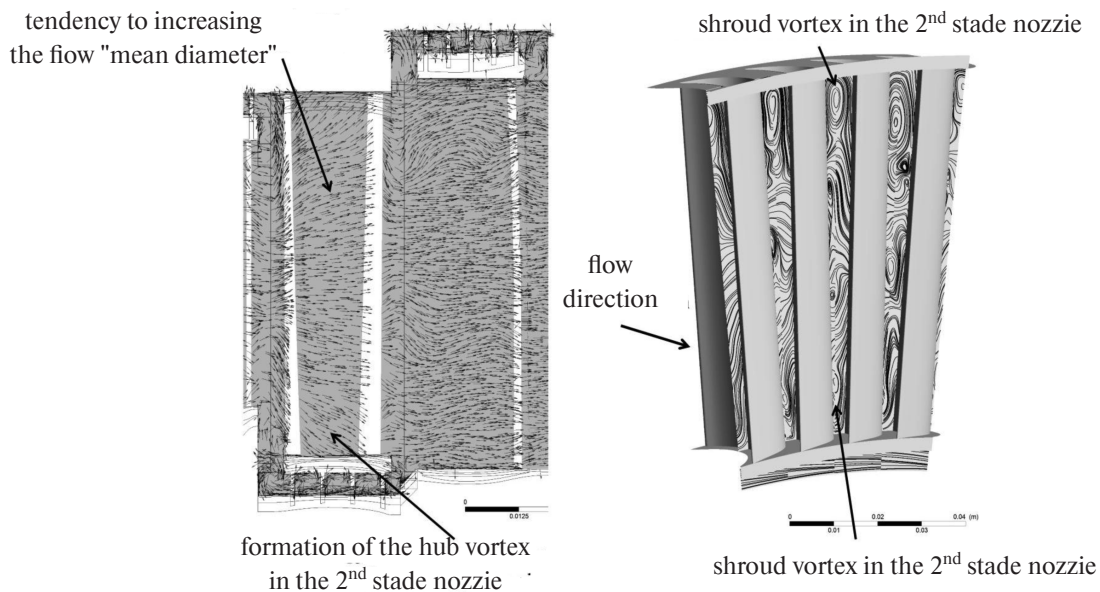


Fig. 7. Flow structure in the 2nd stage

Conclusions

The expansion process in the MDM siloxane turbine was modeled. The peculiarities of his process were outlined. Most of the outlined peculiarities are typical for the supersonic axial turbines because of subcritical initial parameters of the siloxane vapor. However, the strong relation of the siloxane properties to the thermodynamic parameters determines its nonconventional behavior during the expansion in the blade wheel. It was shown that in case of the axial turbines strong radial expansion of the siloxane is the main factor, which leads to dramatic decreasing of the turbine efficiency. As a result, calculated efficiency of the investigated turbine is 0,67–0,68 when its power output is 544 kW.

Nomenclature

GW – Gigawatt
 GWP – Global Warming Potential
 kW – Kilowatt
 MDM – Octamethyltrisiloxane
 ODP – Ozone Depletion Potential
 ORC – Organic Rankine Cycle
 SPbPU – Peter the Great St. Petersburg Polytechnic University
 c – velocity in stationary frame, m/s
 D_m – mean diameter, m
 F – force, N
 G – mass flow rate, kg/s
 \overline{G} – relative leakage (leakage value divided by the mass flow rate)
 H – enthalpy drop, kJ/kg
 l – height, mm
 M – torque, N·m

N – power output, W
 n – rotational speed, rev/min
 p – pressure, MPa
 T – temperature, K
 u/C_{ax} – stage load coefficient
 w – velocity in relative frame, m/s
 Z – number of nozzles (blades)
 α_1 – outlet angle in stationary frame, deg.
 β_1 – blade wheel inlet angle in relative frame, deg.
 β_2^* – blade wheel outlet angle in relative frame, deg.
 ΔL – clearance value, mm
 ε – partial admission ratio
 π – pressure ratio
 η – efficiency
 ρ_t – thermodynamic reaction
 φ – nozzle velocity ratio

Subscript

BW – blade wheel
 N – nozzle
 ax – axial
 d – diaphragm
 $r-s$ – rotor-stator
 tc – tip clearance
 tsh – tip shroud
 $t-s$ – total-to-static
 $t-t$ – total-to-total
 0 – related to the turbine inlet
 1 – related to the area after the nozzle
 2 – related to the area after the blade wheel
 [1] – related to the 1st stage
 [2] – related to the 2nd stage
 * – related to the total parameters

REFERENCES

1. Larjola L. Electricity from industrial waste heat using high-speed organic Rankine cycle (ORC). *International journal of production economics*. 1995. Vol. 41. P. 227–235.
2. Vescovo R. ORC recovering industrial heat. *Co-generation and On-Site Power Production*. 2009. Vol. 2. P. 53–57.
3. Key World Energy Statistics / International Energy Agency. 2015.
4. Lykov A.V., Zabelin N.A., Rassokhin V.A. Estimation of waste heat resources in Russian unified system of gas supply. *St. Petersburg State Polytechnical University Journal*. 2013. № 4 (183). S. 136–145. (rus.)
5. Hung T.C., Shai T.Y., Wang S.K. A review of Organic Rankine Cycles (ORCs) for the recovery of low-grade waste heat. *Energy*. 1997. Vol. 22. P. 661–667.
6. Lecompte S., Huisseune H., van den Broek M., Vanslambrouck B., De Paepe M. Review of organic Rankine cycle (ORC) architectures for waste heat recovery. *Renewable and Sustainable Energy Reviews*. 2015. Vol. 47. P. 448–461.
7. Heberle F., Preißinger M., Brüggemann D. Zeotropic mixtures as working fluids in Organic Rankine Cycles for low-enthalpy geothermal resources. *Renewable Energy*. 2012. Vol. 37. P. 364–370.
8. Chys M., van den Broek M., Vanslambrouck B., De Paepe M. Potential of zeotropic mixtures as working

fluids in organic Rankine cycles. *Energy*. 2012. Vol. 44. P. 623–632.

9. **Weith T., Heberle F., Preißinger M., Brüggemann D.** Performance of siloxane mixtures in a high-temperature Organic Rankine Cycle considering the heat transfer characteristics during evaporation. *Energies*. 2014. Vol. 7. P. 5548–5565.

10. **Lai N.A., Wendland M., Fischer J.** Working fluids for high-temperature organic Rankine cycles. *Energy*. 2011. Vol. 36. P. 199–211.

11. **Fernandez F.J., Prieto M.M., Suarez I.** Thermodynamic analysis of high-temperature regenerative organic Rankine cycles using siloxanes as working fluids. *Energy*. 2011. Vol. 36. P. 5239–5249.

12. **Usitalo A., Turunen-Saaresti T., Honkatukia J., Colonna P., Larjola J.** Siloxanes as working fluids for mini-ORC systems based on high-speed turbogenerator technology. *Journal of Engineering for Gas Turbines and Power*. 2013. Vol. 135. 042305.

13. **Congedo P.M., Corre C., Cinnella P.** Numerical investigation of dense-gas effects in turbomachinery. *Computers & Fluids*. 2011. Vol. 49. P. 290–301.

14. **Guardone A., Spinelli A., Dossena V.** Influence of molecular complexity on nozzle design for an organic vapor wind tunnel. *Journal of Engineering for Gas Turbines and Power*. 2013. Vol. 135. 042307.

15. **Kang S.H.** Design and experimental study of ORC (organic Rankine cycle) and radial turbine using R245fa working fluid. *Energy*. 2012. Vol. 41. P. 514–524.

16. **Pei G., Li J., Li Y., Ji J.** Construction and dynamic test of a small scale organic Rankine cycle. *Energy*. 2011. Vol. 36. P. 3215–3223.

17. **Yamamoto T., Furuhashi T., Arai N., Mori K.** Design and testing of the Organic Rankine Cycle. *Energy*. 2001. Vol. 26. P. 239–251.

18. **Fu B.-R., Lee Y.-R., Hsieh J.-Ch.** Design, construction, and preliminary results of a 250-kW organic Rankine cycle system. *Applied Thermal Engineering*. 2015. Vol. 80. P. 339–346.

19. **Klonowicz P., Borsukiewicz-Gozdur A., Hanaušek P., Krylowicz W., Brüggemann D.** Design and performance measurements of an organic vapour turbine. *Applied Thermal Engineering*. 2014. Vol. 63. P. 297–303.

20. **Li M., Wang J., He W., Gao L., Wang B., Ma Sh., Dai Y.** Construction and preliminary test of a low-temperature regenerative Organic Rankine Cycle (ORC) using R123. *Renewable energy*. 2013. Vol. 57. P. 216–222.

21. **Ngyen V.M., Doherty P.S., Riffat S.B.** Development of a prototype low-temperature Rankine cycle. *Applied Thermal Engineering*. 2001. Vol. 21. P. 169–181.

22. **Klonowicz P., Surwiłło J., Witanowski L., Lampart P.** Design and numerical study of turbines operating with MDM as working fluid. *Open Engineering*. 2015. Vol. 5. P. 485–499.

23. **Sebelev A., Scharf R., Zabelin N., Smirnov M.** Design and numerical analysis of processes in siloxane vapor driven turbine. *Proceedings of the 3rd International Seminar on ORC Power Systems*. Brussels, Belgium. 2015. P. 640–649.

24. **Lapshin K.L.** Теория турбомашин: конспект лекций. Saint-Petersburg: SPbPU, 2014. 86 s. (rus.)

25. **Rassokhin V.A.** Турбины конструкции LPI: преимущества, характеристики, опыт разработки и применение. *Труды СПбГПУ*. 2004. Vol. 491. P. 152–161. (rus.)

26. **Zabelin N.A., Rakov G.L., Rassokhin V.A., Sebelev A.A., Smirnov M.V.** Investigation of fluid flow highlights in low flow-rated LPI turbine stages. *St. Petersburg State Polytechnical University Journal*. 2013. № 1(166). S. 45–53. (rus.)

27. **Natalevich A.S.** Воздушные микротурбины. Moscow: Mashinostroyeniye, 1979. 192 s. (rus.)

28. **Kirillov I.I.** Теория турбомашин. Leningrad: Mashinostroyeniye, 1972. 533 s. (rus.)

29. **Traupel W.** Thermische Turbomaschinen. 3. Aufl. Berlin: Springer, 1977. 579 s.

СПИСОК ЛИТЕРАТУРЫ

1. **Larjola L.** Electricity from industrial waste heat using high-speed organic Rankine cycle (ORC). // *International journal of production economics*. 1995. Vol. 41. P. 227–235.

2. **Vescovo R.** ORC recovering industrial heat. // *Cogeneration and On-Site Power Production*. 2009. Vol. 2. P. 53–57.

3. *Key World Energy Statistics / International Energy Agency*, 2015.

4. **Лыков А.В., Забелин Н.А., Рассохин В.А.** Оценка ресурсов отбросного тепла в российской объединенной системе газоснабжения // *Научно-технические ведомости СПбГПУ*. 2013. № 4 (183). С. 136–145.

5. **Hung T.C., Shai T.Y., Wang S.K.** A review of Organic Rankine Cycles (ORCs) for the recovery of low-grade waste heat. *Energy*. 1997. Vol. 22. P. 661–667.

6. **Lecompte S., Huisseune H., van den Broek M., Vanslambrouck B., De Paepe M.** Review of organic Rankine cycle (ORC) architectures for waste heat recovery // *Renewable and Sustainable Energy Reviews*. 2015. Vol. 47. P. 448–461.

7. **Heberle F., Preißinger M., Brüggemann D.** Zeotropic mixtures as working fluids in Organic Rankine Cycles for low-enthalpy geothermal resources. *Renewable // Energy*. 2012. Vol. 37. P. 364 – 370.

8. **Chys M., van den Broek M., Vanslambrouck B., De Paepe M.** Potential of zeotropic mixtures as working

fluids in organic Rankine cycles. // *Energy*. 2012. Vol. 44. P. 623–632.

9. **Weith T., Heberle F., Preißinger M., Brüggemann D.** Performance of siloxane mixtures in a high-temperature Organic Rankine Cycle considering the heat transfer characteristics during evaporation. // *Energies*. 2014. Vol. 7. P. 5548 – 5565.

10. **Lai N.A., Wendland M., Fischer J.** Working fluids for high-temperature organic Rankine cycles. // *Energy*. 2011. Vol. 36. P. 199–211.

11. **Fernandez F.J., Prieto M.M., Suarez I.** Thermodynamic analysis of high-temperature regenerative organic Rankine cycles using siloxanes as working fluids. // *Energy*. 2011. Vol. 36. P. 5239–5249.

12. **Uusitalo A., Turunen-Saaresti T., Honkatukia J., Colonna P., Larjola J.** Siloxanes as working fluids for mini-ORC systems based on high-speed turbogenerator technology. // *Journal of Engineering for Gas Turbines and Power*. 2013. Vol. 135. 042305.

13. **Congedo P.M., Corre C., Cinnella P.** Numerical investigation of dense-gas effects in turbomachinery. // *Computers & Fluids*. 2011. Vol. 49. P. 290–301.

14. **Guardone A., Spinelli A., Dossena V.** Influence of molecular complexity on nozzle design for an organic vapor wind tunnel. // *Journal of Engineering for Gas Turbines and Power*. 2013. Vol. 135. 042307.

15. **Kang S.H.** Design and experimental study of ORC (organic Rankine cycle) and radial turbine using R245fa working fluid. // *Energy*. 2012. Vol. 41. P. 514–524.

16. **Pei G., Li J., Li Y., Ji J.** Construction and dynamic test of a small scale organic Rankine cycle. // *Energy*, 2011. Vol. 36. P. 3215–3223.

17. **Yamamoto T., Furuhashi T., Arai N., Mori K.** Design and testing of the Organic Rankine Cycle. // *Energy*. 2001. Vol. 26. P. 239–251.

18. **Fu B.-R., Lee Y.-R., Hsieh J.-Ch.** Design, construction, and preliminary results of a 250-kW organic Rankine cycle system. // *Applied Thermal Engineering*, 2015. Vol. 80. P. 339–346.

19. **Klonowicz P., Borsukiewicz-Gozdur A., Hanausek P., Krylowicz W., Brüggemann D.** Design and performance measurements of an organic vapour turbine. // *Applied Thermal Engineering*. 2014. Vol. 63. P. 297–303.

20. **Li M., Wang J., He W., Gao L., Wang B., Ma Sh., Dai Y.** Construction and preliminary test of a low-temperature regenerative Organic Rankine Cycle (ORC) using R123. // *Renewable energy*. 2013. Vol. 57. P. 216–222.

21. **Ngyen V.M., Doherty P.S., Riffat S.B.** Development of a prototype low-temperature Rankine cycle. // *Applied Thermal Engineering*. 2001. Vol. 21. P. 169–181.

22. **Klonowicz P., Surwiłło J., Witanowski L., Lampart P.** Design and numerical study of turbines operating with MDM as working fluid. // *Open Engineering*. 2015. Vol. 5, P. 485–499.

23. **Sebelev A., Scharf R., Zabelin N., Smirnov M.** Design and numerical analysis of processes in siloxane vapor driven turbine. // *Proceedings of the 3rd International Seminar on ORC Power Systems*. Brussels, Belgium. 2015. P. 640–649.

24. **Лапшин К.Л.** Теория турбомашин: конспект лекций. Санкт-Петербург: Изд-во СПбПУ, 2014. 86 с.

25. **Рассохин В.А.** Турбины конструкции ЛПИ: преимущества, характеристики, опыт разработки и применение. // *Труды СПбГПУ*. 2004. Т. 491. С. 152–161.

26. **Забелин Н.А., Раков Г.Л., Рассохин В.А., Себелев А.А., Смирнов М.В.** Investigation of fluid flow highlights in low flow-rated LPI turbine stages. Исследование потока жидкости, выделенное в низкоскоростных ступенях турбины ЛПИ с рейтингом потока // *Научно-технические ведомости СПбГПУ*. 2013. № 1 (166). С. 45–53.

27. **Наталевич А.С.** Воздушные микротурбины. М.: Машиностроение, 1979. 192 с.

28. **Кириллов И.И.** Теория турбомашин. Л.: Машиностроение, 1972. 533 с.

29. **Traupel W.** Thermische Turbomaschinen. 3. Aufl. Berlin: Springer, 1977. 579 p.

СВЕДЕНИЯ ОБ АВТОРАХ/AUTHORS

SEBELEV Aleksandr A. — Peter the Great St. Petersburg Polytechnic University.
29 Politechnicheskaya St., St. Petersburg, 195251, Russia.
E-mail: a.sebelev.turbo@mail.ru

СЕБЕЛЕВ Александр Александрович — ассистент Санкт-Петербургского политехнического университета Петра Великого.
195251, Россия, г. Санкт-Петербург, Политехническая ул., 29.
E-mail: a.sebelev.turbo@mail.ru

SAYCHENKO Aleksandr S. — Peter the Great St. Petersburg Polytechnic University.
29 Politechnicheskaya St., St. Petersburg, 195251, Russia.
E-mail: Saychen@yandex.ru

САЙЧЕНКО Александр Сергеевич – аспирант Санкт-Петербургского политехнического университета Петра Великого.
195251, Россия, г. Санкт-Петербург, Политехническая ул., 29.
E-mail: Saychen@yandex.ru

ZABELIN Nikolai A. – Peter the Great St. Petersburg Polytechnic University.
29 Politechnicheskaya St., St. Petersburg, 195251, Russia.
E-mail: n.zabelin.turbo@mail.ru

ЗАБЕЛИН Николай Алексеевич – кандидат технических наук директор института энергетики и транспортных систем Санкт-Петербургского политехнического университета Петра Великого.
195251, Россия, г. Санкт-Петербург, Политехническая ул., 29.
E-mail: n.zabelin.turbo@mail.ru

SMIRNOV, Maksim V. – Peter the Great St. Petersburg Polytechnic University.
29 Politechnicheskaya St., St. Petersburg, 195251, Russia.
E-mail: m.smirnov.turbo@mail.ru

СМИРНОВ Максим Викторович – аспирант Санкт-Петербургского политехнического университета Петра Великого.
195251, Россия, г. Санкт-Петербург, Политехническая ул., 29.
E-mail: m.smirnov.turbo@mail.ru



DOI 10.5862/JEST.249.5

УДК 621.165

K.N. Borishanskiy

INCREASING THE ACCURACY OF MEASURING THE FLUTTER OF STEAM TURBINE BLADES IN SERVICE

К. Н. Боришанский

ПОВЫШЕНИЕ ТОЧНОСТИ РЕГИСТРАЦИИ АВТОКОЛЕБАНИЙ ЛОПАТОК ПАРОВЫХ ТУРБИН В УСЛОВИЯХ ЭКСПЛУАТАЦИИ

Flutter of turbine blades may be a reason of blade damage. Appearance of power steam turbines last stages shrouded blades flutter, realized with disk natural forms and in-phase natural forms, was registered in service by help of discrete-phase method modern variant. In this paper peculiarities of power steam turbines last stages shrouded blades flutter, realized in service with in-phase natural forms, are considered. Advantages and defects of registration of these natural forms with help of modern variant discrete-phase method induction gauges are studied. Appearance of additional errors during registration of flutter, realized with in-phase natural forms, is marked. These additional errors are called because of torsion and longitudinal vibration of turbine and generator rotors assembly and axial vibration of stator details, in which induction gauges are fastened. Measures, concerning of errors reduction, are recommended.

STEAM TURBINE; BLADE; FLUTTER; DISCRETE-PHASE METHOD; MEASUREMENT; INDUCTION GAUGE; VIBRATION RELIABILITY.

Автоколебания лопаток последних ступеней мощных паровых турбин могут стать причиной их усталостного разрушения. Для успешной борьбы с автоколебаниями необходимо определить собственные формы лопаточных венцов, с которыми автоколебания реализуются в процессе эксплуатации. В настоящей статье рассмотрены особенности автоколебаний бандажированных лопаток последних ступеней мощных паровых турбин, реализующихся в процессе эксплуатации с синфазными собственными формами лопаточных венцов. Проанализированы преимущества и недостатки регистрации подобных колебаний с помощью модернизированного варианта дискретно-фазового метода. Показано, что дополнительные погрешности измерений могут быть связаны с крутильными и продольными колебаниями валопровода, а также осевыми вибрациями деталей статора, в которых закреплены индукционные датчики, вызванными автоколебаниями лопаток с синфазными формами. Рекомендованы мероприятия по минимизации погрешностей измерений.

ПАРОВАЯ ТУРБИНА; РАБОЧАЯ ЛОПАТКА; АВТОКОЛЕБАНИЯ; ДИСКРЕТНО-ФАЗОВЫЙ МЕТОД; ИЗМЕРЕНИЯ; ИНДУКЦИОННЫЙ ДАТЧИК; ВИБРАЦИОННАЯ НАДЕЖНОСТЬ.

It is impossible to determine the dynamic stress levels in turbomachinery blades by calculation, and experimental studies are therefore required for ensuring their fail-safe performance.

Frequency detuning is performed for the blades fabricated for the last stages of high-power steam turbines, i.e., sufficient margins are provided between the operational rotations and the rotations where resonances with the most excitable natural forms occur. In some cases, vibration studies in experimental model and full-scale turbines are not carried out to

the full extent. Furthermore, it should be noted that a number of modes that are potentially dangerous for fatigue strength of the blades can be inspected only when the turbine is operating. In this regard, systems that can continuously monitor the state of vibration in the blades under operating conditions are being developed. Virtually the only measurement technique ensuring the continuous operation of such systems is the so-called discrete phase method (DPM), in which the vibrational state of the blades is assessed by the indications of fixed sensors mounted against the tips

of the rotating blades [1]. In recent years, due to the evolution of computer technology, the capabilities of the DPM have increased extremely.

It should be borne in mind that the DPM can be used to measure the amplitudes of peripheral sections and their oscillation rates or the mutual blade displacements, rather than the dynamic stress values that are of practical interest. In order to substantiate the transition to these values, it is necessary to analyze the experimental data, i.e., to determine the oscillation frequency, the ratio of the tangential and the axial amplitude components, the distribution of amplitudes over the wheel periphery. It is rather important to evaluate and minimize the measurement errors in order to reasonably assess the hazards of the registered oscillations. This paper discusses the errors occurring when registering blade flutter in the last stages of high-power steam turbines using the DPM, and the methods for reducing the influence of these errors.

The last-stage blades of the more high-powered steam turbines are typically shrouded, i.e., a “fully constrained” blade ring is a particular case of a cyclically symmetric system whose natural forms have different values of nodal diameters and nodal circles. Two-types of oscillations can be identified with respect to the turbine blades, the in-phase forms (without nodal diameters) where the amplitudes and phases of all blades on the wheel are identical, and the out-phase forms (with different values of nodal diameters and nodal circles) where the amplitudes vary circumferentially by the sine law. The first group of out-phase forms is commonly called the disc ones.

The last-stage blades in operation may experience resonance or stall oscillations, and sometimes flutter.

Methods for calculating the frequencies of individual and constrained blades have been developed for reducing the risk of resonance oscillations [2–4]. Since the main source of resonant oscillations is the time-constant non-uniformity of the flow parameters on the wheel circumference, the danger of the majority of natural forms for the shrouded blades (and any fully constrained blades) is theoretically equal to zero because the natural forms are orthogonal to the disturbing loads. In particular, the work of the disturbing forces turns out to equal zero for all forms of in-phase and most forms of out-phase oscillations [2]. The only dangerous modes are those for which the equality $m = k$ is satisfied, where m is the number of nodal diameters, and k is the oscillation multiplicity, i.e., the number of blade oscillations per rotor revolution. This fact is taken into account in the design of stan-

dards, with only the disc oscillations for which $k = 2-4$ (and sometimes $k = 5-6$) detuned. The peripheral sections move almost strictly in the axial direction during disc oscillations, because the tangential component of deflection is highly limited due to high tensile and compressive stiffness of the shroud ring.

Stall oscillations of last-stage blades occurs under light or no loads, when the flow around the blades exhibits an off-design behavior due to a sharp decrease in the volumetric flow rate of steam. Stall oscillations happens in disc modes whose frequencies are not multiples of the rotation frequency and whose amplitudes are unstable.

The theoretical possibility of various types of blade flutter was discussed in [4, 5]. The last-stage blade flutter occurring in steam turbines in operation was discovered relatively recently, after a number of power stations installed control systems based on using DPM sensors. Flutter with disc modes with a relatively large number of nodal diameters was the first type registered [6, 7]. In some cases, flutter was the greatest risk factor for blade fatigue strength.

When developing methods for controlling the oscillations in the shrouded blades, the fact that all of the above-described types of the most dangerous oscillations occurred with disc modes was taken into account, i.e., the axial component of the deflection of the peripheral section of the blade had to be measured.

The standard version of the DPM recording the displacements of the peripheral section of the blade could not be used for controlling the oscillations of the shrouded blade, as its tip was ‘enclosed’ by the shroud platform. An upgraded version of the DPM was designed [8, 9] to control these blades. The essence of this version is that a small-diameter magnet is placed within the shroud platform, and the cross-section of the induction DPM sensor is shaped as an elongated rectangle whose minimal inertia axis makes an angle β with the turbine axis. As the magnet moves past the sensor, the magnetic flux changes, and an EMF whose value reverses sign when the magnet moves past the core is induced in the sensor coil. A pair of sensors located in one axial plane at a small distance S from each other is used to best measure the axial component of the oscillations. The minimal inertia axes of the cross-sections of the first and the second sensor make a $+\beta$ and a $-\beta$ angle with the turbine axis, respectively. If the blade deflects by the value x in the axial direction, the distance between

the cross-sections of the sensor cores in the plane of the magnet's rotation changes by ΔS , which must be measured with a high degree of precision.

The number of time pulses generated by the measuring equipment at a frequency of 40 MHz is counted in order to precisely measure the time intervals between the passage of the magnet past the first and the second sensor of the pair. The readings from the revolution sensor located near the half-coupling of the turbine rotor are used to determine the relationship between the time intervals and their corresponding linear values. A slot made in the cylindrical surface of the half-coupling is used as a keyphasor. Using a high frequency of 40 MHz allows to determine both the amplitudes and the revolutions with a very high precision. Even when the rotational speed of the peripheral section is equal to 660 m/s, the amplitude is determined with an error of 0.016 mm, and the number of revolutions per minute, equal to 3000 rpm, with an error of about 0.00375 rpm (the errors are reduced with a decrease in speeds and revolutions).

The proportionality factor k_n between the x and ΔS values depends not only on the angle β , but also on the radial clearance between the magnet and the sensor and on the axial displacement of the magnet relative to the sensor center; it is therefore determined on the calibrator. As the flutter frequencies are not multiples of the rotary speed, the blade moves past the sensors with an arbitrary phase, and therefore the value ΔS_{\max} which is proportional to the oscillation amplitude x_0 can be measured during a short period of time:

$$\Delta S_{\max} = \frac{1}{k_n} x_0. \quad (1)$$

To assess the level of dynamic stress, it is necessary to know the oscillation frequency f in addition to the amplitude x_0 . Since the DPM sensors do not measure the entire oscillation process, but only its discrete values once per revolution and, besides, the blade oscillation frequency f is higher than the rotary speed n , it is fundamentally impossible to determine the true oscillation frequency using a single pair of sensors.

A most detailed description of the measurements using an upgraded version of the DPM is presented in [10]; we adopted a number of the formulae given below from this study. In particular, it was established that the following relation exists between the true frequency f and the frequency f_{meas} "measured" using one pair of sensors:

$$f = kn \pm f_{\text{meas}}, \quad (2)$$

where k is an integer.

To determine the frequency f , it is necessary to use the readings from two pairs of sensors located at an angular distance $\Delta\phi$ from each other, and use the following formula:

$$\cos\left(\frac{\Delta\phi f}{n}\right) \approx \frac{\sum_{i=1}^M \Delta S_{1i} \Delta S_{2i}}{\sqrt{\sum_{i=1}^M \Delta S_{1i}^2 \sum_{i=1}^M \Delta S_{2i}^2}}, \quad (3)$$

where ΔS_{1i} and ΔS_{2i} are the deviations from the mean values for the first and the second pair of sensors at an i -th measurement, M is the total number of measurements. The accuracy of formula (3) increases with an increasing number of measurements, but it becomes practically accurate when measurements are performed for several seconds.

After finding the frequency f when registering flutter with disc modes, it proved possible to determine the number of nodal diameters m , as well as to clarify the features of the oscillations influencing the possibility of supplying the energy from the flow to the blades [7, 10].

The need to change the measurement technique became clear after flutter with in-phase modes was registered, occurring simultaneously with the same frequency in four stages (the blades of the last and penultimate stages of a double-flow low-pressure rotor of a high-power turbine) [10, 11]. Three forms of flutter relatively close in frequency of oscillation were registered, slightly different from the first in-phase frequency of the penultimate-stage blades and the second in-phase frequency of the last stage blades whose calculated values were close to each other.

The peripheral section of the blade in in-phase modes has not only an axial (x_0), but also a tangential (y_0) component, with the inequality $y_0 > x_0$ satisfied for the first mode. Ref. [10] revealed that the following formula holds true with both axial and tangential components present:

$$\Delta S_{\max} = \sqrt{\left(\frac{1}{k_n} x_0 \cos \frac{fS}{2nR}\right)^2 + \left(2y_0 \sin \frac{fS}{2nR}\right)^2}, \quad (4)$$

where R is the radius in which the DPM sensors are installed.

At $y_0 \approx 0$ and $S \ll R$ formula (4) naturally becomes (1). It follows from formula (4) that the ‘normal’ pairs of DPM sensors with small bases S are ineffective for measuring the tangential component of the oscillation. Provided that $y_0 > x_0$, a significant increase in the useful signal can be achieved by composing ‘additional’ pairs from the sensors that are already part of various ‘normal’ pairs.

If the angles β for the sensors making up the ‘additional’ pair with the base S_{add} are the same, the measurement results are described by the formula:

$$\Delta S_{\max} = \left(\pm \frac{1}{k_n} x_0 + 2y_0 \right) \sin \frac{f S_{add}}{2nR}; \quad (5)$$

From now on we are going to use $a + \text{sign}$, which can be always achieved by selecting the sensors with angles $+\beta$ or $-\beta$.

It is noted in [10] that the highest useful signal can be obtained if the mutual blade displacement with the angular coordinates φ_j and φ_k are determined using the same DPM sensor. By introducing the notations $\varphi_k - \varphi_j = \psi$, $\varphi_k + \varphi_j = \psi + 2\varphi_j$, it is possible to determine the mutual displacements at an i^{th} measurement, when the oscillation phase of the j^{th} blade moving past the sensor is equal to α_i :

$$\Delta S_i(jk) = \left(\frac{1}{k_n} x_0 + 2y_0 \right) \times \sin \frac{\psi f}{2n} \cos \left[\alpha_i + \frac{(\psi + 2\varphi_j) f}{2n} \right]. \quad (6)$$

Because the flutter frequency is not a multiple of the rotary rate, the maximum value of the mutual displacements is equal to:

$$\Delta S_i(jk) = \left(\frac{1}{k_n} x_0 + 2y_0 \right) \sin \frac{\psi f}{2n}. \quad (7)$$

The condition $\sin(\psi f / 2n) = 1$ corresponds to the measurement of the mutual displacements of the blades moving past the DPM sensor in antiphase. By changing the value of ψ (this possibility is incorporated in the software for processing the measurement results), it is possible, independent of the location coordinates of the DPM sensors, to determine not only the maximum value of the mutual displacements, but also to refine the oscillation frequency f .

Using the modified measurement technique with formulae (3)–(7) allowed to determine the ratio between the axial and the tangential amplitude components of for the peripheral sections of the blades of different stages with three different forms of in-phase oscillations, the phase shift between the oscillations of different blade rings, the dependence of flutter intensity on the operation mode of the turbine.

A number of errors absent when registering flutter with disc modes were revealed when analyzing the measurement results. For example, the frequencies calculated by formula (3) did not precisely satisfy condition (2). Certain patterns in the variation of amplitudes and oscillation frequencies over the wheel circumference were “registered”, despite the fact that the excited normal mode was in-phase. The x_0/y_0 ratios were significantly different for the blades of two stages of the same type oscillating with equal frequencies and approximately equal total amplitudes.

Let us determine the causes for these discrepancies and consider the possibilities of minimizing the errors detected.

The fundamental difference of flutter with in-phase and disc modes is that in the first case, the principal vector and the principal moment of the forces acting on the rotor from the blade ring are not equal to zero. As a result, these axial forces and torques can cause longitudinal and torsional oscillations of rotors assembly, and the oscillations of the stator components where DPM sensors are mounted.

The experimentally observed equality of the flutter frequencies of all four blade rows is specifically connected to the torsional and longitudinal flexibility of the rotors assembly components, because, due to the inevitable manufacturing deviations, the frequencies of different sets of blades made from the same technical drawing should be slightly different.

The presence of torsional oscillations of the rotors assembly in one of the modes of in-phase flutter is confirmed by the experimental data presented in fig. 1.

Fig. 1,*a* shows the readings of the RPM sensor located near the rotor’s half-coupling. Fig. 16 shows the readings of the sensor pair with a small base S recording almost exclusively the axial component of the peripheral section of the deflection. It can be seen that the oscillations of the blades and the rotor occur with the same ‘measured’ frequency of about 15 Hz. Comparing the readings of two pairs of sensors using formula (3) revealed that the true frequency was $f = 115$ Hz, i.e., relation (2) is satisfied provided that $k = 2$.

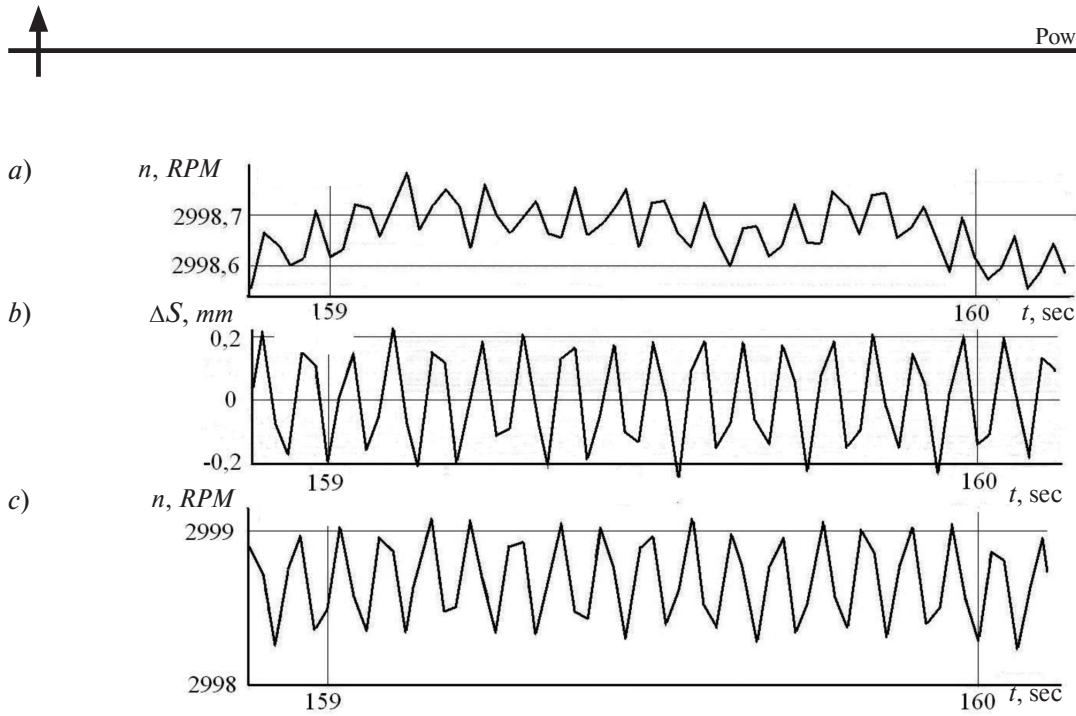


Fig. 1. Data read from: RPM sensor (a); pair of sensors registering the axial component of the oscillations (b); blade sensor used for RPM readings (c), shown versus the time of the readings

The oscillations of the rotor (i.e., the oscillations of the keyphasor) result in errors in finding both the frequency and the intensity of the oscillations. In order to qualitatively and quantitatively assess the effect of rotor vibration on the measurement results, it is necessary to find the amplitude of rotor oscillations, and the possible phase shift between the oscillations of the rotor and the blades (a phase shift may occur because the flutter frequencies are higher than the fundamental frequencies of the torsional and longitudinal oscillations of the rotors assembly).

The data on the connection between the keyphasor and the blades can be obtained if one of the blade sensors is used for RPM readings, and one of the blades is used as the keyphasor. This possibility is incorporated in the software for processing the results, with the signal from only one of the blades with magnets installed used to determine the revolutions. The measurement results are shown in fig. 1,c. It can be seen that the “change in the revolutions” also occurs with $f_{meas.} = 15$ Hz, but with a much greater intensity, as the blade flutter amplitudes are substantially greater than those of the torsional oscillations of the rotor in the half-coupling area.

If the blade used to determine the number of revolutions oscillates with the frequency f and the amplitudes x_0 and y_0 in the axial and tangential directions, and the phase angle at the moment when the blade passes the sensor at an i^{th} measurement equals

α_i , its deviations from the equilibrium position for the i^{th} and the $(i + 1)^{st}$ measurements are equal to:

$$\Delta S_i = \left(\frac{1}{2k_n} + y_0 \right) \sin \alpha_i;$$

$$\Delta S_{i+1} = \left(\frac{1}{2k_n} + y_0 \right) \sin \left(\alpha_i + \frac{2\pi f}{n} \right). \quad (8)$$

Taking into account expressions (8), it is easy to see that the error in determining the circumference using the blade RPM sensor at the i^{th} metering is equal to:

$$\delta S_i = \Delta S_{i+1} - \Delta S_i = \left(\frac{1}{k_n} + 2y_0 \right) \sin \frac{\pi f}{n} \cos \left(\alpha_i + \frac{\pi f}{n} \right). \quad (9)$$

Thus, the distance $2\pi R + \delta S_i$ (and not $2\pi R$) can be measured in the i^{th} revolution; the length of the i^{th} revolution can change, causing the ‘measured’ rotary rate to change as well (see fig. 1,c).

Knowing the time dependence of the keyphasor oscillations, it is possible to assess their effect on the accuracy of the blade amplitudes and their frequencies by calculation, and then compare the results with the experimental data.

Due to the error in determining the circumference, the error in determining the distance between the j^{th} and the k^{th} blades for the i^{th} measurement is found to be:

$$\delta S_i(jk) = -\frac{\Psi}{2\pi} \left(\frac{1}{k_n} x_0 + 2y_0 \right) \cdot \sin \frac{\pi f}{n} \cos \left(\alpha_i + \frac{\pi f}{n} \right). \quad (10)$$

Thus, the ‘measured’ mutual displacement of the j^{th} and the k^{th} blade is given, instead of formula (6), by the expression:

$$\Delta S_{i\Sigma}(jk) = \Delta S_i(jk) + \delta S_i(jk). \quad (11)$$

Let us transform expression (11) to the following form:

$$\Delta S_{i\Sigma}(jk) = \left(\frac{1}{k_i} x_0 + 2y_0\right)(C_1 \cos \alpha_i - C_2 \sin \alpha_i), \quad (12)$$

where

$$C_1 = \sin \frac{\psi f}{2n} \cos \frac{(2\varphi_j + \psi)f}{2n} - \frac{\psi}{4\pi} \sin \frac{2\pi f}{n};$$

$$C_2 = \sin \frac{\psi f}{2n} \sin \frac{(2\varphi_j + \psi)f}{2n} - \frac{\psi}{2\pi} \sin^2 \frac{\pi f}{n}. \quad (13)$$

Because the flutter frequencies are not multiples of the rotary rate, the maximum value of $\Delta S_{\Sigma \max}$ is determined by the formula:

$$\Delta S_{\Sigma \max} = \left(\frac{1}{k_n} x_0 + 2y_0\right) \sqrt{C_1^2 + C_2^2}. \quad (14)$$

In contrast to formula (7), in this case the value of $\Delta S_{\Sigma \max}$ depends not only on the angular distance between the blades ψ , but also on the position of the blade on the wheel circumference, because the C_1 and C_2 coefficients depend on the angular coordinate φ_j .

Let us compare the calculated and the experimental dependences of the effect of the vibration of the keyphasor (in this case, the blade acting as the keyphasor) on the accuracy of determining the flutter intensity. Let us take into account the fact that the margin of error does not depend on the oscillation intensity of the vibrations when using the blade as the keyphasor, because the multiplier $(1/k_n)x_0 + y_0$ is included in the expression both for ΔS_i and for δS_i .

To reduce the effect of random errors in formulae (7) and (14), let us consider the case $\sin(\psi f/2n) = 1$ allowing to obtain the maximum measurement results. In this particular case, let us define the calculated dependence of the oscillation intensity on the angular coordinate φ_j , i.e., the angular distance of the j^{th} blade from the first one determining the start of a revolution.

The relative calculated value of $\Delta S_{\Sigma \max} / \Delta S_{\max}$ is in this case determined by the expression:

$$\Delta S_{\Sigma \max}^{\text{rel}}(\varphi_j) = \sqrt{1 + \frac{n^2}{4f^2} \sin^2 \frac{\pi f}{n} + \frac{n}{f} \sin \frac{\pi f}{n} \sin \frac{f}{n} (\varphi_j - \pi)}. \quad (15)$$

The maximum and the minimum values are achieved provided that $\sin[(f/n)(\varphi_j - \pi)] = \pm 1$ and be equal to $1 \pm (n/2f) \sin(\pi f/n)$. For flutter with a frequency of 115 Hz this means that the maximum and the minimum values differ from ΔS_{\max} by $\pm 17,6\%$. At the same time, the average $\Delta S_{\Sigma \max}$ value for all the blades on the wheel $\Delta S_{\Sigma \max}$ only slightly differs from ΔS_{\max} . In fact, for φ_j varying from 0 to 2π , the sum of the last terms in the radicand of formula (15) is equal to zero and the relative difference, approximately equal to $(n^2/8f^2) \sin^2(\pi f/n)$, is only 1,55%.

Let us compare the calculated dependence obtained by formula (15) to the experimental found using the blade RPM sensor for the case $\sin(\psi f/2n) \approx 1$. We are going to perform the comparison not only for the $\Delta S_{\Sigma \max}$ values but also for the more representative RMS values, which are determined by the results of all measurements rather than the individual points corresponding to the maximum measured values. Furthermore, let us move onto relative values by dividing the calculated and the experimental values into the corresponding averages for the set. The dependence of the calculated and the experimental values on $\varphi_{\text{rel}} = \varphi_j/2\pi$ is shown in fig. 2.

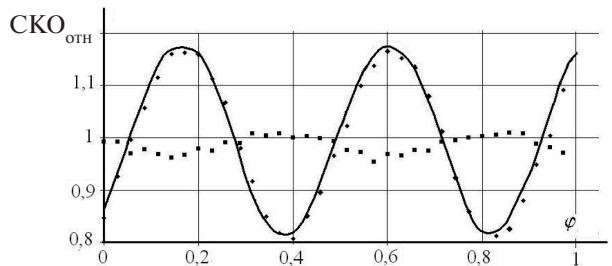


Fig. 2. Oscillation intensity over the wheel circumference versus the keyphasor vibration: calculated (—) and experimental (◆) values using the blade RPM sensor; experimental values (■) using the conventional RPM sensor.

It can be seen that there is a good agreement between the experimental and the calculated results with the blade RPM sensor used. This indicates that the ‘measured’ differences in oscillation intensity over the wheel are fully explained by the vibration of the keyphasor rather than the actual differences in blade amplitudes. Fig. 2 also shows the dependence of RMS- S_{rel} (denoted as CKO_{OTH} in the figure) on φ_{rel} using a

conventional RPM sensor. Evidently, there is also a certain dependence of the oscillation intensity on the angular coordinate. Naturally, the dependence is much weaker, because the amplitude of the torsional oscillations of the rotors assembly near the RPM sensor is smaller than the blade flutter amplitude (see figs. 1, *a* and 1, *б*).

The weak dependence of the average RMS_{rel} value in the set on the vibration of the keyphasor was also confirmed experimentally: the RMS_{rel} value obtained using the blade RPM sensor was only 1,6% higher than the one obtained using the conventional sensor. The differences for the registered flutter with the frequencies of about 108 Hz and 98 Hz were 0,4% and 0,05%, respectively, and did not exceed the measurement and calculation errors (it was previously noted that the error magnitude was proportional to $\sin^2(\pi f/n)$).

The effect of the keyphasor vibration on the errors in determining the oscillation frequency can be revealed by using the transformations similar to the ones previously performed. As before, let us consider virtually the most important case allowing to obtain the maximum results: $\sin(\psi f/2n) = 1$. To find the frequency, we need to calculate the sums that are a part of the right-hand side of formula (3); in this case and provided that $[(1/k_n)x_0 + 2y_0] = 1$ these sums take the following form:

$$\sum_{i=1}^M S_{1\Sigma}^2 = \frac{M}{2} \left[1 + \frac{n^2}{4f^2} \sin^2 \frac{\pi f}{n} + \frac{n}{f} \sin \frac{\pi f}{n} \sin \frac{f}{n} (\varphi_j - \pi) \right]; \quad (16)$$

$$\sum_{i=1}^M \Delta S_{2\Sigma}^2 = \frac{M}{2} \left[1 + \frac{n^2}{4f^2} \sin^2 \frac{\pi f}{n} + \frac{n}{f} \sin \frac{\pi f}{n} \sin \frac{f}{n} (\varphi_j + \Delta\varphi - \pi) \right]; \quad (17)$$

$$\sum_{i=1}^M \Delta S_{1\Sigma} \Delta S_{2\Sigma} = \frac{M}{2} \left[\cos \frac{\Delta\varphi f}{n} + \frac{n^2}{4f^2} \sin^2 \frac{\pi f}{n} + \frac{n}{f} \sin \frac{\pi f}{n} \cos \frac{\Delta\varphi f}{2n} \sin(\varphi_j + \frac{\Delta\varphi}{2} - \pi) \right], \quad (18)$$

where $\Delta S_{2\Sigma}$ are the readings of the second sensor located at an angular distance $\Delta\varphi$ from the first one, also registering the mutual displacements.

The calculations and the experiments show that in this case the ‘change’ of the frequencies is also much stronger if using the blade RPM sensor than if using the conventional one, and is fully explained by the keyphasor vibration (see fig. 3).

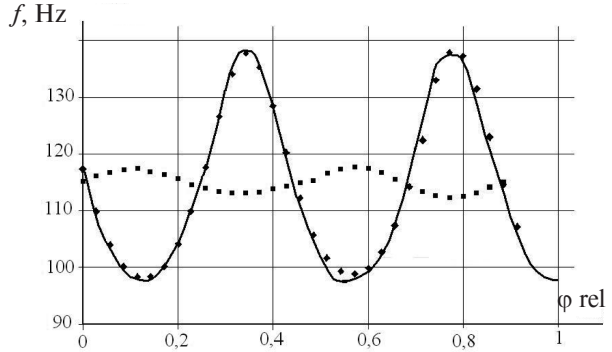


Fig. 3. Oscillation frequency over the wheel circumference versus keyphasor vibration: calculated (—) and experimental (◆) values obtained using the blade RPM sensor; experimental values (■) obtained using the conventional RPM sensor.

The results of the calculations and the experiments also confirm that the average frequencies in the set practically do not depend on the keyphasor vibration. For all three forms of flutter with the frequencies of about 115, 108 and 98 Hz the difference in the average set frequencies when using the blade and the conventional RPM sensors did not exceed a few tenths of percent and was smaller than the measurement and calculation errors.

It also follows from comparing the experimental data presented in figs. 2 and 3 that the torsional oscillations of the rotors assembly near the RPM sensor and the flutter of the stage examined occurred in antiphase.

When using the readings from the sensor pair with small bases S , i.e., when mainly the axial component of the amplitude of the peripheral section is registered, the longitudinal oscillations of the rotors assembly can have a significant effect on the measurement accuracy. The same goes for the axial oscillations of the stator components where the blade DPM sensors are installed, related to the longitudinal oscillations through the thrust bearing. For example, when registering the in-phase oscillations of the right and left blades of the penultimate stage with the frequency $f_{meas} = 7,6$ Hz, it was found that the average total oscillation amplitudes of these stages differed by 15%, while the axial components of the amplitudes differed by 1,5 times. Naturally, the natural forms at the same

frequencies should be very close, and such a large difference in the x_0/y_0 ratios could be explained by the influence of some additional factors. Furthermore, when using formula (3), it was found that the average frequencies were equal to 111,5 Hz for one of the stages, and to 103,4 Hz for the second one, i.e., condition (2) was not satisfied. The measurement results for the average values in the set completely coincided when using the conventional and the blade RPM sensors.

The most likely cause for the significant differences in the x_0/y_0 ratios for the left and right stages are the longitudinal oscillations of the rotors assembly that for one stage were summed with the axial movements of the peripheral sections of the blades, and subtracted from them for the second stage. The differences in the ‘measured’ frequencies most likely depended on the difference in the levels of axial vibration of two pairs of sensors used to determine the frequency and the presence of the phase shift between the vibration of the stator components and the blade flutter. For example, calculations show that for the vibration in one of the pairs of sensors equal to 10% of the axial movement of the blades and the phase shift between the axial vibration and the flutter equal to 0.15π , the ‘measured’ flutter frequency is 103,6 Hz for one stage and 112,4 Hz for another (with the true frequency equal to 107,6 Hz). Approximately the same differences in the frequencies can be obtained provided that the axial vibration is only 5%, but the phase shift is $0,3\pi$.

In some cases, determining the flutter frequencies by formula (3) based on measuring only the axial amplitude component of the peripheral section is impossible. For example, when registering flutter with $f_{meas} = 2,2$ Hz using formula (3), it was obtained that $f = 103,4$ Hz for one of the penultimate stages, and 99,9 Hz for another. Since in view of relation (2) the true frequency could equal either 97,8 or 102,2 Hz, it was necessary to use another, more reliable way to determine the frequency.

The true value of the flutter frequency was determined using formula (7) when determining the dependence of the mutual displacement values on the angular distance ψ between the blades. The results of the calculations for the frequencies of 97,8 and 102,2 Hz are shown in fig. 4. The experimental curve for the mutual displacement values versus ψ is also plotted in that figure. The relative values of the mutual

displacement $A_{rel} = A(\psi)/A_{max}$ are presented versus $\psi_{rel} = \psi/2\pi$.

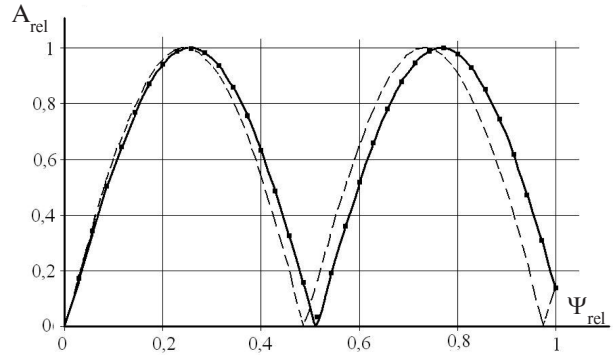


Fig. 4. Mutual displacement values versus angular distance between the blades: the calculated (—) and the experimental (■) values at a frequency of 97,8 Hz; the calculated values (---) at a frequency of 102,2 Hz.

It can be seen that the experimental points practically coincide with the calculated curve for $f = 97,8$ Hz and are significantly different from the calculated curve for $f = 102,2$ Hz (especially for large values of ψ_{rel}).

The described measurement technique allows to obtain not only the data on blade oscillations (including blade flutter with in-phase modes) that is comprehensive from a practical standpoint, but also some interesting data on the state of some other components of the turbine unit, especially when it is operating in the transition modes. For example, data can be obtained on the torsional and longitudinal oscillations of the rotors assembly, as well as on the elastic spin-up of the rotors assembly, the axial shift of the rotor and the static deformation of the blades during rapid ceasing of power; on the change of the relative rotor expansions in the spots where the DPM sensors are installed during a change in the operation mode of the turbine unit. Determining the possibility of a phase shift between the axial and the tangential components of the blade oscillations due to torsional and longitudinal oscillations of the rotors assembly may be of interest for assessing the magnitude of the air damping (or air excitation) when calculating the non-stationary flow effect on the oscillating blade row.

The following conclusions can be formulated based on the above.

1. Using a modified measurement technique allowed to determine the total amplitude, as well as the sum and the difference of the axial and tangential

components with the help of the DPM sensors designed to register only the axial component of oscillations.

2. When registering the flutter with in-phase modes using the upgraded version of the DPM, we have found additional errors that were absent when registering the flutter with disc modes. The appearance of the additional errors can be attributed to the fact that the in-phase blade flutter causes torsional and longitudinal vibrations of the rotors assembly and may cause axial vibration of the stator components where the DPM sensors are installed.

3. The consequence of the keyphasor vibration is the 'natural change' in the amplitudes and frequencies of the blade oscillations over the wheel circumference. However, it should be kept in mind that the average amplitudes and frequencies in the set virtually do not depend on the keyphasor vibration.

4. The axial vibration of the stator components and the longitudinal oscillations of the rotors assembly mainly affect the accuracy of determining the axial amplitude component of the peripheral section of the blade and can lead to errors in determining the oscillation frequency. Therefore, the level of dynamic stresses in the blades must be assessed by the value of the tangential component of the oscillation amplitude.

5. The most accurate value of the flutter frequency can be determined if the experimental dependence of the mutual blade displacements on the angular distance between them is compared with the calculated value obtained using formulae (2) and (7).

6. In order to improve the operational reliability of turbine units, systems for monitoring the vibrational state of the blades, based on the upgraded version of the DPM, should be installed both in new high-power turbines, and in the turbines with fatigue damage of the blades.

REFERENCES

1. **Zablotskiy I.Ye., Korostelev Yu.A., Shipov R.A.** Beskontaktnyye izmereniya kolebaniy lopatok turbomashin. M.: Mashinostroyeniye, 1977. 160 s. (rus.)
2. **Levin A.V., Borishanskiy K.N., Konson Ye.I.** Prochnost i vibratsiya lopatok i diskov parovykh turbin. L.: Mashinostroyeniye, 1981. 710 p. (rus.)
3. **Vorobyev Yu.S.** Kolebaniya lopatochnogo apparata turbomashin. Kiyev: Naukova dumka, 1988. 224 s. (rus.)
4. **Kostyuk A.G.** Dinamika i prochnost turbomashin. M.: Izdatelstvo MEI, 2000. 480 p. (rus.)
5. **Samoylovich G.S.** Vozbuzhdeniye kolebaniy lopatok turbomashin. M.: Mashinostroyeniye, 1975. 288 s. (rus.)
6. **Borishanskiy K.N., Grigoryev B.Ye., Grigoryev S.Yu. [i dr].** Osobennosti reshetochnogo flattera lopatok poslednikh stupeney moshchnykh parovykh turbin. *Ukraina. Nadezhnost i dolgovechnost mashin i sooruzheniy.* 2008. № 30. P. 24–31. (rus.)
7. **Borishanskiy K.N.** Osobennosti avtokolebaniy bandazhirovannykh rabochikh lopatok i mery borby s nimi. *Energetik.* 2010. № 12. S.35–37. (rus.)
8. **Patent RF №2063519.** Ustroystvo dlya zamera amplitud kolebaniy rabochikh lopatok turbomashin diskretno-fazovym metodom / K.N. Borishanskiy, B.Ye. Grigoryev, S.Yu. Grigoryev [i dr]. *BI.* 1996. № 19. (rus.)
9. **Patent RF №2143103** Ustroystvo dlya zamera amplitud kolebaniy bandazhirovannykh lopatok turbin diskretno-fazovym metodom/ K.N. Borishanskiy, B.Ye. Grigoryev, S.Yu. Grigoryev [i dr]. *BI.* 1999. № 35. (rus.)
10. **Borishanskiy K.N.** Kolebaniya rabochikh lopatok parovykh turbin i mery borby s nimi. Germaniya, Saarbrücken: Palmarium Academic Publishing, 2014. 528 p.
11. **Borishanskiy K.N.** Raznovidnosti avtokolebaniy lopatok parovykh turbin i mery borby s nimi. *Nauchno-tekhnicheskiye vedomosti SPbGPU.* 2013. № 2 (171). S. 52–60. (rus.)

СПИСОК ЛИТЕРАТУРЫ

1. **Заблоцкий И.Е., Коростелёв Ю.А., Шипов Р.А.** Бесконтактные измерения колебаний лопаток турбомашин. М.: Машиностроение, 1977. 160 с.
2. **Левин А.В., Боришанский К.Н., Консон Е.И.** Прочность и вибрация лопаток и дисков паровых турбин. Л.: Машиностроение, 1981. 710 с.
3. **Воробьёв Ю.С.** Колебания лопаточного аппарата турбомашин. Киев: Наукова думка, 1988. 224 с.
4. **Костюк А.Г.** Динамика и прочность турбомашин. М.: Издательство МЭИ, 2000. 480 с.
5. **Самойлович Г.С.** Возбуждение колебаний лопаток турбомашин. М.: Машиностроение, 1975. 288 с.
6. **Боришанский К.Н., Григорьев Б.Е., Григорьев С.Ю. [и др].** Особенности решётчатого флаттера лопаток последних ступеней мощных паровых турбин // Украина. Надёжность и долговечность машин и сооружений. 2008. № 30. С. 24–31.
7. **Боришанский К.Н.** Особенности автоколебаний бандажированных рабочих лопаток и меры борьбы с ними // Энергетик. 2010. № 12. С.35–37.
8. **Патент РФ №2063519.** Устройство для замера амплитуд колебаний рабочих лопаток турбомашин дискретно-фазовым методом /К.Н. Боришанский, Б.Е. Григорьев, С.Ю. Григорьев [и др]. // *БИ.* 1996. № 19.

9. Патент РФ №2143103. Устройство для замера амплитуд колебаний бандажированных лопаток турбин дискретно-фазовым методом / К.Н. Боришанский, Б.Е. Григорьев, С.Ю. Григорьев [и др.]. // БИ. 1999, № 35.

10. **Боришанский К.Н.** Колебания рабочих лопаток паровых турбин и меры борьбы с ними. Герма-

ния, Саарбрюккен: Palmarium Academic Publishing, 2014. 528 с.

11. **Боришанский К.Н.** Разновидности автоколебаний лопаток паровых турбин и меры борьбы с ними // Научно-технические ведомости СПбГПУ. 2013. № 2 (171). С. 52–60.

СВЕДЕНИЯ ОБ АВТОРАХ/AUTHORS

BORISHANSKIY Konstantin N. – Peter the Great St. Petersburg Polytechnic University.

29 Politechnicheskaya St., St. Petersburg, 195251, Russia.

E-mail: knb37@mail.ru

БОРИШАНСКИЙ Константин Николаевич – доктор технических наук профессор Санкт-Петербургского политехнического университета Петра Великого.

195251, Россия, г. Санкт-Петербург, Политехническая ул., 29.

E-mail: knb37@mail.ru

**2nT-SHAPED EQUIVALENT CIRCUIT OF A TRANSFORMER
COMPRISING n WINDINGS***M.A. Шакиров***2nT-ОБРАЗНАЯ СХЕМА ЗАМЕЩЕНИЯ ТРАНСФОРМАТОРА,
СОДЕРЖАЩЕГО n ОБМОТОК**

The new detailed $2nT$ -shaped equivalent circuits of a transformer containing n concentric windings, displaying on schematic all magnetic flux between the windings, in the windings, in the elements of the magnetic circuit and between it and the tank in case of saturation of the magnetic circuit is presented. It is based on the idea of stitching the $4T$ -shaped circuit models for two-winding transformers, considered as a unit cell of a more complex $2nT$ -shaped structure. The accuracy of the occurrence in various parts of the magnetic circuit with short-circuit one or more windings of the magnetic super- and counter-fluxes in comparison with the fluxes of idling is confirmed. It is shown that the observation of such anomalous fluxes in the equivalent circuit is possible due to the presence of negative inductances. It is proved that the multi-winding transformer equivalent circuits without negative elements are characterized by a three-diagonal matrix of inductances.

TRANSFORMER; PRIMARY AND SECONDARY WINDINGS; MAGNETIC FLUX; EQUIVALENT CIRCUIT; TREE-WINDING TRANSFORMER; MULTI-WINDING TRANSFORMER; SHORT CIRCUITED; IDLING; COUPLED INDUCTANCE.

Представлены новые развернутые $2nT$ -образные схемы замещения трансформатора, содержащего n концентрических обмоток, с отображением на схемах всех магнитных потоков между обмотками, в самих обмотках, в элементах магнитопровода, а также между ним и баком в случае насыщения магнитопровода. В основу положена идея сшивания $4T$ -образных схемных моделей двух-обмоточных трансформаторов, рассматриваемых в качестве элементарных ячеек более сложной $2nT$ -образной структуры. Подтверждена достоверность возникновения в различных частях магнитопровода при коротких замыканиях одной или нескольких обмоток магнитных сверх- и антипотоков в сравнении с потоками холостого хода. Показано, что наблюдение этих аномальных потоков на схеме замещения возможно благодаря присутствию в ней отрицательных индуктивностей. Доказано, что схемы замещения многообмоточного трансформатора без отрицательных элементов характеризуются трехдиагональной матрицей индуктивностей.

ТРАНСФОРМАТОР; ПЕРВИЧНАЯ И ВТОРИЧНАЯ ОБМОТКИ; МАГНИТНЫЙ ПОТОК; СХЕМА ЗАМЕЩЕНИЯ; ТРЕХОБМОТОЧНЫЙ ТРАНСФОРМАТОР; МНОГООБМОТОЧНЫЙ ТРАНСФОРМАТОР; КОРОТКОЕ ЗАМЫКАНИЕ; ХОЛОСТОЙ ХОД; ВЗАИМНАЯ ИНДУКТИВНОСТЬ.

Introduction

A multi-winding transformer is defined as the one with more than two electrically disconnected windings. Such a transformer can replace two or several

double-winding ones, which simplifies the connection between the electric stations and the distribution networks and, in general, results in reducing the maintenance costs and the total costs of electric power systems. However, the correct conclusion

about the benefits of multi-winding transformers (these also include split-winding transformers) can be made only by understanding the complete picture of the physical processes occurring in these transformers, which have not been clarified up to the present time. A discussion unfolded about the main feature of any of their equivalent circuits (polygonal-type [1-5], tree-type [6], chain-type [1,6], etc.), that is, of the negative inductances present in them, which has been cause for alarmist statements such as “there is no reason to look for a physical explanation of this phenomenon...” (see p. 56 in [4]). Ref. [5, p. 124] described the negative inductances as a mathematical curiosity “due to difference between the RMS and the mean values of the function”. Ref. [6, p. 89] even went as far as to state that these “inductances have no physical meaning”, and the explanation given for their presence is rather nonsensical: “they merely coordinate the equivalent circuit with the existing couplings”. The negative inductances are described in this same vein in all textbooks, and their low numerical value in comparison with other inductances is emphasized [7–10]. Despite this, A. Boyjian “physically interpreted them as a result of mutual-inductance coupling” [3]. Following this study, the authors of [11, 12] made a critical review of the papers on the subject and offered to dispose of these ‘virtual’ values (as described in [3]) by introducing mutual-inductance couplings ($M_{i,j}$) between *all* leakage inductances. Speaking of the three-winding transformer, the authors of [12] write, “we **postulate** that L_{12} and L_{23} must be mutually coupled”, giving a very vague sense to M : “The mutual inductance M gives the magnetic coupling of the leakage fields between windings (flux in air)”, but then go on to specify that “ M does not have any relationship with the commonly used mutual inductance...”. The branch inductance matrix of their equivalent circuit turns out to be completely filled, and its off-diagonal elements $M_{i,j}$ are determined by very complex formulae and have different signs, which raises further questions.

The reason for the above-described vacillations between “the lack of physical sense” and “physical interpretation” based on dubious ‘postulates’ is in the deeply rooted phenomenological approach to modeling the transformer by external characteristics with respect to its $n + 1$ poles (as a rule, by the short-circuit impedance between the pairs of its windings). This approach excludes the possibility of controlling the physical processes inside the transformer, in par-

ticular, the relationship between the magnetic fluxes in the individual parts of the magnetic circuit, the window, the space around the tank, etc., which is extremely important for assessing the magnetic state of the individual components of the magnetic circuit. As a result, the issues related to the analysis of electrodynamic stability of transformers in abnormal conditions remain unsolved. None of the existing theories, as well as the standard packages (Simulink Matlab, EMTR-type, etc.) developed on the basis of these theories, do not allow to even set the problem on assessing the differences in the saturation of the individual components of the magnetic circuit with a sudden short-circuit in one or more of the transformer windings (which is important for correctly assessing the initial short-circuit currents), as it is erroneously assumed that the magnetic circuit is not saturated in a short-circuit event (see [4, p. 307] or [8, p. 81], etc.).

At the same time, as shown in [13,14] for a double-winding transformer, implementing the idea of obtaining circuit models with all magnetic fluxes of the transformer displayed is possible (!) if *primary* quantities, i.e., the electric and magnetic field strengths and the Poynting vector, are used as a basis, and if the operating principles of the transformer are approached from a completely different perspective. The equivalent circuits with fluxes give physical sense to each of the circuit’s elements. It turned out that *allocation of negative inductances* was required to display the magnetic fluxes in the equivalent circuit of even a double-winding transformer; besides, these inductances also play a key role in explaining the physics of magnetic super- and counter-fluxes under short-circuit conditions and in case of sudden short circuits. The existence of these fluxes was conclusively proved both experimentally [15] and by constructing images of the magnetic fields in a short-circuited transformer [16, 17].

The goal of this study is in obtaining similar ‘physical’ circuit models for a multi-winding shell-type transformer with a clear presentation of all magnetic fluxes between its windings, in the windings themselves, in the elements of the magnetic circuit, as well as between the magnetic circuit and the tank in case of saturation of steel (fig. 1). The term ‘physical circuit models’ is arbitrary and is used in order to:

- emphasize the fundamental difference between these models and the existing conventional equivalent circuits which in fact oversimplify the concept of an

n -winding transformer, describing it as a ‘black box’ with $n+1$ poles,

– reflect the universal character of the new models allowing, as a result of slight simplifications, to obtain the known equivalent circuits, as well as to control and correct the errors in any other models, for example, the ones proposed in [11].

Assumptions and notations. In accordance with the general rules [4,11], let us assume that all windings have been reduced to the same number of turns, i.e.,

$$w_a = w_b = w_c = w_d = w_e \rightarrow w_1 \quad (1)$$

which allows to avoid using strokes that usually mark the reduced values. In describing the operating principles and the key features of any device, the secondary factors are initially neglected, and the device is regarded as a system with the optimal (limit) performance indicators, which the real device should approach. In our case, this means moving on to the analysis of the performance of the n -winding idealized transformer (fig. 1) with the following assumptions:

the magnetic circuit is characterized by $\mu_{\text{steel}} = \infty$ and the conductivity $\gamma_{\text{steel}} = \infty$;

the resistances of the windings $R_a = R_b = \dots = R_e = 0$;

additional resistances for the steady state, caused by eddy currents in the windings,

$$R_a^{\text{eddy}} = R_b^{\text{eddy}} = \dots = R_e^{\text{eddy}} = 0;$$

winding height $h_w = h$, where h is the height of the transformer window;

the magnetic field lines in the window are straight and parallel to the core axis.

Fig. 1 shows the arbitrary positive directions of the magnetic fluxes. The absolute values of the flux complexes ($\dot{\Phi}_k$) coincide with their effective values (Φ_k). The typical relationship between the coil voltage and its flux has the form:

$$\dot{U}_k = j\omega w_1 \dot{\Phi}_k = k_0 \dot{\Phi}_k, \quad (2)$$

where the constant

$$k_0 = j\omega w_1. \quad (3)$$

The magnetic fluxes in the magnetic circuit (fig. 1):

$\dot{\Phi}_{leg}$ – in the *leg*;

$\dot{\Phi}_{side}$ – in the *side yoke*;

$\dot{\Phi}_j^a$ – in the *joint yoke* from the side of the leg towards the internal winding w_a ;

$\dot{\Phi}_j^{a\delta}, \dot{\Phi}_j^{b\delta}, \dot{\Phi}_j^{c\delta}, \dot{\Phi}_j^{d\delta}$ – in the *joint yoke* from the side of the windings towards the gaps between the windings;

$\dot{\Phi}_j^{\delta b}, \dot{\Phi}_j^{\delta c}, \dot{\Phi}_j^{\delta d}, \dot{\Phi}_j^{\delta e}$ – in the *joint yoke* from the side of the gaps towards the windings;

$\dot{\Phi}_j^e$ – in the *joint yoke* from the side of the external winding w_e towards the side yoke.

The magnetic fluxes in the transformer window:

$\dot{\Phi}_{\delta 1}, \dot{\Phi}_{\delta 2}, \dot{\Phi}_{\delta 3}, \dot{\Phi}_{\delta 4}$ – in the channels between the windings;

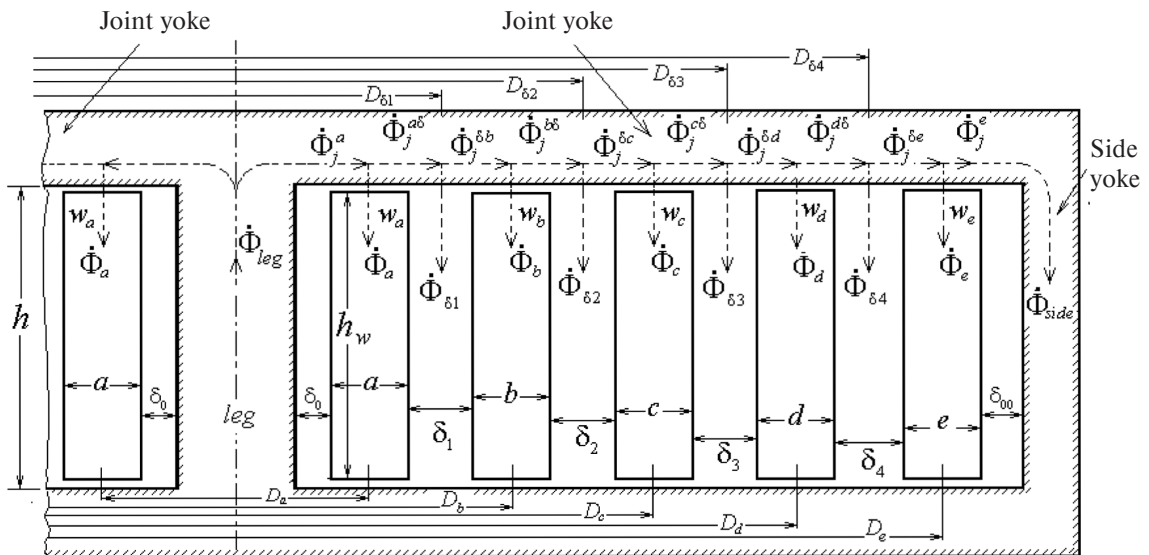


Fig. 1. Magnetic fluxes in the steel and in the window of a 5-winding shell transformer

$\dot{\Phi}_a, \dot{\Phi}_b, \dot{\Phi}_c, \dot{\Phi}_d, \dot{\Phi}_e$ – within the bulk of the windings.

Unlike the fluxes in the window of the idealized double-winding transformer, these fluxes are not in-phase and depend on the nature of the winding loads.

The following relations are obvious between the magnetic fluxes in the nodes of the magnetic circuit:

$$\dot{\Phi}_{leg} \equiv \dot{\Phi}_j^a = \dot{\Phi}_a + \dot{\Phi}_j^{a\delta}; \quad (4)$$

$$\dot{\Phi}_j^{a\delta} = \dot{\Phi}_{\delta 1} + \dot{\Phi}_j^{\delta b}; \quad (5)$$

$$\dot{\Phi}_j^{\delta b} = \dot{\Phi}_b + \dot{\Phi}_j^{b\delta}; \quad (6)$$

$$\dot{\Phi}_j^{b\delta} = \dot{\Phi}_{\delta 2} + \dot{\Phi}_j^{\delta c}; \quad (7)$$

$$\dot{\Phi}_j^{\delta c} = \dot{\Phi}_c + \dot{\Phi}_j^{c\delta}; \quad (8)$$

$$\dot{\Phi}_j^{c\delta} = \dot{\Phi}_{\delta 3} + \dot{\Phi}_j^{\delta d}; \quad (9)$$

$$\dot{\Phi}_j^{\delta d} = \dot{\Phi}_d + \dot{\Phi}_j^{d\delta}; \quad (10)$$

$$\dot{\Phi}_j^{d\delta} = \dot{\Phi}_{\delta 4} + \dot{\Phi}_j^{\delta e}; \quad (11)$$

$$\dot{\Phi}_j^{\delta e} = \dot{\Phi}_e + \dot{\Phi}_j^e \equiv \dot{\Phi}_e + \dot{\Phi}_{side}. \quad (12)$$

The principal idea of creating an *expanded* equivalent electrical circuit (in the sense that, along with the electrical values ($\dot{U}_1, \dot{U}_2, \dots, \dot{U}_5, \dot{I}_1, \dot{I}_2, \dots, \dot{I}_5$), it will display all of the above-listed magnetic fluxes, i.e., they can be *seen*) will be implemented through directly using these relations.

The magnetic resistances of the annular channels in the window:

$$\begin{aligned} R_{\delta 1}^M &= \frac{h}{\mu_0 s_{\delta 1}}; & R_{\delta 2}^M &= \frac{h}{\mu_0 s_{\delta 2}}; \\ R_{\delta 3}^M &= \frac{h}{\mu_0 s_{\delta 3}}; & R_{\delta 4}^M &= \frac{h}{\mu_0 s_{\delta 4}}. \end{aligned} \quad (13)$$

where the lower index in the notation for the surface area (s_k) coincides with the notation for width of the corresponding annular channel:

$$\begin{aligned} s_{\delta 1} &= \pi D_{\delta 1} \delta_1, & s_{\delta 2} &= \pi D_{\delta 2} \delta_2, \\ s_{\delta 3} &= \pi D_{\delta 3} \delta_3, & s_{\delta 4} &= \pi D_{\delta 4} \delta_4. \end{aligned} \quad (14)$$

The magnetic resistances of the annular channels occupied by the windings:

$$\begin{aligned} R_a^M &= \frac{h}{\mu_0 s_a}; & R_b^M &= \frac{h}{\mu_0 s_b}; \\ R_c^M &= \frac{h}{\mu_0 s_c}; & R_d^M &= \frac{h}{\mu_0 s_d}, \end{aligned} \quad (15)$$

where

$$\begin{aligned} s_a &= \pi D_a a, & s_b &= \pi D_b b, & s_c &= \pi D_c c, \\ s_d &= \pi D_d d, & s_e &= \pi D_e e. \end{aligned} \quad (16)$$

These values are used to determine the terms that are part of the expression for the short-circuit (s/c) inductance of the corresponding pair of windings. For convenience of notation for the inductances, let us introduce a coefficient

$$\beta_0 = \frac{w_1^2 \mu_0}{h}. \quad (17)$$

To construct an equivalent circuit for a three-winding transformer with *a, b, c*-windings, we should consider the properties and characteristics of three 4T-shaped circuit models of double-winding transformers (*a/b, b/c* and *a/c*) that can be separated from it and essentially comprising it.

Negative inductances in a model of a double-winding transformer. In view of the notations introduced, the equivalent circuit of an idealized double-winding *a, b*-transformer takes the form shown in fig. 2, *a*. Fig. 2, *b* next to it shows the equivalent circuit for *a, b, c*-transformer.

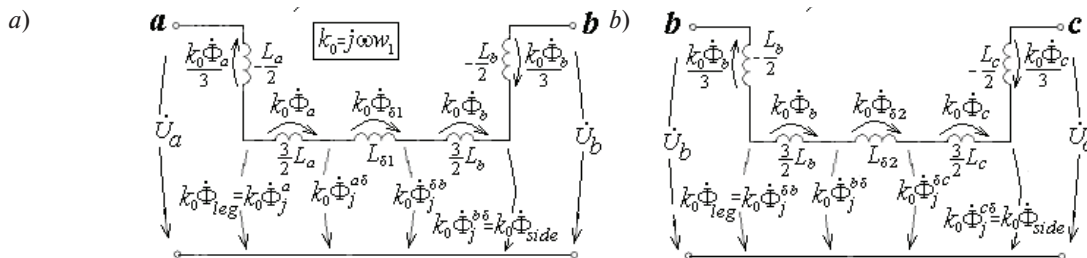


Fig. 2. 4T-shaped equivalent circuits of double-winding *a, b*- (*a*) and *b, c*- (*b*) transformers

In contrast with [13, 14], for the sake of convenience the branches with negative inductances are displayed vertically in both circuits. Both circuits are of the *reduced 4T-shaped*, as they contain four transverse arrows, each *highlighting* a magnetic flux in one of the parts of the magnetic circuit. Using Kirchhoff's second law, we can verify that Eqs. (4), (5), (6) hold in the circuit in Fig. 2a, and Eqs. (6), (7), (8) hold in the circuit in Fig. 2b. All inductances in the circuits (Figs. 2a, 2b) are series-connected. Their total value in each circuit is the typical short-circuit inductance (L^{sh}). For the circuit in fig. 2,a

$$L_{ab}^{sh} = L_a + L_{\delta_1} + L_b \quad (18)$$

and for the circuit in fig. 2,b

$$L_{bc}^{sh} = L_b + L_{\delta_2} + L_c. \quad (19)$$

However, unlike conventional theory (described in textbooks), the new theory [13, 14] regards each component of the short-circuit inductance not as a leakage inductance, but as a functional element of the equivalent circuit, or as a *means* for displaying the power flow (or the Poynting vector) through the corresponding segment of the transformer window. Because of this, the quantities

$$\begin{aligned} L_{\delta_1} &= \beta_0 s_{\delta_1}; & L_{\delta_2} &= \beta_0 s_{\delta_2}; \\ L_{\delta_3} &= \beta_0 s_{\delta_3}; & L_{\delta_4} &= \beta_0 s_{\delta_4} \end{aligned} \quad (20)$$

should be called the *inductance of power transportation* (or the *inductance of Poynting vector transportation*) *in the corridors between the windings* or just *corridor inductances*, while each of the quantities:

$$\begin{aligned} L_a &= \beta_0 \frac{s_a}{3}; & L_b &= \beta_0 \frac{s_b}{3}; & L_c &= \beta_0 \frac{s_c}{3}; \\ L_d &= \beta_0 \frac{s_d}{3}; & L_e &= \beta_0 \frac{s_e}{3} \end{aligned} \quad (21)$$

should be called the *inductance of power flow increase* (or the *inductance of Poynting vector increase*), if it belongs to the primary winding, or the *inductance of power flow decrease* (or the *inductance of Poynting vector decrease*), if it belongs to the secondary winding.

The branches with negative inductances should be allocated in the equivalent circuit of the double-winding transformer for three reasons:

1) for localizing the fluxes passing through the bulk of the windings ($\dot{\Phi}_a, \dot{\Phi}_b$ in fig. 2,a and $\dot{\Phi}_b, \dot{\Phi}_c$ in fig. 2,b); these branches are then used to display the contribution of the fluxes in the bulk of the wind-

ings to their flux linkage (see formulae (57) and (58) in [14]);

2) to clearly demonstrate the super- and counter-fluxes in the magnetic circuit in case of a short circuit in one of the transformer's windings;

3) to conveniently implement the key idea of the paper, which is in constructing the equivalent circuits for multi-winding transformers by *stitching together* (combining) the circuit models of double-winding transformers.

Short-circuit super- and counter-fluxes are determined by comparing the s/c fluxes with the no-load flux ($\dot{\Phi}_0$) in the steel magnetic circuit which, in view of the assumptions made earlier, takes the same value in all parts of the magnetic circuit regardless of which of the windings (fig. 1) is powered by the primary voltage \dot{U}_1 :

$$\dot{\Phi}_0 = \frac{\dot{U}_1}{k_0}. \quad (22)$$

If only two windings are used in a 5-winding transformer, the other three can be regarded as measuring coils, which allows to assess the magnitudes of the super- and counter-fluxes in s/c modes of double-winding transformers.

Note 1. We are going to use the geometric dimensions of the windings for the 5-winding transformer (fig. 1), presented in [11], for our calculations (in millimeters):

$$a = 41, \quad b = 43, \quad c = 10, \quad d = 10, \quad e = 10, \quad D_a = 438, \\ D_b = 578, \quad D_c = 667, \quad D_d = 723, \quad D_e = 769,$$

$$\delta_1 = 28, \quad \delta_2 = 18, \quad \delta_3 = 18, \quad \delta_4 = 13, \quad D_{\delta_1} = 507, \\ D_{\delta_2} = 639, \quad D_{\delta_3} = 695, \quad D_{\delta_4} = 746, \quad h = 979.$$

The number of turns of the winding is $w_1 = 100$.

The cross-sectional areas of the windings are then equal to (in m²):

$$s_a = 0,0564; \quad s_b = 0,0781; \quad s_c = 0,0210; \quad s_d = 0,0227; \\ s_e = 0,0242.$$

The cross-sectional areas of the gaps between the windings are then equal to (in m²):

$$s_{\delta_1} = 0,0446; \quad s_{\delta_2} = 0,0361; \quad s_{\delta_3} = 0,0393; \quad s_{\delta_4} = 0,0305.$$

According to (20) and (21), we obtain that (in mH):

$$L_{\delta_1} = 0,5724; \quad L_{\delta_2} = -0,4638; \quad L_{\delta_3} = 0,05044; \\ L_{\delta_4} = 0,03910;$$

$$L_a = 0,2413; L_b = 0,3340; L_c = 0,0896;$$

$$L_d = 0,0971; L_e = 0,1033.$$

Short-circuit resistances for the pairs of windings are obtained by Eqs. (18), (19) and similar ones (in mH):

$$L_{ab}^{sh} = 1,1479; L_{ac}^{sh} = 2,696; L_{ad}^{sh} = 3,1505;$$

$$L_{ae}^{sh} = 3,8393; L_{bc}^{sh} = 0,8876; L_{bd}^{sh} = 1,6685;$$

$$L_{be}^{sh} = 2,3573; L_{cd}^{sh} = 0,6913; L_{ce}^{sh} = 1,3801;$$

$$L_{de}^{sh} = 0,5916.$$

Let us consider an a,b -transformer (fig. 2, a). The other three windings (c,d and e) are open (fig. 1). Regardless of whether the winding a or b is the primary one, the s/c current is equal to

$$\dot{I}_{sh} = \frac{\dot{U}_1}{j\omega L_{ab}^{sh}} = \frac{\dot{U}_1}{j\omega(L_a + L_{\delta 1} + L_b)}. \quad (23)$$

The a -winding is primary ($\dot{U}_1 = \dot{U}_a$), therefore the flux in the core

$$\dot{\Phi}_{leg}^{sh} \equiv \dot{\Phi}_j^{ash} = \frac{\dot{U}_1 - \left(j\omega \left(-\frac{L_a}{2} \right) \right) \cdot \dot{I}_{sh}}{k_0} =$$

$$= \frac{\dot{U}_1}{k_0} \left(1 + \frac{L_a}{2L_{ab}^{sh}} \right) = \left(1 + \frac{L_a}{2L_{ab}^{sh}} \right) \dot{\Phi}_0, \quad (24)$$

and the flux in the side yoke

$$\dot{\Phi}_{side}^{sh} \equiv \dot{\Phi}_j^{bsh} = \frac{\left(j\omega \left(-\frac{L_b}{2} \right) \right) \cdot \dot{I}_{sh}}{k_0} =$$

$$= -\frac{\dot{U}_1}{k_0} \frac{L_b}{2L_{ab}^{sh}} = -\frac{L_b}{2L_{ab}^{sh}} \dot{\Phi}_0. \quad (25)$$

Since $\dot{\Phi}_{leg}^{sh} > \dot{\Phi}_0$, then the flux $\dot{\Phi}_{leg}^{sh}$ is the *super-flux*. Since $\dot{\Phi}_{side}^{sh}$ is directed towards the flux $\dot{\Phi}_{leg}^{sh}$, then $\dot{\Phi}_{side}^{sh}$ is the *counter-flux*. In our case, we obtain for the super-flux in the leg of the a,b -transformer:

$$\dot{\Phi}_{leg}^{sh} \equiv \dot{\Phi}_{leg}^{ash} = \left(1 + \frac{L_a}{2(L_a + L_{\delta 1} + L_b)} \right) \dot{\Phi}_0 =$$

$$= \left(1 + \frac{s_a}{2s_a + 6s_{\delta 1} + 2s_b} \right) \dot{\Phi}_0 = 1,105 \dot{\Phi}_0.$$

Its counter-flux in the side yoke is equal to

$$\dot{\Phi}_{side}^{sh} = -\frac{L_b}{2(L_a + L_{\delta 1} + L_b)} \dot{\Phi}_0 =$$

$$= -\frac{s_b}{(2s_a + 6s_{\delta 1} + 2s_b)} \dot{\Phi}_0 = -0,146 \dot{\Phi}_0.$$

All windings have the same number of turns, so the voltage readings in the c, d, e windings are identical and equal to:

$$\dot{U}_c^{sh} = \dot{U}_d^{sh} = \dot{U}_e^{sh} = k_0 \dot{\Phi}_{side}^{sh} =$$

$$= -\frac{s_b}{(2s_a + 6s_{\delta 1} + 2s_b)} \dot{U}_1 = -0,146 \dot{U}_1.$$

The first row of table 1 lists the numerical values of currents and voltages in the s/c mode under consideration at $\dot{U}_1 \equiv \dot{U}_a = 1000W$. The frequency $f = 50$ Hz was used when calculating the currents. The frequency is not involved in the ratios for fluxes and voltages. Designation **Tr.** from the word **Transformer**.

Table 1

Examples of calculating voltages and currents in the 5-winding transformer

Example	Quantity	Windings (fig. 1)				
		a	b	c	d	e
1 (a,b -Tr.)	U_k (Volt)	1000	0	-146	-146	-146
	I_k^{sh} (Ampere)	2772,9	2772,9	0	0	0
2 (b,a -Tr.)	U_k (Volt)	0	1000	1146	1146	1146
	I_k^{sh} (Ampere)	2772,9	2772,9	0	0	0
3 (b,a -Tr.)	U_k (Volt)	940,7 (945,3)	1000 (1000)	1018 (1015,3)	1018 (1015,3)	1018 (1015,3)
	$R_H = 1\Omega$ I_k^{sh} (Ampere)	940,7 (945,3)	940,7 (945,3)	0 (0)	0 (0)	0 (0)

Ending table 1

Example	Quantity	Windings (fig. 1)				
		<i>a</i>	<i>b</i>	<i>c</i>	<i>d</i>	<i>e</i>
4	U_k (Volt)	1000	445	0	-18,9	-18,9
(<i>a, c</i> - Tr.)	I_k^{sh} (Ampere)	1343,3	0	1343,3	0	0

Short-circuit super- and counter-fluxes in the same transformer change places if the *b*-winding is primary and $\dot{U}_1 = \dot{U}_b$ (i.e., in the *b, a*-transformer (fig. 2,*a*)). The current \dot{I}_{sh} for the short-circuited *a*-winding coincides with its value (23), and the flux in the leg becomes the counter-flux:

$$\begin{aligned} \dot{\Phi}_{leg}^{sh} &\equiv \dot{\Phi}_j^{ash} = \frac{\left(j\omega \left(-\frac{L_a}{2} \right) \right) \cdot \dot{I}_{sh}}{k_0} = \\ &= -\frac{\dot{U}_1}{k_0} \frac{L_a}{2L_{ab}^{sh}} = -\frac{L_a}{2L_{ab}^{sh}} \dot{\Phi}_0, \end{aligned}$$

while the flux in the side yoke is transformed into the super-flux

$$\begin{aligned} \dot{\Phi}_{side}^{sh} &\equiv \dot{\Phi}_j^{bsh} = \frac{\dot{U}_1 + j\omega \frac{L_b}{2} \cdot \dot{I}_{sh}}{k_0} = \\ &= \frac{\dot{U}_1}{k_0} \left(1 + \frac{L_b}{2L_{ab}^{sh}} \right) = \left(1 + \frac{L_b}{2L_{ab}^{sh}} \right) \dot{\Phi}_0. \end{aligned}$$

The voltage readings from the *c, d, e* windings will exceed the applied voltage, as shown in the second row of Table 1:

$$\begin{aligned} \dot{U}_c^{sh} = \dot{U}_d^{sh} = \dot{U}_e^{sh} &= k_0 \dot{\Phi}_{side}^{sh} = \\ &= \left(1 + \frac{s_b}{2s_a + 6s_{\delta_1} + 2s_b} \right) \dot{U}_1 = 1,146 \dot{U}_1, \end{aligned}$$

thus confirming the occurrence of the s/c super-flux in the side yoke.

The third row of table 1 demonstrates that it is possible for a super-flux to emerge at a loud $R_H = 1 \Omega$. The calculations are given in the Appendix.

Double-winding elements of the three-winding transformer. With the *d* and *e* windings open, the 5-winding transformer becomes a three-winding *a, b, c*-transformer. It contains three double-winding transformers: *a, b*-, *b, c*- and *a, c*-transformers (see figs. 2,*a*, 2,*b*, and 3,*a*).

In the schematic (fig. 3,*a*), L_a is the inductance of power flow increase, and L_c is the inductance of power flow decrease. Since the width of the corridor between the windings *a* and *c* is equal to

$$\delta_1 + b + \delta_2,$$

then the inductance of power transportation in this corridor

$$L_{\delta_1 + b + \delta_2} = \beta_0 (S_{\delta_1} + S_b + S_{\delta_2}). \quad (26)$$

Taking into account (20) and (21), it can be represented as:

$$L_{\delta_1 + b + \delta_2} = L_{\delta_1} + \frac{3}{2} L_b + \frac{3}{2} L_b + L_{\delta_2}. \quad (27)$$

The magnetic flux in the corridor between the windings

$$\dot{\Phi}_{(\delta_1 + b + \delta_2)} = \dot{\Phi}_{\delta_1} + \dot{\Phi}_b + \dot{\Phi}_{\delta_2} = \frac{j\omega L_{(\delta_1 + b + \delta_2)} \dot{I}}{k_0}. \quad (28)$$

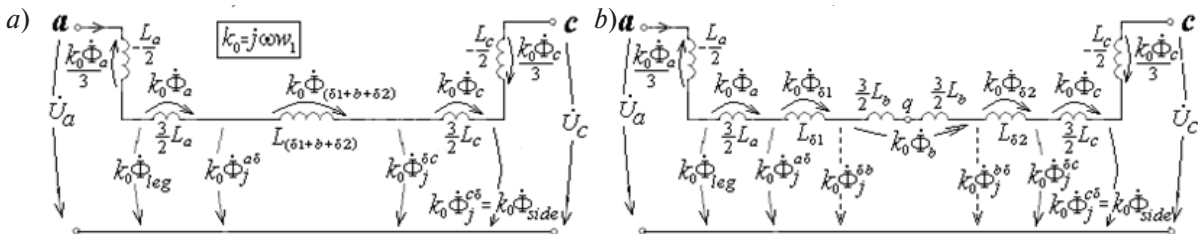


Fig. 3. 4T-shaped equivalent circuit of a double-winding *a, c*-transformer with the concentrated inductance $L_{\delta_1 + b + \delta_2}$ (*a*) and its partition into four components with the central node *q* (*b*)

It follows from (27) and (28) that the flux in the bulk of the open b -winding is equal to

$$\dot{\Phi}_b = \frac{j\omega \left(\frac{3}{2}L_b + \frac{3}{2}L_b \right) \dot{I}}{k_0}, \quad (29)$$

which is shown in fig. 3,b. It is also possible to identify the quantities $k_0 \dot{\Phi}_j^{\delta b}$ and $k_0 \dot{\Phi}_j^{\delta \delta}$ in the schematic, marked by dashed lines. The result is a 6T-shaped equivalent circuit of a double-winding transformer, which was a consequence of dividing the corridor between its a and c windings into three annular channels with the widths $\delta 1$, b and $\delta 2$.

Note 2. By partitioning the corridor into a larger number of channels, it is possible to construct an equivalent circuit with an arbitrary large number of transverse arrows, thus obtaining a *distributed* structure for the equivalent circuit of the double-winding transformer.

The internal inductance of the a,c -transformer (or the s/c inductance) from the side of the a -winding with the c -winding short circuited is equal to:

$$L_{ac}^{sh} = L_a + L_{\delta 1+b+\delta 2} + L_c = L_a + (L_{\delta 1} + 3L_b + L_{\delta 2}) + L_c = L_{ab}^{sh} + L_b + L_{bc}^{sh} = 0,00237 \text{ H.}$$

Note 3. This expression implies a useful relation

$$L_b = L_{ac}^{sh} - (L_{ab}^{sh} + L_{bc}^{sh}) \quad (30)$$

which will be used below when studying a three-winding transformer.

For the s/c current we obtain

$$\dot{I}_{sh} = \frac{\dot{U}_1}{j\omega L_{ac}^{sh}} = 1343,3 \text{ A.}$$

Similar to (24) and (25), we find the fluxes in the s/c mode:

$$\begin{aligned} \dot{\Phi}_{leg}^{sh} &\equiv \dot{\Phi}_j^{a,sh} = \left(1 + \frac{L_a}{2L_{ac}^{sh}} \right) \dot{\Phi}_0 = \\ &= \left(1 + \frac{s_a}{2s_a + 6(s_{\delta 1} + s_b + s_{\delta 2}) + 2s_c} \right) \dot{\Phi}_0 = 1,051 \dot{\Phi}_0; \end{aligned}$$

$$\begin{aligned} \dot{\Phi}_{side}^{sh} &\equiv \dot{\Phi}_j^{b,sh} = -\frac{L_c}{2L_{ac}^{sh}} \dot{\Phi}_0 = \\ &= -\frac{s_c}{2s_a + 6(s_{\delta 1} + s_b + s_{\delta 2}) + 2s_c} = -0,0189 \dot{\Phi}_0. \end{aligned}$$

They are weakened due to the fairly wide gap between the windings (see the last row of table 1). The voltages in the open windings e , d are equal to:

$$\dot{U}_e^{sh} = \dot{U}_d^{sh} = k_0 \dot{\Phi}_{side}^{sh} = -0,0189 \dot{U}_1.$$

The voltage at the terminals of the open b -winding can be found from its flux linkage

$$\dot{U}_b = j\omega \dot{\Psi}_b = k_0 \left[(\dot{\Phi}_{leg} - \dot{\Phi}_a - \dot{\Phi}_{\delta 1}) - \frac{\dot{\Phi}_b}{2} \right]. \quad (31)$$

In the s/c mode we obtain (see Table 1)

$$\begin{aligned} \dot{U}_b^{sh} &= k_0 \left[(\dot{\Phi}_{ct}^{sh} - \dot{\Phi}_a^{sh} - \dot{\Phi}_{\delta 1}^{sh}) - \frac{\dot{\Phi}_b^{sh}}{2} \right] = \\ &= \left(1 + \frac{L_a}{2L_{ac}^{sh}} - \frac{\frac{3L_a}{2} + L_{\delta 1} + \frac{3L_b}{2}}{L_{ac}^{sh}} \right) \dot{U}_1 = 0,445 \dot{U}_1. \end{aligned}$$

Note. The s/c voltages listed in table 1 are presented as the consequences of the emergence of super- and counter-fluxes. This indicates that under real conditions the magnetic circuit is, firstly, unevenly magnetized in an s/c, and, secondly, its part containing the super-flux can turn out to be (depending on the cross-section of the magnetic circuit in this part) an order of magnitude more saturated than under the no-load conditions. With sudden short circuits this may lead to an increase in the initial s/c by 20-30% from its calculated value determined by the formulae of the conventional theory (known to have been derived in disregard of the magnetizing currents, i.e., assuming that the magnetic circuit is demagnetized in the event of an s/c (see [4, p. 307], [8, p.81 and p. 131], etc.)). The error up to 50% occurs in the calculations of electrodynamic forces under a short circuit.

A 6T-shaped equivalent circuit of an idealized three-winding transformer. Comparing the model of the double-winding a,c -transformer (fig. 3,b) with the two circuits in fig. 2, we can conclude that it can be regarded as the result of stitching the equivalent circuits of the a,b - and the b,c -transformers in node q . If we preserve the vertical branch with the negative inductance ($-L_b/2$), we obtain a three-pole circuit, which is the equivalent circuit of a three-winding (a,b,c)-transformer (fig. 4). The proof is in checking whether the *boundary conditions* that the three-winding transformer must satisfy are fulfilled in this scheme, that is to say, that the transformer must be simultaneously:

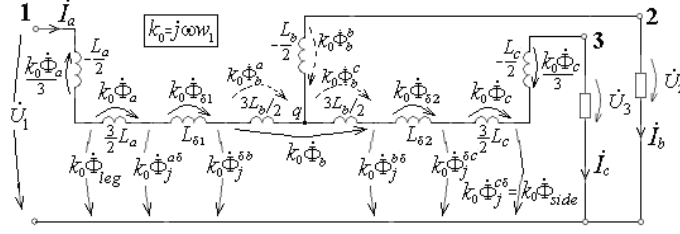


Fig. 4. 6T-shaped equivalent circuit of an idealized three-winding transformer

an a,b -transformer from the side of poles 1 and 2 (with pole 3 idle);

a b,c -transformer from the side of poles 2 and 3 (with pole 1 idle);

an a,c -transformer from the side of poles 1 and 3 (with pole 2 idle), which, obviously, follows from the above-described procedure of stitching the subcircuits along the negative inductance $(-L_b/2)$. A fourth boundary condition is also satisfied, i.e., that the inductance $(-L_b/2)$ is simultaneously included in the a,b - and the b,c -transformers. The circuit obtained also complies with the internal properties of the transformer both in the relationships between the fluxes and in the winding currents:

$$\dot{I}_a = \dot{I}_b + \dot{I}_c. \quad (32)$$

The accuracy of the circuit (fig. 4) is confirmed by the fact that the inductances of the circuit branches emerging from node q coincide with the known expressions for L_{123} , L_{213} and L_{312} that have been first obtained in [1] as combinations of s/c resistances of separate double-winding transformers. In particular, we can write for the inductance of the branch between nodes 1 and q directly by the schematic (fig. 4), taking into account relation (30),

$$\begin{aligned} L_{1,q} &= (L_a + L_{\delta 1} + L_b) + \frac{L_b}{2} = \\ &= L_{ab}^{sh} + \frac{L_{ac}^{sh} - (L_{ab}^{sh} + L_{bc}^{sh})}{2} = \frac{L_{ac}^{sh} + L_{ab}^{sh} - L_{bc}^{sh}}{2} = L_{123}, \end{aligned}$$

where the penultimate fraction coincides with the expression for L_{123} from [4] after its indices a,b,c are substituted for 1,2,3, respectively. The inductance of the branch emerging from node q to node 2 of the central b -winding is negative and can be represented as

$$\begin{aligned} L_{2,q} &= -\frac{L_b}{2} = -\frac{L_{ac}^{sh} - (L_{ab}^{sh} + L_{bc}^{sh})}{2} = \\ &= \frac{L_{ba}^{sh} + L_{bc}^{sh} - L_{ac}^{sh}}{2} = L_{213} < 0. \end{aligned}$$

For the inductance of the branch emerging from node q to node 3 of the external c -winding, we have

$$\begin{aligned} L_{3,q} &= \frac{1}{2}L_b + (L_b + L_{\delta 2} + L_c) = \\ &= \frac{L_{ac}^{sh} - (L_{ab}^{sh} + L_{bc}^{sh})}{2} + L_{bc}^{sh} = \frac{L_{ac}^{sh} + L_{cb}^{sh} - L_{ab}^{sh}}{2} = L_{312}. \end{aligned}$$

When comparing these expressions with the known formulae, it should be borne in mind that in context, of course $L_{pq}^{sh} = L_{qp}^{sh}$.

Flux linkage in the central winding of the three-winding transformer. In an idealized three-winding transformer,

$$\dot{U}_1 = j\omega\dot{\Psi}_a = k_0\dot{\Psi}_a / w_1; \quad (33)$$

$$\dot{U}_2 = j\omega\dot{\Psi}_b = k_0\dot{\Psi}_b / w_1; \quad (34)$$

$$\dot{U}_3 = j\omega\dot{\Psi}_c = k_0\dot{\Psi}_c / w_1; \quad (35)$$

It follows from these expressions and the circuit schematic (fig. 4) that the flux linkage in the windings can be written as:

$$\dot{\Psi}_a = w_1\dot{\Phi}_{leg} - \frac{w_1\dot{\Phi}_a}{3}; \quad (36)$$

$$\dot{\Psi}_b = \frac{\dot{U}_2}{j\omega}; \quad (37)$$

$$\dot{\Psi}_c = w_1\dot{\Phi}_j^{c\delta} + \frac{w_1\dot{\Phi}_c}{3} \rightarrow w_1\dot{\Phi}_{side} + \frac{w_1\dot{\Phi}_c}{3}. \quad (38)$$

The arrow in the last expression indicates the equality of the fluxes $\dot{\Phi}_j^{c\delta} = \dot{\Phi}_{side}$ in the three-winding transformer. Expressions (36) and (38) coincide with formulae (57) and (58) in [14].

To expand (to open) expression (37), it is necessary to determine the voltages shown by the dashed arrows in fig. 4 and denoted as the product of k_0 by $\dot{\Phi}_b^a$, $\dot{\Phi}_b^c$ and $\dot{\Phi}_b^b$. It follows from the circuit that are related through a system of equations

$$\dot{\Phi}_b^a + \dot{\Phi}_b^c = \dot{\Phi}_b; \quad (39)$$

$$k_0 \dot{\Phi}_b^a = j\omega \frac{3}{2} L_b \dot{I}_a; \quad (40)$$

$$k_0 \dot{\Phi}_b^c = j\omega \frac{3}{2} L_b \dot{I}_c, \quad (41)$$

whence it follows that

$$\dot{\Phi}_b^a = \frac{\dot{I}_a}{\dot{I}_a + \dot{I}_c} \dot{\Phi}_b; \quad (42)$$

$$\dot{\Phi}_b^c = \frac{\dot{I}_c}{\dot{I}_a + \dot{I}_c} \dot{\Phi}_b. \quad (43)$$

Then it follows from the expression for the voltage

$$k_0 \dot{\Phi}_b = j\omega \frac{3}{2} L_b \dot{I}_a + j\omega \frac{3}{2} L_b \dot{I}_c \quad (44)$$

that

$$j\omega \frac{L_b}{2} = \frac{k_0 \dot{\Phi}_b}{3(\dot{I}_a + \dot{I}_c)}, \quad (45)$$

and we obtain for the voltage in the vertical branch

$$k_0 \dot{\Phi}_b^b = j\omega \frac{L_b}{2} \dot{I}_b = \frac{\dot{I}_b}{\dot{I}_a + \dot{I}_c} \frac{k_0 \dot{\Phi}_b}{3} \quad (46)$$

or

$$k_0 \dot{\Phi}_b^b = \frac{\dot{I}_a - \dot{I}_c}{\dot{I}_a + \dot{I}_c} \frac{k_0 \dot{\Phi}_b}{3}. \quad (47)$$

As a result, the voltage in the terminals of the central winding can be represented as

$$\begin{aligned} \dot{U}_2 &= k_0 \dot{\Phi}_j^{\delta b} - k_0 \dot{\Phi}_b^a + k_0 \dot{\Phi}_b^b = \\ &= k_0 \dot{\Phi}_j^{\delta b} - \frac{\dot{I}_a}{\dot{I}_a + \dot{I}_c} k_0 \dot{\Phi}_b + \frac{\dot{I}_a - \dot{I}_c}{\dot{I}_a + \dot{I}_c} \frac{k_0 \dot{\Phi}_b}{3}. \end{aligned}$$

Taking into account (3), (32) and (37), we obtain the formula for the desired flux linkage:

$$\dot{\Psi}_b = w_1 \dot{\Phi}_j^{\delta b} - \frac{\dot{I}_a - \dot{I}_c}{\dot{I}_a + \dot{I}_c} w_1 \dot{\Phi}_b. \quad (48)$$

A 6T-shaped equivalent circuit of a real three-winding transformer. Ref. [14] examined in great detail the technique of enhancing the circuit model of the idealized transformer by the winding resistances and the *transverse branches* to take into account the active and reactance losses in the steel, including the sections between the tank and the magnetic circuit parts, in order to obtain the equivalent circuit of a real double-winding transformer. Similarly, the idealized model (fig. 4) can be substituted by the equivalent circuit of a real three-winding transformer, as shown by the dashed lines in fig. 5. The notations for the added inductances and fluxes correspond to the ones adopted in [14]. Nonlinear inductances and the conductivities parallel-connected to them correspond to:

L_{leg}, g_{leg} to the leg in which the flux $\dot{\Phi}_{leg}$ flows (fig. 1);

$L_j^{a\delta}, g_j^{a\delta}$ to the part of the joint yoke in which the flux $\dot{\Phi}_j^{a\delta}$ flows;

$L_j^{\delta b}, g_j^{\delta b}$, to the part of the joint yoke in which the flux $\dot{\Phi}_j^{\delta b}$ flows, etc.

The linear inductances series-connected to them are introduced to take into account the magnetic fluxes occurring due to the finite permeability of steel or its saturation. They correspond to:

$L_{\delta 0} = \mu_0 s_{\delta 0} w_1^2 / h$ to the segment with the width δ_0 between the leg and the internal *a*-winding, in which the flux $\dot{\Phi}_{\delta 0}$ flows (fig. 1);

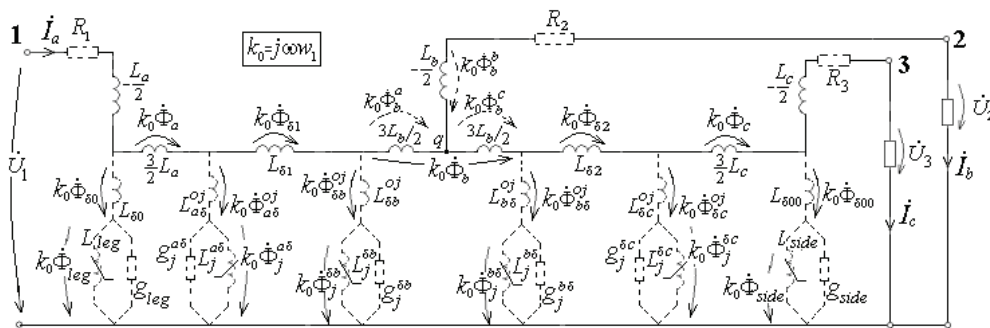


Fig. 5. 6T-shaped equivalent circuit of a real three-winding transformer

$L_{\delta a}^{oj} = \mu_0 s_{\delta a}^{oj} w_1^2 / l_{\delta a}^{oj}$ to the segment with the surface area $s_{\delta a}^{oj}$ and the length $l_{\delta a}^{oj}$ between the joint yoke and the tank, in which the flux $\dot{\Phi}_{\delta a}^{oj}$ flows parallel to the flux $\dot{\Phi}_j^{a\delta}$ in the joint yoke;

$L_{\delta b}^{oj} = \mu_0 s_{\delta b}^{oj} w_1^2 / l_{\delta b}^{oj}$ to the segment with the surface area $s_{\delta b}^{oj}$ and the length $l_{\delta b}^{oj}$ between the joint yoke and the tank, in which the flux $\dot{\Phi}_{\delta b}^{oj}$ flows parallel to the flux $\dot{\Phi}_j^{\delta b}$ in the yoke, etc.

Note 4. The circuit (fig. 5) should also be complemented with the resistances R_a^{eddy} , R_b^{eddy} , R_c^{eddy} by dividing each of them into a positive and a negative part, for example,

$$R_b^{eddy} = \frac{3}{2} R_b^{eddy} + \left(-\frac{R_b^{eddy}}{2} \right). \quad (49)$$

The resistance $3R_b^{eddy} / 2$ should be series-connected with the inductances $3L_b / 3$, and the negative resistance $(-R_b^{eddy} / 2)$ should be series-connected with the inductance $(-L_b / 2)$. This technique is substantiated in [6, p.87]. As a result, the circuit will obtain seven additional resistances for taking into account the eddy currents in the windings. The winding resistances R_a , R_b , R_c should be divided similarly. They are not shown in the schematic, so as not to overload fig. 5.

Note 5. The negative inductances in the equivalent circuits are typically regarded as a ‘minor’ hindrance (*a thorn in the side*). Monograph [6], specifically dedicated to multi-winding transformers, mentioned the negative inductance briefly in seven lines. Ref. [5, p. 125] goes as far as to suggest ‘to disregard the negative

inductances for the modes with high saturation of steel’. However, it follows from the equivalent circuit (fig. 5) that this can lead to an increased error in calculating the super-fluxes in a short-circuited transformer. Indeed, assuming for the sake of simplicity that in this case only the leg is saturated in the event of an s/c, we obtain a circuit (fig. 5) with a left transverse branch whose voltage can be represented as:

$$k_0 \dot{\Phi}_{leg}^{sh} + k_0 \dot{\Phi}_{\delta 0}^{sh} = \dot{U}_1 - \left(-j\omega \frac{L_a}{2} \right) j_a^{sh}. \quad (50)$$

The s/c current j_a^{sh} is high. The second term in the right-hand side of this expression is also fairly substantial. This is why neglecting it will lead to a substantial error in determining the super-flux $\dot{\Phi}_{leg}^{sh}$ in the core. It follows from (50) that the value of the super-flux in a saturated short-circuited transformer exceeds that in an unsaturated transformer.

A 2nT-shaped equivalent circuit of an n-winding idealized transformer. The above-described method of stitching 4T-shaped models of double-winding transformers is fully applicable to designing an equivalent circuit for any n -winding transformer. As an example, fig. 6 shows an equivalent circuit of an idealized 5-winding transformer. The number of transversal voltage arrows (with the fluxes) in the circuit is equal to $2n$, which gave reason to call it the $2nT$ -shaped model. The total number of negative inductances in the circuit is equal to the number of windings, in this case, five. Any winding or group of windings can be regarded as primary, the rest of the windings as secondary ones. The a -winding acts as primary in the schematic in fig. 6. To obtain the model of the real transformer, the circuit in fig. 6 should be complemented by transverse branches taking into account the losses in the steel, as well as the resistances, as described in Note 4.

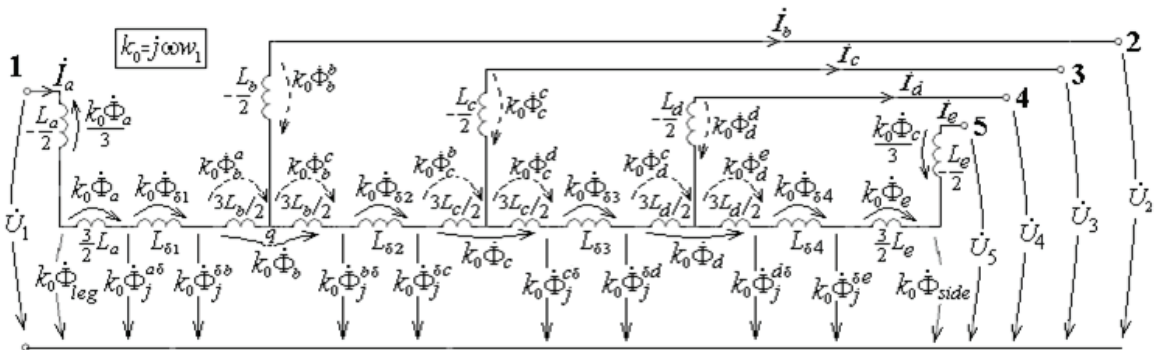


Fig. 6. Equivalent circuit of a 5-winding transformer

Transformation of negative inductances of the internal windings into mutual inductances. Negative inductances can be eliminated by transferring them across the nodes. According to the rules of these transformations [18], when transferring, for example, the inductance $(-L_b / 2)$ across node q (fig. 6), its value should be added to both inductances $3L_b / 2$ (after which they will be equal to L_b) and the mutual inductance, equal to $M_b = L_b / 2$, should be introduced between them, as shown in fig. 7. The negative inductances of two other internal windings $(-L_c / 2)$ and $(-L_d / 2)$ have been transferred in a similar manner, and two new mutually inductive couplings $M_c = L_c / 2$ and $M_d = L_d / 2$ have appeared in the circuit. With the labeling adopted for the schematic in fig. 7, all mutual inductances are positive.

Negative inductances of the external windings $(-L_a / 2)$ and $(-L_e / 2)$ have been preserved, thus ensuring that all transverse voltages remain the same as in the circuit (fig. 6). Therefore, the circuit in Fig. 7 can also be converted into a circuit of a real transformer by adding transverse and longitudinal branches which take into account the additional resistance and reactance losses, as described above for the circuit in fig. 6.

A compact ladder equivalent circuit for an idealized transformer without negative inductances. Combining the series-connected inductances between the nodes of the circuit in fig. 7, we obtain the circuit in fig. 8 with positive inductances equal to the s/c inductances of the corresponding double-winding transformers. In particular, by summing up the inductances between node 1 and node q , in view of (18), we have

$$-\frac{L_a}{2} + \frac{3}{2}L_a + L_{\delta 1} + L_b = L_{ab}^{sh}.$$

Similarly, for the group of series-connected inductances to the right of node q , based on (19), we find

$$L_b + L_{\delta 2} + L_c = L_{bc}^{sh},$$

and so on. As a result, we obtain a compact ladder equivalent circuit of an idealized equivalent n -winding transformer, described by a symmetric tridiagonal inductance matrix \mathbf{L} shown in fig. 8. However, the opportunities for monitoring the fluxes, including the super- and counter-fluxes in case of an s/c, are lost for this circuit. The accuracy of the circuit model (fig. 8) is partially confirmed by the fact that the solutions to the examples in table 1 found using this model coincide with the numerical data for the voltage currents in table 1, previously obtained from the analysis of super- and counter fluxes.

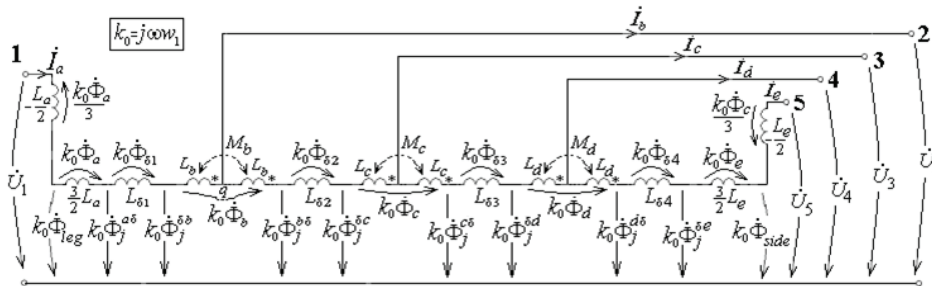


Fig. 7. Equivalent circuit of a 5-winding transformer without negative inductances of the internal windings

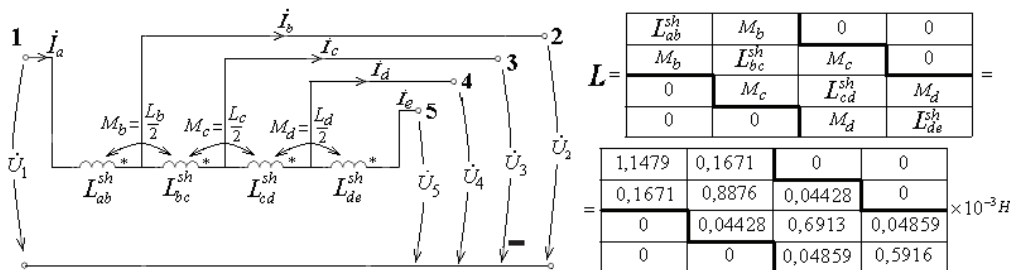


Fig. 8. Compact ladder equivalent circuit of the idealized 5-winding transformer with s/c resistances and its tridiagonal inductance matrix

The structure of the compact circuit (fig. 8) coincides with the topology of the model in [11], but differs from it by the elements of the matrix \mathbf{L} which is completely filled in Ref. [11], as, according to the hypothesis of the authors, mutual inductances M_{ij} should supposedly hold between all inductances of the circuit's branches. The physical interpretation of these mutual inductances seems rather artificial, as they exhibit alternating signs. In contrast to [11, 12], this paper presented a compact model (fig. 8) based on the rigorous methods of circuit theory instead of conjecture and hypotheses. All off-diagonal elements of the matrix \mathbf{L} are positive, which follows from the very method used for obtaining them.

Conclusion. We have obtained a new ladder equivalent circuit of an n -winding transformer, allowing to fully represent the physical picture of the processes occurring in it by displaying the paths of the magnetic fluxes and their values in the circuit. A key feature of the designed circuit is its modular structure resulting from stitching simpler circuit models of conventional double-winding transformers. Unlike previous meaningless assessments of the negative inductances as "referencing the equivalent circuit of the n -winding transformer with the real relations", this paper regards them as elements of the circuit playing a key role in displaying the magnetic fluxes, which is important for the developers of standard software packages for correctly simulating and refining the processes occurring in a multi-winding transformer in abnormal operation modes. It was rigorously proved that the equivalent circuit of an n -winding transformer with mutual inductances introduced instead of the negative ones is characterized by a three-diagonal matrix of positive inductances. The circuits described can be used for the analyzing both steady-state and dynamic processes.

Appendix

It seems interesting to evaluate the fluxes and voltages in the presence of a small resistive load $R = 1 \Omega$ in a b,a -transformer (fig. 2,a) at $\dot{U}_1 = \dot{U}_b = 1000V$ and compare the results with the data obtained in [11, p. 360] for this case. It follows directly from the circuit in fig. 2,a that the current

$$\begin{aligned} \dot{I} &= \frac{\dot{U}_b}{R + j\omega L_{ab}^{sh}} = \frac{\dot{U}_1}{R + j\omega(L_a + L_{\delta 1} + L_b)} = \\ &= (884,9 - j319,1), A, \end{aligned}$$

the absolute value of the current $I = 940,7$ A. The voltage for the load $R = 1 \Omega$ is equal to

$$\dot{U}_a = R\dot{I} = (884,9 - j319,1), V$$

and, consequently, $U_a = 940,7$ V. We can write for the flux in the core

$$\begin{aligned} \dot{\Phi}_{leg} \equiv \dot{\Phi}_j^a &= \frac{\left(R - j\omega \frac{L_a}{2}\right) \cdot \dot{I}_{sh}}{k_0} = \frac{\dot{U}_1 \left(R - j\omega \frac{L_a}{2}\right)}{k_0 (R + j\omega L_{ab}^{sh})} = \\ &= \frac{\left(R - j\omega \frac{L_a}{2}\right)}{(R + j\omega L_{ab}^{sh})} \dot{\Phi}_0 = (0,873 - j0,353) \dot{\Phi}_0, \end{aligned}$$

and, consequently, $\Phi_{leg} \equiv \Phi_j^a = 0,941 \Phi_0$. It also follows directly from the circuit in Fig. 2a that the flux in the side yoke is equal to

$$\begin{aligned} \dot{\Phi}_{side} \equiv \dot{\Phi}_j^b &= \frac{\dot{U}_b - j\omega \left(-\frac{L_b}{2}\right) \cdot \dot{I}}{k_0} = \\ &= \frac{\dot{U}_1 \left(1 + \frac{j\omega L_b}{2(R + j\omega L_{ab}^{sh})}\right)}{k_0} = \left(1 + \frac{j\omega L_b}{2(R + j\omega L_{ab}^{sh})}\right) \dot{\Phi}_0 = \\ &= (1,0167 + j0,0464) \dot{\Phi}_0 \end{aligned}$$

and since $\Phi_{side} \equiv \Phi_j^b = 1,018 \Phi_0$, it can be regarded as a super-flux. The voltages in the windings c, d, e are equal to

$$\begin{aligned} \dot{U}_c = \dot{U}_d = \dot{U}_e &= k_0 \dot{\Phi}_{side} = \left(1 + \frac{j\omega L_b}{2(R + j\omega L_{ab}^{sh})}\right) \dot{U}_1 = \\ &= 1,018 \dot{U}_1 \end{aligned}$$

and exceed by modulus the applied voltage (see row 3 in table 1). The values obtained in [11] are listed in brackets. The reason for the discrepancy between the calculated results and the data of [11] is that the conditions for calculating the s/c voltages are formulated imprecisely in [11, p. 354].

REFERENCES

1. **Boyajian A.** Theory of three circuit transformers. – *AIII Trans.* Feb. 1924, P. 208–528.
2. **Starr F.** Equivalent circuits – I. *AIII Trans.* Jan. 1932. Vol 57. P. 287–298.
3. **Blume L.F., Boyajian A., Gamilly G., Lenox T.C. Minnec S. Montsinger M. V.** Transformer Engineering: A treatise on the Theory, Operation and Application of Transformer. New York: Wiley, 1951. 239 p.
4. **Vasyutinskii, S. B.** Theory and calculation of power transformers. Leningrad: Energiya, 1970. 432 s.
5. **Leites L.V.** Electromagnetic calculations of transformers and reactors. M.: Energy, 1981. 392 s.
6. **Leites L.V., Pinczow A.M.** An equivalent circuit of a multi-winding transformers. M.: Energy, 1974. 192 s.
7. **Petrov G.N.** The electric machine. Part 1. M.: Energy, 1974. 240 s.
8. **Ivanov-Smolensky, A.V.** Electrical machines. M.: Energy, 1980. 927 s.
9. **Hnikov A.V.** Theory and calculation of multiple-winding transformers. Publishing house: Solon-press, 2003. 114 p.
10. **Voldek A.I., Popov V.V.** Electric machine. Introduction to electromechanics. Machines of direct-current and transformers. St. Petersburg: Piter, 2007. 320 s.
11. **Alvarez-Marino C., Leon F., Lopez-Fernandez X.M.** Equivalent Circuit for the Leakage Inductance of Multiwinding Transformers: Unification of terminal and duality models. *IEEE transactions on power delivery.* Jan. 2012. Vol. 27. № 1. P. 353–361.
12. **Leon F., Martinez J.A.** Dual Three-winding Transformer Equivalent Circuit matching Leakage measurements. *IEEE transactions on power delivery.* January 2009. Vol. 24. № 1. P. 160–168.
13. **Shakirov M.A.** The Poynting Vector and the new theory of transformers. Part 1. *Electricity.* 2014. № 9. S. 52–59 (rus.)
14. **Shakirov A.M.** The Poynting vector and the new theory of transformers. Part 2. *Electricity.* 2014. Vol. 10. P. 53–65. (rus.)
15. **Shakirov M.A., Andrushchuk V.V., Duan Lijun.** Anomalous magnetic fluxes in two-winding transformer under short circuit conditions. *Electricity.* 2010. № 3. P. 55–63. (rus.)
16. **Shakirov M.A., Varlamov V.Yu.** Patterns of magnetic SVER – and anti-stream in a short-circuited winding of the transformer. Part 1. Armour transformer. *Electricity.* 2015. № 8. S. 9–19. (rus.)
17. **Malygin V.M.** Lokalization of the Energy flux in the transformer. *Electricity.* 2015. № 4. S. 60–65. (rus.)
18. **Shakirov M.A.** Conversion and diakoptic electrical circuits. Leningrad: Publishing house of Leningrad. University press, 1980. 196 S.

СПИСОК ЛИТЕРАТУРЫ

1. **Boyajian A.** Theory of three circuit transformers. – *AIII Trans.* Feb. 1924, P. 208–528.
2. **Starr F.** Equivalent circuits – I. *AIII Trans.* Jan. 1932. Vol 57. P. 287–298.
3. **Blume L.F., Boyajian A., Gamilly G., Lenox T.C. Minnec S. Montsinger M. V.** Transformer Engineering: A treatise on the Theory, Operation and Application of Transformer. New York: Wiley, 1951. 239 p.
4. **Васютинский С.Б.** Вопросы теории и расчета трансформаторов. Л.: Энергия, 1970. 432 с.
5. **Лейтес Л.В.** Электромагнитные расчеты трансформаторов и реакторов. М.: Энергия, 1981. 392 с.
6. **Лейтес Л.В., Пинцов А.М.** Схемы замещения многообмоточных трансформаторов. М.: Энергия, 1974. 192 с.
7. **Петров Г.Н.** Электрические машины. Часть 1. М.: Энергия, 1974. 240 с.
8. **Иванов-Смоленский А.В.** Электрические машины. М.: Энергия, 1980. 927 с.
9. **Хныков А.В.** Теория и расчет многообмоточных трансформаторов. Изд-во.: Солон-пресс, 2003. 114 с.
10. **Вольдек А.И., Попов В.В.** Электрические машины. Введение в электромеханику. Машины постоянного тока и трансформаторы. СПб: Питер, 2007. 320 с.
11. **Alvarez-Marino C., Leon F., Lopez-Fernandez X.M.** Equivalent Circuit for the Leakage Inductance of Multiwinding Transformers: Unification of terminal and duality models // *IEEE transactions on power delivery.* Jan. 2012. Vol. 27. № 1. P. 353–361.
12. **Leon F., Martinez J.A.** Dual Three-winding Transformer Equivalent Circuit matching Leakage measurements // *IEEE transactions on power delivery.* January 2009. Vol. 24. № 1. P. 160–168.
13. **Шакиров М.А.** Вектор Пойнтинга и новая теория трансформаторов. Часть 1 // *Электричество.* 2014. № 9. С. 52–59.
14. **Шакиров М.А.** Вектор Пойнтинга и новая теория трансформаторов. Часть 2 // *Электричество.* 2014. № 10. С. 53–65.
15. **Шакиров М.А., Андрущук В.В., Дуан Лиюн.** Аномальные магнитные потоки в двухобмоточном трансформаторе при коротком замыкании // *Электричество.* 2010. № 3. С. 55–63.
16. **Шакиров М.А., Варламов Ю.В.** Картины магнитных сверх- и антипотоков в короткозамкнутом двухобмоточном трансформаторе. Часть 1. Броневой трансформатор // *Электричество.* 2015. № 8. С. 9–19.

17. **Малыгин В.М.** Локализация потока энергии в трансформаторе (по поводу статьи М.А. Шакирова, “Электричество”, 2014, № 9 и 10) // Электричество. 2015. № 4. С. 60–65.

18. **Шакиров М.А.** Преобразования и диакоптика электрических цепей. Л.: Изд-во Ленингр. ун-та, 1980. 196 с.

СВЕДЕНИЯ ОБ АВТОРАХ/AUTHORS

ШАКИРОВ Mansur A. – Peter the Great St. Petersburg Polytechnic University.
29 Politechnicheskaya St., St. Petersburg, 195251, Russia.
E-mail: manshak@mail.ru

ШАКИРОВ Мансур Акмелович – доктор технических наук профессор Санкт-Петербургского политехнического университета Петра Великого.
195251, Россия, г. Санкт-Петербург, Политехническая ул., 29.
E-mail: manshak@mail.ru

DOI 10.5862/JEST.249.7

УДК 621.315.35

Yu.V. Solovyev, A.N. Nazarythev, A.I. Tadzhibaev

DEVELOPMENT OF THE METHOD FOR ASSESSING THE COVERED CONDUCTORS STATE DUE TO ELECTRICAL AGEING IN MOIST AND HIGHLY POLLUTED ENVIRONMENTS

Ю.В. Соловьев, А.Н. Назарычев, А.И. Таджибаев

МЕТОД ОЦЕНКИ СОСТОЯНИЯ ЗАЩИЩЕННЫХ ПРОВОДОВ ПРИ ЭЛЕКТРИЧЕСКОМ СТАРЕНИИ В УСЛОВИЯХ ПОВЫШЕННЫХ ЗАГРЯЗНЕНИЙ И УВЛАЖНЕНИЙ

Based on field experience, the paper has proved the practical importance of finding a solution for condition assessment of covered conductors due to electrical ageing under moisture and pollution. The analysis of combined impacts with respect to construction and material properties on tracking erosion of covered conductor and plastic components of OHL accessories was performed for the first time ever. A high-voltage laboratory setup for accelerated ageing tests was designed. A detailed description of the test method is given. We have developed a method for assessing the technical conditions, based on measuring the leakage current. The given diagnostic parameter provides the opportunity to its wide application within diagnostic procedures for condition assessment during electrical ageing in moist and polluted environments. COVERED CONDUCTOR; CONDITION ASSESSMENT, POLLUTION; MOISTURE; ELECTRICAL AGEING; LEAKAGE CURRENT.

Обоснована практическая важность решения задачи оценки технического состояния защищенных проводов в условиях электрического старения при повышенных загрязнениях и увлажнении. Впервые проведен анализ комбинированного воздействия различных факторов на интенсивность развития трекинговой эрозии защищенных проводов, а также пластиковых элементов линейной арматуры с учетом особенностей конструкций и свойств применяемых материалов. Разработана лабораторная высоковольтная установка и методика проведения ускоренных испытаний на электрическое старение защищенных проводов при воздействии солевого тумана, моделирующего загрязнения. Предложен метод оценки состояния защищенных проводов на основе измерения поверхностных токов утечки. Определен безразмерный диагностический признак, а также обоснована возможность универсального его применения в задачах оценки состояния защищенных проводов при их электрическом старении.

ЗАЩИЩЕННЫЙ ПРОВОД; ТЕХНИЧЕСКОЕ СОСТОЯНИЕ; ЗАГРЯЗНЕНИЕ; УВЛАЖНЕНИЕ; ЭЛЕКТРИЧЕСКОЕ СТАРЕНИЕ; ТОК УТЕЧКИ.

Studied experience of operation and maintenance of 10–35 kV overhead lines (OHL) in different countries has shown the significant influence of moisture intensity and environment pollution level on the rate of electrical degradation and erosion of covered conductors (CC) [1–5]. Due to high electric field strength accelerated ageing of polymeric covering material takes place. It leads to high fault indexes on OHL and limits CC lifetime. The intensity of moisture penetration and environment pollution level significantly influence on rates of defects concentration and its growth inside CC un-

der combined electric and mechanical loads on OHL. In this case servicemen from power network utilities are faced to the actual needs for diagnostic of CC for earlier detection of defects with aspects to operating conditions on OHL.

Intensive processes of tracking erosion of CC under moisture and heavy pollution conditions are locally observed nearby of accessories fixing CC to pole insulators. The fact is that there is a high concentration of non-uniform electric field with high strength. Besides there are a number of design factors forming suitable conditions for high local distribution of electrical

charges under combined high electric field stresses, humidity and pollution levels:

1) floating electrical potentials along CC surface leading to surface discharges and forming conductive carbon paths within XLPE (cross-linked polyethylene) covering;

2) electrical charges between insulation materials with different dielectric permittivity. As example, it can be due to the installation of ceramic post insulators on OHL in environment with high humidity and pollution levels. Particularly, dielectric permittivity of XLPE covering and traditional ceramic post insulators differs in three times;

3) metal parts of insulators and fitting accessories for CC. The use of floating helical fittings can cause surface tracking of XLPE sheathed conductor in coastal environments [4, 10]. The combined use of piercing clamps and floating helical fittings leads to forming of non-uniform electrical potentials distribution along CC. These accessories from electrical point of view can be considered as secondary electrodes charging with electrostatic voltage. It provides the forming of leakage currents along CC surface. As result, tracking erosion of XLPE sheathed conductors takes place (fig.1, a).

a)



b)



Fig. 1. Tracking erosion of CC close to:

a) fitting accessories; b) post ceramic insulator

Electrical and thermal effects can lead to damage not only CC but plastic accessories. In this case a low electrical tracking stability of CC can be the reason of decreasing 10-35 kV OHL reliability. For high reliability it is important on design stage to turn attention to environment conditions along 10-35 kV

OHL including the existing levels of humidity and pollution. It helps to provide compatible designs of CC and fitting accessories (incl. materials) with aim to decrease the effect of tracking erosion in heavy environment. Unfortunately, up to now these aspects are not fully considered while OHL design. Moreover, there are no any requirements regarding tracking stability of accessories for CC in European standard EN 50397-2. As to Russia, there is no any standard regarding accessories for OHL with CC. For this reason there are a lot of cases when unsuitable designs of CC and accessories use. It leads to forming of suitable conditions for tracking erosion of CC in heavy environments.

4) volume content of carbon (%) in covering material of CC. Carbon is added to polyethylene for increasing of CC ultraviolet resistance. But it should be noted that carbon as a semiconductor increases the conductivity of covering insulation. It forms the conditions for tracking discharges on the wetted and polluted surface of CC. Therefore, a designer during selection of CC should pay attention to component content of CC covering in terms of carbon quantity. The maximum or minimum volume content of carbon should be defined related to existing environmental conditions along designed OHL route. Unfortunately, the last standard GOST R 31946-2012 [6] regarding the general requirements for CC doesn't consider this aspect. Moreover, this standard (clause 5.2.5) only sets the minimum volume content of carbon inside covering material which equals to 2,5%. It is necessary to note that in mountain areas with clean environment the use of CC with highest value of volume carbon content inside covering material is suitable. Oppositely, while there is an environment with high levels of humidity and pollution volume carbon content should have minimum value. The existing experience [7, 8] abroad has shown that 2,5 % of carbon content is enough for initiation of tracking erosion of CC operated in moisture and pollution environment (fig. 1, b). The last investigations have shown that volume carbon content significantly influences on specific properties of CC surface [9]. It includes water adsorption and surface wetting ability which are important when CC use on OHL's in areas with high wind and snow loads, temperatures. Increasing wetting ability of CC surface leads to forming of solid conductive water films and leakage currents;

5) cracks and another defects inside CC covering. Any outside or inside mechanical damages of CC

covering can exist during CC operation on OHL under service loads. Also mechanical defects can occur during production, storage, transportation, assembly of CC. Cracks grow due to simultaneous existence of internal defects inside covering material structure and high operating loads on OHL. Under combined impacts of non-uniform electric field, mechanical loads, humidity and pollution the discharges and electrical ageing occur along CC surface with cracks. High intensity of discharge activity leads to tracking erosion of CC with its failure. Also cracks can occur due to missing of adhesion between aluminum core and XLPE covering. It concerns with existing of non-uniform molecular structure in local volumes of polyethylene which are closed to CC core. It is due to production specifics: a size of XLPE volume with possible structure heterogeneities and cracks can be up to 40%. Local missing of adhesion leads to forming of air inclusions and partial discharges under applied operating high voltage. It results in tracking erosion and decreasing of CC remaining lifetime.

Research problem statement

Provided analysis has found that considered challenge of CC tracking erosion is not studied enough. It lets us formulate the tasks of performed research with aim to find a diagnostic parameter and use it with developed method for condition assessment of CC while tracking erosion takes place.

Description of developed experimental installation for laboratory tests

For laboratory accelerated ageing tests of CC under combined impacts of moisture and pollution environment an experimental high voltage installation has been developed (fig. 2).

One of features of the test installation is a possibility to provide the aging tests of CC with modeling different environment conditions. It would define the weight ratio of each factor in electrical ageing: intensity of electric field, humidity and pollution levels, different accessories design. Operating voltage is applied to CC under test (CCUT) powered with SF₆ transformer type IOG-50. It is possible to provide a control of test voltage and current load. Nominal voltage of transformer primary winding is 220 V. Test voltage is measured with voltage transformer type JDQXF-66. Measurements methods are set in [10]. Positions of CCUT are corresponding to operating conditions on OHL. CCUT are installed in a testing room with equipment for modeling salt fog environment and different operating conditions on OHL closed to seaside, zones with high pollution levels, etc. Salt fog environment is formed with spray in the air of aqueous solution of NaCl. It is technically provided with using of special sprayers installed on two opposite walls of test room.

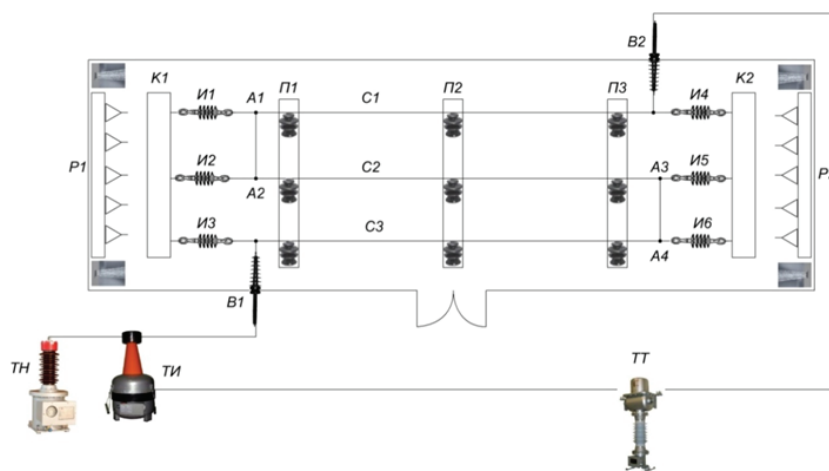


Fig. 2. Schematic drawing of installation for accelerated ageing tests of 10-35 kV covered conductors within wetting and pollution conditions: ТИ – SF₆ power supply source type IOG-50; B1, B2 – high voltage bushings; P1, P2 – salt fog spray disperser; K1, K2 – crossarms of end supports; И1-И6 – tension insulators; П1-П3 – crossarms of intermediate supports; C1-C3 – covered conductors under test; A1A2, A3A4 – cross connections for providing closed loop of circuit; ТН – SF₆ voltage transformer type JDQXF-66; ТТ – SF₆ current transformer type TBMO

Before testing CCUT's surfaces should be carefully cleaned from any pollution, fats, oils, etc. While cleaning no any damages of CCUT's surfaces should be occurred. To characterize pollution level a salt fog density as a main parameter is considered. The parameter is controlled according to the ratio of specific conductivity of salt solution at current temperature and room temperature. As additional parameter describing the intensity of moisture and pollution impacts on CCUT the consumption of aqueous solution needed for every salt fog sprayer could be considered. During tests the intensity of moisture impact on CCUT in vertical and horizontal planes equals to 1 mm/min. For every pollution level CCUT of all phases are tested because using of wire links forming the looped circuit for current. Average surface pollution density for CCUTs is 3 mg/cm². During tests salt fog conductivity at room temperature equals to 202,6 mSm/cm. It corresponds to solution density equals to 224 g/l. Overall test duration is 1000 hours. Date of test beginning is on February 18, 2014. Measured leakage current is taken as the main diagnostic indicator for assessment of CC electrical ageing degree. The analysis of latest investigations of tracking stability of polymeric insulation materials for high voltage OHL applications let to choose a first-to-third harmonics ratio of measured leakage current. Harmonics content is analyzed with using Fourier transform. Leakage current is measured with FLUKE i2000flex (fig. 3).



Fig. 3. Instrument for leakage current measurements FLUKE i2000flex

The measuring instrument has a design providing its safe using without throughout electrical connection to CCUT. It consists of a transducer, a toroidal

coil and connecting coaxial cable. Toroidal coil has a winding which is fixed on thin plastic tube and coated with insulation material. One output of the winding is constantly connected to integrator. Another one winding output has a temporary connection for measurement of leakage currents without electrical connection. Toroidal coil has a flexible design. Measurement interval is 1 min with saving results in database consisting of measurement data during 250 cycles of operating current frequency equals to 50 Hz. Fourier analysis of measurement data provided harmonic contents of leakage currents. The first, third and fifth harmonics of leakage currents have been studied for detailed analysis.

Analysis of results

On the basis of measurement data the comparison of leakage currents through CCUT with its acceptable values when pollution and moisture impacts are lowest is provided. While pollution and moisture impacts are absent the maximum leakage current equals to 0,3 mA [11]. During tests the visual decoloring of CC surface is observed at leakage currents up to 2–5 mA (fig. 4). These measured values of leakage currents are the lowest. Graphs of time-dependent fundamental harmonic of measured leakage current during the period from 18 to 21 day after test beginning are shown in fig. 5–7. According to the data fundamental harmonic is being increased from 6–8 mA up to 10–12 mA during 10 hours on 18th day of testing. As result, water evaporation and drying of CCUT surface are observed.



Fig. 4. Visual decoloring of CCUT surface as an initial sign of tracking erosion

Water evaporation from CC surface leads to decreasing leakage current during short time. But then the current increases after increasing of conductivity of pollution layers due to high concentration of salt pollution on CCUT surface. The visible signs of CC tracking erosion are observed after 543 hours of testing (fig. 8). On 21th day of testing fundamental harmonic of leakage current decreases in 3 times and equals to 4–5 mA (fig. 7).

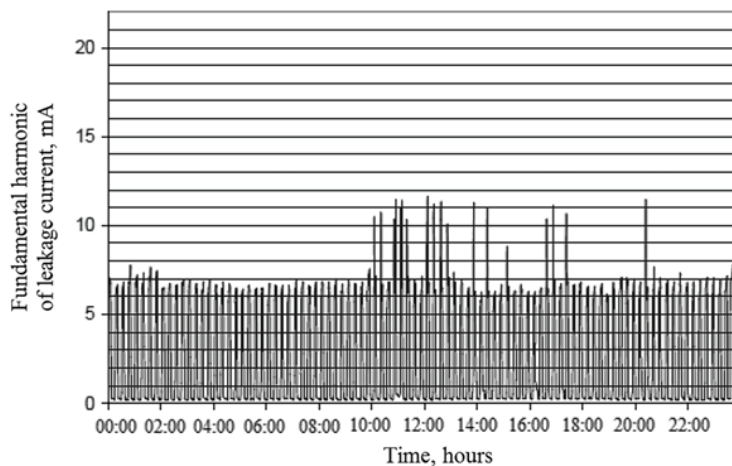


Fig. 5. Time dependent fundamental harmonic of leakage current on 18th day of testing

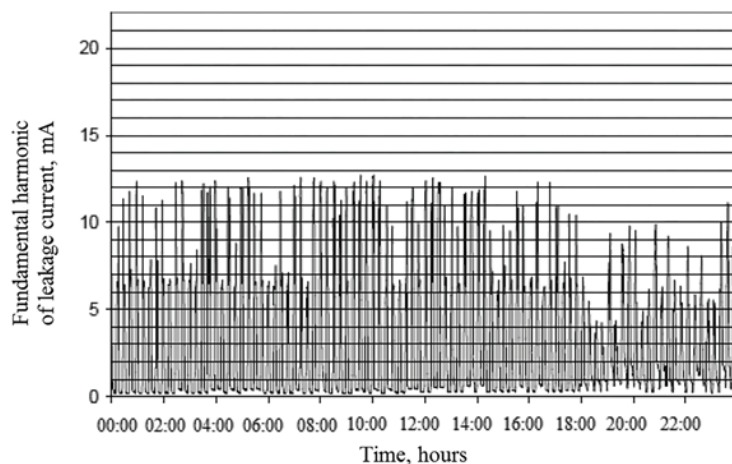


Fig. 6. Time dependent fundamental harmonic of leakage current on 19th day of testing

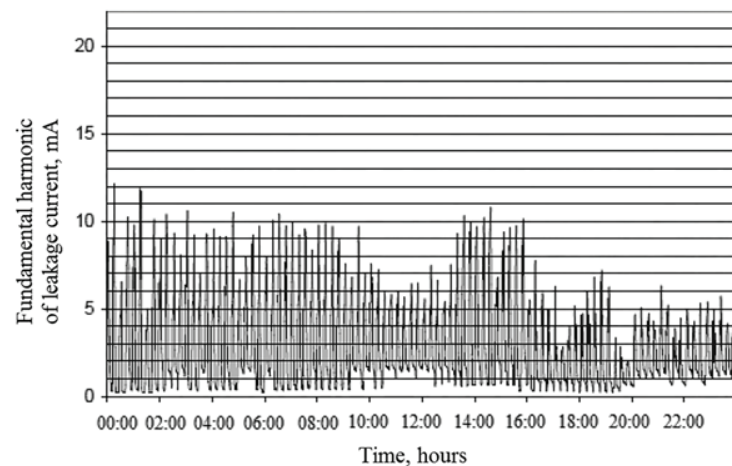


Fig. 7. Time dependent fundamental harmonic of leakage current on 21th day of testing

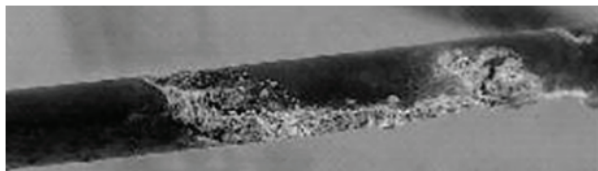


Fig. 8. Visual decoloring of CC surface at maximum leakage current

After Fourier transform the 3rd and the 5th leakage current harmonics are found. Its time dependent functions corresponding to the time interval from 18th to 21th of testing are defined. Analysis of these functions found small changes of the 5th leakage current harmonic in comparison with the 3rd harmonic. Therefore, the 5th harmonic of leakage current is not considered. As a result, a diagnostic parameter equals to the ratio of the 3rd leakage current harmonic to its

fundamental harmonic is offered. This diagnostic parameter I_3/I_1 would be used as an indicator describing technical condition of CC while tracking erosion under combined impacts of high moisture and pollution is observed.

For universal application of diagnostic parameter it is necessary to exclude from consideration its possible deviation depending on the characteristics of measuring equipment. As result, the bands of diagnostic parameter changes are defined. It should be noted that this approach doesn't restrict the use of the parameter. Moreover, the bands let to filter required data from a whole spectrum to assess a technical condition of CC. The marker for restricting the bands of diagnostic parameter changes is based on the frequency of occurring of different values of diagnostic parameter from the bands during tests (fig. 9, 10).

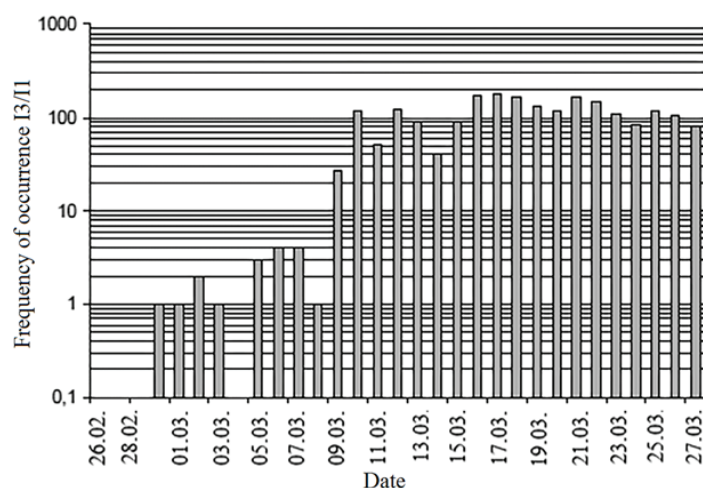


Fig. 9. Frequency of occurring of diagnostic parameter I_3/I_1 within the band $[0,15 \div 0,20]$ during accelerated ageing tests

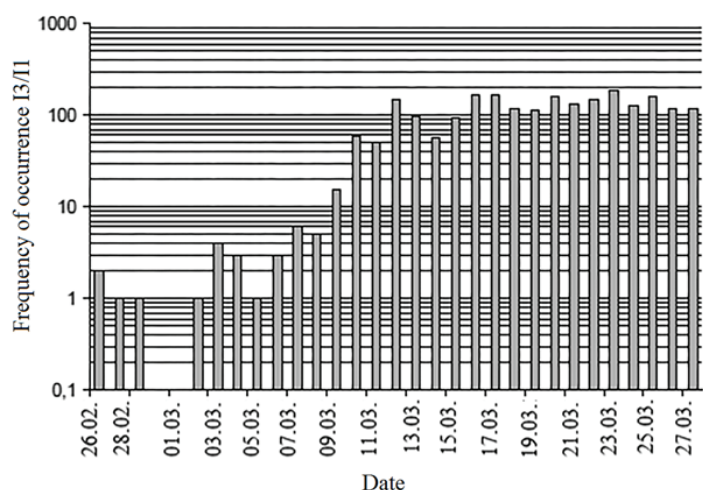


Fig. 10. Frequency of occurring of diagnostic parameter I_3/I_1 within the band $[0,20 \div 0,25]$ during accelerated ageing tests

On the basis of known relations the offered marker helps to define the probability of occurring of diagnostic parameter belonging to different bands. It characterizes the dynamic properties of electrical ageing of CC. The analysis of given graphs let to find the similar character in marker changes in two considered bands.

It opens the possibilities for use of diagnostic parameter with the aim to assess a technical state of CC

from operation in heavy environment. Fixed time of detection of visual tracking erosion signs of CC during tests correlates with dynamic properties of offered marker. The ageing degree of CC increases with increasing of frequency of diagnostic parameter occurring in two bands.

Given results of the research proves the possibility to use the correlations for assessment of technical condition of CC operating in heavy environment with high moisture and pollution levels.

REFERENCES

1. **Rokowska A.** Overhead CC lines experience in design, construction and service with reliability assessment in central Europe. *Proc. of the Fourth International Covered Conductor Conference ICCC.* – Helsinki, 2000. P. 56–68.
2. **Lovrenčić V.** Slovene experience about using covered conductors (PAS system) in Medium Voltage Network. *Proc. of International Conference on Electricity Distribution (CIRED 2000).* Shanghai, 2000. P. 35–48.
3. **Wareing J., Ward A.** The tracking performance of 50 mm² AMO Kraft BLX Triple compared with XLPE (3% carbon) sheathed conductor using helical fittings. *EATL Report T3805.* 2001. 80 p.
4. **Wareing J.** Tracking tests on new and old CC samples from Finland and Sweden. *EATL Report 5779.* 2004. 75 p.
5. **Yano K., Wareing J.** The Japanese experience. *EATL Report 4373.* 1997.
6. **GOST 31946-2012.** Провода самонесущие и изолированные и защищенные для воздушных линий электропередачи. Общие технические условия. – Введ. 2014-01-01. М.: Стандартинформ, 2013. 20 с. (rus.)
7. **Wald D.** The use of track resistant XLPE insulation for MV aerial cables. *Proc. of Covered Conductor Seminar.* Capenhurst. 1996. P. 18–27.
8. **Wald D., Campus A.** The influence of carbon black in XLPE compounds in MV aerial cables. *Proc. of the 1st International Covered Conductor Conference ICCC.* Capenhurst, 1997. P. 25–36.
9. **Soloviev Iu.V., Tadzhibaev A.I., Nazarythev A.N.** Анализ технического состояния защищенных проводов линий электропередачи. Saint-Petersburg: Izd-vo PEIPK, 2015. 193 с. (rus.)
10. **GOST 17512.** Электрооборудование и электроустановки на напряжение 3 кВ и выше. Методы измерения при испытаниях высоким напряжением. – Введ. 1984-01-01. М.: ИПК Изд-во стандартов, 1984. 23 с. (rus.)
11. **Wareing J.** Covered conductor systems for distribution. *EATL Report 5925.* 2005. 66 p.

СПИСОК ЛИТЕРАТУРЫ

1. **Rokowska A.** Overhead CC lines experience in design, construction and service with reliability assessment in central Europe // *Proc. of the Fourth International Covered Conductor Conference ICCC.* Helsinki, 2000. P. 56–68.
2. **Lovrenčić V.** Slovene experience about using covered conductors (PAS system) in Medium Voltage Network // *Proc. of International Conference on Electricity Distribution (CIRED 2000).* Shanghai, 2000. P. 35–48.
3. **Wareing J., Ward A.** The tracking performance of 50 mm² AMO Kraft BLX Triple compared with XLPE (3% carbon) sheathed conductor using helical fittings // *EATL Report T3805.* 2001. 80 p.
4. **Wareing J.** Tracking tests on new and old CC samples from Finland and Sweden // *EATL Report 5779.* 2004. 75 p.
5. **Yano K., Wareing J.** The Japanese experience // *EATL Report 4373.* 1997.
6. **ГОСТ 31946-2012.** Провода самонесущие изолированные и защищенные для воздушных линий электропередачи. Общие технические условия. – Введ. 2014-01-01. М.: Стандартинформ, 2013. 20 с.
7. **Wald D.** The use of track resistant XLPE insulation for MV aerial cables // *Proc. of Covered Conductor Seminar.* Capenhurst, 1996. P. 18–27.
8. **Wald D., Campus A.** The influence of carbon black in XLPE compounds in MV aerial cables // *Proc. of the 1st International Covered Conductor Conference ICCC.* Capenhurst, 1997. P. 25–36.
9. **Соловьев Ю.В., Таджибаев А.И., Назарычев А.Н., Ярмаркин М.К.** Анализ технического состояния защищенных проводов линий электропередачи. СПб.: Изд-во ПЭИПК, 2015. 193 с.
10. **ГОСТ 17512.** Электрооборудование и электроустановки на напряжение 3 кВ и выше. Методы измерения при испытаниях высоким напряжением. – Введ. 1984-01-01. М.: ИПК Изд-во стандартов, 1984. 23 с.
11. **Wareing J.** Covered conductor systems for distribution // *EATL Report 5925.* 2005. 66 p.

СВЕДЕНИЯ ОБ АВТОРАХ/AUTHORS

SOLOVYEV Yurii V. – ALSIB Company Ltd.
12, Michurinskaya St., Saint-Petersburg, 197046.
E-mail: yury.solovyev@yahoo.com

СОЛОВЬЕВ Юрий Владимирович – кандидат технических наук генеральный директор
ООО «Компания АЛСИБ».
197046, Санкт-Петербург, ул. Мичуринская, 12.
E-mail: yury.solovyev@yahoo.com

NAZARYTHEV Aleksandr N. – Petersburg Power Engineering Institute of professional development.
23, Aviatsionnaya st., Saint-Petersburg, Russia, 196135.
E-mail: nazarythev@mail.ru

НАЗАРЫЧЕВ Александр Николаевич – доктор технических наук ректор Петербургского
энергетического института повышения квалификации.
196135, Санкт-Петербург, ул. Авиационная, 23.
E-mail: nazarythev@mail.ru

TADZHIBAЕV Aleksei I. – Petersburg Power Engineering Institute of professional development.
23, Aviatsionnaya st., Saint-Petersburg, 196135.
E-mail: iec@peipk.spb.ru

ТАДЖИБАЕВ Алексей Ибрагимович – доктор технических наук заведующий кафедрой
«Диагностика энергетического оборудования» Петербургского энергетического института
повышения квалификации.
196135, Санкт-Петербург, Авиационная ул., 23.
E-mail: iec@peipk.spb.ru

DOI 10.5862/JEST.249.8

УДК 669.1.017:669.018.44:669.018.28

*S.Yu. Kondrat'ev, G.P. Anastasiadi, A.V. Ptashnik***MICROSTRUCTURAL EVOLUTION OF HEAT- RESISTANT HP ALLOYS
UNDER LONG-TIME OPERATION AT HIGH TEMPERATURES***С.Ю. Кондратьев, Г.П. Анастасиади, А.В. Пташник***ЭВОЛЮЦИЯ МИКРОСТРУКТУРЫ ЖАРОПРОЧНЫХ HP СПЛАВОВ
ПРИ ДЛИТЕЛЬНОЙ ВЫСОКОТЕМПЕРАТУРНОЙ ЭКСПЛУАТАЦИИ**

The structural instability of Fe-Cr-Ni-based superalloys and the mechanism of softening at operating temperatures were studied. We investigated the continuous changes in the structure and kinetics of dissolution of initial phases with formation and dissolution of intermediate phases of the cast superalloy 0,45C-26Cr-33Ni-2Si-2Nb under long-time operation at high temperature. The character and the sequence of phase transformations in Fe-Cr-Ni-based alloys at a temperature of 0,85-0,90 of their solidus, also under external loading, were found out. The structural instability of Fe-Cr-Ni-based superalloys and the mechanism of softening at operating temperatures were studied.

MICROSTRUCTURE; PHASE COMPOSITION; CAST MODIFIED 25CR-35NI HEAT-RESISTANT ALLOYS; DIFFUSION IN ALLOYS; STRUCTURAL STABILITY; KINETICS OF PHASE TRANSFORMATIONS.

Изучены структурная нестабильность и механизм разупрочнения при температурах эксплуатации жаропрочных сплавов на основе системы Fe-Cr-Ni. Исследованы непрерывные изменения структуры и кинетика растворения первичных фаз с образованием и последующим растворением промежуточных фаз в литом жаропрочном сплаве 0,45C-26Cr-33Ni-2Si-2Nb при длительной высокотемпературной эксплуатации. Выявлены характер и природа фазовых превращений в сплавах на основе системы Fe-Cr-Ni при температурах 0,85-0,90 от температуры солидус, а также под действием внешней нагрузки. Изучены структурная нестабильность и механизм разупрочнения жаропрочных сплавов на основе системы Fe-Cr-Ni при температурах эксплуатации. МИКРОСТРУКТУРА; ФАЗОВЫЙ СОСТАВ; ЛИТЫЕ МОДИФИЦИРОВАННЫЕ ЖАРОПРОЧНЫЕ СПЛАВЫ 25CR-35NI; ДИФУЗИЯ В СПЛАВАХ; СТРУКТУРНАЯ СТАБИЛЬНОСТЬ; КИНЕТИКА ФАЗОВЫХ ПРЕВРАЩЕНИЙ.

Introduction

The iron-nickel and nickel-based alloys are used for operation in dynamic conditions with load up to 100 thousand hours at temperatures to 700–900 °C, i.e. $T_{op} = (0,60-0,80) sol$ (T_{op} and T_{sol} – operating temperature and alloy solidus). They have an unstable structure and are prone to a continuous change during the operation [1–5]. This process can't be stabilized by thermal pre-treatment, including heating up to 1050–1200 °C followed by cooling and prolonged aging. During continuous operation alloys embrittle

due to the evolution in the structure of the intermediate phases σ , χ , μ , G, Z, γ . Intermediate phases have different chemical composition, significantly different from the average composition of the alloy and the composition of the matrix γ -phase [6–14].

The primarily alloys of iron-chromium-nickel-based are used for manufacturing of equipment used in the processing of oil and gas, operating at temperatures of 900–1000 °C with a brief overheating to 1100–1200 °C. They contain a high amount of carbon – to 0,30–0,70 % (wt.) and are stabilized with Nb,

Ti, Mo, W, N and other elements. Alloys operating temperature under these conditions reaches $T_{op} = (0,80-0,85) T_{sol}$, which is an unique example of the use of heat-resistant material. Large blanks with wall thickness up to 50 mm are made by stationary and centrifugal casting. Structure of Cr25Ni35-alloys, containing (% wt.) 0,4–0,5 C, 2 Si, 2 Nb, has an explicit metallographically inhomogeneous dendritic structure with the length of the first-order branches up to 3000 μm , a width of 200 μm , the length second-order branches up to 300 μm and width up to 100 μm . The original cast structure consists of three main phases: matrix solid solution (γ -phase) (75–80 %, vol.), eutectic consisting of γ -phase (~ 16 %) and chromium carbides ($\sim 4,0$ %), matrix carbide of niobium (~ 2 %). Such structure are formed because of a low solubility of carbon in γ -phase ($< 0,1$ %) and segregation of chromium (up to 35 %) with a formation of eutectic liquid, which should comprise (at 80 %, vol. of γ -phase) the component balance of 2 % C and up to 35 % Cr. The mechanism of formation of niobium carbide is less clear. Perhaps the key factor is the low solubility of Nb in a γ -phase ($< 0,5$ % in comparison with its concentration in the composition of the alloy – 2 %). The structure of such alloys, formed during crystallization, is relatively stable because to change the alloy structure a substantial atoms redistribution of metal elements of basis (Fe, Cr, Ni) is needed. However, at a concentration of them of 25–40 % at the temperature of operation, when the diffusion coefficient is $D < 10^{-10} \text{ cm}^2/\text{s}$ and the mean free path of atoms per 1 hour $l = (D\tau)^{0,5} < 6 \mu\text{m}$, it is very difficult. This is a major factor in determining a preferred use of cast alloys at temperatures up to $0,8 T_{sol}$.

However, the problems of structural instability in these alloys, nevertheless, appear to a large extent due to: firstly - cast condition characterized by a large initial structural and chemical heterogeneity, and the secondly - the impact of higher operating temperatures and significantly longer duration of operation, reaching 140 thousand hours. Price P and Grant N were the first who experimentally constructed phase diagram of the Fe-Cr-Ni-system for a temperature of 1300 °C [Price P and Grant N. Trans AIME 1959; 215:635–37]. Apparently, it remains the only one because to reach equilibrium at lower temperatures in this system of components long holding are required – more than 100 thousand hours.

Due to the availability of strong carbide and nitride-forming elements – Cr, Ti, Nb, and the ele-

ments forming intermediate intermetallic phases with bases elements (iron, nickel and chromium) – Si and Nb in alloys of this type take place a continuous transformation of structure during high temperature holding, especially under the influence of operating stress [1–6]. Significant operating problems of parts made of alloys of this type with multiphase structure are: individual features of melting; the presence of uncontrolled impurities; blanks production technology, including foundries, plastic deformation, welding and other operations. Essentially, each batch of blanks made out of such alloys is unique with individual behavior during processing and operation. Consequently, there is an uncertainty in the comparison on the results of numerous studies of Fe-Cr-Ni-alloys, received using electron microprobe analysis, scanning electron microscopy and other techniques, published mainly in 2000s. A detailed description of alloy compositions, production technology of blanks, features of heat treatment and operation, etc. is needed for the comparative analysis of continuous structural transformations observed in them at high holding. This makes it difficult to analyze and forecast the performance of alloys at extreme temperatures and duration of usage.

Thus, the study of the structural stability of Fe-Cr-Ni-based superalloys and detection of the mechanism of softening at operating temperatures is an urgent challenge, the solution of which will help to find the way to extend the life of high temperature constructions produced out of them.

The purpose of this study is to investigate the stability of the structure and phase composition of the cast alloy based on the basic composition 25Cr–35Ni during prolonged high temperature holding.

Experimental procedures

Chemical composition of the investigated alloy comprises (% wt.): 0,45C, 25Cr, 33Ni, 2Si, 2Nb, as well as additives W, Mo, Ti, Al – up to 1 % of each element and N – up to 0,2 %. Melting of the alloy was performed in an induction furnace with a capacity of 500 kg, castings were produced in a sand mold. Then, structure stabilization heating up to 1200 °C with cooling in a furnace or in water was carried out. The research on microstructure of the alloy was performed on the optical metallographic microscope Carl Zeiss Axiovert 40 at magnifications $\times 50 \dots 1000$ with the use of the automatic quantitative image analysis program according to ASTM E 1245-03. Microprobe analysis of the distribution of chemical

elements in the matrix and composition of the phases was carried out on the equipment Tescan VEGA 5136 LM with a precise determination of the concentration (% , relative.): for Fe, Ni, Cr, Si, Nb, Mo, W, Ti – 3 % for C, N – 20 %. To identify the structure of the alloy there was used electrolytic etching with oxalic acid 10 %. Production and preparation of thin sections were performed on the equipment «Buehler» according to ASTM E 3-95. Alloy structure was investigated using scanning electron microscope Quanta 200 3D FEG.

Results

The research has shown that the structure of alloys C-25Cr-35Ni-Si-Nb in cast condition consists of matrix γ - solid substitutional solution and carbides (fig. 1).

Solid solution has a pronounced dendritic structure with thin intercrystalline boundaries. According to statistics of microprobe analysis it contains (% , wt.): 38Fe, 35Ni, 23Cr, 2Si, < 1 % (each) - Nb, W, Mo. It was found that after high temperature exposure the homogeneity of the matrix increases. Thus, already after 2 hours of exposure at 1150 °C the difference in content of Fe, Cr, Mn in different parts of the solid solution is practically absent, and the difference in the content of Si decreases from 0,4–0,9 to 0,1–0,3 %. The phase γ remains stable in chemical composition and crystal structure in the temperature range of $T_{op} = (0,80-0,85)T_{sol}$ at longtime holding under stress.

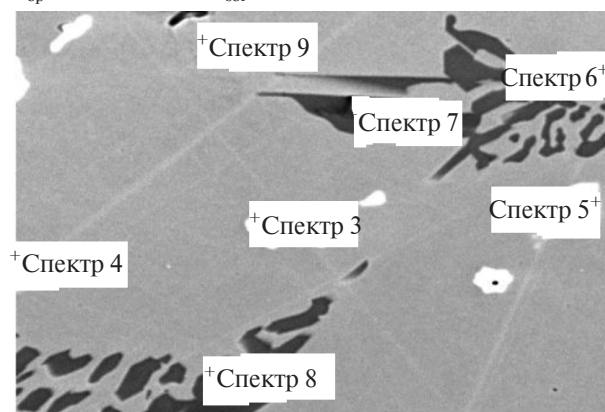
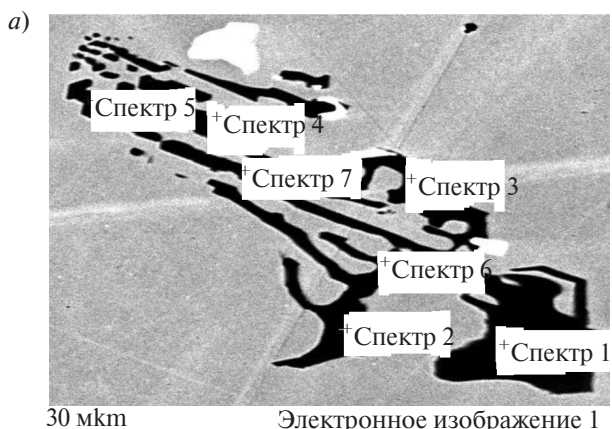


Fig. 1. Structure of alloy in cast state: matrix solid solution – γ -phase (base); carbides Me_7C_3 in eutectic (spectrum 7, 8) and NbC (spectrum 5, 6); carbonitrides TiN (spectrum 3, 4, 9)

Initial carbide phases consist of a eutectic carbide M_7C_3 on chromium base and niobium carbide, which has titanium carbonitride inside (fig. 2, 3). In carbide M_7C_3 are being dissolved (% , wt.) up to 9 Fe and 2

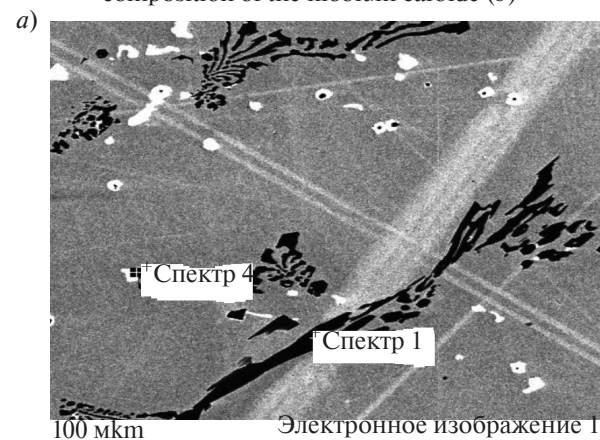
– Ni, W, Mo (each) and in NbC – up to 1 Fe, Cr, Ni, Ti (each). During the electron microscope research of the alloy structure in the initial cast condition no fragmentation of chromium and niobium carbides was detected.



b)

Spectrum	Content of elements, % (wt.)					
	C	Cr	Fe	Ni	Mo	W
1	9.27	79.36	7.65	1.47	0.73	1.52
2	9.36	79.77	7.38	1.53	0.55	1.41
3	8.87	78.71	8.84	1.70	0.58	1.30
4	9.25	78.69	8.36	1.88	0.53	1.29
5	9.38	77.07	9.38	1.97	0.67	1.53
6	9.17	77.35	9.24	2.06	0.74	1.44
7	8.94	78.29	9.13	1.65	0.61	1.38

Fig. 2. Structure of cast alloy (a) and the composition of the niobium carbide (b)



b)

Spectrum	Content of elements, % (wt.)					
	C	Ti	Cr	Fe	Ni	Nb
4	11.40	0.86	1.09	0.68	0.67	85.30

Fig. 3. Structure of cast alloy (a) and the composition of the niobium carbide (b)

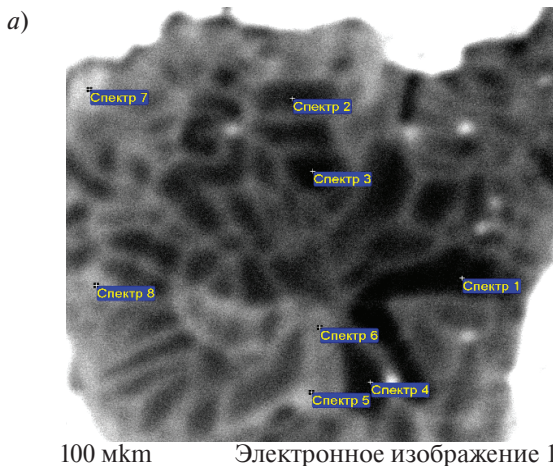
After holding at 1150 °C for 2 hours chromium carbide M_7C_3 with hexagonal lattice is transforming into $M_{23}C_6$ with FCC lattice (fig. 4, 5 and table 1). The excess carbon is used for the formation of intermediate dispersed carbides, formed in the matrix outside the zone of 5 μm from the boundaries of

eutectic chromium carbides (fig. 5–6, 7a). After high-temperature holding fragmentation of carbides is detected (fig. 4, 5). Analysis of the shape of carbides in the alloy structure allows assuming that chromium carbide with a smooth convex surface grew in the liquid melt and niobium carbide with drawn surface portions – in the solid phase.

Table 1

The average chemical composition of eutectic carbides in the structure of alloy in cast state and after holding at 1150 °C of varying duration

№	State of the alloy	Region of the carbide	Content of elements, % (wt.)					
			C	Cr	Fe	Ni	Mo	W
1	as-cast	—	9,10	78,76	8,51	1,55	0,66	1,42
2	1150 °C, 2 h	Dark	10,31	71,14	11,82	4,40	0,78	1,55
		Light	9,23	69,61	12,26	4,62	1,33	2,95
3	1150 °C, 50 h	—	5,61	72,84	12,76	4,38	1,24	3,17
4	1150 °C, 100 h	—	5,42	73,16	12,63	4,37	1,16	3,26



100 мкм Электронное изображение 1

Spectrum	Content of elements, % (wt.)					
	C	Cr	Fe	Ni	Mo	W
1	10.06	71.65	11.82	4.21	0.78	1.48
2	9.85	71.62	12.36	3.97	0.68	1.52
3	9.23	71.75	11.89	4.76	0.84	1.53
4	10.29	70.58	12.24	4.56	0.76	1.57
5	9.28	68.83	12.99	4.75	1.28	2.87
6	9.61	69.56	12.10	4.43	1.36	2.94
7	8.80	70.27	11.75	4.77	1.25	3.16
8	9.26	69.89	12.27	4.34	1.48	2.76

Fig. 4. Structure (a) and chemical composition of different parts (b) of the eutectic carbide M_eC_y in the alloy after holding at 1150 °C for 2 h

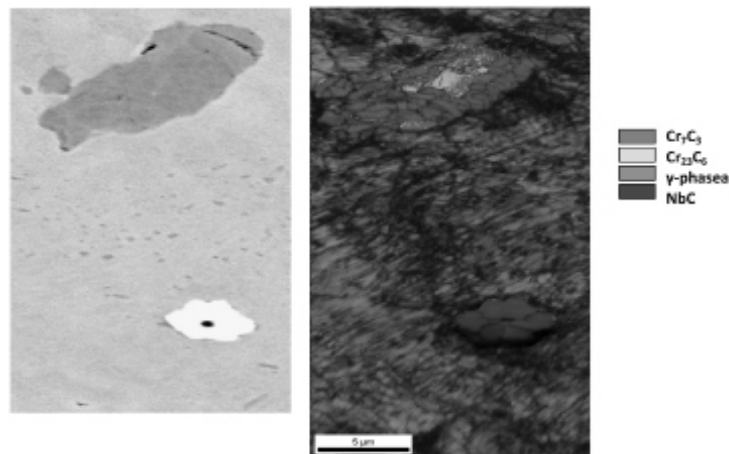


Fig. 5. Structure of alloy after holding at 1150 °C for 50 hours in back-scattered electron (a) and phase distribution map, superimposed on quality diffraction patterns map (b)

Intermediate intermetallic phases with different and changing composition types of σ -phase and γ' -phase with niobium, silicon or niobium and silicon simultaneously are being formed at the boundary of the matrix phase with eutectic chromium carbide and at the boundary of the matrix with niobium carbide, as well as isolated in the matrix at a high temperature holding (fig. 7, *b*). Increasing of the duration of high temperature holding of the alloy leads to the partial

dissolution of primary carbides both chromium and niobium based. This is evidenced by the formation of jagged (relief) boundaries between carbides and matrix (fig. 8, *a*). Also possible is «sprouting» of individual niobium carbides (fig. 8, *b*, spectrum 2) through branches of eutectic chromium carbides, this process goes by stages – with formation of the intermediate γ' -phase (fig. 8, *b*, spectrum 3) containing up to 16 % (wt.) of niobium.

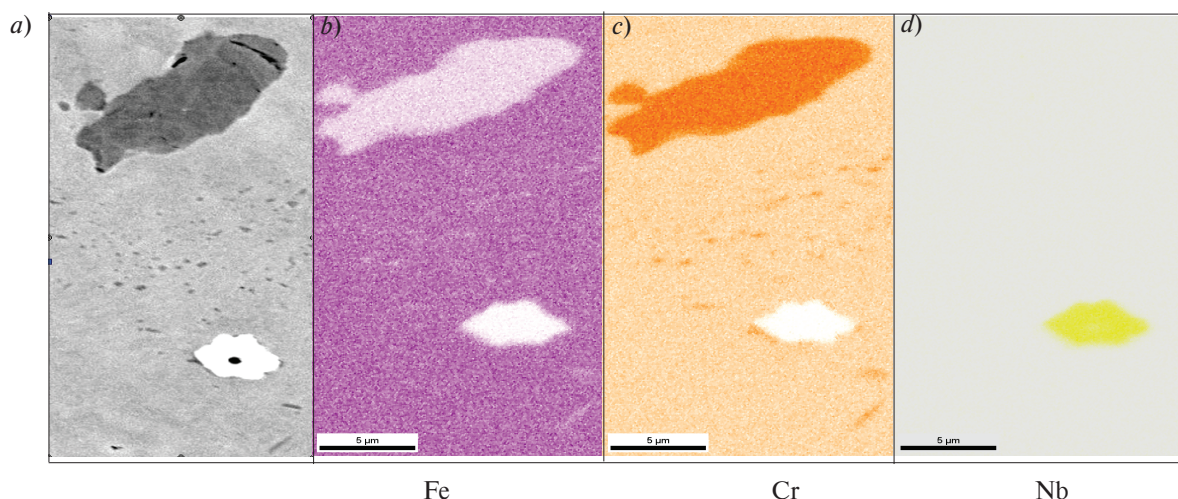


Fig. 6. Structure of alloy in back-scattered electrons (*a*) and the distribution map of the chemical elements (iron, chromium and niobium) after holding at 1150 °C for 100 h

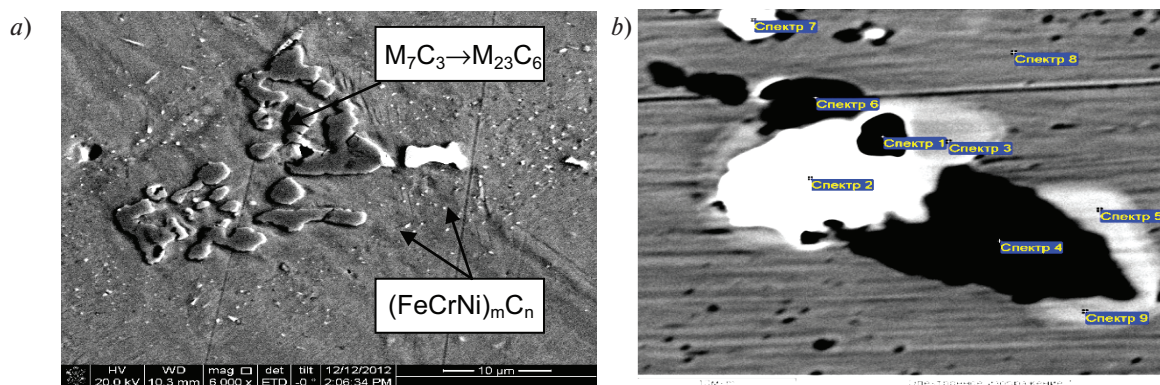


Fig. 7. Structure of alloy after holding at 1150 °C: *a* – transformation of eutectic carbide M_7C_3 to $M_{23}C_6$ and formation of the intermediate carbide $(FeCrNi)_mC_n$ in the matrix ($\tau = 2$ h); *b* – formation of intermetallic phases σ ($FeCr, Cr_5NiFe$) and γ' ($Fe_7Cr_4Ni_8Si, Cr_7Ni_5Si_3N_3FeNb$) ($\tau = 100$ h)

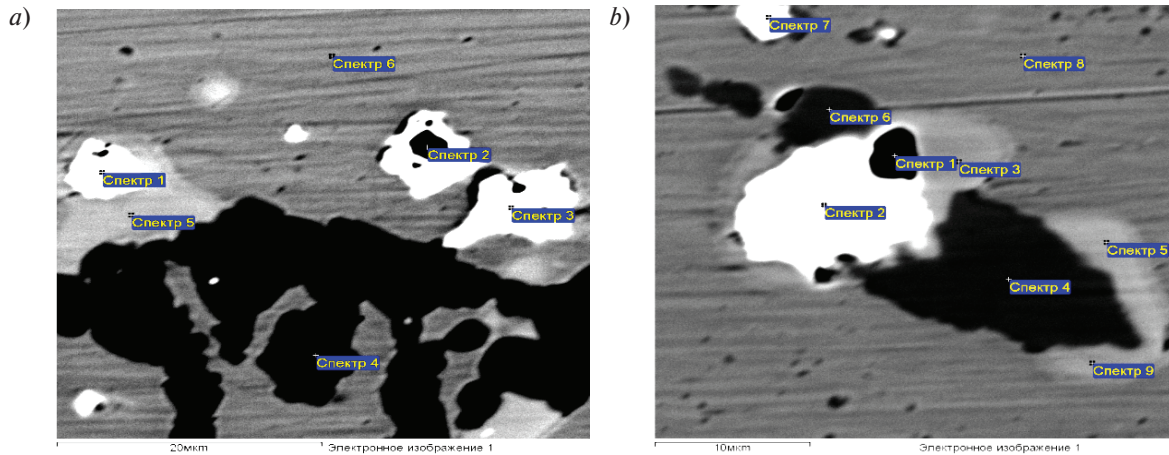


Fig. 8. Structure of alloy after holding at 1150 °C for 100 h: *a* – merging of niobium carbide (spectrum 1) and chromium carbide (spectrum 4) through formation of intermediate γ' -phase (spectrum 5), *b* – merging of chromium carbide (spectrum 4, 6) and niobium carbide (spectrum 2) through formation of intermediate γ -phase (spectrum 3, 5, 9)

Thus, cast structure of alloys of system C-25Cr-35Ni-Si-Nb is thermodynamic nonequilibrium. Analysis of the results of research suggests that in this case the main factors that provide high performance of Fe-Cr-Ni based superalloys are:

relatively low level of static loadings from 5 MPa for operating temperature of 1150 °C up to 70 MPa - for 800 °C;

presence in the original cast structure, along with the matrix solid solution γ , a large number (up to 20 %, vol.) of coarse eutectic: base carbide (M_7C_3 or $M_{23}C_6$) and γ -phase;

the formation of dispersed inclusions of carbide M_mC_n in matrix outside of 5 μm zone from the boundaries of eutectic chromium carbides due to diffusion to carbide M_mC_n of excess carbon, produced at the modification of the eutectic chromium carbide at the reaction $23M_7C_3 \rightarrow 7M_{23}C_6 + 27C$. Containing of metal elements in the carbide M_mC_n at the initial stage of holding (2 hours) is (% wt.): 30 Cr, 40 Fe, 20 Ni. This is close to their concentration in the matrix. By increasing the holding time to 50 hours, composition of dispersed carbides M_mC_n in the matrix approaches the composition of eutectic carbide (% wt.): 55-60 Cr, 13-20 Fe, 8-12 Ni, 5 Nb, 3 W, 6-9 C;

additional hardening of structure by inclusion of relatively stable niobium carbide (NbC);

continuous transformation of the initial phases in the structure at prolonged high temperature holding: chromium carbides (M_7C_3) change their crystal struc-

ture and transform to other ones (with lower relation of C / M concentration), niobium carbides dissolve with separation of niobium in solid matrix solution and formation of intermetallic phases;

continuous release and dissolution of various intermediate intermetallic phases at a stable matrix in the alloy structure of complex chemical composition. The intermetallic phases are formed at the boundary of the matrix and carbide phases. They have a conditional formula (in accordance with the results of determining of the chemical composition by microprobe analysis): FeCr , Cr_5NiFe , $\text{Fe}_7\text{Cr}_4\text{Ni}_8\text{Si}$, $\text{Cr}_7\text{Ni}_5\text{Si}_3\text{N}_3\text{FeNb}$.

Obviously, growth and dissolution of intermediate carbide and intermetallic phases are determined by diffusion processes. For growth of chromium based carbides, these processes are determined by the diffusion of chromium in the conditions of "drift" under the influence of a potential field around the center of the new phase. Diffusion of the carbon does not limit the process at $T = 1150$ °C due to the high diffusion coefficient $D < 10^{-8}$ cm^2/s and the mean free path of atoms in 1 hour $l = (D\tau)^{0.5} < 60$ μm . For growth and dissolution of intermetallic phases this process is limited by diffusion of silicon and niobium. This demonstrates the kinetics of the increase or decrease in particle size of particular phase in time, if the process of growth or dissolution of the particles has already begun for some reason.

Forecast of formation of various intermediate phases in alloys containing more than 10 active

chemical elements without explicit base (solvent), whose role play iron, nickel and chromium with about 90 % (wt.) of the composition, at high temperatures and prolonged holdings, is a difficult analysis problem. Studies in recent years [1–4, 6, 10–14] show that the phase composition of these alloys changes continuously during prolonged high temperature holding. Currently, there are results of determining the composition of the intermediate phases, formed in the structure of the alloys after holding for up to 160 thousand hours [2], and the number of possible phases reaches up to 20 kinds.

Research conducted in this study show that the application of external low stress at high temperature holding stimulates the formation of a new phases – intermetallic or carbonitride – in the structure of alloy. Growth kinetics of phases changes at a longtime load holding. Thus, at the boundaries of intragranular dislocation cells chromium carbides can be released, as well as intermetallic phases and nitrides.

Conclusions

Conditions of use for parts made of refractory heat resistant alloys C-25Cr-35Ni-Si-Nb-system at temperatures of 900–1000 °C with a possible temporary overheating to 1100–1200 °C (0,80–0,85 from the solidus temperature) are extreme, considering tem-

perature, as well as structural instability. Structural instability in this case is the continuous formation, growth and dissolution of intermediate carbide and intermetallic phases of variable composition, which are not in thermodynamic equilibrium. Argued thermodynamic evaluation of existence of intermediate phases in alloys of this components system, comprising multicomponent base – iron-chromium-nickel and several active structure stabilizing elements, is currently difficult. This is due to obvious experimentally confirmed (high holding at 0,80–0,85 from the solidus temperature longer than 100 thousand hours) absence of thermodynamic equilibrium, which corresponds the achievement of final structural state with a stable set of phases. Thus, an important task at the present stage of research of such alloys is the accumulation of statistically compatible experimental results of direct instrumental determination of the chemical composition of the intermediate phases, formed in their structure during high temperature (0,70–0,85 from the solidus temperature) long (200 thousand hours or more) holding under operating stress. The results of these studies may help to determine the mechanisms of processes leading to the continuous changes in the structure of these alloys and to assess the likelihood of achieving of final structural state in them.

REFERENCES

1. Kenik E.A, Maziasz P.J, Swindeman R.W, Cervenka J, May D. Structure and phase stability in cast modified-HP austenite after long-term ageing. *Scripta Materialia*. 2003. Vol. 49. P. 117–122.
2. Rudskoy A.I., Oryshchenko A.S., Kondrat'ev S.Yu., Anastasiadi G.P., Fuks M.D., Petrov S.N. Special Features of Structure and Long-Term Strength of Cast Refractory Alloy 45Kh26N33S2B2. *Metal Science and Heat Treatment*. 2013. Vol. 55. № 3–4. P. 209–215.
3. Ilman M.N. Kusmono Analysis of material degradation and life assessment of 25Cr-38Ni-Mo-Ti wrought alloy steel (HPM) for cracking tubes in an ethylene plant. *Eng Fail Anal*. 2014. T. 42. № 100-8.
4. Rudskoy A.I., Kondrat'ev S.Yu., Anastasiadi G.P., Oryshchenko A.S., Fuks M.D., Petrov S.N. Transformation of the Structure of Refractory Alloy 0.45C-26Cr-33Ni-2Si-2Nb During a Long-Term High-Temperature Hold. *Metal Science and Heat Treatment*. 2014. Vol. 55. № 9–10. P. 517–525.
5. Rudskoy A.I., Oryshchenko A.S., Kondrat'ev S.Yu., Anastasiadi G.P., Fuks M.D. Mechanisms and Kinetics of Phase Transformations in Refractory Alloy 45Kh26N-33S2B2 in Long-Term High-Temperature Holds. Part 1. *Metal Science and Heat Treatment*. 2014. Vol. 56. № 1–2. P. 3–8.
6. Rudskoy A.I., Kondrat'ev S.Yu., Anastasiadi G.P., Oryshchenko A.S., Fuks M.D. Mechanism and Kinetics of Phase Transformations in Refractory Alloy 45Kh26N-33S2B2 Under Long-Term High-Temperature Holds. Part 2. *Metal Science and Heat Treatment*. 2014. Vol. 56. № 3–4. P. 124–130.
7. Sourmail T. Precipitates in creep resistant austenitic stainless steels. *Mater Sci Technol*. 2001;17/1:1-14.
8. Garbiak M, Chylińska R. Precipitation kinetics in austenitic 18Cr-30Ni-Nb cast steel. *Arch Foundry Eng*. 2008;8/3:27-30.
9. Rudskoi A.I., Anastasiadi G.P., Kondrat'ev S.Yu., Oryshchenko A.S., Fuks M.D. Effect of Electron Factor (Number of Electron Holes) on Kinetics of Nucleation, Growth, and Dissolution of Phases during Long-Term High-Temperature Holdings of 0.45C-26Cr-33Ni-2Si-2Nb Superalloy. *The Physics of Metals and Metallography*. 2014. Vol. 115. № 1. P. 1–11.
10. Sustaita-Torres IA, Haro-Rodriguez S, Guerrero-Mata MP, De la Garza M, Valdes E, Deschaux-Beaume F, Colas R. Aging of cast 35Cr-45Ni heat resistant alloy. *Materials Chemistry Physics*. 2012. Vol. 133. P. 1018–1023.
11. Kondrat'ev S.Yu., Kraposhin V.S., Anastasiadi G.P., Talis A.L. Experimental observation and crystallographic

description of M7C3 carbide transformation in Fe–Cr–Ni–C HP type alloy. *Acta Materialia*. 2015. Vol. 100. P. 275–281.

12. **Monobe L.S., Schön C.G.** Microstructural and fractographic investigation of a centrifugally cast 20Cr32Ni+Nb alloy tube in the as cast and aged states. *J Mater Res Technol*. 2013;2/2:195–201.

13. **Borjali S, Allahkaram S.R, Khosravi H.** Effects of working temperature and carbon diffusion on the microstructure of high pressure heat-resistant stainless steel tubes used in pyrolysis furnaces during service condition. *Mater Des*. 2012;34:65–73.

14. **Nunes F.C, De Almeida L.H, Dille J, Deldlancke J-L, Le May I.** Microstructural changes caused by yttrium

addition to NbTi-modified centrifugally cast HP-type stainless steels. *Mater Char*. 2007;58:132–42.

15. **De Almeida L.H, Ribeiro A.F, Le May I.** Microstructural characterization of modified 25Cr–35Ni centrifugally cast steel furnace tubes. *Mater Char*. 2003;49/3:219–29.

16. **Buchanan K.G, Kral M.V.** Crystallography and Morphology of Niobium Carbide in As-Cast HP-Niobium Reformer Tubes. *Metall Mater Trans A*. 2012;43A/6:1760–69.

17. **Vander Voort G.F, Lucas G.M, Manilova E.P.** Metallography and Microstructures of Heat-Resistant Alloys. In: Davis J.R., Davis & Associates, editors. ASM International ASM Handbook, 2004, Vol. 9: Metallography and Microstructures. P. 820–59.

СПИСОК ЛИТЕРАТУРЫ

1. **Kenik E.A, Maziasz P.J, Swindeman R.W, Cervenka J, May D.** Structure and phase stability in cast modified-HP austenite after long-term ageing. // *Scripta Materialia*. 2003. Vol. 49. P. 117–122.

2. **Rudskoy A.I., Oryshchenko A.S., Kondrat'ev S.Yu., Anastasiadi G.P., Fuks M.D., Petrov S.N.** Special Features of Structure and Long-Term Strength of Cast Refractory Alloy 45Kh26N33S2B2 // *Metal Science and Heat Treatment*. 2013. № 3–4. P. 209–215.

3. **Ilman M.N.** Kusmono Analysis of material degradation and life assessment of 25Cr–38Ni–Mo–Ti wrought alloy steel (HPM) for cracking tubes in an ethylene plant // *Eng Fail Anal*. 2014. 42:100–8.

4. **Rudskoy A.I., Kondrat'ev S.Yu., Anastasiadi G.P., Oryshchenko A.S., Fuks M.D., Petrov S.N.** Transformation of the Structure of Refractory Alloy 0.45C–26Cr–33Ni–2Si–2Nb During a Long-Term High-Temperature Hold // *Metal Science and Heat Treatment*. 2014. Vol. 55. № 9–10. P. 517–525.

5. **Rudskoy A.I., Oryshchenko A.S., Kondrat'ev S.Yu., Anastasiadi G.P., Fuks M.D.** Mechanisms and Kinetics of Phase Transformations in Refractory Alloy 45Kh26N–33S2B2 in Long-Term High-Temperature Holds. Part 1 // *Metal Science and Heat Treatment*. 2014. Vol. 56. № 1–2. P. 3–8.

6. **Rudskoy A.I., Kondrat'ev S.Yu., Anastasiadi G.P., Oryshchenko A.S., Fuks M.D.** Mechanism and Kinetics of Phase Transformations in Refractory Alloy 45Kh26N–33S2B2 Under Long-Term High-Temperature Holds. Part 2 // *Metal Science and Heat Treatment*. 2014. Vol. 56. № 3–4. P. 124–130.

7. **Sourmail T.** Precipitates in creep resistant austenitic stainless steels // *Mater Sci Technol*. 2001. 17/1:1–14.

8. **Garbiak M, Chylińska R.** Precipitation kinetics in austenitic 18Cr–30Ni–Nb cast steel // *Arch Foundry Eng*. 2008. 8/3:27–30.

9. **Rudskoi A.I., Anastasiadi G.P., Kondrat'ev S.Yu., Oryshchenko A.S., Fuks M.D.** Effect of Electron Factor (Number of Electron Holes) on Kinetics of Nucleation,

Growth, and Dissolution of Phases during Long-Term High-Temperature Holdings of 0.45C–26Cr–33Ni–2Si–2Nb Superalloy // *The Physics of Metals and Metallography*. 2014. Vol. 115. № 1. P. 1–11.

10. **Sustaita-Torres I.A, Haro-Rodrigues S., Guerrero-Mata M.P., De la Garza M., Valdes E., Deschaux-Beaume F., Colas R.** Aging of cast 35Cr–45Ni heat resistant alloy // *Materials Chemistry Physics*. 2012. Vol. 133. P. 1018–1023.

11. **Kondrat'ev S.Yu., Kraposhin V.S., Anastasiadi G.P., Talis A.L.** Experimental observation and crystallographic description of M7C3 carbide transformation in Fe–Cr–Ni–C HP type alloy // *Acta Materialia*. 2015. Vol. 100. P. 275–281.

12. **Monobe L.S., Schön CG.** Microstructural and fractographic investigation of a centrifugally cast 20Cr32Ni+Nb alloy tube in the as cast and aged states // *J. Mater Res Technol*. 2013. 2/2:195–201.

13. **Borjali S, Allahkaram SR, Khosravi H.** Effects of working temperature and carbon diffusion on the microstructure of high pressure heat-resistant stainless steel tubes used in pyrolysis furnaces during service condition // *Mater Des*. 2012. 34:65–73.

14. **Nunes F.C, De Almeida L.H, Dille J., Deldlancke J-L, Le May I.** Microstructural changes caused by yttrium addition to NbTi-modified centrifugally cast HP-type stainless steels // *Mater Char*. 2007. 58:132–42.

15. **De Almeida L.H., Ribeiro A.F., Le May I.** Microstructural characterization of modified 25Cr–35Ni centrifugally cast steel furnace tubes // *Mater Char*. 2003. 49/3:219–29.

16. **Buchanan K.G, Kral M.V.** Crystallography and Morphology of Niobium Carbide in As-Cast HP-Niobium Reformer Tubes // *Metall Mater Trans A*. 2012. 43A/6:1760–69.

17. **Vander Voort G.F, Lucas G.M, Manilova E.P.** Metallography and Microstructures of Heat-Resistant Alloys. In: Davis J.R., Davis & Associates, editors. ASM International ASM Handbook, 2004, Vol. 9: Metallography and Microstructures. P. 820–59.

СВЕДЕНИЯ ОБ АВТОРАХ/AUTHORS

KONDRAT'EV Sergei Yu. – Peter the Great St. Petersburg Polytechnic University.
29 Politechnicheskaya St., St. Petersburg, 195251, Russia.
E-mail: petroprom2013@yandex.ru

КОНДРАТЬЕВ Сергей Юрьевич – доктор технических наук профессор Санкт-Петербургского политехнического университета Петра Великого.
195251, Россия, г. Санкт-Петербург, Политехническая ул., 29.
E-mail: petroprom2013@yandex.ru

ANASTASIADI Grigorii P. – Peter the Great St. Petersburg Polytechnic University.
29 Politechnicheskaya St., St. Petersburg, 195251, Russia.
E-mail: anastas45@yandex.ru

АНАСТАСИАДИ Григорий Панеодович – доктор технических наук профессор Санкт-Петербургского политехнического университета Петра Великого.
195251, Россия, г. Санкт-Петербург, Политехническая ул., 29.
E-mail: anastas45@yandex.ru

PTASHNIK Alina V. – Central Research Institute of Structural Materials “Prometey”.
49, Shpalernaya str., St. Petersburg, 191015.
E-mail: alina_pv@mail.ru

ПТАШНИК Алина Вадимовна – инженер ЦНИИ «КМ «Прометей».
191015, Санкт-Петербург, Шпалерная ул., 49.
E-mail: alina_pv@mail.ru

DOI 10.5862/JEST.249.9

УДК 54.057; 66.08, 669

*A. Tonitzki, A.N. Skvortsova, T.S. Koltsova,
S.V. Ganin, M.A. Danilova, A.I. Shamshurin*

ALUMINUM – CARBON NANOFIBERS COMPOSITE COATING PRODUCED BY COLD SPRAYING

*А. Тоницки, А.Н. Скворцова, Т.С. Кольцова,
С.В. Ганин, М.А. Данилова, А.И. Шамшури*

ХОЛОДНОЕ ГАЗОДИНАМИЧЕСКОЕ НАПЫЛЕНИЕ ПОКРЫТИЙ СИСТЕМЫ АЛЮМИНИЙ – УГЛЕРОДНЫЕ НАНОВОЛОКНА

Carbon nanofiber (CNF) / aluminum hybrid material was prepared by direct synthesis of CNFs on the surface of aluminum powder particles in a fluidized bed reactor using acetylene and hydrogen at the temperature of 550 °C. This allowed to achieve a good dispersion of CNFs in an aluminum matrix with the CNF content up to 2%. The possibility for producing coatings based on aluminum, reinforced by carbon nanostructures in cold gas-dynamic spraying was shown. The Al-CNFs coatings showed about a 60% increase in the hardness compared with pure Al coatings.

ALUMINUM; SYNTHESIS; CARBON NANOFIBERS; COATING; POWDER METALLURGY.

В статье представлены результаты работ по получению гибридного материала системы «углеродные нановолокна (УНВ) / алюминий» газофазным методом в реакторе кипящего слоя. Хорошая дисперсия углеродных структур была достигнута путем синтеза нановолокон из газовой фазы, с использованием ацетилен - водородной атмосферы при температуре 550 °C, непосредственно на поверхности матричных металлических частиц в присутствии никелевого катализатора. Показана возможность получения покрытий на основе алюминия, армированного углеродными нановолокнами методом холодного газодинамического напыления при использовании гибридного порошкового материала с содержанием углерода до 2 масс. %. Полученные покрытия при содержании 1 и 2 масс. % углеродных нановолокон показали увеличение твердости на 60% по сравнению с покрытием из чистого алюминия.

АЛЮМИНИЙ; СИНТЕЗ; УГЛЕРОДНЫЕ НАНОВОЛОКНА; ПОКРЫТИЯ; ПОРОШКОВАЯ МЕТАЛЛУРГИЯ.

Introduction

Recently, metal matrix composite materials reinforced with carbon nanotubes (CNT) and carbon nanofibers (CNF), is the object of study of a large number of researchers [1]. This is due to the unique properties of CNTs, such as the strength of up to 63 GPa [2] and the thermal conductivity of 3000 W/mK [3]. Uniform distribution of carbon nanotubes in the metal matrix remains a challenge due to their high propensity for agglomeration. The authors try to solve the problem in the stage of preparation of the composite powder and in stage of compaction [1].

Most traditional methods of mixing powders of the matrix and the CNTs is a mechanical grinding in

a ball mill [4–6], ultrasonic mixing [7] and spray drying of small metal particles with CNTs [8]. To create a compact materials based on metals, reinforced by CNTs, technology of powder metallurgy [9, 10], galvanic plating [11], sintering in spark plasma [12, 13], mechanical alloying [14] and thermal spraying are used [15, 16].

Thermal spraying is a very promising method for the production of metal-CNT based composites. It can be used for the production of coatings with high wear resistance. The method has the great advantage over conventional powder metallurgy, since it allows to obtain uniform distribution of the carbon nanotubes in complex shaped structures and coatings.

However, the high speed impact along with high temperatures may lead to the destruction of carbon nanostructures [17].

Cold gas dynamic spraying or just cold spraying (CS) is a process in which solid powders are accelerated in a Laval nozzle toward to a substrate at a temperature significantly below the melting point [18]. When unmelted metal particles bumps on a substrate of plastic deformation occurs and the kinetic energy of the particles is converted to heat and, in part, to binding energy with the substrate, providing the formation of a continuous layer of densely packed metal particles. CS is a high deposition rate coating process that utilizes kinetic rather than thermal energy. The cold spray process has several advantages, as there is no oxidation and phase transformation involved due to the low temperature of the process.

In [8] it was possibility to obtain coatings based on aluminum reinforced by multilayer carbon nanotubes using cold gas dynamic spraying, up to a thickness of 500 microns. To obtain a good distribution of carbon nanostructures in the matrix, the authors used spray drying of Al-Si eutectic powder with pure CNTs. The dry powder contained 5 wt% of CNT and were mixed with pure aluminum in a ball mill. After ball milling the Al-Si particles agglomerated with the CNTs to a size of ~50 microns. The final content of the carbon nanostructures in the powder was 0,5–1 wt.%. The authors obtained a good distribution of carbon nanostructures in the coating.

The presented article devoted to obtain a composite powder material based on aluminum, in which a good dispersion of carbon nanostructures achieved by synthesis of nanofibers from the gas phase of the metal matrix particles directly on the surface by addition of the nickel based catalyst. The possibility of using this composite powder for the production of coatings by cold gas-dynamic spraying was examined.

Experiment details

As the starting material aluminum powder (brand PA-4) with a purity of 99,5 wt.% was used. The main impurities are silicon, iron and copper with a content of not more than 0,4; 0,35 and 0,02 wt.%, respectively.

The composite particulate material was synthesized by a chemical vapor deposition (CVD) in a fluidized bed reactor as shown in the fig.1. This method is considered as the most viable and efficient process for high-yield production of carbon nanotubes. For the synthesis a fluidized bed reactor (fig. 1,a) which consists of a quartz tube inserted into a vertical furnace (hot zone 60 cm). The quartz tube was conically shaped with a junction from internal diameters of 6 to 34 mm with a cone zone length of 20 cm.

Gas-dynamic spraying was conducted on a 405 DYMET installation in an air jet at a pressure of 7 kg/cm² and 600 m/s speed, the gas temperature reached 450 °C. The substrate used was steel sheet which was grit blasted prior to spray deposition.

The structure and morphology of the powder materials and coatings was studied by scanning electron microscopy (TESCAN Mira-3M). Hardness of coatings was measured by PMT-3 equipment. The amount of carbon was determined from the difference of mass change after oxidation at 700 °C for 30 minutes with catalyst coated aluminum powder before and after synthesis.

For one experiment, 35 grams of aluminum powder were filled up from the top and kept in an argon atmosphere of 400 cm³/min to replace oxygen and to heat the powder to the synthesis temperature for 10 min. After heating the reactor to 550 °C hydrogen was added at a rate of 440 cm³/min for 20 minutes, to convert catalyst particles to Ni. Further acetylene was substituted for argon at a flow rate 53 cm³/min. The Synthesis was also carried out for 20 minutes. Cooling to room temperature was carried out in argon at a flow rate 400 cm³/min outside of the furnace. Synthesis parameters are shown graphically in fig. 1,b.

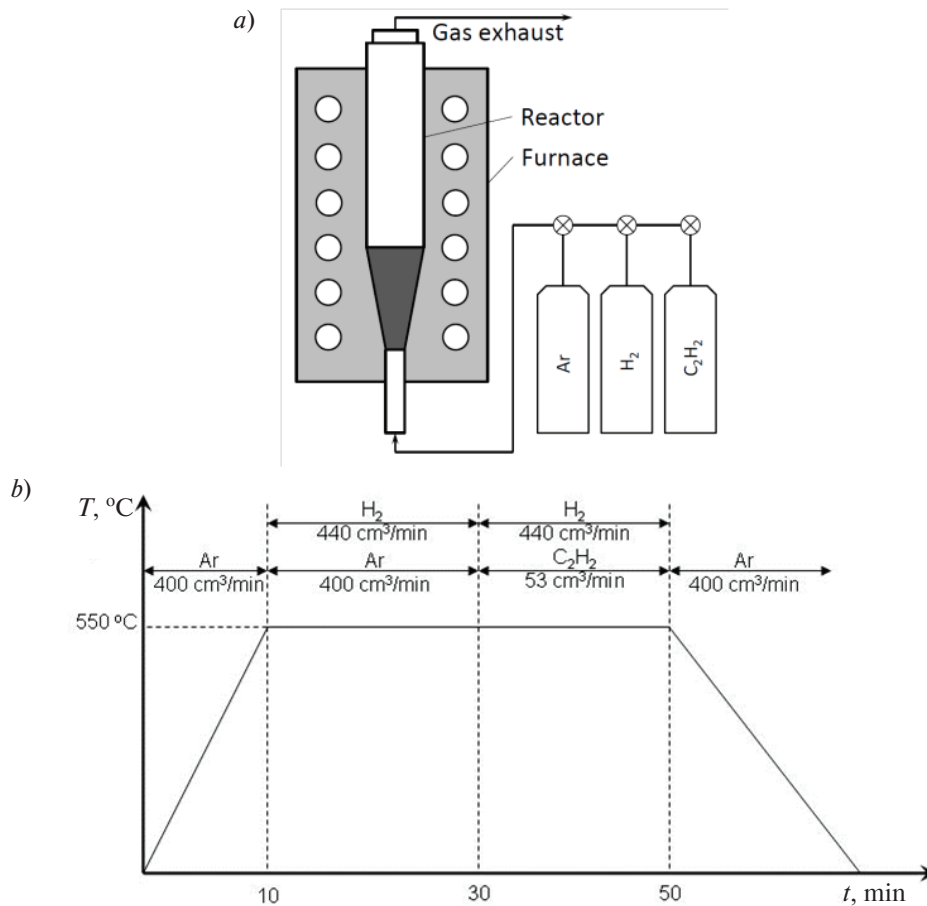


Fig. 1. Schematic of the experimental setup (a) and synthesis mode (b)

Experimental results

To grow carbon nanostructures, a nickel was preliminary deposited on the surface of the aluminum powder. Application of a nickel catalyst was conducted by vacuum-drying the powder in a water solution of nickel nitrate $\text{Ni}(\text{NO}_3)_2 \cdot 6\text{H}_2\text{O}$. Solution concentration varied from 10 to 80 g/l. After deposition on aluminum the salt-particle powder was subjected to a heat treatment step to remove residual moisture and convert salt decomposition oxide (NiO). Annealing was performed under an argon atmosphere at temperatures of 100 and 250 °C for 30 minutes and at 400 °C for 60 minutes.

By varying the concentration of Ni catalyst were obtained composite materials containing from 0,63 to 2,2 wt. % carbon. The obtained powders were studied by scanning electron microscopy (fig. 2). From micro images seen that the carbon product has

a tubular structure and cover the matrix particles virtually fully. Carbon structures have a diameter from 50 to 100 nm and a length more than 1 micron.

The resulting powders were applied onto a steel substrate by cold gas-dynamic spraying. The composite powders with 1 and 2 wt.% CNFs were used to create coatings.

The resulting coating is plastically deformed aluminum particles stuck together (fig. 3, a, c) wherein the carbon nanostructures are evenly distributed over the coverage area. At high magnifications it can be seen carbon nanostructures are present in the sample, however, their number became significantly less and the length less than 1 micron. This may be due to the separation of longer nanofibers from the surface of aluminum particles during spraying. Reduction of fiber length could occur as well due to fiber fracture, which occurs upon impact of the particles with substrate.

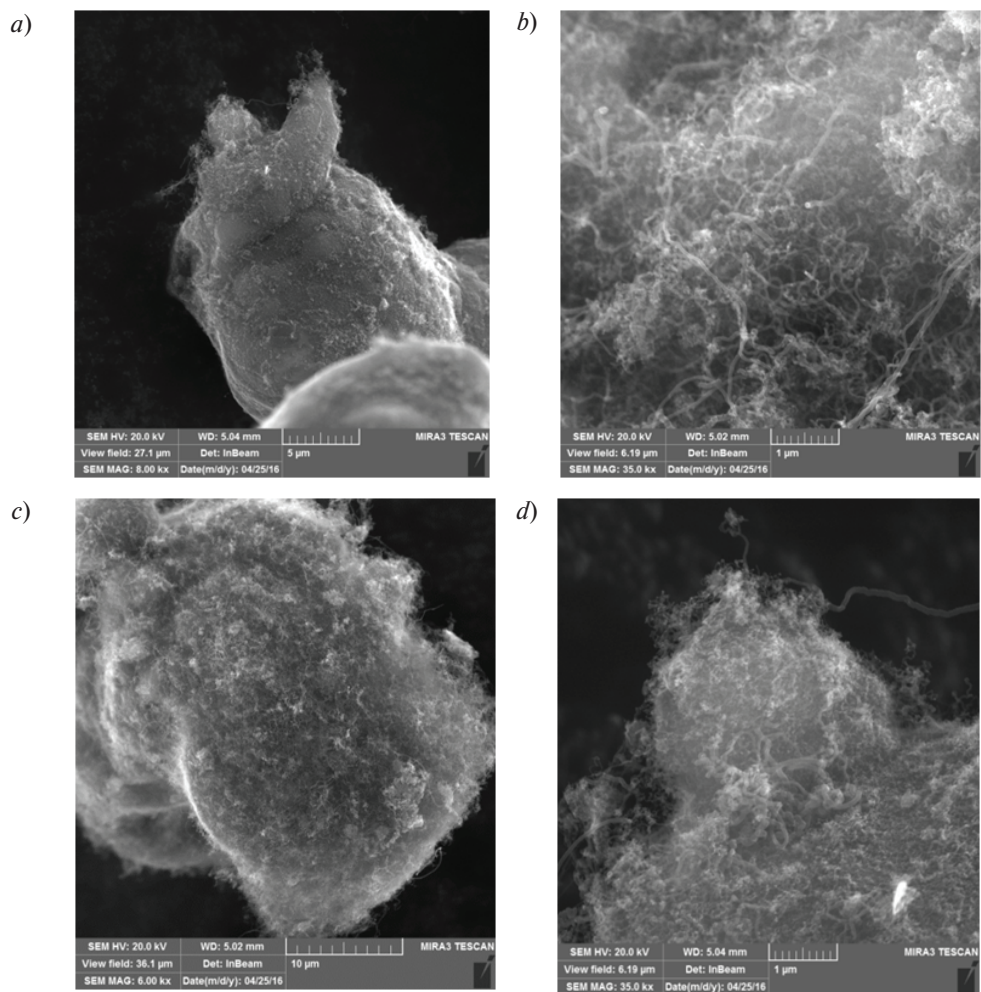


Fig. 2. SEM images of the powder composite material with carbon content of 1 wt. % (a, b) and 2 wt. % (c, d)

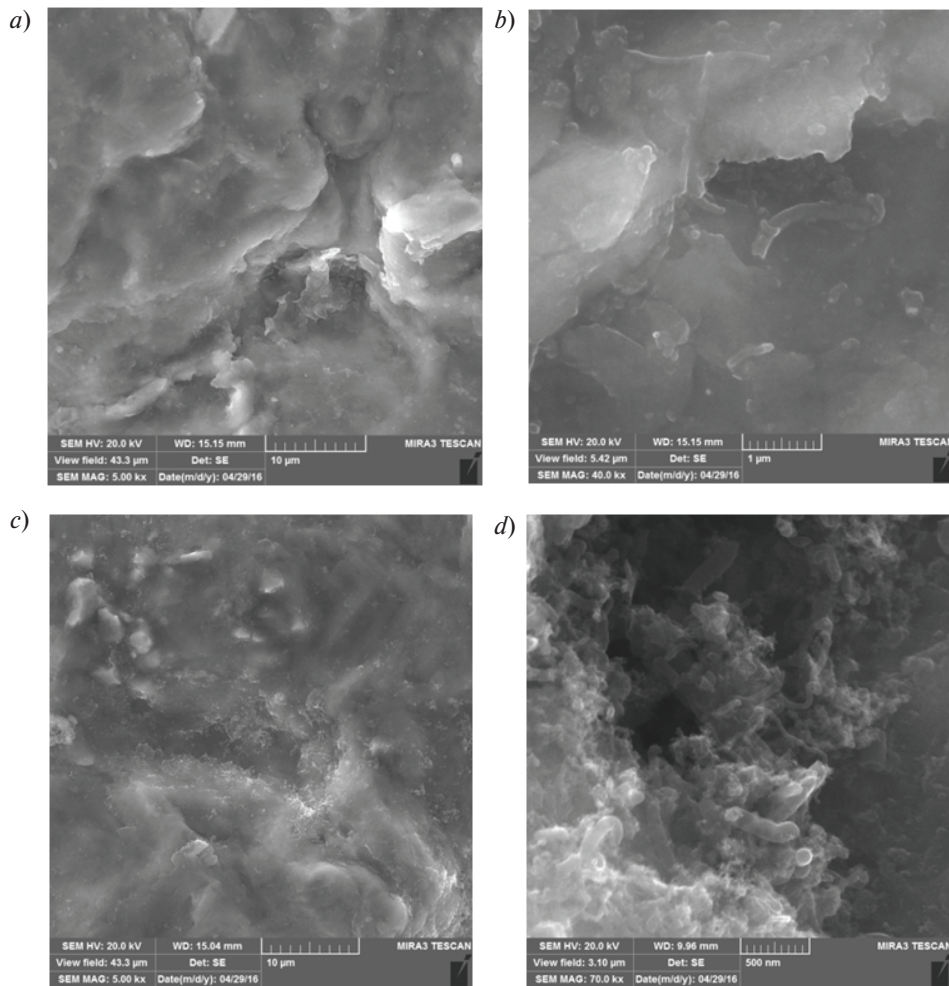


Fig. 3. SEM image surface coatings obtained by CS when the content in powders of 1 wt. % (a, b) and 2 wt. % (c, d) of carbon

Fig. 4 shows SEM images of the polished cross-section of Al-1wt.% CNFs and Al-2wt.% CNFs coatings. It can be seen that thin coatings of about 20 μm were formed by cold spraying. A coating with 1% CNFs has a more dense structure than a coating with 2% CNFs. Porosity between particles was a result of insufficient deformation of aluminum particles. The increasing of CNT content leads to deterioration of adhesion between the aluminum particles.

The Al-CNFs coatings demonstrated about 60% increase in the hardness compared with pure Al coatings. If the average Vickers microhardness for Al coating is 32 HV then the Al-1 wt.% CNFs and Al-2 wt.% CNFs coating amounts to 51 HV and 53 HV respectively. The hardness of the samples which contained 2% CNF has no significant changes compared to 1% of the CNF - it is a result of increased porosity.

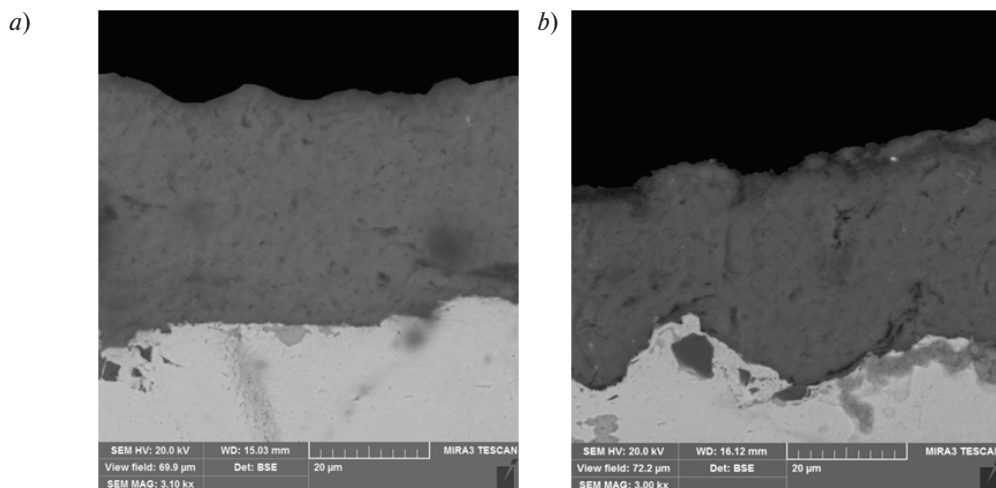


Fig. 4. SEM images of the polished cross-section of Al-1 wt.% CNFs (a) and 2wt% CNFs (b) coatings

Conclusions

Composite Al-based powder with carbon nanofibers uniformly distributed over the surface had been successfully synthesized by CVD process in a fluidized bed reactor. Content of CNF on the powder surface can be varied by variation of Ni catalyst content from 0,5 up to 2 mass.%. The provided apparatus for synthesis allow to obtain tens grams of powdered material per hour, as well of its advantages of uniform processing of carbon nanostruc-

tures across the surface of the powder, as well as the process scalability. The obtained composite powder has the possibility to be used in cold spray process to create coatings. It was determined that the carbon fibers are present and evenly distributed in the coatings. The Al-CNFs coatings showed about 60% increase in the hardness compared with pure Al coatings.

This study was supported by Russian Foundation for Basic Research (project no. 16-32-80092)

REFERENCES

1. Bakshi [et al]. Carbon Nanotube Reinforced Metal Matrix Composites. *International Materials Reviews*. 2010. Vol. 55 (1). P. 41–64.
2. Min-Feng Yu, Laurie O., Dyer M.J., Moloni K., Kelly T.F., Ruoff R.S. Strength and breaking mechanism of multiwalled carbon nanotubes under tensile load. *Science*. 2000. Vol. 287. P. 637–640.
3. Kim P., Shi L., Majumdar A., McEuen P.L. Thermal Transport Measurements of Individual Multiwalled Nanotubes. *Phys. Rev. Lett.* 2001. Vol. 87 (21). P. 215502-1–215502-4.
4. Chen W.X., Tu J.P., Wang L.Y., Gan H.Y., Xu Z.D., Zhang X.B. Tribological application of carbon nanotubes in a metal-based composite coating and composites. *Carbon*. 2003. Vol. 41. P. 215–222.
5. Tu J.P., Yang Y.Z., Wang L.Y., Ma X.C., Zhang X.B. Tribological properties of carbon-nanotube-reinforced copper composites. *Tribol. Lett.* 2001. Vol. 10. P. 225–228.
6. He C., Zhao N., Shi C., Du X., Li J., Li H., Cui Q. An Approach to Obtaining Homogeneously Dispersed Carbon Nanotubes in Al Powders for Preparing Reinforced Al-Matrix Composites. *Adv.Mater.* 2007. Vol. 19. P. 1128–1132.
7. Tokunaga T., Kaneko K., Horita Z. Production of aluminum-matrix carbon nanotube composite using high pressure torsion. *Mater. Sci. Eng. A*. 2008. Vol. 490. P. 300–304.
8. Bakshi S.R., Singh V., Balani K., McCartney D.G., Seal S., Agarwal A. Carbon nanotube reinforced aluminum composite coating via cold spraying. *Surface & Coatings Technology*. 2008, Vol. 202. P. 5162–5169.
9. Carreno-Morelli E., Yang J., Couteau E., Hernadi K., Seo J.W., Bonjour C., Forro L., Schaller R. Carbon nanotube/magnesium composites. *Phys. Status Solidi (a)*. 2004. Vol. 201 (8). R53–R55.
10. Feng Y., Yuan H.L., Zhang M. Fabrication and Properties of Silver-Matrix Composites Reinforced by Carbon Nanotubes. *Mater. Charact.* 2005. Vol. 55. P. 211–218.
11. Arai S., Endo M., Kaneko N. Ni-deposited Multiwalled Carbon Nanotubes by Electrodeposition. *Carbon*. 2004. Vol. 42. P. 641–644.
12. Kim K.T., Cha S.I., Hong S.H., Hong S.H. Microstructures and tensile behavior of carbon nanotube reinforced Cu matrix nanocomposites. *Mater. Sci. Eng., A*. 2006. Vol. 430. P. 27–33.

13. **Pang L.-X., Sun K.-N., Ren S., Sun C., Fan R.-H., Lu Z.-H.** Fabrication and microstructure of Fe₃Al matrix composite reinforced by carbon nanotube. *Mater. Sci. Eng., A*. 2007. Vol. 447. P. 146–149.

14. **Esawi A.M.K., El Borady M.A.** Carbon nanotube-reinforced aluminium strips. *Comput. Sci. Tech.* 2008. Vol. 68 (2). P. 486–492.

15. **Laha T., Agarwal A., McKechnie T., Seal S.** Synthesis and characterization of plasma spray formed carbon nanotube reinforced aluminum composite. *Mater. Sci. Eng., A*. 2004. Vol. 381. P. 249–258.

16. **Laha T., Agarwal A.** Effect of sintering on thermally sprayed carbon nanotube reinforced aluminum nanocomposite. *Mater. Sci. Eng., A*. 2008. Vol. 480. P. 323–332.

17. **Moridi A., Hassani-Gangaraj S. M., Guagliano M., Dao M.** Cold spray coating: review of material systems and future perspectives. *Surface Engineering*. 2014. Vol. 36 (6). P. 369–395.

18. **Zhang D., Shipway P.H., McCartney D.G.** Cold gas dynamic spraying of aluminum: The role of substrate characteristics in deposit formation. *J. Therm. Spray Technol.* 2005. Vol. 14. P. 109–116.

СПИСОК ЛИТЕРАТУРЫ

1. **Bakshi [et al].** Carbon Nanotube Reinforced Metal Matrix Composites // *International Materials Reviews*. 2010, Vol. 55 (1). P. 41–64.

2. **Min-Feng Yu, Laurie O., Dyer M.J., Moloni K., Kelly T.F., Ruoff R.S.** Strength and breaking mechanism of multiwalled carbon nanotubes under tensile load // *Science*. 2000. Vol. 287. P. 637–640.

3. **Kim P., Shi L., Majumdar A., McEuen P.L.** Thermal Transport Measurements of Individual Multiwalled Nanotubes // *Phys. Rev. Lett.* 2001. Vol. 87 (21) P. 215502–1–215502-4.

4. **Chen W.X., Tu J.P., Wang L.Y., Gan H.Y., Xu Z.D., Zhang X.B.** Tribological application of carbon nanotubes in a metal-based composite coating and composites // *Carbon*. 2003. Vol. 41. P. 215–222.

5. **Tu J.P., Yang Y.Z., Wang L.Y., Ma X.C., Zhang X.B.** Tribological properties of carbon-nanotube-reinforced copper composites // *Tribol. Lett.* 2001. Vol. 10. P. 225–228.

6. **He C., Zhao N., Shi C., Du X., Li J., Li H., Cui Q.** An Approach to Obtaining Homogeneously Dispersed Carbon Nanotubes in Al Powders for Preparing Reinforced Al-Matrix Composites // *Adv.Mater.* 2007. Vol. 19. P. 1128–1132.

7. **Tokunaga T., Kaneko K., Horita Z.** Production of aluminum-matrix carbon nanotube composite using high pressure torsion // *Mater. Sci. Eng. A*. 2008. Vol. 490. P. 300–304.

8. **Bakshi S.R., Singh V., Balani K., McCartney D.G., Seal S., Agarwal A.** Carbon nanotube reinforced aluminum composite coating via cold spraying // *Surface & Coatings Technology*. 2008. Vol. 202. P. 5162–5169.

9. **Carreno-Morelli E., Yang J., Couteau E., Hernadi K., Seo J.W., Bonjour C., Forro L., Schaller R.** Carbon

nanotube/magnesium composites // *Phys. Status Solidi (a)*. 2004. Vol. 201 (8). R53–R55.

10. **Feng Y., Yuan H.L., Zhang M.** Fabrication and Properties of Silver-Matrix Composites Reinforced by Carbon Nanotubes // *Mater. Charact.* 2005. Vol. 55. P. 211–218.

11. **Arai S., Endo M., Kaneko N.** Ni-deposited Multiwalled Carbon Nanotubes by Electrodeposition // *Carbon*. 2004. Vol. 42. P. 641–644.

12. **Kim K.T., Cha S.I., Hong S.H., Hong S.H.** Microstructures and tensile behavior of carbon nanotube reinforced Cu matrix nanocomposites. // *Mater. Sci. Eng., A*. 2006. Vol. 430. P. 27–33.

13. **Pang L.-X., Sun K.-N., Ren S., Sun C., Fan R.-H., Lu Z.-H.** Fabrication and microstructure of Fe₃Al matrix composite reinforced by carbon nanotube // *Mater. Sci. Eng., A*. 2007. Vol. 447. P. 146–149.

14. **Esawi A.M.K., El Borady M.A.** Carbon nanotube-reinforced aluminium strips // *Comput. Sci. Tech.* 2008. Vol. 68 (2). P. 486–492.

15. **Laha T., Agarwal A., McKechnie T., Seal S.** Synthesis and characterization of plasma spray formed carbon nanotube reinforced aluminum composite // *Mater. Sci. Eng., A*. 2004. Vol. 381. P. 249–258.

16. **Laha T., Agarwal A.** Effect of sintering on thermally sprayed carbon nanotube reinforced aluminum nanocomposite // *Mater. Sci. Eng., A*. 2008. Vol. 480. P. 323–332.

17. **Moridi A., Hassani-Gangaraj S. M., Guagliano M., Dao M.** Cold spray coating: review of material systems and future perspectives // *Surface Engineering*. 2014. Vol. 36 (6). P. 369–395.

18. **Zhang D., Shipway P.H., McCartney D.G.** Cold gas dynamic spraying of aluminum: The role of substrate characteristics in deposit formation // *J. Therm. Spray Technol.* 2005. Vol. 14. P. 109–116.

СВЕДЕНИЯ ОБ АВТОРАХ/AUTHORS

TONITZKI Andreas – Peter the Great St. Petersburg Polytechnic University.

29 Politechnicheskaya St., St. Petersburg, 195251, Russia.

E-mail: a.tonitzki@gmx.de

ТОНИИТЗКИ Андреас – студент Санкт-Петербургского политехнического университета Петра Великого.

195251, Россия, г. Санкт-Петербург, Политехническая ул., 29.

E-mail: a.tonitzki@gmx.de

SKVORTSOVA Aleksandra N. – Peter the Great St. Petersburg Polytechnic University.

29 Politechnicheskaya St., St. Petersburg, 195251, Russia.

E-mail: hlobystic@mail.ru

СКВОРЦОВА Александра Николаевна – аспирант Санкт-Петербургского политехнического университета Петра Великого.

195251, Россия, г. Санкт-Петербург, Политехническая ул., 29.

E-mail: hlobystic@mail.ru

KOLTSOVA Tatiiana S. – Peter the Great St. Petersburg Polytechnic University.

29 Politechnicheskaya St., St. Petersburg, 195251, Russia.

E-mail: annelet@yandex.ru

КОЛЬЦОВА Татьяна Сергеевна – кандидат технических наук инженер Санкт-Петербургского политехнического университета Петра Великого.

195251, Россия, г. Санкт-Петербург, Политехническая ул., 29.

E-mail: annelet@yandex.ru

GANIN Sergei V. – Peter the Great St. Petersburg Polytechnic University.

29 Politechnicheskaya St., St. Petersburg, 195251, Russia.

E-mail: s.v.ganin@gmail.com

ГАНИН Сергей Владимирович – кандидат технических наук доцент Санкт-Петербургского политехнического университета Петра Великого.

195251, Россия, г. Санкт-Петербург, Политехническая ул., 29.

E-mail: s.v.ganin@gmail.com

DANILOVA Marina A. – Peter the Great St. Petersburg Polytechnic University.

29 Politechnicheskaya St., St. Petersburg, 195251, Russia.

E-mail: marina.rakovskay@yandex.ru

ДАНИЛОВА Марина Андреевна – аспирант Санкт-Петербургского политехнического университета Петра Великого.

195251, Россия, г. Санкт-Петербург, Политехническая ул., 29.

E-mail: marina.rakovskay@yandex.ru

SHAMSHURIN Aleksei I. – Peter the Great St. Petersburg Polytechnic University.

29 Politechnicheskaya St., St. Petersburg, 195251, Russia.

E-mail: sham_a@mail.ru

ШАМШУРИН Алексей Игоревич – научный сотрудник Санкт-Петербургского политехнического университета Петра Великого.

195251, Россия, г. Санкт-Петербург, Политехническая ул., 29.

E-mail: sham_a@mail.ru

DOI 10.5862/JEST.249.10

УДК 669.295: 669.018

N.A. Krylov, M.A. Skotnikova, G.V. Tsvetkova, G.V. Ivanova

INFLUENCE OF STRUCTURE AND PHASE COMPOSITION OF THE MATERIAL OF STEAM TURBINE BLADES FROM TITANIUM ALLOYS ON THEIR RESISTANCE TO EROSION DESTRUCTION

Н.А. Крылов, М.А. Скотникова, Г.В. Цветкова, Г.В. Иванова

ВЛИЯНИЕ СТРУКТУРЫ И ФАЗОВОГО СОСТАВА МАТЕРИАЛА ЛОПАТОК ПАРОВЫХ ТУРБИН ИЗ ТИТАНОВЫХ СПЛАВОВ НА ИХ УСТОЙЧИВОСТЬ К ЭРОЗИОННОМУ РАЗРУШЕНИЮ

Titanium alloys keep a leading position in manufacturing steam turbine blades. The unique combination of high specific strength and fracture toughness, corrosion resistance, polymorphism, a tendency to phase transformations and high resistance to shock loading determined their wide application in power engineering. However, power engineering is still facing a problem of erosion damage of steam turbine blades as a result of a drop impact of vapor particles at speeds of 150...600 m / s. The complication in solving this problem is that it is difficult to establish a link between wear and structural-phase composition of the surface of turbine blades. In this paper, using optical metallography, electron microscopy, ray analysis and X-ray microspectral analysis, we developed a method for studying structural and phase transformations in the material of steam turbine blades of titanium alloy VT6 after technological treatments in different modes. An attempt was made to establish a link between resistance to erosion destruction and structural and phase composition of titanium alloys.

STEAM TURBINE; STRUCTURAL AND PHASE TRANSFORMATIONS; OPTICAL METALLOGRAPHY; ELECTRON MICROSCOPY; X-RAY MICROSPECTRAL ANALYSIS.

Титановые сплавы сохраняют лидирующее положение в производстве лопаток паровых турбин. Уникальное сочетание высокой удельной прочности и вязкости разрушения, коррозионной стойкости, полиморфизм, склонность к фазовым превращениям и высокая устойчивость к ударной нагрузке определили их широкое применение в энергетике. Тем не менее в энергетическом машиностроении до сих пор существует проблема эрозионного повреждения лопаток паровых турбин в результате каплеударного воздействия частиц пара со скоростями 150–600 м / с. Сложность решения этой проблемы заключается в том, что трудно установить связь между износом и структурно-фазовым составом поверхности лопаток турбин. В данной работе с использованием оптической металлографии, электронной микроскопии, рентгеноструктурного анализа и рентгеновского микроспектрального анализа разработан метод исследования для изучения структурных и фазовых превращений в материале паровых лопаток турбин из титанового сплава ВТ6, после технологической обработки на различных режимах. Предпринята попытка установить связь между устойчивостью к эрозионному разрушению и структурно-фазовым составом титановых сплавов.

ПАРОВЫЕ ТУРБИНЫ; СТРУКТУРНЫЕ И ФАЗОВЫЕ ПРЕВРАЩЕНИЯ; ОПТИЧЕСКАЯ МЕТАЛЛОГРАФИЯ; ЭЛЕКТРОННАЯ МИКРОСКОПИЯ; МИКРО-РЕНТГЕНСПЕКТРАЛЬНЫЙ АНАЛИЗ.

Introduction

Titanium alloys keep a leading position in the creation of steam turbine blades. The unique combination of high specific strength and fracture

toughness, corrosion resistance, polymorphism, a tendency to phase transformations and high resistance to shock loading defined their wide application in power engineering (for example see fig. 1, a, b)) [1, 2].

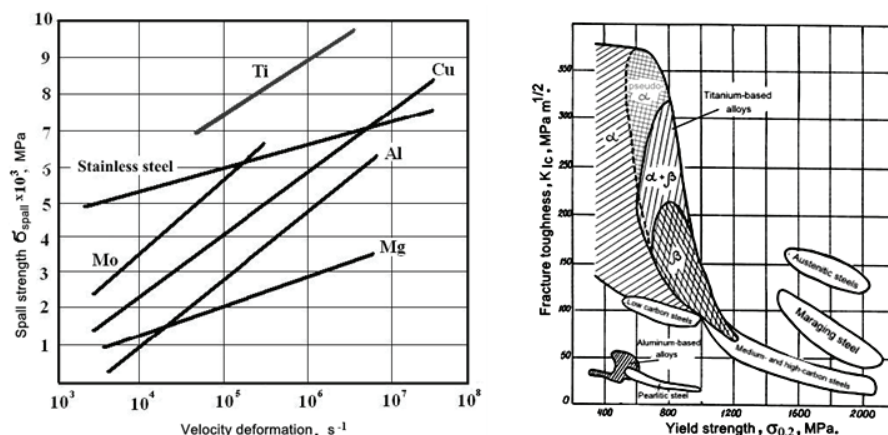


Fig. 1. Dependence of spall strength from velocity deformation for different metals (a); dependence of fracture toughness from yield strength for titanium alloys (b)

However, the power engineering still has a problem of erosion damage of steam turbine blades as a result of a drop impact of vapor particles at a speed of 150–600 m / s. The difficulty of solving the problem is that difficult to establish a link between wear and structural-phase composition of the surface of turbine blades (the typical example of erosion destruction of steam turbine blades is shown in fig. 2).

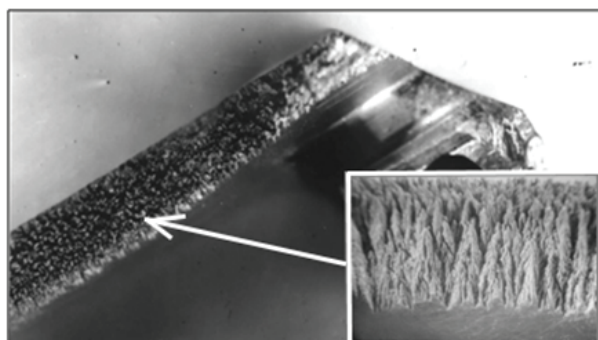


Fig. 2. Example of erosion destruction of steam turbine blades

Two-phase titanium alloys found wide application in turbine construction due to opinion [3], that the greatest resistance to effect of exposure steam drops should be two-phase alloys with low internal stresses and high plastic properties, during which time of stress there exist phase transformations strengthening the subject material.

At effect of exposure steam drops, field sizes of a stressing are commensurable with sizes of structural components, and redistribution of internal stresses between them is impossible. The role of individual durability, intensity, a chemical composition and phase transformations in separate structural compo-

nents therefore increases. To solve this problem it is necessary find the relation between the wear and structural-phase state of the surface and axial layers of blades material.

The object of research

The object of research has been samples of steam turbine blades of the two-phase titanium alloy VT6 (Ti-6Al-4V) average strength after deformation in b area and final deformed by stamping in areas $\alpha+\beta$ next to the reduced temperatures T_{50} and T_{70} , corresponding to the first and second technology. The temperature of final transition of an alloy in b- region (T_{pt}) was made 1015 °C.

As follows from earlier carried out works [4–8], on the basis of complex research of mechanisms of formation and decomposition nonequilibrium $\beta(\alpha)$ - and $\alpha(\beta)$ - phases, redistribution between them of alloying elements, physical and mechanical properties of the deformed titanium alloys of a different alloying, and also the established laws, the generalized kinetic diagram, fig. 3, has been constructed. Thus we took into account not only a temperature of heating absolute (T), but also produced the identical contents of high-temperature β -phases (T_{β}). We established, that the more nonequilibrium $\beta(\alpha)$ - and $\alpha(\beta)$ -solid solutions contained the same alloying elements; their polystage decomposition occurred at lower temperatures, and for greater time. It is shown, that titanium blanks possess high technological properties in a temperature-time interval two-phase ($\alpha+\beta$)- region at temperatures identical (50 %) contents high-temperature α - and β - phases (T_{50}) and near to a temperature of transition in single-phase β - region (T_{75}).

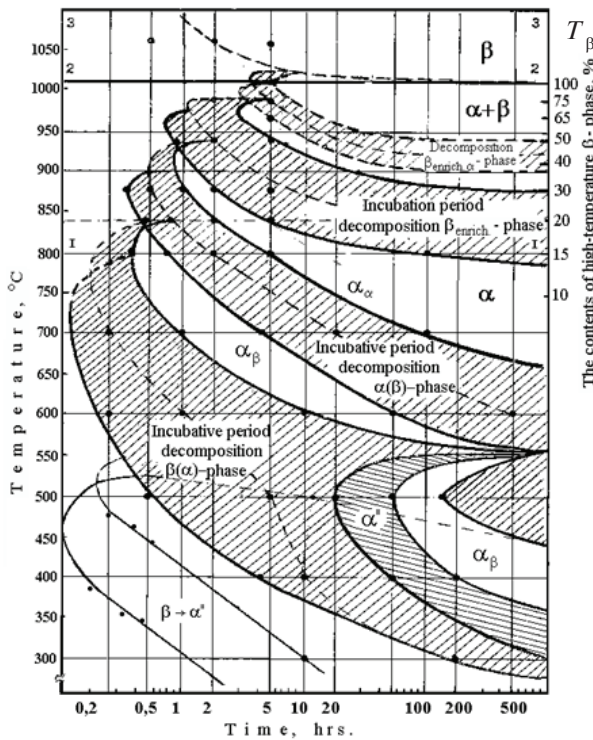


Fig. 3. Generalized kinetic diagram of structure and phase transformation in titanium alloys

The product possesses material with high operational properties after an isothermal exposure near to temperature T_{15} . In these cases α - and β - phase components appear enriched, the as α - and β - stabilizing alloying elements, in these processes of a polygonization that causes increase of plasticity characteristics and allows crack origin of alloys to develop.

Thus, construction of serial curves of increase of the contents high-temperature β - phases depending on a temperature of heating (a method of hardening), will allow us to estimate the resulted temperatures of heating and to develop the scientifically-grounded modes of technological treatment of titanium blanks [6].

Structure and the Phase Composition

Both stamping technology provides a bimodal structure α -phase globular (α_1) and platelet-shaped (α_{II}), divided by layers of β_{II} - phases (fig. 4, *a, b*). Electron microscope photos (fig. 4, *c, d*) shows that the boundaries of phase components (α_1 , α_{II} , β_{II}) for the first technology much better relaxation, due to

customizations of dislocation. The second technology is seen less of number curved extinction contours, indicate the presence of internal stresses.

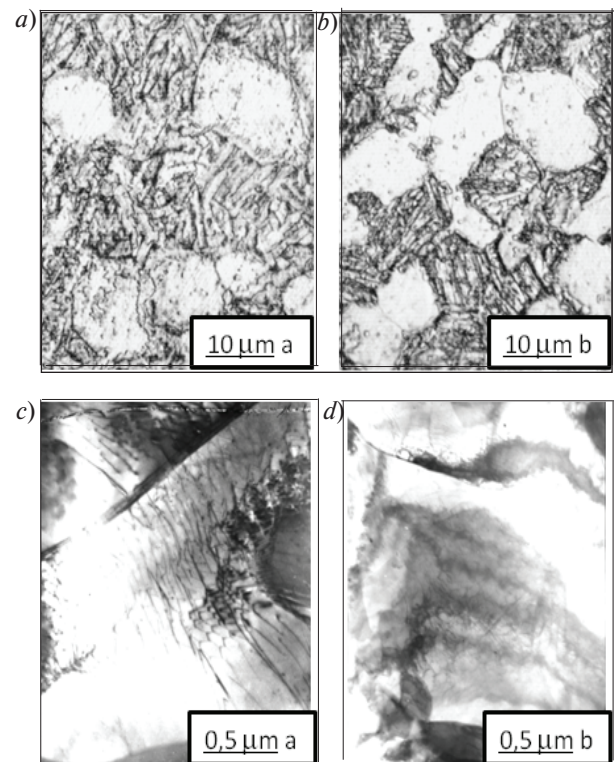


Fig. 4. The microstructure after stamping on the first (*a*) and second (*b*) technologies; the electron microscope structure after stamping on the first (*c*) and second (*d*) to technologies

As seen from the table 1, width plate of α_{II} - phase by the first technology in 3 times and interlayers of β_{II} -phase in 8 times greater than by the second technology. This evidence different temperatures and cooling rates. By the first technology, at low-temperature is formed structure similar to the Widmanstätten. Such structure, in a number of sources, has a higher fatigue strength than the martensite-like by the second technology [9]. In materials of both blades with bimodal structure, the size lamellar ($\beta_{II} + \alpha_{II}$) - a component was more size globular α_1 - phases.

Distribution of Alloying Elements

The research results obtained by X-ray microspectral analysis of the contents of alloying elements (aluminum, vanadium, titanium, iron) in separate phase components shows in table 2.

Table 1

The particles size of phase components of metal blades, fabricated on two technologies

Phase components	Size of particles of phases after the first technology, μm	Size of particles of phases after the second technology, μm
α_I	15	12
α_{II}	2,2	0,7
β_{II}	0,8	0,1
$\alpha_{II} + \beta_{II}$	22	18

Table 2

The contents of alloying elements in phase components of metal blades, fabricated on two technologies

Phase components	Concentration after the first technology, weight %		Concentration after the second technology, weight %	
	Al	V	Al	V
α_I	7,30	1,35	6,97	2,04
α_{II}	6,01	3,60	5,68	4,21
β_{II}	4,14	9,64	4,61	8,28

As seen from the table for both technologies, the secondary plates of α_{II} - phase have a chemical composition that is comparable to the average composition of the alloy Ti-6AL-4V. The globular primary α_I - phase, compared with the plate α_{II} - phase contains less than 2,2% vanadium and more than 1,3% aluminum. Thin layers of secondary β_I - phase have been enriched by vanadium (β -stabilizer). In the material by the first technology β_{II} - phase contains vanadium more at 1,3% and aluminum less at 0,5%, than the second technology.

Such distribution alloying elements provides relative softness of layers β_{II} - phase and higher perfor-

mance as compared with the second technology, in which inverse ratio of alloying elements [10]. On the contrary, globalizes primary α_I - phases in blades material fabricated on the first technology, in comparison with the second, contained a vanadium less on 0,6 % and aluminum more on 1,3 % (weight).

The fig. 5 shows a typical distribution of the alloying elements with step 0,5 microns. It is seen, that is most non-uniform in a material the vanadium is distributed, being focused in β_{II} - phase. Its concentration changes from 1 up to 20 %. Aluminum is distributed more similarly, its concentration changes from 3 up to 7 %.

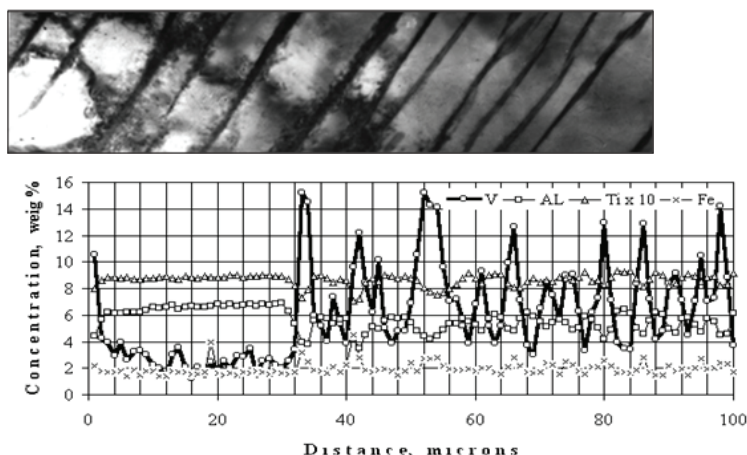


Fig. 5. The microstructure and distribution of alloying elements in structural components of material blades from alloy VT6.

Microhardness of phase components

In Table 3 are shown the data of statistical treatment of results of measurements microhardness of separate phase components. It is seen that the microhardness of the material by the second technology is higher than the first, which confirms the presence of internal stresses. It is necessary noted that the first technology makes less the difference between the hardness of globular and lamellar structure.

The blades material fabricated on both technologies had a bimodal structure. Probably, the strength balance α_1 - and $(\alpha_{II} + \beta_1)$ – structural fashions can guarantee high serviceability of a material under loading. Apparently from table 3, in blades materials fabricated on the first technology, in comparison with the second, the smaller difference in hardness between globular and lamellar structures, which made 551 and 644 MPa, accordingly has been achieved.

On fig. 6 correlation dependences of results of measurements of microhardness on a chemical compound of separate phases (α_1 , α_{II} , β_{II}) in a condition of delivery and in a martensite phase after hardenings from different temperatures are submitted. It is seen that the microhardness of plates α_{II} -phase and the globules of α_1 -phase increases with them a and b stabilizing elements. It should be noted that the microhardness increases with growth of a-stabilizer, probably due to the formation α^1 - martensite and decreases with increasing amount of β stabilizing elements, leading to the formation α^{II} - martensite. This agrees with what was seen earlier in the material by the first technology in comparison with the second technology is formed β -phase with a large content of β -stabilizing elements. This agrees with the figure, such a distribution of vanadium, gives less microhardness and greater softness of layers β_{II} -phase.

Table 3

Microhardness of phase components of blades metal fabricated on two technologies

Phase components	Microhardness of particles of phases after the first technology, MPa	Microhardness of particles of phases after the second technology, MPa
α_1	3550	3664
α_{II}	3830	4091
β_{II}	2584	3000
$\alpha_{II} + \beta_{II}$	2999	3020

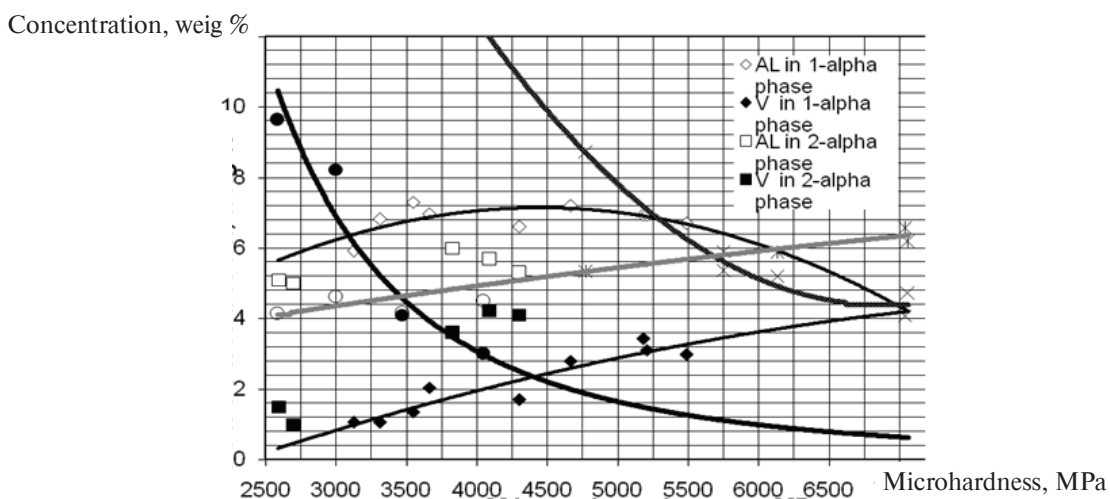


Fig. 6. Dependence of results of a rating of microhardness on a chemical compound of separate phase components (α_1 , α_{II} , β_{II} , martensite) alloy VT6

Conclusion

As results of research have shown, blades materials of steam turbines from alloy VT6 fabricated by final stamping under two technological circuits had bimodal structure, in which the share lamellar ($\alpha_{II} + \beta_{II}$)-structures (50–70 %) prevailed of a share globular α_I - structures (30–50 %). The blades material fabricated on the first technology, in comparison with the second, possessed wider layers “soft” β_{II} - the phases, enriched same it b-stabilizers. At the same time, this material contained higher concentration of aluminum in primary globalizes α_I - phases, that provided strength balance (close microhardness) structural components.

It is known, that at cyclic loadings in regular intervals distributed soft faltering layers β_{II} - phases, transiting on the contour of rather solid secondary α_{II} - phases and of strength balance globalizes α_I -phases, complicating premature localization of plastic deformation and origin of a crack in separate phases. And at the stage of distribution, the crack is more difficult to increase the length in ($\alpha_{II} + \alpha_{II}$)-lamellar structure as it is always braked by soft layers of β_{II} - phase and is compelled to change the trajectory, bending around globalized particles α_I - phases. Thus operational properties of product material increase [9–11].

Feature of effect of exposure steam drops loadings is not only recurrence and cyclicity of the enclosed stress, but also its dynamism. Through of short duration of influence, internal stresses have insufficient time to be redistributed, there is localization of the big loadings in small microvolumes, in separate structural and phase components of material. The suc-

cessful combination of structure, chemical compound and properties, abilities to resist the microshock influence of these components, determines durability of products.

Researched alloy VT6 concerning martensite class, in stable condition contains 10–18 % β - phases, which at sharp cooling turns in α^I - or α^{II} - martensite. However, $\beta \rightarrow \alpha^{II}$ - transformation can take place and at room temperature. It is known, that plastic deformation accelerates decomposition enriched b- stabilizers of b- solid solution with education α^{II} - phases, as a result of a high level of internal stresses [12]. The subsequent ageing at temperatures 450–500 °C, results in its decomposition and education $\alpha^I + (\beta)$ - phases [13]. Presence of phase transformation $\alpha^{II} \rightarrow \alpha^I + (\beta)$ results in significant strengthening of an alloy.

It is possible to believe, that in result of effect blows by pair, in soft enriched of vanadium, wide, regular intervals distributed β - layers there is an accumulation of defects of crystal structure and internal stresses. Transition deformed β - phases in a non-equilibrium condition, causes phase $\beta \rightarrow \alpha^{II}$ - transformation, accompanying with local frictional [14], and as consequence, – the subsequent ageing strengthening of microvolumes of alloy in result $\alpha^{II} \rightarrow \alpha^I + (\beta)$ - transformations. According to generalized kinetic diagram shown in fig. 3, the more layers of β - phase contain quantity isomorphous β - stabilizing elements, those at lower temperatures and for a longer time will be $\beta \rightarrow \alpha^{II}$ - takes transformation (more completely). Thus, the most important factor is strengthening of borders between solid particles of α - phases which will be increase terms of operation of a finished product, due to increase the resistance to steam drop impact.

REFERENCES

1. Fedotov S.G., Konstantinov K.M. Novyy konstruksionnyy material – Titan: Monografiya. M.: Mashinostroyeniye, 1987. 220 s. (rus.)
2. Kanel G.I., Razorenov S.V., Utkin A.V. Udarnovolnovyye yavleniya v kondensirovannykh sredakh. M.: «Yanus-K», 1999. 408 s. (rus.)
3. Deych M.Ye., Filippov G.A. Dvukhfaznyye techeniya v elementakh teploenergeticheskogo oborudovaniya: Monografiya. M.: Energoatomizdat, 1987. 328 s. (rus.)
4. Skotnikova M.A., Parshin A.M. Diagramma raspada i rezhim termicheskoy obrabotki dvukhfaznykh splavov titana. *Metallovedeniye i termicheskaya obrabotka metallov*. 1997. № 7. S. 31–37. (rus.)
5. Skotnikova M.A., Lanina A.A. Krylov N.A., Ivanov Ye.K. Strukturno-fazovyye prevrashcheniya v poverkhnostnom sloye lopatki parovoy turbiny pri kapleudar-noy erozii. *Problemy resursa i bezopasnoy ekspluatatsii materialov*. SPb: Izd-vo SPBGUNiPT, 2007. S. 102–107.
6. Skotnikova M.A., Ushkov S.S. Razrabotka nauchnogo printsip v'ybora okonchatel'noy termicheskoy obrabotki dvukhfaznykh goryachedeformirovannykh polufabrikatov iz splavov titana. *Progressivnyye materialy i tekhnologii. / TsNII KM Prometey*. 1999. Vyp. 3. S. 91–98. (rus.)

7. Skotnikova M.A., Chizhik T.A., Tsybulina I.N., Lanina A.A., Krylov N.A.. Ispol'zovaniye titanovykh splavov v kachestve materiala lopatok parovykh turbin. *Voprosy materialovedeniya*. 2007. № 3 (51) S. 61–70. (rus.)

8. Skotnikova M.A., Lanina A.A. Krylov N.A. Khomchenko Ye.V. Osobennosti stroeniya materiala lopatok parovykh turbin iz titanovogo splava VT6. *Sbornik trudov: Problemy materialovedeniya pri proyektirovanii, izgotovlenii i ekspluatatsii oborudovaniya AES*. SPb: Izd-vo FGUP TsNII KM "Prometey", 2010. S. 231–238. (rus.)

9. Park Js., Margolin H. Role α - and β -phases in distribution of fatigue crack to alloys Ti-Mn. *Metallurgical Transaction*. 1984. Vol. 15A. № 1. P. 155–169.

10. Holl I., Khammond K. Distribution of alloying elements between the phases Titanium alloys during ther-

mo-mechanical processing. *Proceedings Conference Titanium-77*. Moscow, Russia, 1977. Vol. 1. P. 351.

11. Skotnikova M.A., Chizhik T.A., Lisyanskiy A.S., Simin O.N., Tsybulina I.N., Lanina A.A. Issledovaniye rabochikh lopatok turbin bolshoy moshchnosti s uchedom strukturno-fazovykh prevrashcheniy v metalle shtampovok iz titanovogo splava VT6. *Metalloobrabotka*. 2009. № 6(54). S. 12–21. (rus.)

12. Gridnev V.N., Ivasishin O.M., Oshkaderov S.P. Fizicheskiye osnovy skorostnogo termouprochneniya titanovykh splavov. Kiev: Naukova dumka, 1986. 256 s. (rus.)

13. Yermolov M.I., Solonina O.P. Rentgenostrukturnoye issledovaniye fazovykh prevrashcheniy pri termoobrabotke titanovogo splava VT3-1. *Fizika metallov i metalovedeniye*. 1967. T. 23. № 1. S. 63–69.

СПИСОК ЛИТЕРАТУРЫ

1. Федотов С.Г., Константинов К.М. Новый конструкционный материал – Титан: Монография. М.: Машиностроение, 1987. – 220 с.

2. Канель Г.И., Разоренов С.В., Уткин А.В. Ударно-волновые явления в конденсированных средах – М.: «Янус-К», 1999. 408 с.

3. Дейч М.Е., Филиппов Г.А. Двухфазные течения в элементах теплоэнергетического оборудования. Монография. М.: Энергоатомиздат, 1987. -328 с.

4. Скотникова М.А., Паршин А.М. Диаграмма распада и режим термической обработки двухфазных сплавов титана. // *Металловедение и термическая обработка металлов*. 1997. № 7. С. 31–37.

5. Скотникова М.А., Ланина А.А. Крылов Н.А., Иванов Е.К. Структурно-фазовые превращения в поверхностном слое лопатки паровой турбины при каплеударной эрозии // *Проблемы ресурса и безопасной эксплуатации материалов*, СПб: Изд-во СПбГУНИИПТ, 2007. С. 102–107.

6. Скотникова М.А., Ушков С.С. Разработка научного принцип выбора окончательной термической обработки двухфазных горячедеформированных полуфабрикатов из сплавов титана // *Прогрессивные материалы и технологии*. / ЦНИИ КМ Прометей. – 1999. Вып. 3. С. 91–98.

7. Скотникова М.А., Чижик Т.А., Цыбулина И.Н. Ланина А.А., Крылов Н.А. Использование титановых сплавов в качестве материала лопаток паровых турбин. // *Вопросы материаловедения*. 2007. № 3 (51). С. 61–70.

8. Скотникова М.А., Ланина А.А. Крылов Н.А. Хомченко Е.В. Особенности строения материала лопаток паровых турбин из титанового сплава VT6. // *Сборник трудов: Проблемы материаловедения при проектировании, изготовлении и эксплуатации оборудования АЭС*. СПб: Изд-во ФГУП ЦНИИ КМ "Прометей", 2010. С. 231–238.

9. Park Js., Margolin H. Role α - and β -phases in distribution of fatigue crack to alloys Ti-Mn. // *Metallurgical Transaction*. 1984, Vol. 15A. № 1. P. 155–169.

10. Holl I., Khammond K. Distribution of alloying elements between the phases Titanium alloys during thermo-mechanical processing. // *Proceedings Conference Titanium-77*. Moscow, Russia, 1977. Vol. 1. P. 351.

11. Скотникова М.А., Чижик Т.А., Лисьянский А.С., Симин О.Н., Цыбулина И.Н., Ланина А.А. Исследование рабочих лопаток турбин большой мощности с учетом структурно-фазовых превращений в металле штамповок из титанового сплава VT6 // *Металлообработка*. 2009. № 6(54). С. 12–21.

12. Gridnev V.N., Ivasishin O.M., Oshkaderov S.P. Физические основы скоростного термоупрочнения титановых сплавов. Киев: Наукова думка, 1986. 256 с.

13. Ермолов М.И., Солонина О.П. Рентгеноструктурное исследование фазовых превращений при термообработке титанового сплава VT3-1 // *Физика металлов и материаловедение*. 1967. Т. 23. № 1. С. 63–69.

СВЕДЕНИЯ ОБ АВТОРАХ/AUTHORS

KRYLOV Nikolai A. – Peter the Great St. Petersburg Polytechnic University.

29 Politechnicheskaya St., St. Petersburg, 195251, Russia.

E-mail: cryoff@rambler.ru

КРЫЛОВ Николай Александрович – кандидат технических наук ведущий научный сотрудник

Санкт-Петербургского политехнического университета Петра Великого.

195251, Россия, г. Санкт-Петербург, Политехническая ул., 29.

E-mail: cryoff@rambler.ru

СКОТНИКОВА Margarita A. – Peter the Great St. Petersburg Polytechnic University.

29 Politechnicheskaya St., St. Petersburg, 195251, Russia.

E-mail: skotnikova@mail.ru

СКОТНИКОВА Маргарита Александровна – доктор технических наук заведующая кафедрой

Санкт-Петербургского политехнического университета Петра Великого.

195251, Россия, г. Санкт-Петербург, Политехническая ул., 29.

E-mail: skotnikova@mail.ru

TSVETKOVA Galina V. – Peter the Great St. Petersburg Polytechnic University.

29 Politechnicheskaya St., St. Petersburg, 195251, Russia.

E-mail: tsvetkova_gv@mail.ru

ЦВЕТКОВА Галина Викторовна – кандидат технических наук доцент Санкт-Петербургского политехнического университета Петра Великого.

195251, Россия, г. Санкт-Петербург, Политехническая ул., 29.

E-mail: tsvetkova_gv@mail.ru

IVANOVA Galina V. – Peter the Great St. Petersburg Polytechnic University.

29 Politechnicheskaya St., St. Petersburg, 195251, Russia.

E-mail: galura@yandex.ru

ИВАНОВА Галина Валерьевна – заведующая лабораторией Санкт-Петербургского политехнического университета Петра Великого.

195251, Россия, г. Санкт-Петербург, Политехническая ул., 29.

E-mail: galura@yandex.ru

DOI 10.5862/JEST.249.11

УДК 539.232

*E.A. Bogdanov, E.G. Chupakhin, E.B. Sotnikov, E.S. Vasilyeva,
S.S. Bulanov, M.V. Patrushev, N.N. Shusharina, A.Y. Goikhman*

NEW MATERIALS FOR DNA ISOLATION

*Е.А. Богданов, Е.Г. Чупахин, Е.Б. Сотников, Е.С. Васильева,
С.С. Буланов, М.В. Патрушев, Н.Н. Шушарина, А.Ю. Гойхман*

НОВЫЕ МАТЕРИАЛЫ ДЛЯ ВЫДЕЛЕНИЯ ДНК

Except silicon dioxide, commonly used for DNA isolation, such metal oxides (V) as Ta₂O₅, Nb₂O₅ and V₂O₅ were proposed for this purpose. A method for covering magnetic iron-based nanoparticles with metal oxides (V) was suggested. The synthesized nanoparticles were used for DNA extraction and the amount of isolated DNA was compared with the commercially available magnetic particles coated with silicon dioxide. Magnetic nanoparticles covered with Ta₂O₅ and Nb₂O₅ showed a greater adsorption capacity as compared with the same nanoparticles covered with silica and commercial samples. The synthesized nanoparticles can be suitable for DNA extraction in clinical or research laboratories. The functional thin films for fast and effective DNA extraction are of great interest for neurobiology investigations.

SOLGEL; THIN FILMS; DNA, MAGNETICAL NANOPARTICLES; XPS.

За исключением диоксида кремния, обычно используемого для выделения ДНК, для этой цели были предложены такие оксиды металлов (V), как Ta₂O₅, Nb₂O₅ и V₂O₅. В данной статье рассмотрен метод покрытия этими оксидами магнитных наночастиц на основе железа, исследованы химические и структурные свойства. Синтезированные наночастицы были использованы для выделения ДНК, проведено сравнение с имеющимися в продаже магнитными частицами, покрытыми диоксидом кремния. Магнитные наночастицы, покрытые Ta₂O₅ и Nb₂O₅ показывают наибольшую адсорбционную способность по сравнению с наночастицами, покрытыми диоксидом кремния и с коммерчески доступными. Синтезированные наночастицы могут быть использованы для экстракции ДНК в клинических или научно-исследовательских лабораториях. Функциональные тонкие пленки для быстрой и эффективной экстракции ДНК представляют большой интерес для исследований в нейробиологии.

ТОНКИЕ ПЛЕНКИ; ЗОЛЬ-ГЕЛЬ; ДНК; МАГНИТНЫЕ НАНОЧАСТИЦЫ; РФЭС.

Introduction

Over the last decade the studies on the magnetic nanoparticles (MNP) have become popular in wide range of biomedical applications, such as biosensors, contrast agents for magnetic resonance imaging, drug delivery, etc [1–5]. One of the most common applications of magnetic nanoparticles is DNA isolation. In that application the surface of magnetic nanoparticles is covered with materials which are active for DNA isolation. So, at the first step MNP surface actively absorbs DNA molecules and at the next step MNP are efficiently separated from chemical or biological suspensions with the magnetic field [6]. Magnetic

separation is recognized as simple and effective method for nucleic acids purification.

On the other hand materials with high surface area, such as nanoparticles, are preferred for the nucleic acids binding. Magnetic particles with shape of nanospheres, are more preferred in the process of selection, as they have a greater ability to bind-conductive [7]. Many different DNA isolation kits with magnetic particles are presents in the market, such as: AGOWA® mag, Dynabeads® DNA and other [8]. In general, surface cover materials of these magnetic nanoparticles is silicon dioxide SiO₂ or a compound based on it [9–13].

The principle of DNA isolation on silicon dioxide matrix is based on the high-affinity of negatively charged DNA strands to the positively charged sodium ions, which are in turn bound to negatively charged particles of silicon dioxide. Sodium ions act as a cation bridges, which attract negatively charged oxygen of the phosphates in the nucleic acid chain. Sodium ions treat the bonds between hydrogen in water and negatively charged oxygen ions on silica surface under high salt ($pH \leq 7$). Thus, DNA is firmly connected to the matrix. Purified DNA molecules can be eluted by low salt solution using Elution buffer or distilled water [14–16](fig. 1).

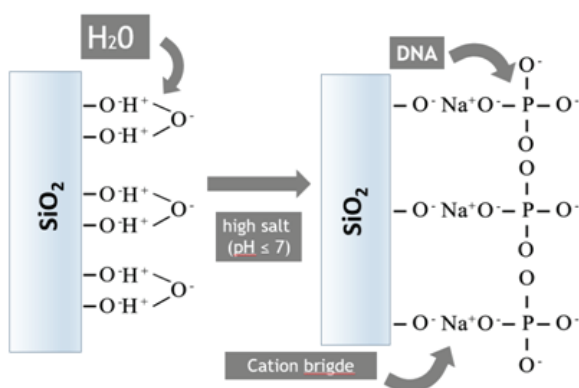


Fig. 1. SiO_2 –DNA interaction under high salt ($pH \leq 7$)

In the previous work [17] it was assumed that using of metal oxides (V) (tantalum, niobium and vanadium) would provide more effective DNA extraction than silicon dioxide. Since their crystal lattices close to stoichiometric ratio 2:5, while the silicon dioxide stoichiometric composition is close to 1:2. More effective DNA extraction can be explained by the ability of metal oxide (V) surface to form 25% more chemical bonds than SiO_2 according to oxides stoichiometry. In recent study we proposed a technological framework for fabrication of the magnetic iron-based nanoparticles covered by SiO_2 and Ta, Nb, V oxides in order to verify this assumption. Synthesised magnetic nanoparticles with bioactive surface were used for DNA extraction and quantitative characteristics of isolated DNA [18] were compared with commercial Syntol® magnetic particles.

Materials and Methods

The non-agglomerative spherical magnetic nanoparticles of Fe_3O_4 were produced by aerosol CVD synthesis method. The experimental setup for the

CVC synthesis of nanoparticles has been described elsewhere [19, 20]. Briefly, the liquid precursor, $\text{Fe}(\text{CO})_5$, was heated in a bubbler, evaporate and transported by inert gas (argon or helium) flow into a heated tubular furnace. The tubular furnace provides a heat source for the controlled decomposition of the precursor. The product of the precursor decomposition was collected in a vacuum chamber on the surface of a rotating chiller cooled by liquid nitrogen. An iron particle passivation process was achieved by dosing oxygen before opening the chamber to air. The precursor decomposition temperature was set at 400 °C. After the synthesis initial Fe-based nanoparticles have core-shell structure: core is pure iron and shell is 1-2 nm thick magnetite. SEM micrograph of as-produced nanoparticles are shown in the fig. 2.

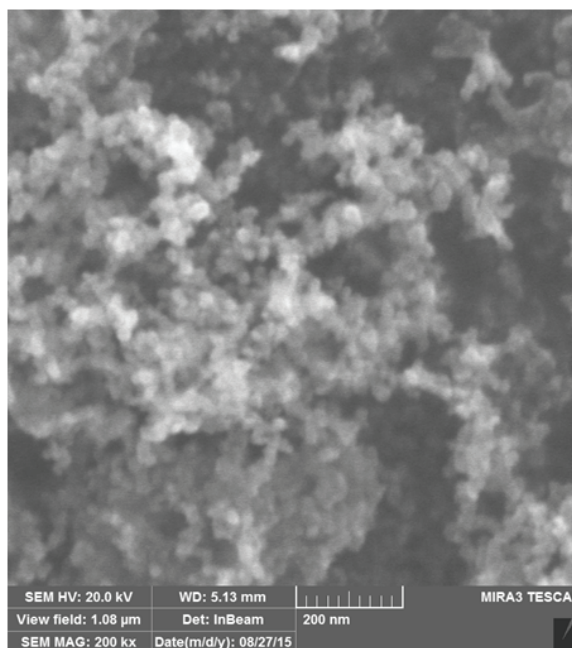


Fig. 2. SEM electron micrograph of Fe_3O_4 MNPs

Magnetic nanoparticles we covered with oxides using sol-gel synthesis method. MNPs were covered with metal oxides in the following compositions: $\text{Fe}_3\text{O}_4/\text{SiO}_2$; $\text{Fe}_3\text{O}_4/\text{SiO}_2/\text{Nb}_2\text{O}_5$; $\text{Fe}_3\text{O}_4/\text{SiO}_2/\text{Ta}_2\text{O}_5$; $\text{Fe}_3\text{O}_4/\text{SiO}_2/\text{V}_2\text{O}_5$. All reagents and materials are commercially available in Sigma Aldrich: tantalum (V) chloride, niobium (V) chloride, vanadium (V) oxide, isoamyl alcohol, thionyl chloride and ethanol.

The structure of the materials was analyzed by scanning electron microscopy (SEM, Leo DSM 982 Gemini and JEOL JSM_7500F microscopes). The

phase composition of the materials was studied by X-ray photoelectron spectroscopy (XPS) on a Thermo Scientific K-alpha spectrometer (USA) with monochrome radiation source (Al K α). Ion etching of samples was carried out until the element content became constant as a function of the etching depth.

The biological material obtaining and DNA isolation process was carried out in the Immanuel Kant Baltic Federal University.

Real-time polymerase chain reaction (RT-PCR) was carried out using PCR CFX96 Real-Time PCR Detection System («Bio-Rad», USA). PCR tube contained 20 μ l reaction mixture: DNA-polymerase buffer Taq («Evrogen», Russia) – 1x, 2,5 mM MgCl₂ («Syntol», Russia, 0,25 mM of each dNTPs («Syntol», Russia, Taq-polymerase («Syntol», Russia) – 1x, the neurotrophin receptor gene primer - TrkB - 0,5 μ M. The amplification reaction was started with the following conditions: 95 °C for 3 min (once), 95 °C for 10 s, 63 °C for 40 s, (50 cycles).

Results and discussion

Preparation of metal oxides (V) thin film on the surface of MNPs precursors

At the first step the nanoparticles were covered by silicon dioxide thin films by sol-gel synthesis method by using the well-known process described in [21]. We mixed 15 mg of MNPs, 500 μ l ethanol, 500 μ l deionized and deoxygenated water, 50 μ l ammonium solution (25% wt) and 3 μ l tetraethoxysilane. Mixture was shaken on vortex and sonicated for 0,5 h. The tube with MNPs was placed in the magnetic rack/ After the separation particles, liquid was removed by pipetting.

Silicon dioxide thin film on the surface of MNPs was used as a substrate for formation of metal oxide (V) thin-films. For the synthesis of thin layers of metal oxides on the silica surface of MNPs corresponding etoxides (Nb(C₂H₅O)₅; Ta(C₂H₅O)₅) were used as precursors for Ta and Nb oxides coating and vanadium oxychloride (VOCl₃) was used for vanadium ones. Precursors were synthesized in laboratory using reaction between metal chlorides and absolute ethanol [22–24], excess of HCl was removed by reaction with gaseous ammonium.

For the synthesis 15 mg MNPs (Fe/SiO₂) - coated by SiO₂ (described above), was added 0.7 ml deionized water, 0,05 ml 25% ammonia solution for HCl

neutralizing (which released during VOCl₃ hydrolysis process) and 0.01 ml ethylenglycol (is a complexing agent). In the resulting solution dropwise 0.03 ml 10% solution corresponding precursor – (Nb(C₂H₅O)₅; Ta(C₂H₅O)₅ – wherein the metal oxides are sol. The mixture was stirred for 10 min and placed on an ultrasonic bath under room temperature for 10 min - 3 times. The tube with MNPs was placed in the magnetic rack, after the separation particles, liquid was removed by pipetting. Then MNPs were washed three times with 1 ml deionized water under magnetic separation process.

As the results four type of coating had been synthesized on the surface of MNPs: 1) Fe/SiO₂; 2) Fe/SiO₂/Ta₂O₅; 3) Fe/SiO₂/Nb₂O₅; 4) Fe/SiO₂/V₂O₅. These particles were used in further experiments.

Particles characterization

Chemical composition of MNP's surface with different coatings was studied by X-ray photoelectron spectroscopy (XPS) The X-ray beam size was 400 microns. Overview spectra were obtained with electron transmission energy 200 eV with step 1,0 eV, the number of scans was 15. High-resolution spectra (Si, Nb, Ta, V, O) were obtained with electron transmission energy 50 eV with step 1,0 eV, the number of scans 7. Cleaning of the samples after air contamination was carried out by Ar⁺ ion etching under at 200 eV for 30 sec. XPS spectra before and after ion etching are shown in fig. 3. The ion beam with 20 mm diameter had a uniform radial distribution of ion current.

SEM electron micrographs of MNPs coated by silica and niobium oxide are shown in fig. 4.

SEM electron micrographs confirmed the fact that coated MNPs do not form agglomerates in fluids. The average MNP size is 25 nm, MNPs shape is close to spherical.

Testing MNP's for DNA isolation

The sorption efficiency of metal oxides (V) was analysed by conducting real-time polymerase chain reaction. For this purpose we isolated DNA using standard protocol based on magnetic particles DNA isolation method, described in [10]. In order to determine the optimal conditions for DNA binding by metal oxides (V) we have changed some parameters of standard protocol.

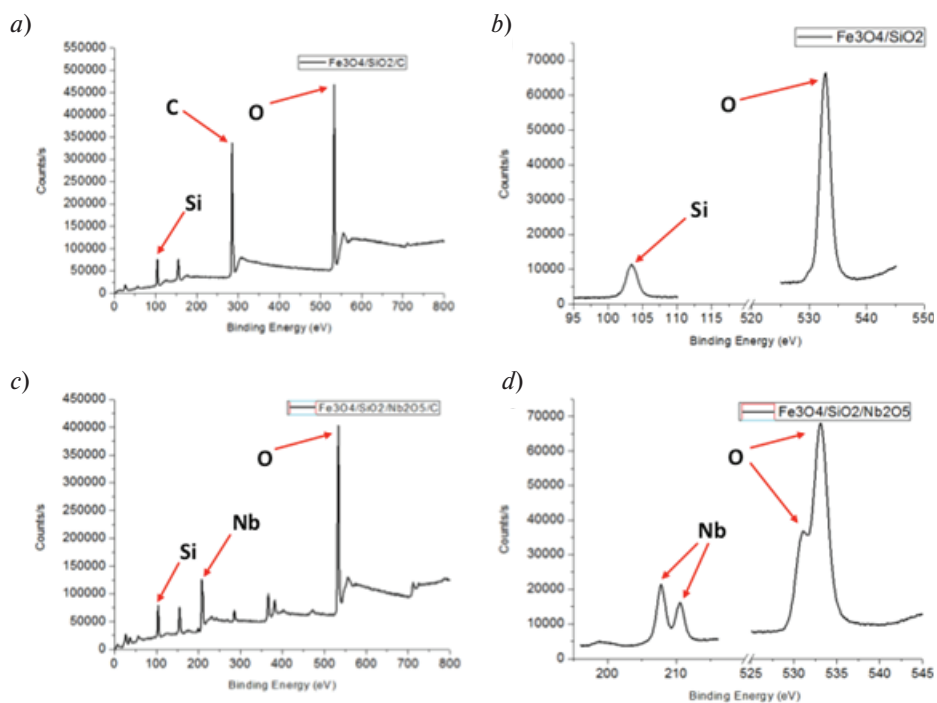


Fig. 3. XPS spectra of $\text{Fe}_3\text{O}_4/\text{SiO}_2$ and $\text{Fe}_3\text{O}_4/\text{SiO}_2/\text{Nb}_2\text{O}_5$ before (a, c) and after (b, d) etching

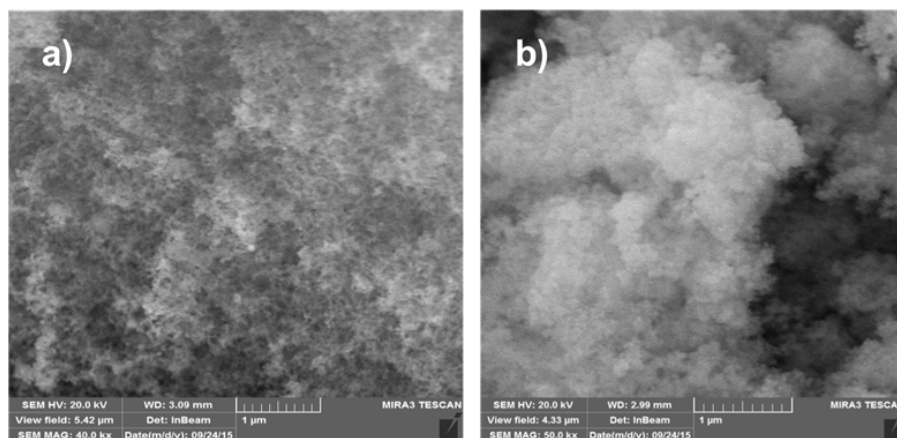


Fig. 4. SEM electron micrographs of: a) MNPs coated SiO_2 , b) MNPs coated $\text{SiO}_2/\text{Nb}_2\text{O}_5$.

DNA isolation was carried out with standard protocol, described previously, with metal oxides (V) and commercially available sorbents (“Syntol”, Russia). The resulting amplification curves are shown in fig. 5.

Basing on the values of average DNA threshold cycles (fig. 5) we can conclude that MNPs covered by niobium oxide (V) thin films have the highest sorption properties.

The worst result was shown by commercial MNPs produced by «Syntol» (Russia). The average difference in threshold cycles between the MNPs covered by metal oxides (V) and MNPs covered by silicon dioxide («Syntol») was about 3 cycles.

This phenomenon can be explained by the difference in amount of formed chemical bonds available for DNA binding and it turn to decreased the quantity of extracted DNA.

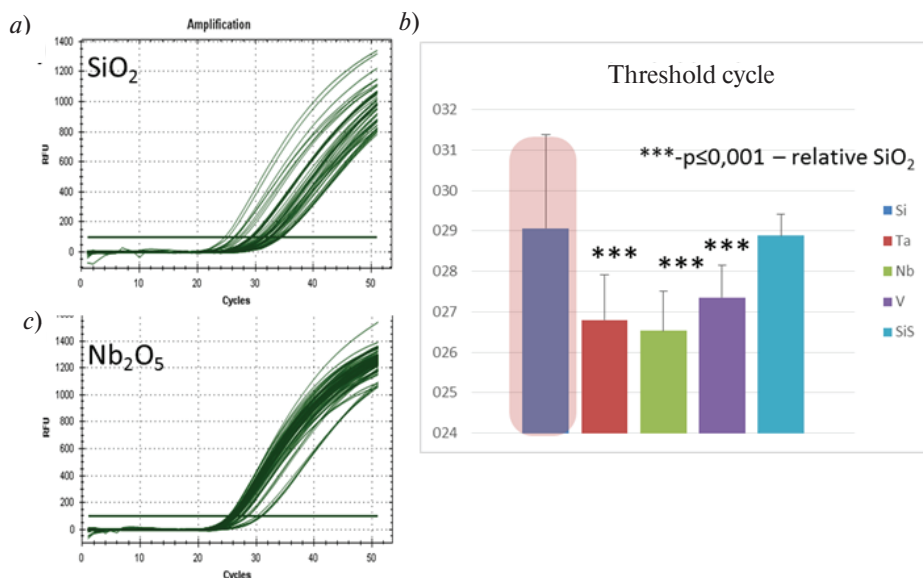


Fig. 5. The amplification curves obtained during the real-time PCR for isolated DNA using the standard protocol with SiO₂ and Nb₂O₅ as sorption materials (a) and (c) respectively and average DNA threshold cycles with silicon dioxide; tantalum oxide (V); niobium oxide (V); vanadium oxide (V); silicon dioxide («Syntol») as sorption materials

Conclusions

The metal oxides (V) have ability to form additional chemical bonds, which increase sorption capacity of MNPs covered by the metal oxides (V) thin film for DNA binding. However, the total usable area of surface is a dominant factor for achieving high sensitivity and efficiency of DNA extraction using MNPs. This fact was confirmed by the example of MNPs obtained by aerosol synthesis with silica compound as a sorbent, obtained by sol-gel method and commercial magnetic particles “Syntol”. Furthermore, obtained results suggest that the developed

thin film materials based on metal oxides (V) are suitable for the DNA extraction in clinical or research laboratories. Described above investigation results are relevant for future developments of micro- and nanodiagnostic systems, which might be realized “on-chip”, since the thin film materials are shown prospective for DNA isolation.

Acknowledgments

The authors are grateful for financial support from Russian Science Foundation: Grant № 15-12-10038.

REFERENCES

1. Takenaka S. [et al.] DNA sensing on a DNA probe-modified electrode using ferrocenylnaphthalene diimide as the electrochemically active ligand. *Analytical chemistry*. 2000. Vol. 72. № 6. P. 1334–1341.
2. Azek F., Grossiord C., Joannes M. [et al.] Hybridization assay at a disposable electrochemical biosensor for the attomole detection of amplified human cytomegalovirus DNA. *Analytical biochemistry*. 2000. Vol. 284. P. 107–113.
3. Drummond T.G., Hill M.G., and Barton J.K. Electrochemical DNA Sensors. *Nature Biotechnology*. 2003. Vol. 21. P. 1192–1199.
4. Willard M.A., Kurihara L.K., Carpenter E.E., Calvin S., Harris V. G. In *Encyclopedia of Nanoscience and Nanotechnology*. Vol. 1 / Ed. H.S. Nalwa. American Scientific Publishers, Stevenson Ranch, CA. 2004. 815 p.
5. *Nanoscience and Nanotechnology*, Stevenson Ranch, CA. American Scientific Publishers, 2004. 815 p.
6. McBain S.C., Yiu H.P., Dobson J. Magnetic nanoparticles for gene and drug delivery. *International journal of nanomedicine*. 2008. Vol. 3. № 2. P. 169–180.
7. Davies M.J., Taylor J.I., Sachsinger N., Bruce I.J. Isolation of plasmid DNA using magnetite as a solid-phase adsorbent. *Analytical biochemistry*. 1998. Vol. 262. P. 92–94.
8. United States patent US №6855499 B1. Magnetic isolation and purification of nucleic acids / R.D. Nargessi. Priority 16 February 2001.
9. Berensmeier S. Magnetic particles for the separation and purification of nucleic acids. *Applied Microbiology and Biotechnology*. 2006. Vol. 73. №. 3. P. 495–504.

10. **Vogelstein B., Gillespie D.** Preparative and analytical purification of DNA from agarose. *Proceedings of the National Academy of Sciences*. 1979. Vol. 76. № 2. P. 615–619.
11. **Boom R., Sol C.J., Salimans M.M., Jansen C.L., Wertheim-van Dillen P.M., van der Noordaa J.** Rapid and simple method for purification of nucleic acids. *Journal of clinical microbiology*. 1990. Vol. 28. № 3. P. 495–503.
12. **Boom R., Sol C., Beld M., Weel J., Goudsmit J., Wertheim-van Dillen P.** Improved silica-guanidinium thiocyanate DNA isolation procedure based on selective binding of bovine alpha-casein to silica particles. *Journal of clinical microbiology*. 1999. Vol. 37. № 3. P. 615–619.
13. **Tian H., Hühmer A. F. R., Landers J. P.** Evaluation of silica resins for direct and efficient extraction of DNA from complex biological matrices in a miniaturized format. *Analytical biochemistry*. 2000. Vol. 283. № 2. P. 175–191.
14. **Breadmore M. C. et al.** Microchip-based purification of DNA from biological samples. *Analytical chemistry*. 2003. Vol. 75. № 8. P. 1880–1886.
15. **Esser K. H., Marx W. H., Lisowsky T.** MaxXbond: first regeneration system for DNA binding silica matrices. *Nature Methods*. 2006. № 3. P. 1–2.
16. **Gribanov O. G. [et al.]** A simple method for RNA isolation and purification. *Bioorganicheskaja khimiia*. 1997. Vol. 23. № 9. S. 763–765.
17. **Parida S. K. [et al.]** Adsorption of organic molecules on silica surface. *Advances in colloid and interface science*. 2006. Vol. 121. № 1. P. 77–110.
18. **Bogdanov E., Dominova I., Shusharina N., Botman S., Kasymov V. [et al.]** Silicon Dioxide Thin Film Mediated Single Cell. *Nucleic Acid Isolation. PLoS ONE*. 2013. Vol. 8. № 7. P. e68280.
19. **Scheffe J. H., Lehmann K. E., Buschmann I. R., Unger T., Funke-Kaiser H.** Quantitative real-time RT-PCR data analysis: current concepts and the novel “gene expression’s CT difference” formula. *Journal of Molecular Medicine*. 2006. Vol. 84. № 11. P. 901–910.
20. **Choi C.J., Kim B.K., Tolochko O. [et al.]** Preparation and characterization of magnetic Fe, Fe/C and Fe/N nanoparticles synthesized by chemical vapor condensation process. *Reviews on Advanced Materials Science*. 2003. Vol. 5. № 5. P. 487–492.
21. **Tolochko O.V., Arif M., Lee D.W., Choi C.J., Kim D.** Structure and magnetic properties of iron based nanoparticles with oxide shells. *Technical Physics Letters*. 2005. Vol. 31. № 9. P. 779–781.
22. **Wang J. [et al.]** Synthesis of Fe₃O₄, SiO₂, ZnO–Ag core–shell microspheres for the repeated photocatalytic degradation of rhodamine B under UV irradiation. *Journal of Molecular Catalysis A: Chemical*. 2015. Vol. 406. P. 97–105.
23. **Epifani M. [et al.]** Soft chemistry routes to transparent metal oxide thin films. The case of sol–gel synthesis and structural characterization of Ta₂O₅ thin films from tantalum chloromethoxide. *Thin Solid Films*. 2014. Vol. 555. P. 39–41.
24. **Wolf M. J. [et al.]** Fabrication of ultrathin films of Ta₂O₅ by a sol–gel method. *Thin solid films*. 2013. Vol. 527. P. 354–357.
25. **Tyree S.** Inorganic Syntheses. Volume IX. McGraw-Hill, New-York, 1967. 80 p.

СПИСОК ЛИТЕРАТУРЫ

1. **Takenaka S. [et al.]** DNA sensing on a DNA probe-modified electrode using ferrocenylnaphthalene diimide as the electrochemically active ligand // *Analytical chemistry*. 2000. Vol. 72. № 6. P. 1334–1341.
2. **Azek F., Grossiord C., Joannes M. [et al.]** Hybridization assay at a disposable electrochemical biosensor for the attomole detection of amplified human cytomegalovirus DNA // *Analytical biochemistry*. 2000. Vol. 284. P. 107–113.
3. **Drummond T.G., Hill M.G., Barton J.K.** Electrochemical DNA Sensors // *Nature Biotechnology*. 2003. Vol. 21. P. 1192–1199.
4. **Willard M. A., Kurihara L. K., Carpenter E. E., Calvin S., Harris V. G.** In *Encyclopedia of Nanoscience and Nanotechnology*. Vol. 1 / Ed. H.S. Nalwa. American Scientific Publishers, Stevenson Ranch, CA. 2004. 815 p.
5. *Nanoscience and Nanotechnology*, Stevenson Ranch. CA: American Scientific Publishers, 2004. 815 p.
6. **McBain S.C., Yiu H.P., Dobson J.** Magnetic nanoparticles for gene and drug delivery // *International journal of nanomedicine*. 2008. Vol. 3. № 2. P. 169–180.
7. **Davies M.J., Taylor J.I., Sachsinger N., Bruce I.J.** Isolation of plasmid DNA using magnetite as a solid-phase adsorbent // *Analytical biochemistry*. 1998. Vol. 262. P. 92–94.
8. **United States patent US №6855499 B1.** Magnetic isolation and purification of nucleic acids // R.D. Nargessi. Priority 16 February 2001.
9. **Berensmeier S.** Magnetic particles for the separation and purification of nucleic acids // *Applied Microbiology and Biotechnology*. 2006. Vol. 73. 2001.
10. **Vogelstein B., Gillespie D.** Preparative and analytical purification of DNA from agarose // *Proceedings of the National Academy of Sciences*. 1979. Vol. 76. № 2. P. 615–619.
11. **Boom R., Sol C.J., Salimans M.M., Jansen C.L., Wertheim-van Dillen P.M., van der Noordaa J.** Rapid and simple method for purification of nucleic acids // *Journal of clinical microbiology*. 1990. Vol. 28. № 3. P. 495–503.
12. **Boom R., Sol C., Beld M., Weel J., Goudsmit J., Wertheim-van Dillen P.** Improved silica-guanidinium thiocyanate DNA isolation procedure based on selective binding of bovine alpha-casein to silica particles //

Journal of clinical microbiology. 1999. Vol. 37. № 3. P. 615–619.

13. **Tian H., Hühmer A. F. R., Landers J. P.** Evaluation of silica resins for direct and efficient extraction of DNA from complex biological matrices in a miniaturized format // *Analytical biochemistry*. 2000. Vol. 283. № 2. P. 175–191.

14. **Breadmore M.C. [et al.]** Microchip-based purification of DNA from biological samples // *Analytical chemistry*. 2003. Vol. 75. № 8. P. 1880–1886.

15. **Esser K. H., Marx W. H., Lisowsky T.** MaxxBond: first regeneration system for DNA binding silica matrices // *Nature Methods*. 2006. № 3. P. 1–2.

16. **Gribanov O.G. [et al.]** A simple method for RNA isolation and purification // *Bioorganicheskaya khimiya*. 1997. Vol. 23. № 9. P. 763–765.

17. **Parida S. K. [et al.]** Adsorption of organic molecules on silica surface // *Advances in colloid and interface science*. 2006. Vol. 121. № 1. P. 77–110.

18. **Bogdanov E., Dominova I., Shusharina N., Botman S., Kasymov V. [et al.]** Silicon Dioxide Thin Film Mediated Single Cell. Nucleic Acid Isolation // *PLoS ONE*. 2013. Vol. 8. № 7. P. e68280.

19. **Scheffe J.H., Lehmann K.E., Buschmann I.R., Unger T., Funke-Kaiser H.** Quantitative real-time RT-PCR data analysis: current concepts and the novel

“gene expression’s CT difference” formula // *Journal of Molecular Medicine*. 2006. Vol. 84. № 11. P. 901–910.

20. **Choi C.J., Kim B.K., Tolochko O. et al.** Preparation and characterization of magnetic Fe, Fe/C and Fe/N nanoparticles synthesized by chemical vapor condensation process // *Reviews on Advanced Materials Science*. 2003. Vol. 5. № 5. P. 487–492.

21. **Tolochko O.V., Arif M., Lee D.W., Choi C.J., Kim D.** Structure and magnetic properties of iron based nanoparticles with oxide shells // *Technical Physics Letters*. 2005. Vol. 31. № 9. P. 779–781.

22. **Wang J. [et al.]** Synthesis of Fe₃O₄, SiO₂, ZnO–Ag core–shell microspheres for the repeated photocatalytic degradation of rhodamine B under UV irradiation. *Journal of Molecular Catalysis A: Chemical*. 2015. Vol. 406. P. 97–105.

23. **Epifani M. [et al.]** Soft chemistry routes to transparent metal oxide thin films. The case of sol-gel synthesis and structural characterization of Ta₂O₅ thin films from tantalum chloromethoxide // *Thin Solid Films*. 2014. Vol. 555. P. 39–41.

24. **Wolf M.J. [et al.]** Fabrication of ultrathin films of Ta₂O₅ by a sol–gel method // *Thin solid films*. 2013. Vol. 527. P. 354–357.

25. **Tyree S.** *Inorganic Syntheses. Volume IX.* McGraw-Hill, New-York, 1967. 80 p.

СВЕДЕНИЯ ОБ АВТОРАХ/AUTHORS

BOGDANOV Evgenii A. – Immanuel Kant Baltic Federal University.
14 A. Nevskogo ul., Kaliningrad, 236041.
E-mail: eubogdanov@gmail.com

БОГДАНОВ Евгений Анатольевич – научный сотрудник Балтийского федерального университета имени Иммануила Канта.
236016, г. Калининград, ул. А.Невского, д. 14.
E-mail: eubogdanov@gmail.com

CHUPAKHIN Evgenii G. – Immanuel Kant Baltic Federal University.
14 A. Nevskogo ul., Kaliningrad, 236041.
E-mail: chupakhinevgen@gmail.com

ЧУПАХИН Евгений Геннадьевич – аспирант Балтийского федерального университета имени Иммануила Канта.
236016, г. Калининград, ул. А. Невского, д. 14.
E-mail: chupakhinevgen@gmail.com

SOTNIKOV Egor B. – Immanuel Kant Baltic Federal University.
14 A. Nevskogo ul., Kaliningrad, 236041.
E-mail: sotnikovregor94@gmail.com

СОТНИКОВ Егор Борисович – аспирант Балтийского федерального университета имени Иммануила Канта.
236016, г. Калининград, ул. А. Невского, д. 14.
E-mail: sotnikovregor94@gmail.com

VASILYEVA Ekaterina S. – Skolkovo Institute of Science and Technology.
Skolkovo Innovation Center, Building 3 Moscow 143026 Russia.
E-mail: katrinfr@inbox.ru

ВАСИЛЬЕВА Екатерина Сергеевна – кандидат технических наук, Facilitator CREI Photonics and Photo electronics, Сколковский институт науки и технологий.
улица Нобеля, д. 3 Москва 143026 Россия.
E-mail: katrinfr@inbox.ru

BULANOV Sergei S. – Immanuel Kant Baltic Federal University.
14 A. Nevskogo ul., Kaliningrad, 236041..
E-mail: sbulanovs@gmail.com

БУЛАНОВ Сергей Сергеевич – менеджер Балтийского федерального университета имени Иммануила Канта.
236016, г. Калининград, ул. А. Невского, д. 14.
E-mail: sbulanovs@gmail.com

PATRUSHEV Maksim V. – Immanuel Kant Baltic Federal University.
14 A. Nevskogo ul., Kaliningrad, 236041..
E-mail: maxpatrushev@gmail.com

ПАТРУШЕВ Максим Владимирович – кандидат биологических наук директор Балтийского федерального университета имени Иммануила Канта.
236016, г. Калининград, ул. А. Невского, д. 14.
E-mail: maxpatrushev@gmail.com

SHUSHARINA Nataliia N. – Immanuel Kant Baltic Federal University.
14 A. Nevskogo ul., Kaliningrad, 236041..
E-mail: nnshusharina@gmail.com

ШУШАРИНА Наталья Николаевна – кандидат педагогических наук заместитель директора Балтийского федерального университета имени Иммануила Канта.
236016, г. Калининград, ул. А. Невского, д. 14.
E-mail: nnshusharina@gmail.com

GOIKHMAN Aleksandr Y. – Immanuel Kant Baltic Federal University.
14 A. Nevskogo ul., Kaliningrad, 236041..
E-mail: aygoikhman@gmail.com

ГОЙХМАН Александр Юрьевич – кандидат физико-математических наук директор НОЦ «Функциональные наноматериалы» Балтийского федерального университета имени Иммануила Канта.
236016, г. Калининград, ул. А. Невского, 14.
E-mail: aygoikhman@gmail.com

CONTROL OF FRICTION PROPERTIES IN POLYAMIDE COATINGS IN TENSION JOINTS

A.B. Кущенко, А.Я. Башкарев

КОНТРОЛЬ СВОЙСТВ ТРЕНИЯ В ПОЛИАМИДНЫХ ПОКРЫТИЯХ НАПРЯЖЕННЫХ СОЕДИНЕНИЙ

Tension joints are used to transfer twisting moments and axial loads due to friction forces, which occur on contacting surfaces as a result of their elastic deformation created by tension in assembly. During operation, joints made of steel elements deteriorate due to fretting corrosion caused by alternating loads, common for many types of machines and equipment. One of the ways to fight this condition is to apply thin-layer polymer coatings. The paper presents the results of research in adhesion strength and the static coefficient of friction of a thin-layer polyamide coating and polyamide-based composites on steel. It is revealed that the best friction and adhesion properties are demonstrated by a polyamide composite with 20–40% of mass fraction of red iron oxide. Its static coefficient of friction on steel is comparable to the static coefficient of friction of steel on steel while adhesion to a steel surface on failure is 40% higher than that of a pure polyamide coating.

TENSION JOINTS; POLYAMIDE COATINGS; ADHESION; STATIC COEFFICIENT OF FRICTION; FRETTING CORROSION.

Напряженные соединения используются, чтобы передать крутящий момент и осевую нагрузку благодаря силам трения, которые возникают при контакте с поверхностями в результате их упругой деформации, созданной комплексными напряжениями. При эксплуатации соединения, изготовленные из стальных элементов, ухудшаются из-за фреттинг коррозии, вызванной переменной нагрузкой, характерной для многих типов машин и оборудования. Один из способов борьбы с этим явлением – применение тонкослойных полимерных покрытий. Статья представляет результаты исследований адгезионной прочности и статического коэффициента трения тонкослойного полиамидного покрытия и композитов на основе полиамида на стальных соединениях. Выявлено, что лучшие свойства трения и адгезии имеет полиамидный композит с 20–40 % масс фракции красной окиси железа. Его статический коэффициент трения по стали сопоставим со статическим коэффициентом трения стали по стали, в то время как адгезия к стальной поверхности на 40 % больше, чем у чисто полиамидного покрытия.

НАПРЯЖЕННЫЕ СОЕДИНЕНИЯ; ПОЛИАМИДНЫЕ ПОКРЫТИЯ; АДГЕЗИЯ; СТАТИЧЕСКИЙ КОЭФФИЦИЕНТ ТРЕНИЯ; ФРЕТТИНГ КОРРОЗИЯ.

Introduction

It is common knowledge that tension joints are used to transfer twisting moments and axial forces without accessory mountings. Immobility of parts in relation to each other is ensured with friction forces

that appear on contact surfaces due to their elastic deformation created by tension in the assembled joint.

Demountable tension joints are simple and easy to make and their expected service life is long. But it is known [1–3] that deterioration of such joints made

of steel parts can occur earlier than the service life has expired due to fretting corrosion which develops because of alternating loads, common for a lot of machinery. One of the effective methods both to protect tension joints from fretting corrosion and to repair damaged ones may be to use polymer materials, in particular, polyamides.

It was believed earlier that if polymers are used in tension joints, tension may disappear due to relaxation phenomena. However, for some polymers, for example, polyamides, which belong to the group of elastomers, the Poisson's ratio is practically equal to 0,5, i.e. in terms of the classical theory of elasticity they are practically an incompressible material. In reality they easily deform due to plastic deformations that occur without change of volume. If deformation occurs while there is no capability for the material to move, i.e. no plastic shears are possible, then deformation of polyamides can only happen thanks to change in intermolecular distances, which requires considerable forces comparable to deformation forces of metallic supra-molecular structures. Herein, such deformation can be considered almost ideally elastic.

Accordingly, thin-layer polyamide coatings or polyamide-based composite coatings can be applied both to protect new tension joints from fretting-corrosion and to repair damaged ones. So, the target of the research is the new design of tension joints with application of thin-layer coatings made of polyamide or polyamide-based composites (fig. 1) to increase durability and reparability of machine parts.

The objective of this paper is to conduct an experimental study of friction characteristics of thin-layer (0.1 – 0.5 mm) polymer coatings made of different types of polyamides and to search for ways to increase their static coefficient of friction on steel.

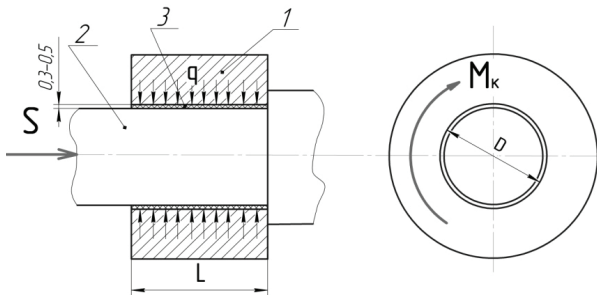


Fig. 1. Application scheme of a polyamide coating for tension joints: 1 – bush; 2 – shaft; 3 – thin-layer polyamide coating of the shaft; S – axial load; M_k – external twisting moment; q – radial pressure in the contact area; D – nominal bore diameter; L – length of the articulation

Methods and Materials

It is known [4–6] that polyamides are widely used in friction units of machines as antifriction materials, since their coefficient of sliding friction is rather low and their operating capabilities are quite high [7, 8]. However, so far there has been no experience in applying thin-layer polyamide coatings in tension joints, and traditional methods for increasing friction characteristics by adding metal chips, asbestos etc. [6] in polyamide cannot be used in this case due to technological specifics of thin-layer coatings application.

In order to assess friction properties of thin-layer polyamide coatings, their static coefficient of friction on steel was measured depending on the pressure in the friction area. The range of 0,065–0,53 mm thick coatings made of PA-6, PA-6/66, PA-68 polyamides were used in the experiments.

The value of the static coefficient of friction was measured on a “IR 5047-50-11” test machine. Samples with polyamide coating had been made. Force was exerted through steel plates, which allowed creating pressure in the friction area up to 30 MPa. The samples with the loader were fixed in the transverse beam of the test machine and were affected by a growing load, to the extent when the steel plates got to slide on the polymer coating. A computer recorded the loading diagram.

Experiment Results

According to the results of the experiments, the static coefficient of friction of the polyamide coating on steel is not constant. It decreases as the pressure is growing and, at the same time, it is 30–40 % lower than the coefficient for the pair “steel-steel” (fig. 2).

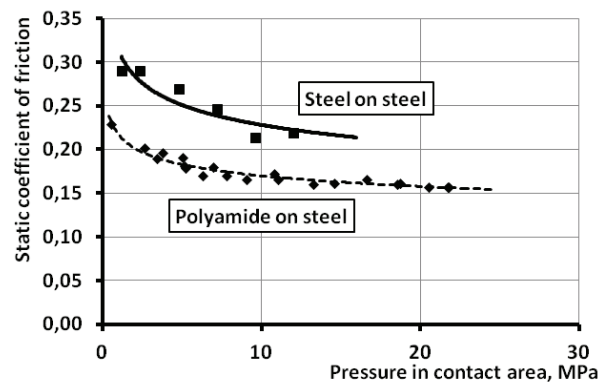


Fig. 2. Static coefficients of friction of polyamide on steel and steel on steel

The experiments have also revealed that the static coefficient of friction of polyamide on steel depends not only on the pressure in the friction area, but also on how thick the polyamide layer is. In case the thickness of the layer is decreased from 0,12 down to 0,065 mm in the whole range of pressures from 1 to 30 MPa, it is observed that the static coefficient of friction grows (for example, from 0,17 up to 0,25 at the pressure of 1 MPa in the friction area and from 0,08 up to 0,14 at 30 MPa). In case the coating is more than 0,12 mm thick, the static coefficient of friction of polyamide on steel is constant (fig. 3).

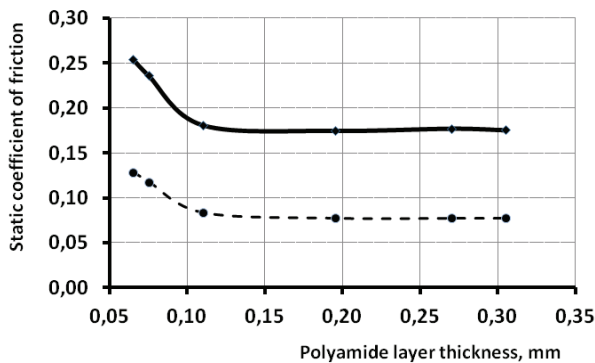


Fig. 3. Change in the value of the static coefficient of friction of polyamide on steel depending on the thickness of the layer. (The solid line is at the pressure of 1 MPa in the friction area, the dashed line is at 30 MPa)

A lower static coefficient of friction of polyamide on steel than that of the pair “steel-steel” gives evidence that when thin-layer polymer coatings are used in tension joints, a method must be found to increase the static coefficient of friction of polymer on steel with the use of different additives, i.e. by creating composite mixtures.

The use of polyamide coatings and polyamide-based composites in tension joints can be limited due to insufficient adhesion of the polyamide layer to the steel substrate. So, measurements of the value of adhesion were made, i.e. measurements of the ultimate strength of the coating adhesion to steel by simple stresses. There are a lot of papers dedicated to adhesion of polymers to steel [11, 12, 15–17]. However, these studies have been made for polymer slide bearings rather than coatings in tension joints.

Adhesion has been researched by a well-known method of breaking a steel pin from the deposited polymer compound [8]. The loading diagram and general view of the test samples are given in figure 4. The samples represent pivot 1, which finishes in a 3 mm pin. Disc 2 is planted on the pin with a sliding attachment. The surface of the disc and the end of the pin coincide. Polymer or polymer-based composite is applied on the surface of the disc. In order to lower friction between the pin and the hole of the disc, the pin is covered with graphite lubrication.

The value of breaking stress of the end of the pin from polymer was measured on a “IR 5047-50-11” test machine. For this, the disc of the sample was fixed in the clench of the machine transverse beam and the pivot of the sample was exerted with a growing force to the extent when the pin broke off polymer. At the same time a computer recorded the loading diagram.

As applied to the operation conditions of polyamide coatings in tension joints, adhesion properties to steel of pure polyamide and polyamide-based compositions with lead oxide, red iron oxide and powdered glass were studied.

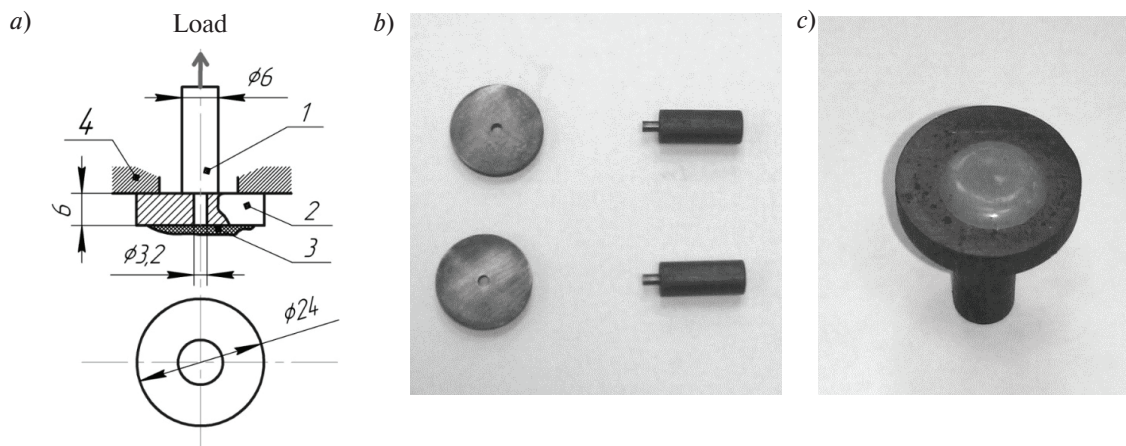


Fig. 4. The loading diagram and general view of the samples for defining the adhesion value: 1 – pivot; 2 – disc; 3 – polymer coating; 4 – block stop

According to the results of the experiment (fig. 5): the value of adhesion on failure for a pure polyamide coating is about 35 MPa;

with the values of mass content of lead oxide up to 20%, the value of adhesion of this composite to steel practically does not change and can be defined as 35 MPa and goes down dramatically if the content is larger;

with the values of mass content of powdered glass up to 15%, the value of adhesion of this composite to steel grows by approximately 20% (up to 40 MPa) and goes down if the content is larger;

with the values of mass content of red iron oxide up to 30%, the value of adhesion of this composite to steel grows by approximately 60% (up to 50 MPa) and goes down if the content is larger.

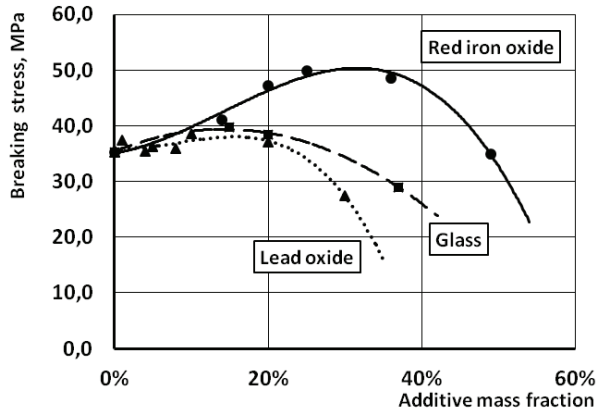


Fig. 5. Change of adhesive characteristics of polyamide-based composites depending on the type and mass fraction of additives

The measured static coefficient of friction of the polyamide-based composite which contained 20% of red iron oxide showed that its values coincided with the corresponding ones for the pair “steel-steel” (fig. 6).

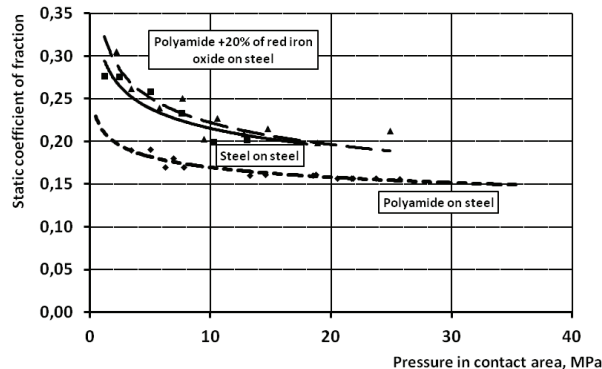


Fig. 6. Change of the static coefficient of friction of polyamide based composite with 20% of red iron oxide on steel because of pressure in the contact area

Discussion of the results

According to the molecular-mechanical theory of friction [14], friction force forms due to:

resistance to motion of one body towards another due to interatomic and intermolecular interactions in the actual contact areas of the bodies, i.e. adhesion forces;

when solid bodies come in contact due to their varying stiffness or their inhomogeneous properties in different areas and due to varying stiffness of individual micro-irregularities, stiffer elements penetrate less stiff sections. As relative motion begins, more solid sections deform the surface of one of the bodies. Resistance forces, which occur at that time, can be called deformation components of friction.

According to this theory, the coefficient of sliding friction f_f can be presented as:

$$f_f = f_0 \left(1 + \frac{S_a p_0}{N} \right), \quad (1)$$

where p_0 is the specific force of molecular attraction, S_a – area of actual contact, N – load, f_0 – the value of the coefficient of sliding friction as $p_0 = 0$.

Thus, when the load grows, the contact area remains constant and the pressure in the friction area grows, the coefficient of friction must decrease. The intensity of this decrease depends on mechanical and adhesive properties of the materials, which also affect the intensity with which the surface area of actual contact is changing due to a growing load.

The obtained results are confirmed with the data from literature sources, according to which the coefficient of sliding friction of polyamide goes down if pressure grows in the friction area. For instance, [6] for PA-68 polyamide the coefficient of sliding friction changes from 0,15 at the pressure of 2,5 MPa to 0,07 at 9,0 MPa, while for polycaprolactam it varies from 0,25 to 0,15.

The results of the experiments confirm the assumption [9, 10] that in case thin-layer coatings are applied on steel substrate, strong compression strains (up to 400 MPa) develop in 0,1 mm thick polyamide layer which directly adjoins the steel surface. This happens due to coordination bonds between iron ions, which are part of red iron oxide and steel substrate, and nitrogen atoms in polyamide hotmelt. As a result, surface hardness grows dramatically and so does the mechanical component in friction forces and, consequently, adhesion increases. There are no iron ions in lead oxide or powdered glass.

Conclusions

1. The values have been determined experimentally for the static coefficient of friction and adhesion strength on failure of thin-layer polyamide and some polyamide-based composite coatings on steel surfaces.

2. It has been identified that the static coefficient of friction for the pair “polyamide – steel” is 40% lower than that for the pair “steel – steel”.

3. It has been revealed how the effect of polyamide coating layer thickness impacts the static coefficient of friction on steel. With coating thickness more

than 0,12 mm, the static coefficient of friction of polyamide on steel does not change.

4. In case additives such as red iron oxide are added to polyamide, a composite forms, whose adhesion to steel is bigger than that of pure polyamide, up to 50% of red iron oxide mass fraction. Adhesion reaches maximum values of 50 MPa with red iron oxide content of 30% in mass fraction.

5. In tension joints it is reasonable to use thin-layer coatings consisting of a polyamide-based composite with 20–40 % of red iron oxide mass fraction, rather than pure polyamide.

REFERENCES

1. **Alisin V.V. [et al.]**. Friction, Wear and Lubrication / Edited by Kragelsky I.V., Alisin V.V. Moscow: Mechanical Engineering, 1978. 400 s. (rus.)
2. **Grechishev E.S., Ilyashenko A.A.** Tension Joints. Calculations, Design, Manufacturing, Moscow. Mechanical Engineering, 1981. – 247 s. (rus.)
3. **Kaisa A.M. Joda** Increasing Durability and Maintainability of Construction Machines Parts with Polymer Materials: PhD thesis. / Leningrad, LPI, 1984.
4. **Bilik M.M., Slyudikova N.N.** Antifriction Properties of Some Polymer Materials in Monolith and Thin-Layer Coating. *Polymers in Manufacturing Industry*. Homel', 1968. P. 26–32.
5. **Stukach A.V.** Research in Efficiency of Friction Units with Polymer Coatings in Caterpillar Tread of Construction Machines: PhD thesis / Leningrad, LPI, 1980. 125 s. (rus.)
6. **Chichinadze A.V. [et al.]** Polymers in Friction Units of Machines and Devices: Reference book / Edited by A.V. Chichinadze. Moscow: Mechanical Engineering, 1988. 328 s. (rus.)
7. **Mitrovich V.P.** Research In Friction of Polyamides on Steel. Moscow, 1963. 96 s. (rus.)
8. **Stukach A.V.** Research and Control over the Properties of Polymer Coatings in Their Formation When Worn Surfaces Are Repaired and Given Antifriction Properties. *Scientific and technical journal of St. Petersburg State University of Service and Economics “Engineering and Technological Problems of Service”*. St. Petersburg, 2009. № 10. S. 42–50. (rus.)
9. **Vettegren' V.I. [et al.]** Tension and Wear Resistance of Polymer Coatings. *Solid State Physics*. Vol. 57, issue 7. St. Petersburg, Ioffe Institute. 2015. S. 1365–1372.
10. **Petrov V.A., Bashkarev A.Y., Vettegren' V.I.** Physics of Forecasting Construction Materials Durability. St. Petersburg: Politekhnik, 1993. 475 s. *Lems of Service”*. St. Petersburg, 2009. № 10. S. 42–50. (rus.)
11. **Berlin A.A., Basin I.V.** Fundamentals of Polymer Adhesion. Moscow: Chemistry, 1974. 392 s.
12. **Ivan'kov S.A., Bashkarev A.Y.** About Durability and Strength of Composites. *Scientific and Technical Journal of SPbPU*. St. Petersburg, Publishing House of SPbPU. 2011. № 4 (110). S. 196–199. (rus.)
13. **Ivanov A.S., Popov B.A.** Calculation of Tension Joints Given Contact Stiffness of Conjugated Surfaces. *Mechanical Engineering Journal*. 2005. № 4. S. 31–36. (rus.)
14. **Chichinadze A.V. [et al.]** Fundamentals of Tribology / Edited by Chichinadze A.V. Moscow, Mechanical Engineering, 2001. 663 s. (rus.)
15. **Bikermann J.J.** The science of Adhesives Joints, New York: Academic Press, 1968. 241 p.
16. **Gardon J.** Treatise on adhesion and adhesives. New York, Academic Press 1967, P. 67–70.
17. **Pakham D., Grad R.** Aspects of adhesion. London, 1971, № 6. P. 127–149.

СПИСОК ЛИТЕРАТУРЫ

1. **Алисин В.В. [и др.]** Трение, износ и скольжение / Под ред. Крагельского И.В., Алисина В.В. М.: Машиностроение, 1978. 400 с.
2. **Гречищев Е.С., Пященко А.А.** Напряженные соединения. Расчеты, конструирование, производство. М.: Машиностроение, 1981. 247 с.
3. **Кайса А.М. Джожа.** Повышение работоспособности и надежности деталей машин с полимерными материалами: Дисс. ... канд техн. наук / Л., ЛПИ, 1984. 122 с.
4. **Bilik M.M., Slyudikova N.N.** Antifriction Properties of Some Polymer Materials in Monolith and Thin-Layer Coating // *Polymers in Manufacturing Industry*, Homel', 1968. P. 26–32.
5. **Стукач А.В.** Исследование эффективности узлов трения с полимерными покрытиями в конструкциях машин фирмы Катерпиллер: Дисс. ... канд техн. наук / Л., ЛПИ, 1980. 125 с.
6. **Чичинадзе А.В. [и др.]** Полимеры в узлах трения машин и механизмов / Под ред. А.В. Чичинадзе, М.: Машиностроение, 1988. 328 с.
7. **Митрович В.П.** Исследование трения полиамидов по стали. М.: Машиностроение, 1963. 96 с.

8. **Стукач А.В.** Исследование и контроль свойств полимерных покрытий при их образовании на рабочих поверхностях в процессе восстановления и получаемые антифрикционные свойства // Журнал Санкт-Петербургского государственного университета сервиса и экономики “Инженерные и технологические проблемы сервиса”. Санкт-Петербург. 2009. № 10. С. 42–50.

9. **Vettegren’ V.I. [et al.]** Tension and Wear Resistance of Polymer Coatings // *Solid State Physics*. 2015. Vol. 57, Is. 7. P. 1365–1372.

10. **Петров В.А., Башкарев А.Я., Веттегрэн В.И.** Физика прогнозирования работоспособности конструкционных материалов. СПб.: Политехника, 1993. 475 с.

11. **Берлин А.А., Басин И.В.** Основы полимерной адгезии. М.: Химия, 1974. 392 с.

12. **Иваньков С.А., Башкарев А.Я.** О работоспособности и прочности композитов // Научно-технические ведомости СПбГПУ. 2011. № 4(110). С. 196–199.

13. **Иванов А.С., Попов В.А.** Расчет напряженных соединений с заданной жесткостью контакта сопрягаемых поверхностей // *Машиностроение*, 2005. № 4. С. 31–36.

14. **Чичинадзе А.В. [и др.]** Основы трибологии / Под ред. А.В. Чичивадзе. М.: Машиностроение, 2001. 663 с.

15. **Bikermann J.J.** The science of Adhesives Joints, New York: Academic Press, 1968. 241 p.

16. **Gardon J.** Treatise on adhesion and adhesives. New York, Academic Press 1967. P. 67–70.

17. **Pakham D., Grad R.** Aspects of adhesion. London, 1971. № 6. P. 127–149.

СВЕДЕНИЯ ОБ АВТОРАХ/AUTHORS

KUSCHENKO Alexandra V. – post graduate student of the department “Transport and Technology Systems”, Institute of Metallurgy, Mechanical Engineering and Transport, Peter the Great St. Petersburg State Autonomous Polytechnic University, Russia, St. Petersburg, 195251, Polytekhnicheskaya Street, 29. E-mail: aleksandra.kushchenko@rambler.ru

КУЩЕНКО Александра Владимировна – аспирант Санкт-Петербургского политехнического университета Петра Великого. 195251, Россия, г. Санкт-Петербург, Политехническая ул., 29. E-mail: aleksandra.kushchenko@rambler.ru

BASHKAREV Albert Ya. – Doctor of Technical Sciences Professor of the department “Transport and Technology Systems”, Institute of Metallurgy, Mechanical Engineering and Transport, Peter the Great St. Petersburg Polytechnic University. 29 Politekhnicheskaya St., St. Petersburg, 195251, Russia. E-mail: bashkarev@spbstu.ru

БАШКАРЕВ Альберт Яковлевич – доктор технических наук советник при ректорате Санкт-Петербургского политехнического университета Петра Великого. 195251, Россия, г. Санкт-Петербург, Политехническая ул., 29. E-mail: bashkarev@spbstu.ru



DOI 10.5862/JEST.249.13

УДК 621.73.011

*V.S. Mamutov, A.V. Mamutov, S.N. Kunkin, X.S. Arsentyeva***METHOD OF OBTAINING FLD FOR USE IN SIMULATION OF METAL FORMING BY MOVABLE MEDIA***B.C. Мамутов, А.В. Мамутов, С.Н. Кункин, К.С. Арсентьева***ДИАГРАММЫ ПРЕДЕЛЬНЫХ ДЕФОРМАЦИЙ ТОНКОЛИСТОВОГО МЕТАЛЛА ПРИ ФОРМОВКЕ ПОДВИЖНЫМИ СРЕДАМИ**

A combined numerical and experimental technique to obtain a Forming Limit Diagram of thin sheet metal for metal forming by movable media was developed. The technique is based on deforming sheet samples until failure by pressure of polyurethane into a variety of the elliptical dies. The required strain state is defined by the proportion of elliptical die window. Through-thickness strain of the sample near to a zone of failure or necking was measured, and major in-plane strains were obtained by finite-element simulation based on the known metal properties. The simplicity of measurements and the absence of a grid on the surface of the sample are the advantages of the suggested technique. Points of the Forming Limit Diagram for the specific thin sheet stainless steel were obtained.

METAL FORMING BY MOVABLE MEDIA; FORMING LIMIT DIAGRAM; COMBINED NUMERICAL-EXPERIMENTAL TECHNIQUE; DESTRUCTION OF SAMPLES BY PRESSURE OF POLYURETHANE; MEASUREMENT OF THICKNESS OF THE SAMPLE; FINITE-ELEMENT CALCULATION OF RELATIONSHIPS BETWEEN THE MAJOR STR.

Разработана расчетно-экспериментальная методика получения диаграммы предельных деформаций тонколистового металла для процессов формовки подвижными средами. Суть методики заключается в разрушении образцов давлением полиуретана при вариации размеров эллиптических матриц для создания требуемого деформированного состояния. В экспериментах и расчетах использованы матрица с круглым отверстием диаметром 100 мм и матрицы с овальными отверстиями с размерами 38x100 мм и 50x100 мм. Измеряется толщина образца вблизи зоны разрушения или шейкообразования и вычисляется деформация по толщине. Соотношения между главными деформациями определяются конечно-элементным расчетом на основе известной кривой деформационного упрочнения материала. Простота измерений, отсутствие сетки на поверхности образца являются достоинствами предлагаемой методики. Получены точки диаграммы предельных деформаций тонколистовой стали 12Х18Н10Т.

ЛИСТОВАЯ ФОРМОВКА ПОДВИЖНЫМИ СРЕДАМИ; ДИАГРАММА ПРЕДЕЛЬНЫХ ДЕФОРМАЦИЙ; РАСЧЕТНО-ЭКСПЕРИМЕНТАЛЬНАЯ МЕТОДИКА; РАЗРУШЕНИЕ ОБРАЗЦОВ ПОЛИУРЕТАНОМ; ИЗМЕРЕНИЕ ТОЛЩИННОЙ ДЕФОРМАЦИИ; КОНЕЧНО-ЭЛЕМЕНТНЫЙ РАСЧЕТ СООТНОШЕНИЯ ДЕФОРМАЦИЙ.

Introduction

The modern level of computers and finite-element (FE) complexes and their availability for simulation of sheet metal stamping enable numerical simulation and prediction of the stress-strain parameters of stamped blank with high precision. When using a general purpose FE code such as LS-DYNA[®], it is possible to obtain the detailed distribution of all the components of deformation tensor at every moment

during the deformation process [1]. In turn, it makes possible to achieve one of the important goals of the stamping process design – predicting the moment of the blank fracture using Forming Limit Diagrams (FLD) [2].

The processes of forming using elastomers (for instance polyurethane) have some differences from those where liquids are used as a pressure transmitting media. Both liquid and elastomer accumulate some

excessive energy during forming due to the uniform compression, but, unlike liquid, elastomers cannot leak through small openings, and pressure inside the media drops slower after plastic instability starts. In the work [3] experiments with piezoelectric sensors of pulse pressure were conducted performing calibration by a “pressure leap” technique using polyurethane. The experiments have shown that there is a time gap of 10–100 μs (depending on fractured material) from the beginning of plastic instability up to the fracture occurs, after that the pressure starts dropping rapidly. In the conditions of the pulse stamping, this resource of plasticity can be used for instance when a formed blank is stopped by a rigid die or by precise dosage of the pulse energy [4].

At loading with using the polyurethane until the moment of instability the blank is accelerated by accumulated energy to the high velocity, and the strain rate at the fracture zone can reach $de/dt = (1-5) \cdot 10^3 \text{ s}^{-1}$ [5]. Many of the works on obtaining and using FLD's, for instance [6], note that FLD at higher strain rates significantly differs from that obtained in quasistatic conditions. When simulating phenomena and processes with high strain rates such as Electro-Hydraulic Forming (EHF), Electro-Magnetic Forming (EMF), crash tests, etc., it is vital to provide FLD corresponded in terms of strain rates to the process that is simulated. The purpose of this work is the developing of a method of obtaining FLD of thin sheet metals for the processes of pulse stamping with elastomers.

Selection and rationale of the method of obtaining FLD

Stuart P. Keeler first suggested the empirical criteria of blank fracture based on measuring two planar principal strains at the moment before fracture starts [7]. Keeler obtained the FLDs for some carbon steels for the area where both principal strains are positive (i.e. the right part of diagram). The moment of fracture beginning was defined as the moment when plastic instability starts or, in other words, the moment when necking becomes visible. Later, Gorton M. Goodwin obtained similar data for the case when one of the principal strains is negative (i.e. the left part of the diagram) [8]. At the present time, the two variants of FLD are distinguished: when deformations are measured at the moment before necking and when the deformations are measured after the fracture occurred [2].

There are many ways to obtain FLD experimentally. All of them essentially are the destruction of the blank sample at predictable or measurable deformation conditions. The most popular are the Nakazima Test (by K. Nakazima [9]), Marciniak Test (by Z. Marciniak [10]), and also known from the beginning of the 20th century the Hydraulic Bulge Test when a clamped blank hydrostatically formed by liquid. The tests of Nakazima and Marciniak differ from each other mostly in shape of the punch – cylindrical with hemi-spherical end and cylindrical with flat end with rounded edges respectively. It is often called by combined name Nakazima-Marciniak test (fig. 1, *a, b*).

The essence of the Nakazima-Marciniak test is that the clamped blank sample of different shape is formed until the fracture using a punch. To reduce the effect from the friction between the punch and the blank in the Nakazima test, lubrication or a layer of antifriction material can be used. In the Marciniak test, a companion layer with a hole in the center or a punch with a center cut can be used which prevent the blank from touching the punch at the center.

The deformation state (the proportion between two principal planar strains ε_1 and ε_2) is defined by the shape and the size of the side cuts in the sample. The side cuts can be of different shape, but the most often used shape is circular cuts. A sample without cuts provides biaxial state of deformation at the center, which is: $\varepsilon_1 = \varepsilon_2$. A sample with maximum cuts gives an FLD point which approximately corresponds to the uniaxial tension, i.e. $\varepsilon_1 = -2\varepsilon_2$.

The actual principal strains are measured using a mesh or some pattern on the surface of the sample. This approach has some disadvantages. It is necessary to determine the moment of starting plastic instability, because this is the moment of fracture by definition. It is difficult to register such a moment by visual observation, so many researchers measured deformations after the fracture, and in this case measured strains included the necking deformation. Using a mesh or a pattern on the surface needs not only an operation of measuring this mesh but also corrections to take into account the neutral layer offset. In the past, that was done manually using a microscope and was very labor intensive. Now it is more common to use digital cameras and digital image correlation software which requires expensive hardware and software.

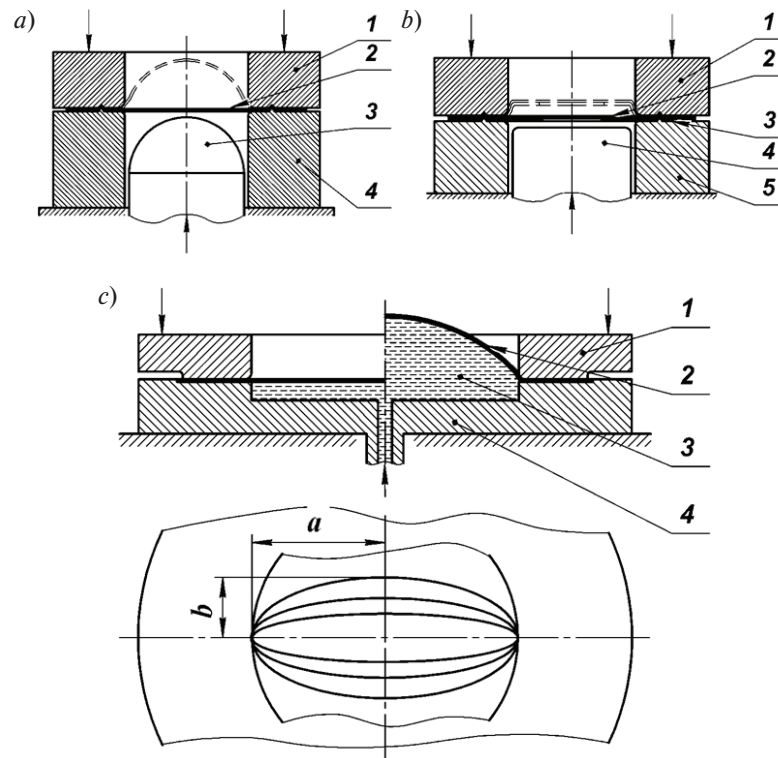


Fig. 1. Traditional methods of obtaining FLD: *a* – Nakazima Test (1 – upper die, 2 – sample, 3 – spherical punch, 4 – lower die); *b* – Marciniak Test (1 – upper die, 2 – sample, 3 – antifriction layer, 4 – cylindrical punch, 5 – lower die); *c* – Hydraulic Bulge Test (1 – die, 2 – sample, 3 – liquid, 4 – chamber)

Furthermore, the mechanics of quasistatic deformation and fracture, which is typical conditions at Nakazima-Marciniak test, significantly differs from that at pulse stamping by movable media, such as EHF and EMF. From that perspective more appropriate is to use the Hydraulic Bulge Test (fig. 1, *b*). In this approach, forming of the sample 2 is performed by the hydrostatic pressure of liquid (usually oil) 3, enclosed in chamber 4. The die 1 has rounded edges to prevent fracture at the clamping contour. The proportion between principal strains is defined by the width a to height b dimensions of the elliptical die cavity. The equality $a = b$ creates uniaxial tensions ($\varepsilon_1 = \varepsilon_2$), and when $a \gg b$, the second principal strain can be almost zero ($\varepsilon_2 \cong 0$).

That way it is possible to obtain the right part of FLD (with both principal strains positive). At the typical conditions of forming by movable media the right part of FLD is usually enough from practical

perspective. Nevertheless, all the disadvantages of measuring strains are the same as in the Nakazima-Marciniak test. In this work, an experimental-numerical method of obtaining FLD similar to Hydraulic Bulge Test is suggested that allows measuring very close to the necking zone.

Combined experimental-numerical method of obtaining FLD

The prerequisite data for the method is the hardening curve in the form of the power law

$$\sigma_s = B \cdot \varepsilon_i^m,$$

where σ_s – true stress; ε_i – true strain; B and m – parameters of the power law approximation. The blank used in experiment was stainless steel 12X18H10T (approximate US equivalent is S32100) of thickness $h_0 = 0,55$ mm. The parameters of the power law were approximated as: $B = 1250$ MPa, $m = 0,287$. The experimental setup is shown in fig. 2,*a*.

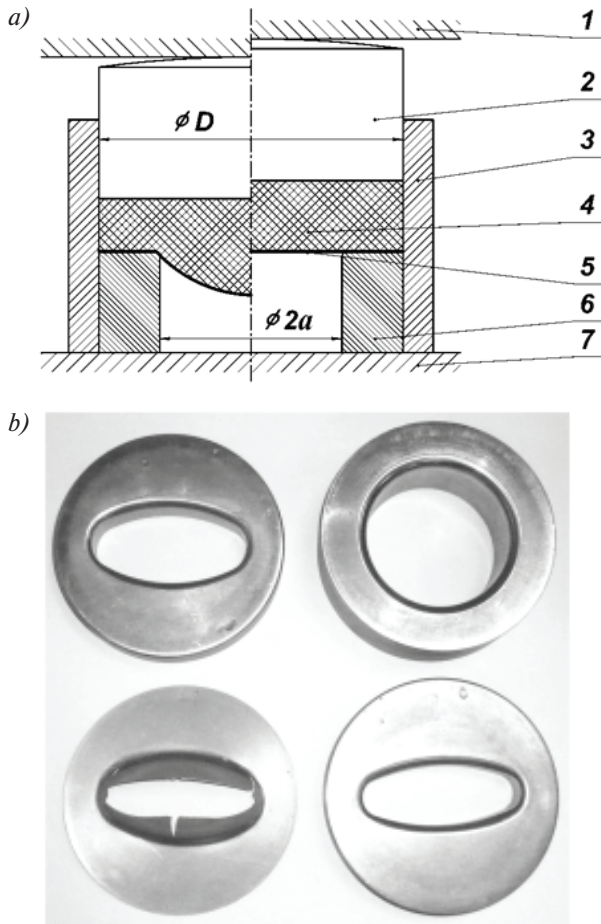


Fig. 2. Toolset for obtaining FLD: *a* – assembled toolset, cross-sectional view (1, 7 – die beds, 2 – piston, 3 – container-chamber, 4 – polyurethane, 5 – sample, 6 – die); *b* – die set: round-shaped, diameter – 100 mm; oval-shaped 38×100 mm, and 50×100 mm; the fractured sample corresponding the die 50×100 mm

Loading of the blank sample 5 is performed by the elastomer 4, enclosed in the container 3, where pressure is created by moving the piston 2. By pressure of the elastomer the sample is formed into the cavity of the die 6 until fracture. The hydraulic press of 100 tones was used.

The polyurethane with Shore hardness of 55–60 units was used as a pressure transmitting media. The friction coefficient is $\mu \leq 0,01–0,05$ for this type of polyurethane in the conditions of the given process [11]. Therefore it is not necessary to use antifriction layer between the blank and the elastomer. The polyurethane also serves as a binder that holds the flange of the sample 5 on the surface of the die 6.

The inner radius of the round-shaped die as well as the major radius of the elliptic cavity of the oval-

shaped die was $b = 50$ mm. The inside diameter of the container and corresponding outside diameter of the die was $D = 150$ mm. The sample diameter is 0,5 mm less than the container diameter. Although there is no special clamping of the flange, as it is usually done in the conventional test, such a proportion between the sample size and the die cavity size provides enough flange resistance and prevents flange from draw into the die thus ensuring that the strain (and the fracture) will happen in the center of the sample. The set of dies included round shaped die with radius 50 mm and two oval-shaped dies 50×19 mm, 50×25 mm. The edge fillet has the radius of 6 mm.

The chosen design of the toolset provided stable fracture conditions (fig. 2, *b*). After forming a sample up to the fracture, the thickness h of the sample was measured as close to the necking zone as possible using a dial indicator. About 5–10 measurements were taken for each sample with averaging the resulting value. Then the average true normal deformation is calculating as:

$$\varepsilon_h = \varepsilon_3 = \ln(h_0/h).$$

The round-shaped die provides uniaxial strain condition in the center of the sample ($\varepsilon_1 = \varepsilon_2$). For this point two principal strains are calculated as:

$$\varepsilon_1 = \varepsilon_2 = \varepsilon_3/2.$$

To obtain points of FLD other than for uniaxial strain it is needed to know the proportion between the major and the minor strain. That can be done using numerical simulation of the deformation process similar to that done in [12].

Simulation was performed with general purpose finite element complex LSDYNA 971. The material assumed as isotropic with the following parameters: Young modulus $E = 202$ GPa, Poisson coefficient $n = 0,31$; power law parameters: $B = 1250$ MPa, $m = 0,287$; density $\rho = 7800$ kg/m³. The LSDYNA material card used was: *MAT_POWER_LAW_PLASTICITY*. The die was simulated as a rigid object. The friction assumed as Coulomb with friction coefficient changing from static $\mu = 0,2$ to dynamic $\mu = 0,15$. The pressure in the elastomer assumed linearly increasing from zero to maximum necessary to fracture the sample in 0,2 s. With given dimensions of the die and sample it provided nearly quasistatic forming conditions [12].

The results of the computer simulation are shown in fig. 3.

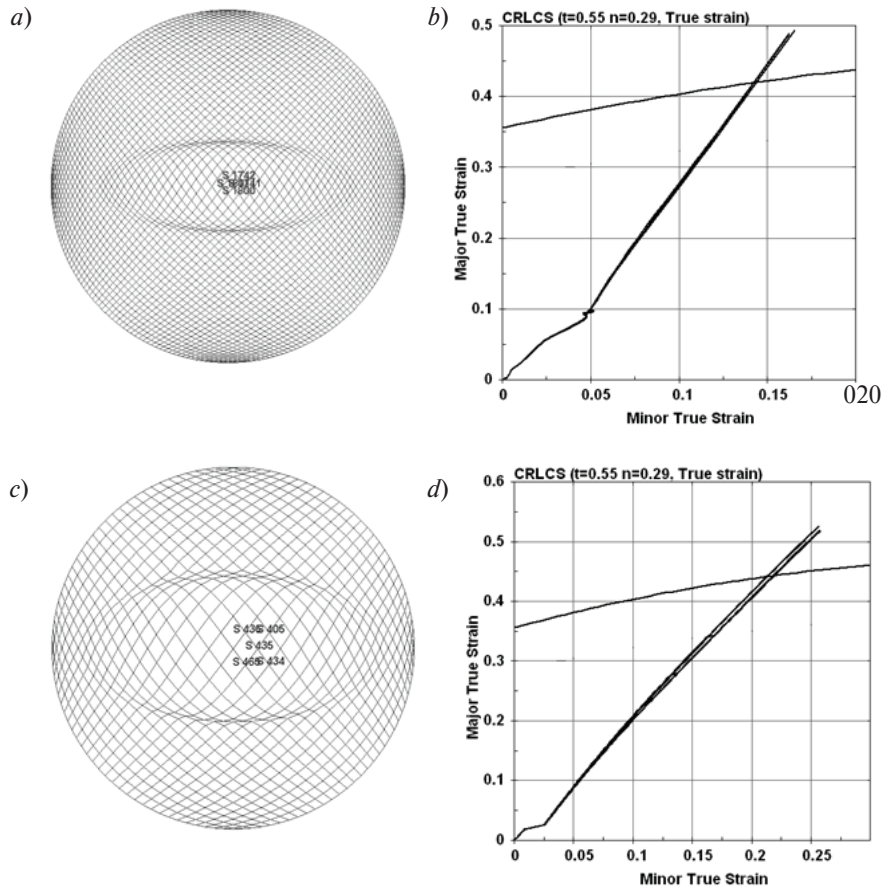


Fig. 3. Deformation paths for the marked points of the samples when forming in the oval-shaped dies 38×100 mm (a, b) and 50×100 mm (c, d) respectively

The diagrams on fig. 3,b and 3,d show paths of deformation at the center of the four samples. The same diagrams show the FLD obtained analytically from hardening data. The calculated deformation path defines the proportion between the principle strains $\alpha = \varepsilon_2/\varepsilon_1$. Together with the experimentally measured thinning (the third principal strain ε_3) it gives a point on FLD:

$$\varepsilon_1 = -\varepsilon_3/(1 + \alpha), \varepsilon_2 = \alpha \varepsilon_1.$$

The obtained FLD points are shown in tab. 1. The deviation of the measured thinning is 10–15%.

It can be noted that the obtained points are lower than that obtained from hardening data. It can be explained by the fact that the deformation in this experiment happens at high strain rate [5], which can cause such change in fracture limits [6]. The detailed distribution of FLD values in the range of $\varepsilon_2 > 0$ can be achieved by using dies with other proportion of the die cavity a/b.

Table

The components of the deformation tensor of the central point depending on the die

Shape of die cavity	<i>h</i>	$-\varepsilon_3$	$\alpha = \varepsilon_2/\varepsilon_1$	ε_2	ε_1
Round with radius 50 mm	0,25±0,02	0,79	1	0,395	0,395
Oval 50×100 mm	0,35±0,03	0,45	0,48	0,146	0,304
Oval 38×100 mm	0,38±0,03	0,37	0,35	0,096	0,274

Conclusion

The method of obtaining forming limit diagrams for thin sheet metal for using in simulation of pulse forming by movable media is developed. Because loading of the sample is performed by elastomer (polyurethane), the forming and fracture conditions in developed method are close to those in the said technologies such as electro-hydraulic and electro-magnetic forming. The distribution of FLD values in the range of $\varepsilon_2 > 0$ can be obtained by using dies with different proportion of the elliptical die cavity. The

range of FLD $\varepsilon_2 > 0$ is usually enough for practical use in simulation of pulse stamping methods. The point of FLD is obtained as a combination of thinning measured in the necking area and principal strains proportion obtained from numerical simulation using finite element code. The advantage of the developed method is the simplicity of used tooling, simplicity of measurement, no need to use meshes and expensive hardware and software to obtain strains. The experiment is conducted and the FLD is obtained for the stainless steel 12X18H10T (approximate US equivalent is S32100) of 0,55 mm.

REFERENCES

1. **Hallquist J.O.** LS-DYNA theoretical manual. Livermore Software Technology Corporation: Livermore, SA, 2006. 498 p.
2. **Dorel Banabic.** Sheet Metal Forming Processes. Constitutive Modelling and Numerical Simulation. Springer Heidelberg Dordrecht: London-New York, 2010. 301 p.
3. **Patent USSR № 697851** Ustroystvo dlia tarirovki p'ezoelektricheskikh datchikov davleniia / Bogoiavlenskii K.N., Vagin V.A., Mamutov V.S., Oreshnikov A.I. Prioritet 14.06.1979. (rus).
4. **Vagin V.A., Zdor G.N., Mamutov V.S.** Metody issledovaniya vysokoskorostnogo deformirovaniya metallov. Minsk: Nauka i tekhnika, 1990. 208 s. (rus).
5. **Aksenov L.B., Mamutov V.S., Mamutov A.V.** Postroenie diagramm predel'nyh deformatsiy dlia prognozirovaniia razrusheniia tonkolistovoy zagotovki pri vysokoskorostnoy vytyazhke-formovke. *Forging-Stamping Production*. 2002. № 4. S. 9–12. (rus.)
6. **Persy J.N.** The effect of strain rate on the forming limit diagram for sheet metal. *Annals of CIPP*. 1980. Vol. 29. № 1. P. 131–132.
7. **Keeler S.P.** Rating the Formability of Sheet Metal. *Metal Progress*. 1966. Vol. 90. P. 148–153.
8. **Goodwin G. M.** Application of Strain Analysis to Sheet Metal Forming Problems in the Press Shop. *Presented at SAE Automotive Engineering Congress, Detroit* (January 1968). Paper 680093, 8 p.
9. **Nakazima K., Kikuma T.** (1967) Forming limits under biaxial stretching of sheet metals. *Testu-to Hagane* 53:455–458 (in Japanese).
10. **Marciniak Z., Kuczynski K.** Limit strain in the process of stretch forming sheet metal. *International Journal of Mechanical Science*. Vol. 9. 1967. P. 609–620.
11. **Komarov A.D.** Shtampovka listovykh i trubchatykh detaley poliuretanom. Leningrad: LDNTP, 1975. 36 s. (rus).
12. **Mamutov A.V., Mamutov V.S.** Rascheti processov shtampovki podvizhnimi sredami pri pomoshi kompleksa LS-DYNA. *St. Petersburg State Polytechnical University Journal : Science and education*. 2012. № 2. Vol. 1 (147). S. 127–131. (rus).

СПИСОК ЛИТЕРАТУРЫ

1. **Hallquist J.O.** LS-DYNA theoretical manual. Livermore Software Technology Corporation: Livermore, CA, 2006. 498 p.
2. **Dorel Banabic.** Sheet Metal Forming Processes. Constitutive Modelling and Numerical Simulation. Springer Heidelberg Dordrecht: London-New York, 2010. 301 p.
3. **Патент СССР № 697851.** Устройство для тарировки пьезоэлектрических датчиков давления / Богоявленский К.Н., Вагин В.А., Мамутов В.С., ОRESHNIKOV A.I. Приоритет 14.06.1979.
4. **Вагин В.А., Здор Г.Н., Мамутов В.С.** Методы исследования высокоскоростного деформирования металлов. Минск: Наука и техника, 1990. 208 с.
5. **Аксенов Л.Б. Мамутов В.С., Мамутов А.В.** Построение диаграмм предельных деформаций для прогнозирования разрушения тонколистовой заготовки при высокоскоростной вытяжке-формовке // КШП. 2002. № 4. С. 9–12.
6. **Persy J.N.** The effect of strain rate on the forming limit diagram for sheet metal // *Annals of CIPP*. 1980. Vol. 29. № 1. P. 131–132.
7. **Keeler S.P.** Rating the Formability of Sheet Metal // *Metal Progress*. 1966. Vol. 90. P. 148–153.
8. **Goodwin G.M.** Application of Strain Analysis to Sheet Metal Forming Problems in the Press Shop // *Presented at SAE Automotive Engineering Congress, Detroit*. January 1968. Paper 680093, 8 p.
9. **Nakazima K., Kikuma T.** (1967) Forming limits under biaxial stretching of sheet metals // *Testu-to Hagane* 53:455–458 (in Japanese).
10. **Marciniak Z., Kuczynski K.** Limit strain in the process of stretch forming sheet metal // *International Journal of Mechanical Science*. 1967. Vol. 9. P. 609–620.

11. **Комаров А.Д.** Штамповка листовых и трубчатых деталей полиуретаном. Л.: ЛДНТП, 1975. 36 с.
12. **Мамутов А.В., Мамутов В.С.** Расчеты процессов штамповки подвижными средами при помощи комплекса LS-DYNA // Научно-технические ведомости СПбГПУ. Наука и образование. 2012, № 2. Vol. 1 (147). С. 127–131.

СВЕДЕНИЯ ОБ АВТОРАХ/AUTHORS

MAMUTOV Viatcheslav S. – Peter the Great St. Petersburg Polytechnic University.
29 Politechnicheskaya St., St. Petersburg, 195251, Russia.
E-mail: mamutov_vs@spbstu.ru

МАМУТОВ Вячеслав Сабайдинович – доктор техн. наук профессор Санкт-Петербургского политехнического университета Петра Великого.
195251, Россия, г. Санкт-Петербург, Политехническая ул., 29.
E-mail: mamutov_vs@spbstu.ru

MAMUTOV Aleksandr V. – Oakland University.
2200 N Squirrel Rd. Rochester, Michigan, 48309.
E-mail: a.mamutov@yahoo.com

МАМУТОВ Александр Вячеславович – кандидат технических наук приглашенный ученый Оклендского университета
48309, США, Мичиган, 2200 N Squirrel Rd. Rochester.
E-mail: a.mamutov@yahoo.com

KUNKIN Sergei N. – Peter the Great St. Petersburg Polytechnic University.
29 Politechnicheskaya St., St. Petersburg, 195251, Russia.
E-mail: ksn54@mail.ru

КУНКИН Сергей Николаевич – кандидат технических наук доцент Санкт-Петербургского политехнического университета Петра Великого.
195251, Россия, г. Санкт-Петербург, Политехническая ул., 29.
E-mail: ksn54@mail.ru

ARSENTYEVA Kseniia S. – Peter the Great St. Petersburg Polytechnic University.
29 Politechnicheskaya St., St. Petersburg, 195251, Russia.
E-mail: fartran@li.ru

АРСЕНТЬЕВА Ксения Сергеевна – аспирант Санкт-Петербургского политехнического университета Петра Великого.
195251, Россия, г. Санкт-Петербург, Политехническая ул., 29.
E-mail: fartran@li.ru

DOI 10.5862/JEST.249.14

УДК 621.85

S.I. Hoodorozhkov

THE MECHANICAL STEPLESS IMPULSE TYPE TRANSMISSION FOR ADVANCED SMALL-SIZED TRANSPORT

С.И. Худорожков

МЕХАНИЧЕСКАЯ БЕССТУПЕНЧАТАЯ ИМПУЛЬСНАЯ ПЕРЕДАЧА ДЛЯ СОВРЕМЕННОЙ МАЛОГАБАРИТНОЙ ТРАНСПОРТНОЙ ТЕХНИКИ

An alternative option of mechanical stepless impulse type transmission for small-sized transport is considered in this paper. The proposed self-regulating automatic stepless transmission allows to significantly improve the technical characteristics of modern CVTs- with respect to power and kinematic ranges as well as design simplicity. In this investigation, the theoretical analysis findings of the operating processes- dynamics and kinematics in impulse transmission are presented for the ATV case in the MATLAB – Simulink visual programming environment. It also contains the project efficiency assessment. The results showed that the proposed scheme of mechanical stepless transmission of impulse type has the property of velocity ratio self-regulation. The transmission provides the vehicle's smooth acceleration and uniform motion, without the center differential required. At each wheel's slipping a tractive effort will be transmitted up to the traction limit. As a result the wheel lock is not required in order to improve traction properties. The design of mechanical stepless transmission of impulse type is significantly simpler and cheaper than that of the existing automatic transmissions, it has smaller internal power loss and high application potential in small-sized vehicles.

MECHANICAL STEPLESS TRANSMISSION; IMPULSE TRANSMISSION; CVT; SMALL-SIZED TRANSPORT; SIMULATION; MATLAB; SIMSCAPE; DYNAMICS; OPERATING PROCEDURE; ACCELERATION CHARACTERISTIC.

Рассмотрен альтернативный вариант механической бесступенчатой передачи импульсного типа применительно к современной малогабаритной транспортной технике. Предлагаемая саморегулируемая автоматическая бесступенчатая передача позволяет существенно улучшить технические характеристики трансмиссий, выполненных по технологии CVT, в части силового и кинематического диапазонов, а также упрощает конструкцию. Представлены результаты анализа в среде визуального программирования MATLAB – Simulink кинематики и динамики рабочих процессов в импульсной трансмиссии на примере мотовездехода, а также дана оценка эффективности ее применения. Показано, что предложенная схема простейшей механической бесступенчатой передачи импульсного типа обладает свойством саморегулирования передаточного отношения. Передача обеспечивает плавный разгон и равномерное движение транспортного средства. Применение межосевого дифференциала не требуется. При буксовании каждое колесо будет передавать тяговое усилие вплоть до предельного по сцеплению. При этом блокировки колес для повышения тяговых свойств не требуется. Предлагаемая конструкция значительно проще и дешевле существующих конструкций автоматических трансмиссий, имеет меньшие внутренние потери мощности и высокий потенциал применения в малогабаритной транспортной технике.

МЕХАНИЧЕСКАЯ БЕССТУПЕНЧАТАЯ ПЕРЕДАЧА; ИМПУЛЬСНАЯ ТРАНСМИССИЯ; CVT; МОТОТРАНСПОРТНАЯ ТЕХНИКА; МОДЕЛИРОВАНИЕ; MATLAB; SIMSCAPE; ДИНАМИКА; РАБОЧИЕ ПРОЦЕССЫ; ХАРАКТЕРИСТИКИ РАЗГОНА.

Advanced motor transport is a huge segment of small-sized vehicles, which includes motorcycles, scooters, mopeds, ATV, snowmobiles, jet skis and other equipment. These vehicles manufactured by famous brands, have been steadily improved, their variety and innovative design being amazing. In recent years motobikes, ATV, snowmobiles have been in increasing demand. ATV (All Terrain Vehicle) and UTV (Utility Task Vehicle) are vehicles intended for traveling and cargo transportation in cross-country conditions, not accessible for conventional cars or motorcycles.

High cross-country capability and maneuverability of such vehicles is provided by application of advanced chassis components and mechanical continuously variable transmission (CVT) with automatic control (Duramatic type, [1]). The latter normally consist of a clutch and an electronically controlled CVT V-belt, which provides stepless torque transmission from the engine to the driving wheels depending on traffic conditions.

The disadvantages of vehicles with CVT are also well known:

1. Narrow range of torque transformation and necessity of additional speed gearbox application.

2. Intensive deterioration of tires and reduction of their service life in full lock of power drive (4x4) that is caused by parasitic power circulation (without the interaxle differential).

3. Unavailability of a self-regulation gear ratio (load-dependent) and the necessity of a CVT electronic control system that does not fully satisfy the working conditions.

4. Limited use of this type vehicles by domestic motorists due to high cost of imported equipment.

The novelty of the presented engineering project is that it provides theoretical basis for efficiency of alternative stepless self-regulated impulse transmission (instead of CVT [2]) for small-sized vehicles. There are various designs of mechanical impulse transmissions [3, 4, 5, 6]. They are based on conversion of the drive shaft rotation into angular oscillation of the intermediate link, amplitude of these oscillations changing automatically or manually at loading change on the driven shaft. Then angular oscillations of the intermediate link are transformed into unidirectional rotation of the driven shaft by means of a

free wheeling clutch (FWC), the greater the oscillations amplitude of the intermediate link the greater the driven shaft velocity.

Application of impulse transmissions for vehicles increases their efficiency, namely:

- an additional speed gearbox is not required due to a wider range of torque transformation;

- manoeuvrability and cross-country capability are increased due to internal automaticity (self-regulation of gear ratio);

- the permanent wheel drive without circulation of parasitic power with automatic compensation of kinematic discrepancy is provided;

- transmission is simplified and reduced in cost by eliminating the use of imported components and application of a simple design implemented at an accessible technological level;

- maximum efficiency is ensured due to the replacement of the friction variator (CVT) and torque transmission by self-braking friction in FWC instead of friction-slip like in CVT.

Analysis shows that in order to raise technical and economic efficiency of modern small-sized vehicles it would be advisable to use simple self-regulating mechanical stepless transmissions, having a compact, simple design and low cost. According to the published evidence [4, 7, 8, 9, 10] it is known that gear ratio changes in impulse transmission can be achieved not only by changing the oscillations amplitude but also due to the links elastic deformation, for example that of the torsion shaft, connected with the FWC. Such engineering solution simplifies the design of impulse transmission and allows to arrange the parts of transmission in overall dimensions of the existing CVT (Duramatic).

This study is aimed at the investigation of vehicle dynamic characteristics with such transmission, namely joint operation of the engine, clutch and stepless impulse transmission during acceleration and uniform motion. An example of the kinematics of an elementary impulse type transmission for all-wheel drive (ATV) is shown in fig. 1.

At the heart of such transmission is the principle of the gear ratio regulation in response of to load changes by automatically changing the swirl angle of torsion shafts 6 connecting the driven links of FWC 5 with the output shafts 7.

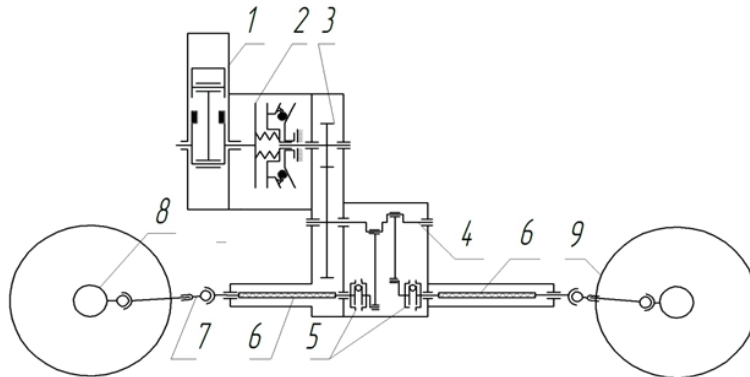


Fig. 1 The kinematics of an elementary impulse type transmission for all-wheel drive (ATV): 1 – engine; 2 – automatic centrifugal clutch; 3 – reducer; 4 – hinged-lever mechanism (generator of mechanical oscillations); 5 – free wheeling clutch (FWC); 6 – torsion shaft; 7 – cardan drive; 8 – differential; 9 – driving wheels.

Transmission operates as follows. The rotation from the engine 1, the centrifugal clutch 2 and the reducer 3 with angular velocity ω is transmitted to the hinged-lever mechanism 4, generating angular oscillations of the FWC driving parts 5 with constant amplitude φ_0 . In case of harmonic oscillations its angular speed is equal to

$$\omega_1 = \varphi_0 \omega \sin(\omega t).$$

If there is no resisting torque on the driving wheels 9 (theoretically), the torsion shafts 6, connected through the cardan drives 7 and differentials 8 with the drive wheels 9, are not loaded by torque. Their swirl angles for a cycle oscillation are theoretically equal to zero, while gear ratio due the torsion shaft deformation $\delta i = 1$. If angular velocity of the driving wheels 9 and cardan drive 7 becomes smaller by resisting torque, the swirl angles of the torsion shafts vary proportionally to the load; in case of maximum deformation of the torsion shaft 6 in the “stale condition”, the internal gear ratio will be equal to $i = 0$. In operating procedure, the smaller gear ratio i , the earlier FWC 5 is switched on and later switched off, and the greater are maximum and average swirl angles of torsion shafts 6, as well as the average torque transmitted to the driving wheels 9. In this case, torque transmission from the engine 1 through FWC 5 to the front and rear axles is carried out with a phase lag 180 deg.

The clutch 2 is used for smooth breakaway and acceleration with a necessary intensity. The reducer 3 is required to lower the engine speed with a view to decreasing the frequency of FWC engaging. Reverse motion at this scheme, is provided by the FWC reverse

operation [11, 12] (not shown). The procedure of determination of ATV tractive-dynamic characteristics and the simulation results are presented below.

Initial data:

Gross vehicle weight – 550 kg; maximum speed – 80 km/h; engine capacity - 38 kW; type of driving-wheels – AT25h8-12 (26h8-14); wheel arrangement – 4×4; traffic conditions: coefficient of motion resistance $f = 0,015$, and traction coefficient of $\mu = 0,65$, without considering the wind load; upgrading – at least 25 degrees.

The operating procedures simulation of the mechanical impuls transmission was performed in MATLAB-SIMULINK [13, 14]. The block diagram of power train consisting of several subsystems is shown in fig. 2.

Inertial properties of the rotating shafts and gears are taken into account by means of the “Inertia” blocks. The inertial properties of the engine, clutches, driving wheels and ATV chassis options are embedded in the parameters of the relevant subsystems. Sensors of angular velocity and torque, as well as the signal receivers are not shown.

SIMULINK block diagram is made up of several subsystems.

1. Subsystem 1 – “Engine”, includes:

block «Engine» from the Simulink library «Sim-scape - SimDriveline» with the following parameters: the engine type – petrol, the maximum power – 50 hp, the maximum speed – 6500 rev/min; inertia – $0,1 \text{ kg} \cdot \text{m}^2$; Engine power speed characteristic is approximated by a polynomial of the third degree;

block «Signal Builder / Throttle» [15], determining the engine fuel supply.

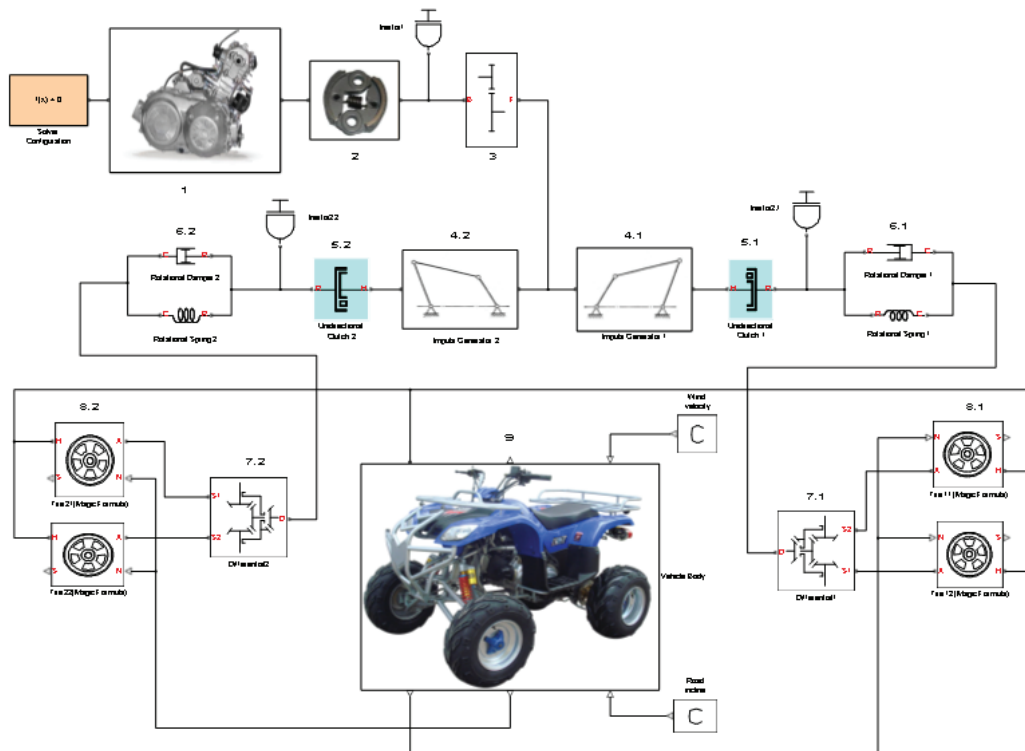


Fig. 2. SIMULINK block diagram of the ATV with simplest stepless mechanical impuls transmission Here: 1 – engine; 2 – clutch; 3 – reducer; 4.1 and 4.2 – generators of mechanical oscillations in the front and rear power circuit, respectively; 5.1 and 5.2 – free wheeling clutches; 6.1 and 6.2 – torsion shafts (taking into account hysteresis losses); 7.1 and 7.2 – cross-axle differentials in the front and rear axles; 8.1 and 8.2 – driving wheels of the front and rear axles; 9 – ATV body

2. Subsystem 2 – “Clutch” includes:

block «Disk Friction Clutch» from the Simulink library «Simscape – SimDriveline» with the following parameters: the type – disk, the effective radius of the friction discs – 60 mm; the discs number – 2; the clutch type – hydraulic; the piston actuator cylinder area – 0,005m²; friction coefficient (static / dynamic) – 0,7 / 0,55;

block «Signal Builder/Pressure» determining the acceleration rate in clutch switching.

3. Inertia of rotating masses – «Inertia» blocks from Simulink library «Simscape – Mechanical – Rotational Elements» – on transmission inlet «Inertia1» and on the FWC outlet «Inertia2.1» and «Inertia2.2» are equal respectively 0,5 and 0,0001 kg · m².

4. Reducer (3) – a standard bloc «Simple Gear» from Simulink library «Simulink – Simscape – SimDriveline – Gears» with a ratio equal to 3.

5. Hinged-lever mechanisms «Impuls Generator» (4.1 and 4.2) form mechanical harmonic oscillations with a constant amplitude $\varphi_0 = 0,35$ rad in two power flows (front and rear axles) with a phase lag 180 degrees.

6. FWC «Unidirectional Clutch» (5.1 and 5.2) converts harmonic oscillations into unidirectional motion of torsion shafts – block of Simulink library «Simscape – SimDriveline – Clutches».

7. Torsion shafts «Torsional Spring – Damper» (6.1 and 6.2) – block from Simulink library «Simscape – SimDriveline – Couplings & Drives». They have the following parameters: angular stiffness of 2100 N·m/rad, damping coefficient of 0,01 N · m / (rad/sec).

8. The cross-axle differential mechanisms 7.1 and 7.2 «Differential» – distributes torque to the driving wheels of the front and rear axles with a ratio of 0,7. Blocks from a library «Simulink – Simscape – SimDriveline – Gears».

9. The driving wheels 8.1 and 8.2 – form a longitudinal traction force proportional to the weight and traction coefficient. The wheels radius is 0,32 m, the load on the wheel in a static position is uniform. Longitudinal linear stiffness of the tires – 1000 kN/m; longitudinal tire damping coefficient – 1000 N/(m/s); inertia – 0,5 kg · m².

10. Subsystem 9 – «Vehicle body», includes:

«Vehicle body» block from the library «Simscape - SimDriveline – Tires & Vehicles» with parameters: mass – 550 kg; number of wheels per axle – 2; front area – 1,5m²; drag coefficient – 0,4; mass center coordinates – 0,6/0,6/0,5 m.

The total efficiency of the mechanical power train (including losses in the gearing, differentials, bearings and others) is assumed equal to $\eta = 0,92$.

The simulation results of the stepless transmission's operation parameters in accelerating from stop to maximum speed are shown in fig. 3 – 6.

At the initial starting point (smooth clutch switching and the fuel feed increasing) the engine torque is transmitted through the reducer 3 to the second intermediate shaft. Next, by means of unregulated hinged-lever mechanisms 4.1 and 4.2 the rotation is converted into the angular oscillations of FWC leading links 5.1 and 5.2 with phase bias 180 degrees (fig. 3).

Two FWC (one for each axle) transmit torque only in one direction. Idle running is carried out in the other direction. Therefore, they convert the angular oscillations into unidirectional rotation, that is transmitted by means of the torsion shafts 6.1, 6.2 and cross-axle differentials 7.1 and 7.2 to the front and rear driving wheels.

The larger the oscillation amplitude, the higher rotation speed of the driving wheels. In this case the wheel's speed changes automatically according to the resistance movement at constant of FWC oscillation amplitude.

If the resistance on driving wheels is great (acceleration start) and they rotate at a low speed, the main part of the FWC cycle is switched on, its driven links oscillate together with the driving links and only a small portion of the FWC cycle is switched off. This is accompanied by the appearance of free oscillations of the driven links – splined end of the torsion shaft (see fig. 4,a).

It is important to observe that frequency of natural oscillations of the torsion shaft with the driven links of FWC is much higher than oscillation frequency generated by the hinged-lever mechanisms. This is a prerequisite that must be provided by the design, because transmission can work only below resonance band.

If resistance at the driving wheels is small (at the acceleration end), the oscillations of FWC driven links of are very close to the maximum value of the angular velocity of the driving links (fig. 4,b), the torsion shaft twisting is reduced. Inertia of transmission's driven parts is sufficiently large, therefore angular velocity reduction during one cycle (one revolution driving shaft) is immaterial.

Swirl angles of torsion shafts per cycle vary from zero up to a maximum value equal to twice the oscillations amplitude of the FWC driving links (fig. 5, a, b).

If resistance on the driving wheels is smaller than torque from the swirl angle of the torsion shaft, the wheels are driven, if otherwise, the wheels are in the "stale condition" (with the fired engine). The average torsion shaft's swirl angle is equal to the oscillations' amplitude of the FWC's driving links, and the average torque on the driving wheels is equal to the average twist angle multiplied by the angular stiffness of the torsion shaft and the gear ratio of the wheel differential.

The maximum torsion swirl angle is reduced from 24 to 10 degrees, with ATV increasing speed (fig 5, a, b). The decreasing deformation of the torsion shafts occurs automatically and is proportional to the vehicle's acceleration reduction, being determined by the engine's excess capacity over the resistance power.

Fragments of operating curves of transmission – the input torque (links 4.1 and 4.2, fig. 2) and output torque (links 7.1 and 7.2) in timing are shown in fig. 6,a.

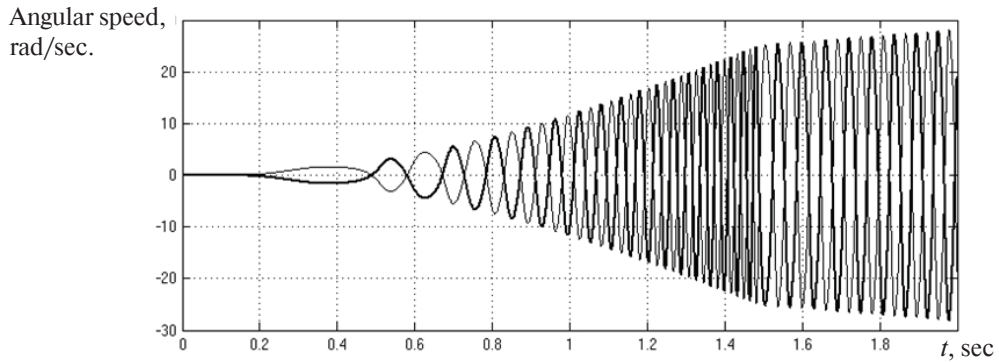
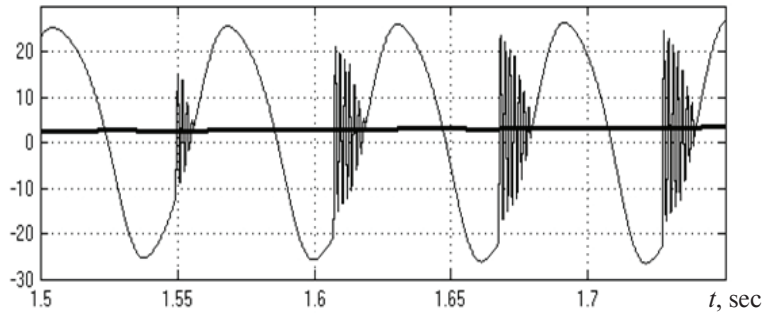


Fig. 3. Angular speed (rad/sec) of the FWC driving links formed by mechanical oscillations generator in the acceleration initial period in the interval from 0 to 2 seconds

a) Angular velocity, rad/sec.



b) Angular velocity, rad/sec.

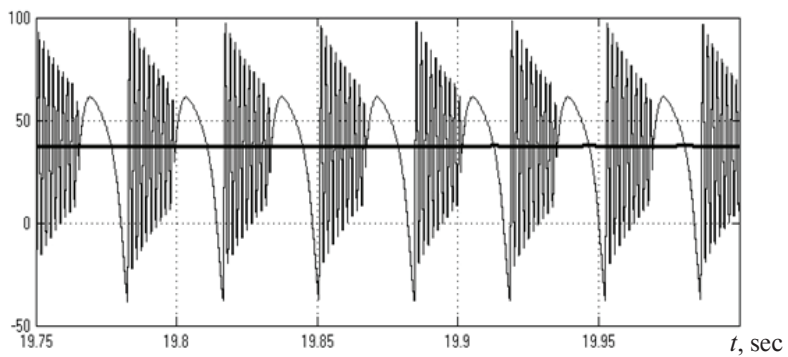
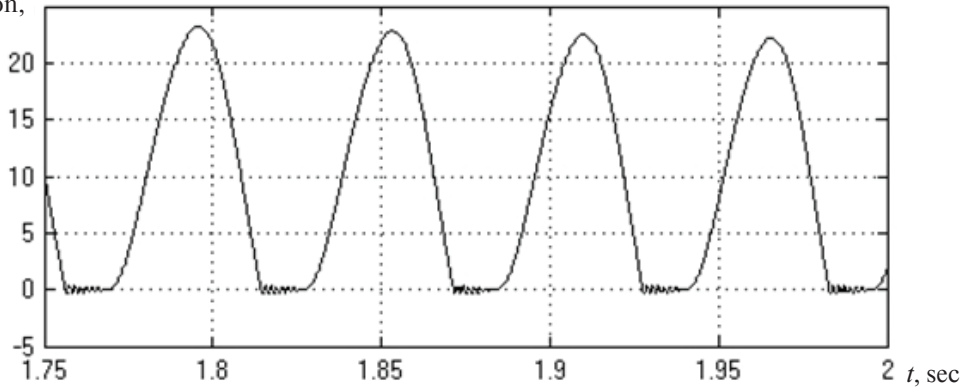


Fig. 4. Angular velocity (rad/s) of driving and driven ends of torsion shaft: a) at the acceleration start for a period of 0,25 seconds (from 1,5 to 1,75 sec.); b) at the acceleration end for a period of 0,25 seconds (from 19,75 to 20,0 sec.)

a) Cyclic angle deformation, degr.



b) Cyclic angle deformation, degr.

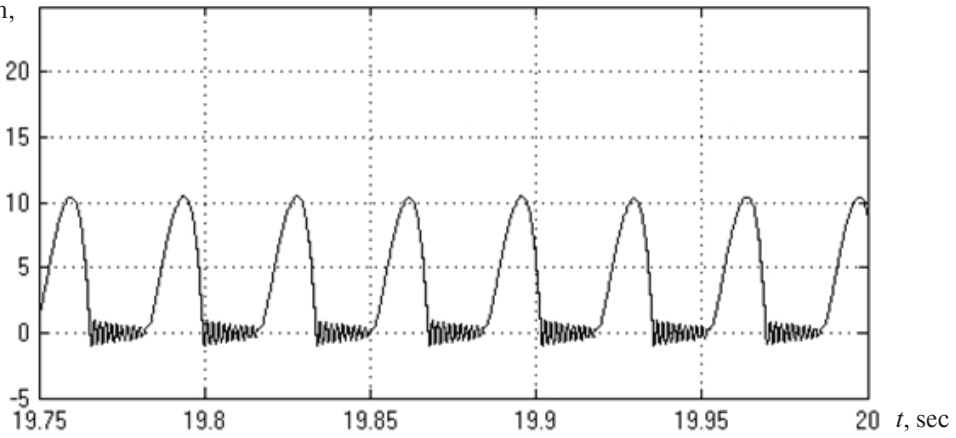


Fig. 5. Cyclic angle deformation (degrees) of the torsion shaft: *a*) at the acceleration start for a period of 0,25 seconds (from 1,5 to 1,75 sec.); *b*) at the of acceleration end for a period of 0,25 seconds (from 19,75 to 20,0 sec.)

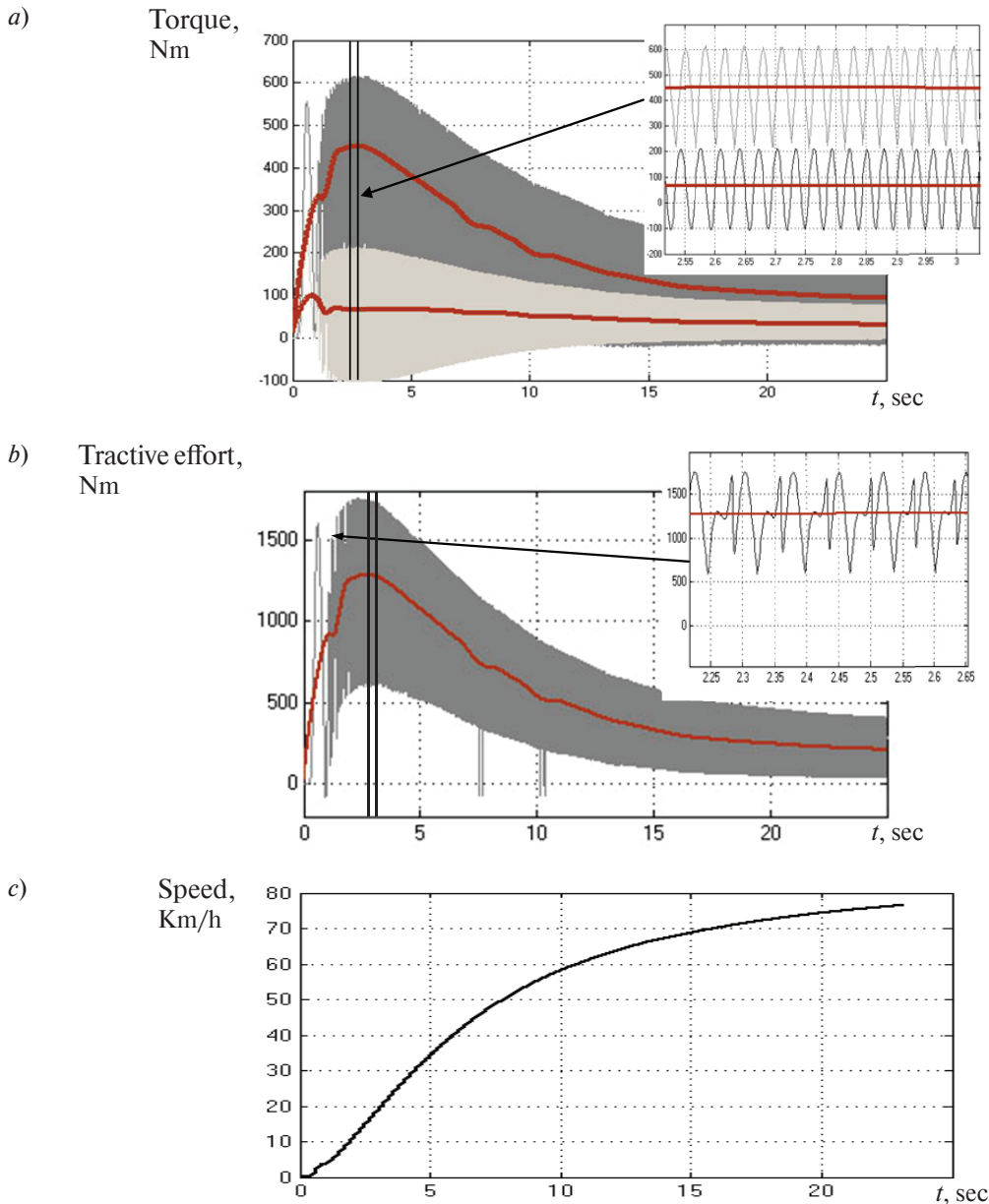


Fig. 6. Dynamic parameters of ATV acceleration: *a* – momentary and average torque values (N·m) at the input (white background, black curve) and aggregate momentary and average torque values on output shaft of impulse transmission (dark background, the black curve) in the time interval from 0 to 25 seconds; *b* – change of total momentary and average tractive effort (N) of driving wheels (light background, black curve) in the time interval from 0 to 25 seconds; *c* – change of ATV's speed (km/h) in the time interval from 0 to 25 seconds

The transmission power range *d* (output to input torque ratio) is:

$$d = \frac{\text{mean}[(2 \cdot M_{81} + 2 \cdot M_{82})_{\max}]}{\text{mean}(M_{3_{\max}})} = \frac{400}{65} = 6,2$$

that exceeds the torque transformation range of the existing continuously variable transmissions. Here the subscript «max» means the maximum average value of torque over the whole range of gear ratios.

An additional advantage of impulse transmission is that it allows to work a long time in so-called “stale condition” (driving wheels stop when transmitting torque from the engine) and has at the same time the theoretical transformation ratio K , equal to infinity. Real K factor has a finite value, because there are hysteresis losses in loading-unloading cycles, but these losses are negligible.

Total traction's changes (N) of the ATV's driving axles during the acceleration are shown in fig. 6, *b*. Maximum oscillation amplitude of the total tractive force amounts to 600 H with an average of 1200 N and is implemented at the acceleration start, then traction gradually declines. The oscillations amplitude of the total tractive force at the acceleration end is about of 150 N with an average of 250 N.

The oscillation amplitude of the intermediate links' torque (at a frequency of 10 to 30 cycles/sec) and driving wheels traction (20–60 cycles/sec) is filtered and provides ATV smooth acceleration and uniform motion (fig. 6, *c*) due to the vehicle inertia and the chassis damping properties. The graph shows that the ATV accelerates smoothly to a speed of about 80 km/h in 25 seconds. The driving wheels' slip at constant engine speeds is of the order 1%.

As a result of the performed theoretical study it was determined:

1. The proposed scheme of simple mechanical stepless transmission of impulse type has the prop-

erty of self-regulation control. Thus, for the period of ATV acceleration from a standstill to 80 km/hour with an increase in the engine's angular velocity from 75 to 600 rad/sec, the average angle of the torsion shafts' twist has changed from 15 degrees in the initial phase up 5 degrees - at the end, i.e. transformation ratio is 3. At the same time, taking into account the engine acceleration and tire traction the total average tractive force of the driving wheels has changed from 400 to 100 N. This transmission provides the ATV's smooth acceleration and uniform motion.

2. The FWC driven links are not connected to each other kinematically, and therefore, the power to the driving wheels of the front and rear axles is transmitted independently in accordance with the elastic characteristic of the torsion shafts, i.e. the driving wheels can rotate with different angular velocities; the torques transmitted to the driving axles are determined by elastic characteristics of their own torsion shaft. Application of the center differential is not required. When wheels of one driving axle slip, the other driving axle will transmit tractive force up to the traction limits. Therefore, the central differential locking in order to improve traction properties of the driving wheels is not required.

3. The design of the self-regulating mechanical impulse transmission is significantly simpler and cheaper than available automatic transmissions, it has less internal power loss and a high application potential in small-sized vehicles [16].

REFERENCES

1. **POLARIS**. The Way Out. 2003 ATV. Universal Owner's Manual for Vehicle Maintenance and Safety // Polaris Industries Inc. Copyright 2002. P. 153.
2. **Arctic Cat Service** Manual for the 2012 Arctic Cat XC 450i ATV // Product Service and Warranty Department Arctic Cat Inc. Copyright 2011. P. 123.
3. **George Constantinesco**. Inertial Transmission. <http://www.rexresearch.com/constran/Iconstran.htm>.
4. **Blagonravov A.A.** The mechanical continuously variable transmission / Ural Branch of Russian Academy of Sciences. Ekaterinburg, 2004. P. 203–204.
5. **Blagonravov A.A., Hoodorozhkov S.I.** Dynamics of the mechanical continuously variable transmission [The dynamics of the mechanical continuously variable transmission]. *Problems of mechanical engineering and reliability*, 2002. 6. P. 19–24.
6. **The patent of Russia №2252351**. The mechanical self-regulating continuously variable transmission / Hoodorozhkov S.I.
7. **Blagonravov A.A., Hoodorozhkov S.I.** Dynamic behavior of the self-regulating mechanical continuously variable transmission. *Materials of the All-Russian scientific-practical conference «Reducer's building of Russia: state, problems and opportunity»*. St. Petersburg, 2003. P. 192–194.
8. **Blagonravov A.A., Revnyakov Ye.N.** The mechanical continuously variable impulse type transmission. *Motor-car industry*. 2007. № 5. P. 11–14.
9. **Hoodorozhkov S.I.** Simulation of the impulse transmission's dynamics with an elastic linkage. *Interuniversity collection of learned works «The continuously variable transmissions and freewheel mechanisms»*. Kaliningrad, 2001. P. 142–148.
10. **Blagonravov A.A., Hoodorozhkov S.I.** External characteristic of the multithreaded continuously variable transmission with elastic linkages. *Collection of Short Message «XXII Russian School on Science and Technology»*. Yekaterinburg, 2002. P. 82–84.
11. **Lester W.T.** Infinitely Variable Transmission Utilizing Oscillating Torque. <http://ebookbrowse.com/infinitely-variable-transmission-utilizing-oscillating-torque-doc-d420263879>.

12. **The patent of Russia №2373441.** Free-wheel clutch mechanism / Hudorozhkov S.I.

13. **Hudorozhkov S.I.** Theory and automatic control systems. Analysis and synthesis of transport systems in Simulink environment: tutorial. SPb: Publishing house of the Polytechnic University Press, 2014. 110 p.

14. **Hudorozhkov S.I.** Theory and automatic control system. Design of automatic control system performance in Simulink environment: tutorial. SPb: Publishing house of the Polytechnic University Press, 2014. 53 p.

15. **Hudorozhkov S.I.** Theory and automatic control system. Analysis and synthesis in Simulink environment. Standard blocks' library: tutorial. SPb: Publishing house of the Polytechnic University Press, 2013. 90 p.

16. **Khudorozhkov S.I., Galyshev Yu.V.** Dinamika rekuperativnogo mekhanicheskogo besstupenchatogo privoda transportnogo sredstva. *Nauchno-tekhnicheskiye vedomosti SPbPU / [St.Petersburg Polytechnic University Journal of Engineering Sciences And Technology]*. 2013. № 3 (178). S. 216–222. (rus.)

СПИСОК ЛИТЕРАТУРЫ

1. **POLARIS.** The Way Out. 2003 ATV. Universal Owner's Manual for Vehicle Maintenance and Safety // Polaris Industries Inc. Copyright 2002. P.153

2. **Arctic Cat Service Manual** for the 2012 Arctic Cat XC 450i ATV // Product Service and Warranty Department Arctic Cat Inc. Copyright 2011. P. 123.

3. **George Constantinesco:** Inertial Transmission, <http://www.rexresearch.com/constran/1constran.htm>.

4. **Благонравов А.А.** Механические бесступенчатые передачи УрО РАН. Екатеринбург, 2004. 203 с.

5. **Благонравов А.А., Худорожков С.И.** Динамика механической бесступенчатой передачи // Проблемы машиностроения и надежности машин. 2002. № 6. С. 19–24.

6. **Патент РФ №2252351.** Механическая саморегулируемая бесступенчатая передача / С.И. Худорожков. Приоритет 20.05.2005.

7. **Благонравов А.А., Худорожков С.И.** Динамическая характеристика саморегулируемой механической бесступенчатой передачи // Материалы Всероссийской научно-практической конференции «Редукторостроение России: состояние, проблемы, перспективы». СПб, 2003. С. 192–194.

8. **Благонравов А.А., Ревняков Е.Н.** Механическая бесступенчатая передача импульсного типа // Автомобильная промышленность. 2007. № 5. С. 11–14.

9. **Худорожков С.И.** Компьютерное моделирование динамики импульсной передачи с упругим звеном // Межвузовский сборник научных трудов

«Бесступенчатые передачи и механизмы свободного хода». Калининград, 2001. С.1 42–148.

10. **Благонравов А.А., Худорожков С.И.** Внешняя характеристика многопоточной бесступенчатой передачи с упругими звеньями // Сборник кратких сообщений «XXII Российская школа по проблемам науки и технологий». Екатеринбург, 2002. С. 82–84.

11. **Lester W. T.,** Infinitely Variable Transmission Utilizing Oscillating Torque // <http://ebookbrowse.com/infinitely-variable-transmission-utilizing-oscillating-torque-doc-d420263879>.

12. **Патент РФ №2373441.** Механизм свободного хода / С.И. Худорожков. Приоритет 20.11.2009.

13. **Худорожков С.И.** Теория и системы автоматического управления. Анализ и синтез САУ транспортных систем в среде Simulink: учеб. пособие. СПб.: Изд-во Политехн. ун-та, 2014. 110 с.

14. **Худорожков С.И.** Теория и системы автоматического управления. Построение характеристик САУ в среде Simulink: Учеб. пособие. СПб.: Изд-во Политехн. ун-та, 2014. 53 с.

15. **Худорожков С.И.** Теория и системы автоматического управления. Анализ и синтез в среде Simulink. Библиотека стандартных блоков: Учеб. пособие. СПб.: Изд-во Политехн. ун-та, 2013. 90 с.

16. **Худорожков С.И., Галышев Ю.В.** Динамика рекуперативного механического бесступенчатого привода транспортного средства // Научно-технические ведомости СПбПУ. 2013. № 3 (178). С. 216–222.

СВЕДЕНИЯ ОБ АВТОРАХ/AUTHORS

HOODOROZHNIKOV Sergey I. – Peter the Great St. Petersburg Polytechnic University.

29 Politechnicheskaya St., St. Petersburg, 195251, Russia.

E-mail: xcu-55@mail.ru

ХУДОРОЖКОВ Сергей Иванович – доктор технических наук профессор Санкт-Петербургского политехнического университета Петра Великого.

195251, Россия, г. Санкт-Петербург, Политехническая ул., 29.

E-mail: xcu-55@mail.ru

DOI 10.5862/JEST.249.15

УДК 621.873

P.A. Gavrilov

SEISMIC ANALYSIS OF CRANES REGARDING GEOMETRIC AND PHYSICAL NONLINEARITIES

П.А. Гаврилов

УЧЕТ ФИЗИЧЕСКОЙ И ГЕОМЕТРИЧЕСКОЙ НЕЛИНЕЙНОСТЕЙ ПРИ РАСЧЕТЕ СЕЙСМОСТОЙКОСТИ КРАНОВЫХ МЕТАЛЛИЧЕСКИХ КОНСТРУКЦИЙ

The paper studies the problem of factoring geometric and physical nonlinearities in seismic analysis of cranes. An experimental study of factoring nonlinear characteristics of dynamics model was conducted. A series of mathematical models were developed to describe different ways of linearization of the experimental model. Comparison of results shows that physical nonlinearity of wire ropes is not required as factor in seismic analysis of cranes. Therefore, contact between wheel and rail and one-sided stiffness of wire ropes are required to be taken into account. Any liberalization of the dynamical model entails deviation of stresses, displacements and accelerations as results of the analysis.

SEISMIC ANALYSIS; CRANE; EXPERIMENTAL STUDY; NONLINEAR DYNAMICS MODEL; MECHANICS.

В работе рассматривается вопрос учета нелинейных характеристик динамических моделей при расчете сейсмостойкости грузоподъемных кранов общего назначения. Проведено экспериментальное исследование влияния геометрической и физической нелинейностей на параметры колебаний динамической системы. Составлен ряд математических моделей, описывающих колебательный процесс нелинейной динамической системы. Предложен метод аппроксимации нелинейных ступенчатых функций с разрывами в производных. Рассмотрены геометрически нелинейные математические модели, допускающие разрыв односторонних связей механической системы, а так же физически нелинейные системы. Проведен сравнительный анализ влияния различных нелинейностей на параметры колебательного процесса. Результаты исследования показывают, что линейаризация нелинейной механической системы приводит к значительным отклонениям количественных параметров колебаний и искажению их общего характера. При этом предлагаемая математическая модель показала удовлетворительную погрешность расчета нелинейных колебаний.

СЕЙСМОСТОЙКОСТЬ; КРАН ГРУЗОПОДЪЕМНЫЙ; ЭКСПЕРИМЕНТАЛЬНОЕ ИССЛЕДОВАНИЕ; НЕЛИНЕЙНАЯ ДИНАМИЧЕСКАЯ МОДЕЛЬ; МЕХАНИКА.

Introduction

Currently, calculating the seismic resistance of metal cargo crane structures that do not make up the equipment of nuclear power plants is regulated by [1] and [2]. Both of these documents establish possible methods for analyzing the seismic resistance of a structure: the eigenmode expansion (in accordance with Biot–Benioff's response spectrum theory of seismic resistance [3, 4]) and the direct integration of a system of differential equations. The response

spectrum theory of seismic resistance allows to determine additional seismic loads on a structure using as input data the so-called response spectra of the foundation of a crane (a structure) and the magnitude of the design basis earthquake (DBE). The methodology of calculations by the response spectrum theory of seismic resistance was described in [5]. The input data for direct dynamical analysis of a structure are either recorded or synthesized accelerograms, velocigrams, or seismograms of earthquakes and the DBE magnitude.

In engineering practice, strength, stiffness and stability analysis of metal structures of cargo cranes is typically performed using the finite element method (FEM). Therefore, as computing power grows and calculation costs are reduced, direct dynamical methods are becoming increasingly used. Solving differential equations by numerical methods allows to more accurately determine the dynamical coefficients of displacements, stresses and strains, and as a result, to reduce the metal intensity and the construction costs of the crane.

However, the aforementioned regulations do not provide either specific guidance on choosing dynamical models for the seismic analysis of cranes, or recommendations on factoring in unilateral contacts (such as the rail-wheel contact, or hoist rope) and the nonlinear nature of the deformation of the suspended elements. This gap in the explanations can be attributed to the fact that the response spectrum theory of seismic resistance has been developed for building structures, where such nonlinearities occur much less frequently in metal cranes, and are therefore not taken into account in the calculations. However, these factors can play a very significant role for hoisting machines. The problem of taking into account the geometric and physical nonlinearities in seismic calculations of cargo cranes is being actively discussed in scientific circles [6–8]. The mathematical models and methods offered for solving these problems allow for potential bounces of the trolley wheels and the crane on the rail, unilateral contact of the ropes, physical nonlinearities of the structural materials, etc. The urgency of the research in this area is due to the need to improve the safety of hoisting machines operating in seismically hazardous zones.

This study is dedicated to investigating the influence of physical and geometrical nonlinearities in a dynamical system with regard to calculating the seismic resistance of cargo cranes. The ultimate goal of the study is in developing recommendations for taking into account the nonlinear properties of metal structures of general-purpose cargo cranes subjected to seismic analysis. The study consisted of the experimental part, mathematical simulation and the analysis of results.

Experimental setup

The experimental model simulates the construction of an overhead crane, sensing vertical oscillations and schematized as a geometrically and physically nonlinear dynamical three-mass system. A

schematic for the experimental setup is shown in fig. 3. The main elements of the model are conventionally referred to as bridge 3, trolley 4 and weight 6. The bridge is secured in hinged supports 1 and 2, with the movable support 2 allowing the bridge to move in the direction of its longitudinal axis. Strain gauges 7 are fixed to the bridge at the distance of a quarter of the span from the supports. The trolley is located at the center of the bridge span. The trolley can bounce on the bridge. If the trolley separates from the bridge, sensor 8 is triggered, registering the bounce event. Thus, the experiment simulates the contact between the trolley wheels and the rail. Weights 10 and accelerometer 9 measuring the vertical accelerations of the pendant emerging during oscillations are secured to the trolley. Guide ropes 12, stretched along the vertical axis and passing through special holes in the trolley, are used to eliminate the swinging of the trolley from the vertical plane. A pendant, referred to as weight in the experiment, is fixed to the trolley by a flexible elastic suspension element. The pendant, as well as the trolley, is equipped with an accelerometer for recording accelerations and with additional calibrated weights. Before the start of the experiment the whole system was pulled downward and secured using hook 11 mounted to the lower suspension element. The measurements started at the moment when this constraint was removed (i.e., the thread connecting the weight to the foundation was cut).

The general characteristics of the experimental model were the following: the bridge span was 1,520 mm; the bridge weight was 0,503 kg; the mass of the suspended trolley with the accelerometer and additional weights was 1,9 kg; the mass of the suspended pendant with the accelerometer and additional weights was 2,63 kg.

In order to determine the actual stress-strain curve for the stretched flexible suspension element, a series of measurements was carried out for the elongation of the sample under various loads. Fig. 2 shows a plot for the stiffness of the flexible suspension element versus absolute elongation. The interpolating curve is described by the following expression with a conditional operator:

$$y(x) = \begin{cases} a + b \cdot e^{-c \cdot x} & \text{if } x \geq d; \\ C3 & \text{if } 0 \leq x < d; \\ 0 & \text{otherwise,} \end{cases} \quad (1)$$

where $a = 0,34$ N/mm; $b = 2,5$ N/mm; $c = 0,02$; $d = 82$ mm; $C3 = 0,87$ N/mm.

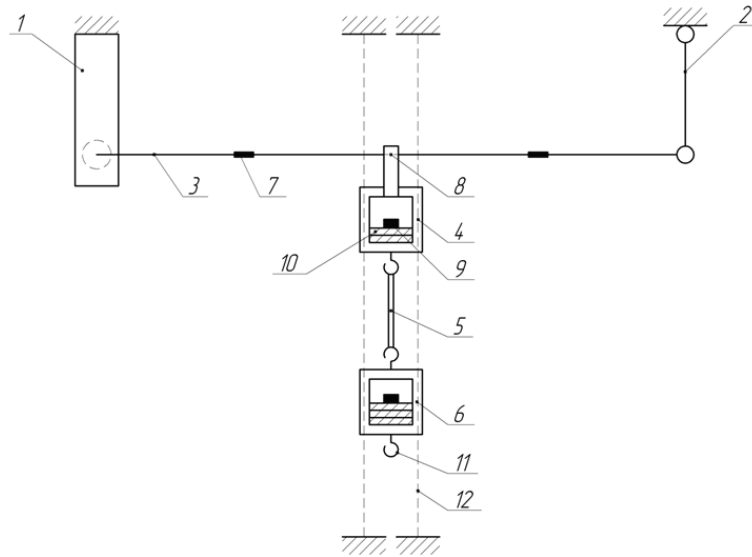


Fig. 1. Schematic of the experimental setup: fixed support 1; movable support 2; bridge 3; suspended trolley 4; flexible suspension element 5; suspended 'weight' pendant 6; strain gauge 7; bounce sensor 8; accelerometer 9; additional weight 10; hook 11; guide ropes 12

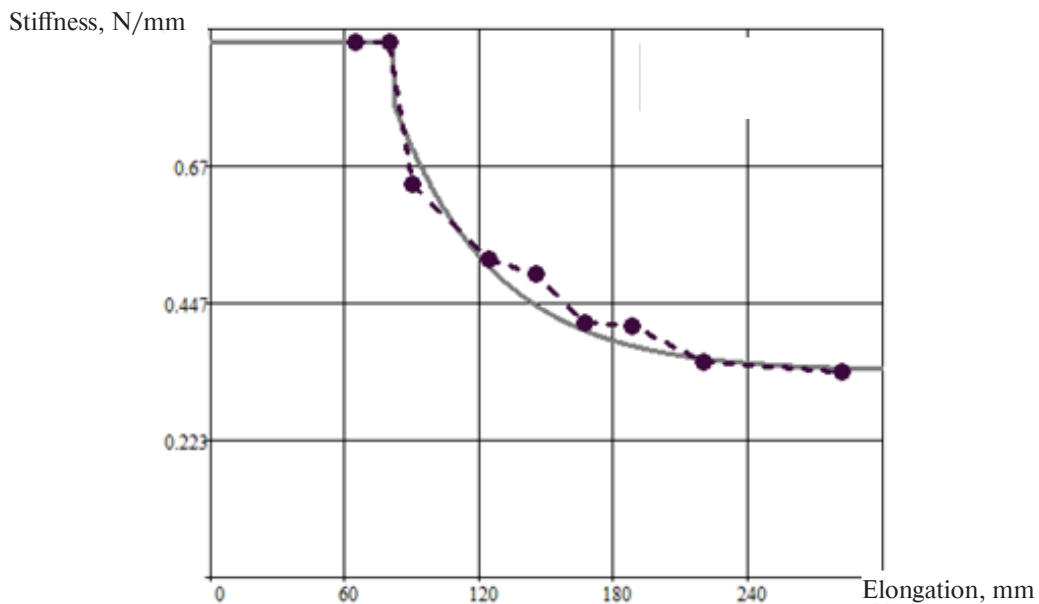


Fig. 2. Stiffness of the flexible suspension element versus elongation (— interpolation, - - - experiment)

The results of the experiment are the recordings of the strain gauge, the bounce sensor and the accelerometers.

The experiment conducted demonstrated the effect of the geometric (weight and trolley bounce) and the physical (change in the stiffness of the flexible suspension element) nonlinearities.

Mathematical modeling

In accordance with the input experimental data, a number of mathematical models describing the vibrations of a dynamical three-mass system were constructed in MathCAD. Four models were designed: 1—a linear dynamical model; 2—a physically nonlinear dynamical model taking into account the

actual nature of the tension of the flexible suspension element; 3—a geometrically nonlinear dynamical model taking into account the possibility that the weight may bounce on the flexible suspension element and the trolley may bounce on the bridge; 4—a physically and geometrically nonlinear dynamical model. The schematic for the dynamical three-mass system is shown in fig. 3.

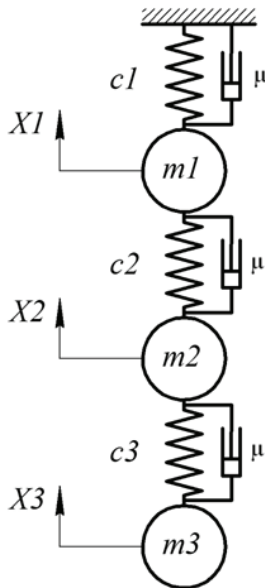


Fig. 3. Dynamical system schematic

The mathematical models are based on the Lagrange equation of the second kind, which has the form:

$$[M]\{\ddot{u}\} + [C]\{\dot{u}\} + [K]\{u\} = \{R\}, \quad (2)$$

where $[M]$ is the mass matrix of the structure, $[C]$ is the damping matrix, $[K]$ is the stiffness matrix; $\{R\}$ is the known time-dependent vector of the external load; $\{u\}$ is the unknown time-dependent vector of mass displacements in the model.

The systems of differential equations were solved numerically in MathCAD 14 via the Radau solver which uses the eponymous algorithm. The process of energy dissipation during fluctuations is taken into account through equivalent viscous friction for all mathematical models. The coefficient of viscous friction was determined from the equality condition of the decay times for the oscillations of the experimental and mathematical models. For all of the mathematical models described below the coefficient of equivalent viscous friction was $\mu = 5 \text{ kg/s}$.

The linear dynamical model is the simplest of all the ones presented. The system of differential equa-

tions describes the oscillations of the dynamical three-mass system.

$$\begin{cases} \ddot{X}1(t) \cdot m1 + c1 \cdot \dot{X}1(t) - c2 \cdot (X2(t) - X1(t)) + \\ + \mu \cdot \dot{X}1(t) - \mu \cdot (\dot{X}2(t) - \dot{X}1(t)) = g \cdot m1; \\ \ddot{X}2(t) \cdot m2 + c2 \cdot (X2(t) - X1(t)) - \\ - C3' \cdot (X3(t) - X2(t)) + \mu \cdot (\dot{X}2(t) - \dot{X}1(t)) - \\ - \mu \cdot (\dot{X}3(t) - \dot{X}2(t)) = g \cdot m2; \\ \ddot{X}3(t) \cdot m3 + C3' \cdot (X3(t) - X2(t)) + \\ + \mu \cdot (\dot{X}3(t) - \dot{X}2(t)) = g \cdot m3. \end{cases} \quad (3)$$

Here $c1$ is the bridge stiffness, N/mm; $c2$ is the stiffness of the 'trolley-bridge' contact pair, N/mm; $c3$ is the equivalent stiffness of the flexible suspension element, N/mm; $X1(t)$, $X2(t)$ and $X3(t)$ are the generalized coordinates of the bridge, the trolley and the weight, respectively, mm; $m1$ is the reduced mass of the bridge, kg; $m2$ and $m3$ are the masses of the trolley and the weight, including the accelerometers, kg; g is acceleration of free fall, mm/s²; μ is the coefficient of viscous friction, kg/s.

The stiffness of the flexible suspension element $c3(t)$ is in this case taken to be constant. The greatest oscillation time is in the linear non-zero segment of the curve shown in fig. 2; however, the stiffness of the flexible suspension element for the initial time is calculated from Eq. (1). The equivalent stiffness used during the physical linearization of the model is taken as the average of the above values:

$$C3' = \frac{y(X2(0) - X3(0)) + C3}{2} = 0,68, \text{ N/mm}.$$

System (3) was solved with the following initial conditions:

$$\begin{cases} \dot{X}1(0) = 0, \text{ mm/s}; \\ \dot{X}2(0) = 0, \text{ mm/s}; \\ \dot{X}3(0) = 0, \text{ mm/s}; \\ X1(0) = -69,3 \text{ mm}; \\ X2(0) = -69,3 \text{ mm}; \\ X3(0) = -188,2 \text{ mm}. \end{cases} \quad (4)$$

In this study the geometric linearity was represented by the so-called buckling constraints. This means that the $c2$ and $c3$ stiffnesses only experienced uniaxial tension. Otherwise, the stiffnesses vanish and do not create reaction forces affecting the oscillation process. At the same time, given the specifics

of the experimental setup, the dissipative elements retain their functions for any values of the relative displacements of the masses with respect to each other.

The variable stiffness is represented in the mathematical model as a continuous differentiable function:

$$c(x) = \frac{C}{\pi} \operatorname{arctg}(x \cdot k) + \frac{C}{2}, \quad (5)$$

where C is the maximum constant stiffness, N/mm; k is the coefficient determining the slope of the function.

The system of differential equations describing a geometrically linear dynamical system has the form:

$$\begin{cases} \ddot{X}1(t) \cdot m1 + c1 \cdot X1(t) - c2(t) \cdot (X2(t) - X1(t)) + \\ + \mu \cdot \dot{X}1(t) - \mu \cdot (\dot{X}2(t) - \dot{X}1(t)) = g \cdot m1; \\ \ddot{X}2(t) \cdot m2 + c2(t) \cdot (X2(t) - X1(t)) - \\ - c3(t) \cdot (X3(t) - X2(t)) + \mu \cdot (\dot{X}2(t) - \dot{X}1(t)) - \\ - \mu \cdot (\dot{X}3(t) - \dot{X}2(t)) = g \cdot m2; \\ \ddot{X}3(t) \cdot m3 + c3(t) \cdot (X3(t) - X2(t)) + \\ + \mu \cdot (\dot{X}3(t) - \dot{X}2(t)) = g \cdot m3; \\ c2(t) = \frac{C2}{\pi} \cdot \operatorname{arctg}((X1(t) - X2(t)) \cdot k) + \frac{C2}{2} \\ c3(t) = \frac{C3}{\pi} \cdot \operatorname{arctg}((X2(t) - X3(t)) \cdot k) + \frac{C3}{2}, \end{cases} \quad (6)$$

where $k = 1000$ is the dimensionless slope coefficient of the stiffness function.

System (6) was solved with the following initial conditions:

$$\begin{cases} \dot{X}1(0) = 0, \text{ mm / s;} \\ \dot{X}2(0) = 0, \text{ mm / s;} \\ \dot{X}3(0) = 0, \text{ mm / s;} \\ X1(0) = -69,3, \text{ mm;} \\ X2(0) = -69,3, \text{ mm;} \\ X3(0) = -188,2, \text{ mm;} \\ c2(0) = 10000, \text{ N / mm;} \\ c3(0) = 0,68, \text{ N / mm.} \end{cases} \quad (7)$$

The relative stiffness of the flexible suspension element under geometric linearization of the model is simulated according to Eq. (1), the difference being that the argument of the function is the absolute value of the argument:

$$yd(x) = \begin{cases} a + b \cdot e^{-c \cdot |x|} & \text{if } |x| \geq d; \\ C3 & \text{otherwise.} \end{cases} \quad (8)$$

The system of differential equations describing a physically nonlinear system has the form:

$$\begin{cases} \ddot{X}1(t) \cdot m1 + c1 \cdot X1(t) - c2 \cdot (X2(t) - X1(t)) + \\ + \mu \cdot \dot{X}1(t) - \mu \cdot (\dot{X}2(t) - \dot{X}1(t)) = g \cdot m1; \\ \ddot{X}2(t) \cdot m2 + c2 \cdot (X2(t) - X1(t)) - \\ - c3(t) \cdot (X3(t) - X2(t)) + \mu \cdot (\dot{X}2(t) - \dot{X}1(t)); \\ - \mu \cdot (\dot{X}3(t) - \dot{X}2(t)) = g \cdot m2; \\ \ddot{X}3(t) \cdot m3 + c3(t) \cdot (X3(t) - X2(t)) + \\ + \mu \cdot (\dot{X}3(t) - \dot{X}2(t)) = g \cdot m3; \\ c3(t) = \begin{cases} a + b \cdot e^{-c \cdot (X1(t) - X2(t))} & \text{if } |X1(t) - X2(t)| \geq d; \\ C3 & \text{otherwise.} \end{cases} \end{cases} \quad (9)$$

System (13) can be solved with the following initial conditions:

$$\begin{cases} \dot{X}1(0) = 0, \text{ mm / s;} \\ \dot{X}2(0) = 0, \text{ mm / s;} \\ \dot{X}3(0) = 0, \text{ mm / s;} \\ X1(0) = -69,3, \text{ mm;} \\ X2(0) = -69,3, \text{ mm;} \\ X3(0) = -211,6, \text{ mm;} \\ c3(0) = yd(X2(0) - X3(0)), \text{ N / mm.} \end{cases} \quad (10)$$

The geometrically and physically nonlinear mathematical model contains all of these types of nonlinearities, and is described by a system of differential equations:

$$\begin{cases} \ddot{X}1(t) \cdot m1 + c1 \cdot X1(t) - c2(t) \cdot (X2(t) - X1(t)) + \\ + \mu \cdot \dot{X}1(t) - \mu \cdot (\dot{X}2(t) - \dot{X}1(t)) = g \cdot m1; \\ \ddot{X}2(t) \cdot m2 + c2(t) \cdot (X2(t) - X1(t)) - \\ - c3(t) \cdot (X3(t) - X2(t)) + \mu \cdot (\dot{X}2(t) - \dot{X}1(t)); \\ - \mu \cdot (\dot{X}3(t) - \dot{X}2(t)) = g \cdot m2; \\ \ddot{X}3(t) \cdot m3 + c3(t) \cdot (X3(t) - X2(t)) + \\ + \mu \cdot (\dot{X}3(t) - \dot{X}2(t)) = g \cdot m3; \\ c2(t) = \frac{C2}{\pi} \cdot \operatorname{arctg}((X1(t) - X2(t)) \cdot k) + \frac{C2}{2}; \\ c3(t) = \begin{cases} a + b \cdot e^{-c \cdot (X1(t) - X2(t))} & \text{if } (X1(t) - X2(t)) \geq d; \\ C3 & \text{if } 0 < (X1(t) - X2(t)) < d; \\ 0 & \text{otherwise.} \end{cases} \end{cases} \quad (11)$$

System (11) can be solved with the following initial conditions:

$$\begin{cases} \dot{X}1(0) = 0, \text{ mm / s;} \\ \dot{X}2(0) = 0, \text{ mm / s;} \\ \dot{X}3(0) = 0, \text{ mm / s;} \\ X1(0) = -69,3, \text{ mm;} \\ X2(0) = -69,3, \text{ mm;} \\ X3(0) = -211,6, \text{ mm;} \\ c2(0) = 10000, \text{ N / mm;} \\ c3(0) = y(X2(0) - X3(0)), \text{ N / mm.} \end{cases} \quad (12)$$

Analysis of the results

As previously stated, the following parameters of the setup’s oscillations were recorded during the experiment:

- 1) stresses on the surface of the rod in the points where the strain gauges were attached;
- 2) the vertical accelerations of the trolley;
- 3) the vertical accelerations of the weight;

4) the separation of the trolley from the bridge.

We should note that in this case, the stresses registered by the strain gauges are directly proportional to the displacements of the central point of the bridge span. Figs. 4–6 show comparative plots for the displacements of the central point of the bridge, and the accelerations of the trolley and the weight during oscillations.

In view of the requirements of engineering analysis, we compared the experimental results with the analytical calculations by the following parameters:

- the amplitude of the first wave of bridge displacement oscillations A ;
- the duration of the bounce;
- the amplitude of the trolley acceleration oscillations excluding the first half-wave;
- the amplitude of weight acceleration oscillations excluding the first half-wave.

The results of the comparison of different mathematical models with the experimental data are listed in Table.

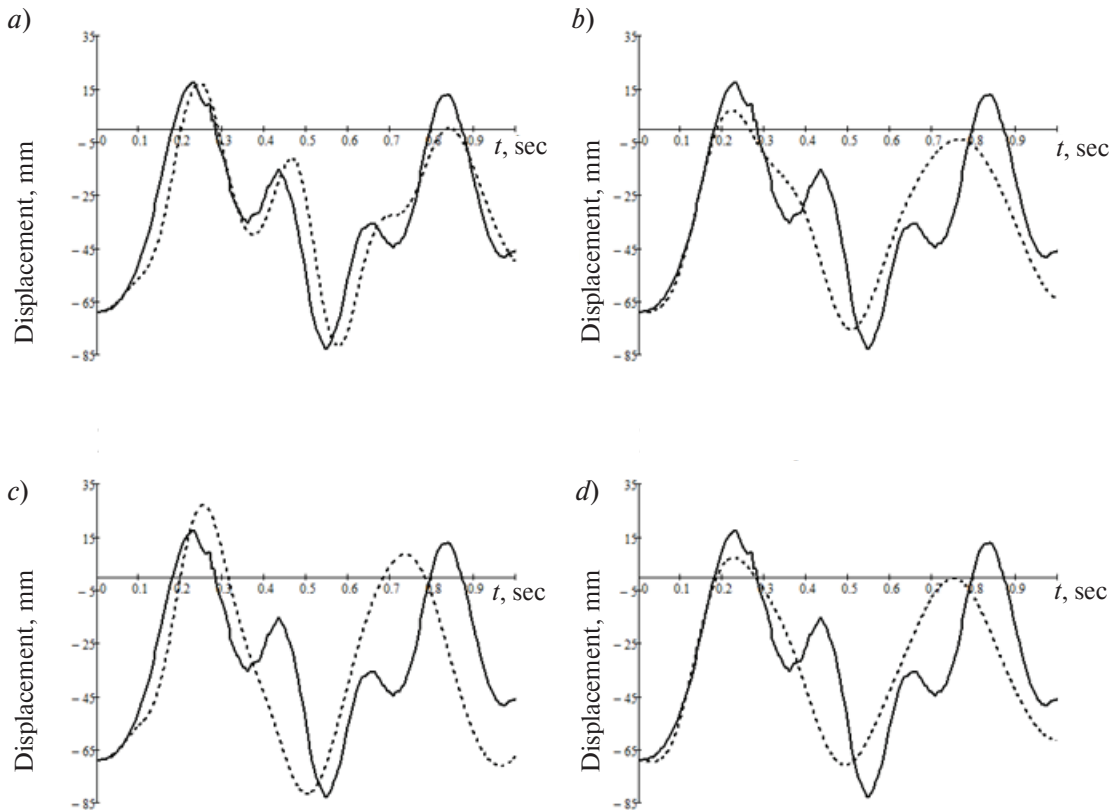


Fig. 4. Bridge displacements versus time: — experiment; model (a – physical and geometrical nonlinear; b – geometrical nonlinear; c – physical nonlinear; d – linear)

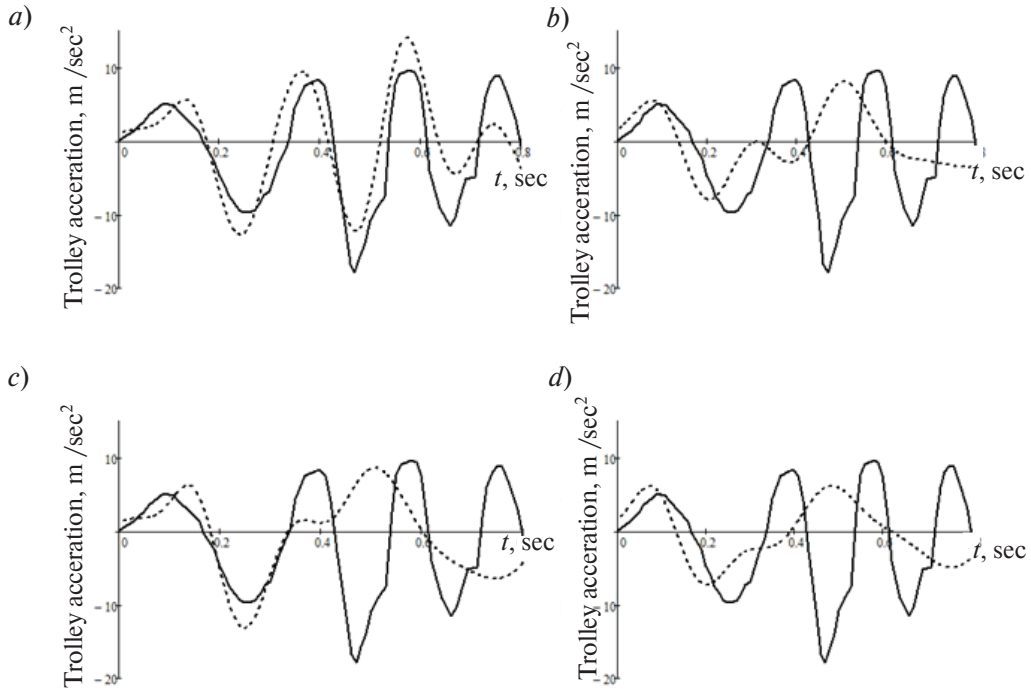


Fig. 5. Trolley accelerations versus time: —— experiment; model (a – physical and geometrically nonlinear; b – geometrically nonlinear; c – physical nonlinear; d – linear)

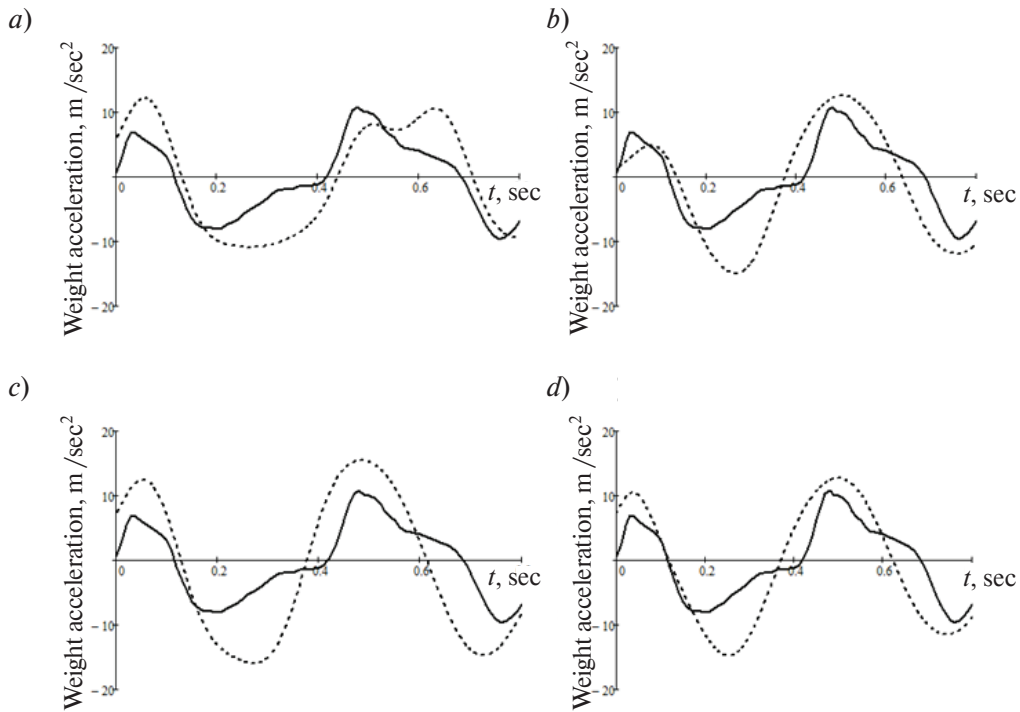


Fig. 6. Weight accelerations versus time: —— experiment; model (a – physical and geometrically nonlinear; b – geometrically nonlinear; c – physical nonlinear; d – linear)

Table

Parameter	Amplitude of bridge displacements		Amplitude of trolley accelerations		Amplitude of weight accelerations		Bounce duration	
	Value, mm	Deviation, %	Value, m/s ²	Deviation, %	Value, m/s ²	Deviation, %	Value, s	Deviation, %
Experiment	86,3	—	17,8	—	18,8	—	0,06	—
Nonlinear model	86,4	0,1	22,2	24,7	18,9	0,5	0,065	8,3
Linear geometry	96,3	11,6	21,8	22,5	31,4	67,0	0,146	143,3
Linear stiffness	76,1	-11,8	16,1	-9,6	27,5	46,3	0,038	-36,7
Linear model	76,5	-11,4	13,3	-25,3	27,5	46,3	0,023	-61,7

It is evident from the results of the study that the nonlinear mathematical model best describes the oscillations of the experimental setup. The linearization of the model leads to a significant deviation in the criteria for comparing the models and changes the behavior of the oscillatory process in the system. Without a doubt, the seismic calculation of a crane is not the most accurate type of analysis since it is impossible to predict the input effect. Therefore, this calculation should be carried out with a safety margin, with some results deliberately set too high. The choice of the mathematical model and its linearization are of interest. Let us consider the options for linearizing the mathematical model used for calculating the seismic stability of the cargo crane, based on the results of the experimental study.

Steel wire ropes used in hoisting equipment often have stiffnesses significantly higher than that of the crane structure. The safety factor adopted for the ropes is usually in the range of values $n = 4...25$ [9] depending on the operation mode of the crane, the purpose of the rope, and other characteristics of the particular installation. As shown in Ref. [10], the nonlinear properties of the ropes manifest themselves at relatively high loads with respect to the breaking force, if the safety factor is close to 3. In view of the above, modeling the nonlinear properties of steel wire ropes while calculating the seismic resistance of general-purpose cargo cranes in the absence of additional requirements for the calculation accuracy can be deemed ineffective.

Geometric linearization of the model in this study led to an overestimation of all evaluation criteria, and

the behavior of the oscillations in the system changed to a large extent.

Constructing a physically and geometrically nonlinear model of a cargo crane is not economically feasible. A project designer does not require the bulk material of the supporting structures to be physically nonlinear, since the situation when the calculated stresses in the metal are located in the yield region is inadmissible. Modeling the nonlinear properties of steel wire ropes is also infeasible for the reasons described above. However, geometric linearization of the crane structure would unreasonably increase the safety factors that would in turn increase the overall costs of the crane.

Conclusions

The following conclusions can be reached from the results of the study conducted:

The experimental study has shown that physical and geometrical linearization of the mathematical model describing the process of free damped oscillations of a dynamical three-mass system causes the calculated displacements and accelerations to deviate from the true values by 11%-67%.

Physical linearization of the stiffness of hoist ropes is the most preferable from the standpoint of labor costs and feasibility, as it has no significant impact on the result of the dynamical analysis.

It can be concluded from the results of the study that unilateral constraints (steel wire ropes, the wheel-rail contact) should be taken into account when calculating the seismic resistance of general-purpose hoisting equipment.

REFERENCES

1. **GOST 30546.1-98.** Obshchiye trebovaniya k mashinam, priboram i drugim tekhnicheskim izdeliyam i metody rascheta ikh slozhnykh konstruksiy v chasti seysmostoykosti. Minsk: IPK Izdatelstvo standartov, 1998. (rus.)
2. **SNiP II-7-81*** Stroitelstvo v seysmicheski rayonakh. Moscow. 2011. (rus)
3. **Biot M.A.** Theory of elastic systems vibrating under transient impulse with an application to earthquake-proof buildings. *Proc Nat Acad Sci.* 1933. № 19(2). Is. 262. P. 8.
4. **Biot M.A.** Theory of vibration of buildings during earthquakes. *Zeitschrift for Angewandte Matematik und Mechanik.* 1934. № 14(4). Is. 213. P. 23.
5. **Birbrayer A.N.** Raschet konstruksiy na seysmostoykost [Seismic analysis of structures]. Saint-Petersburg: Nauka, 1998.
6. **Kobayashi N., Kuribara H., Honda T., Watanabe M.** Nonlinear Seismic Responses of Container Cranes Including the Contact Problem Between Wheels and Rails. *Journal of Pressure Vessel Technology.* 2004. № 126(1). P. 59–65.
7. **Suzuki K., Inagaki M., Iijima T.** Seismic Capacity Test of Overhead Crane Under Horizontal and Vertical Excitation. *Journal of Disaster Research.* 2010. № 4. P. 369–377.
8. **Sinelshchikov A.V.** Osnovy teorii seysmostoykosti podzemnykh sooruzheniy. *Izvestiya Tulskogo gosudarstvennogo universiteta. Tekhnicheskiye nauki.* 2009. № 2. T. 1. S. 133–141. (rus.)
9. **Braude V.I., Gokhberg M.M., Zvyagin I.Ye., Kovin A.A., Orlov A.N., Plavnik B.I., Serlin L.G., Sirotskiy V.F., Sokolov S.A., Tarkhov A.I., Yushkevich V.N.** Spravochnik po kranam. Vol. I. Moscow: Mashinostroyeniye, 1988. 536 s. (rus.)
10. **Malinovskiy V.A.** Stalnyye kanaty. Chast I: Nekotoryye voprosy tekhnologii, rascheta i proyektirovaniya. Odessa: Asptroprint, 2001. 188 s. (rus.)

СПИСОК ЛИТЕРАТУРЫ

1. **ГОСТ 30546.1-98.** Общие требования к машинам, приборам и другим техническим изделиям и методы расчета их сложных конструкций в части сейсмостойкости». Минск: ИПК Издательство стандартов, 1998.
2. **СНиП II-7-81*** Строительство в сейсмически районах. Москва, 2011.
3. **Biot M.A.** Theory of elastic systems vibrating under transient impulse with an application to earthquake-proof buildings. // *Proc Nat Acad Sci.* 1933. № 19(2). Is. 262. P. 8.
4. **Biot M.A.** Theory of vibration of buildings during earthquakes. // *Zeitschrift for Angewandte Matematik und Mechanik.* 1934. № 14(4). Is. 213. P. 23.
5. **Бирбраер А.Н.** Расчет конструкций на сейсмостойкость. Санкт-Петербург: Наука, 1998.
6. **Kobayashi N., Kuribara H., Honda T., Watanabe M.** Nonlinear Seismic Responses of Container Cranes Including the Contact Problem Between Wheels and Rails // *Journal of Pressure Vessel Technology.* 2004. № 126(1). P. 59–65.
7. **Suzuki K., Inagaki M., and Iijima T.** Seismic Capacity Test of Overhead Crane Under Horizontal and Vertical Excitation // *Journal of Disaster Research.* 2010. № 4. P. 369–377.
8. **Синельщиков А.В.** Основы теории сейсмостойкости подъемных сооружений // *Известия Тульского государственного университета. Технические науки.* 2009. № 2. Т. 1. С. 133–141.
9. **Брауде В.И., Гохберг М.М., Звягин И.Е., Ковин А.А., Орлов А.Н., Плавник Б.И., Серлин Л.Г., Сиротский В.Ф., Соколов С.А., Тархов А.И., Юшкевич В.Н.** Справочник по кранам. Т. I. М.: Машиностроение, 1988. 536 с.
10. **Малиновский В.А.** Стальные канаты. Часть I: Некоторые вопросы технологии, расчета и проектирования. Одесса: Асптропринт, 2001. 188 с.

СВЕДЕНИЯ ОБ АВТОРАХ/AUTHORS

GAVRILOV Petr A. – Peter the Great St. Petersburg Polytechnic University.
29 Politechnicheskaya St., St. Petersburg, 195251, Russia.
E-mail: issahel@mail.ru

ГАВРИЛОВ Петр Александрович – аспирант Санкт-Петербургского политехнического университета Петра Великого.
195251, Россия, г. Санкт-Петербург, Политехническая ул., 29.
E-mail: issahel@mail.ru

Научное издание

НАУЧНО-ТЕХНИЧЕСКИЕ ВЕДОМОСТИ СПбПУ

№3(249)2016

Учредитель — Санкт-Петербургский политехнический университет Петра Великого

Издание зарегистрировано в Федеральной службе по надзору за соблюдением законодательства
в сфере массовых коммуникаций и охраны культурного наследия
(свидетельство ПИ № ФС77-25981 от 13 октября 2006 г.)

Научный редактор, корректор — канд. техн. наук доцент *Л.В. Спиридонова*
Технический секретарь — *О.А. Матенев*
Компьютерная верстка — *Е.Н. Никулкина*

Телефон редакции (812) 294-47-72

E-mail: ntv-nauka@spbstu.ru

Подписано в печать 23.09.2016. Формат 60×84 1/8. Бум. тип. № 1.
Печать цифровая. Усл. печ. л. 18.0. Тираж 1000. Заказ 14824b.

Отпечатано с готового оригинал-макета,
предоставленного Издательством Политехнического университета,
в Типографии Политехнического университета.
195251, Санкт-Петербург, Политехническая ул., 29.
Тел.: (812) 552-77-17; 550-40-14.

УСЛОВИЯ ПУБЛИКАЦИИ СТАТЕЙ
в журнале «Научно-технические ведомости СПбГПУ»

1. ОБЩИЕ ПОЛОЖЕНИЯ

Журнал «Научно-технические ведомости СПбГПУ» является периодическим печатным научным рецензируемым изданием:
— зарегистрирован в Федеральной службе по надзору за соблюдением законодательства в сфере массовых коммуникаций и охране культурного наследия (свидетельство ПИ № ФС77-25981 от 13 октября 2006г.) и распространяется по подписке через объединенный каталог «Пресса России» (индекс 18390);

— имеет международный стандартный номер сериального периодического издания (ISSN 1994-2354);
— внесен Высшей аттестационной комиссией Минобрнауки РФ в Перечень периодических научных и научно-технических изданий, в которых рекомендуется публикация основных результатов диссертаций на соискание ученой степени доктора наук, ученой степени кандидата наук;

— с 2009 г. входит в национальную информационно-аналитическую систему «Российский индекс научного цитирования (РИНЦ)»;

— сведения о публикациях представлены в Реферативном журнале ВИНИТИ РАН и включены в фонд научно-технической литературы (НТЛ) ВИНИТИ РАН, а также в международную систему по периодическим изданиям “Ulrich’s Periodicals Directory”.

Журнал публикует результаты работ в следующих областях науки и техники: энергетика, электротехника, материаловедение, металлургия, машиностроение.

Редакция журнала соблюдает права интеллектуальной собственности и со всеми авторами научных статей заключает издательский лицензионный договор.

Публикация материалов, в том числе соискателей ученых степеней, осуществляется бесплатно.

2. ТРЕБОВАНИЯ К ПРЕДСТАВЛЯЕМЫМ МАТЕРИАЛАМ

2.1. Представление материалов

В статье должны быть кратко изложены новые и оригинальные результаты исследований, полученные авторами; следует избегать повторений, излишних подробностей и известных положений, подробных выводов, формул и уравнений (приводить лишь окончательные формулы, пояснив, как они получены).

При написании оригинальной научной статьи и оформлении рукописи авторы должны придерживаться следующих правил. Статья должна представлять собой описание выполненных исследований с указанием их места в соответствующей области наук и обсуждением значения выполненной работы. Рукопись должна содержать достаточное количество информации и ссылок на общедоступные источники для того, чтобы работа могла быть повторена независимо от авторов.

Название статьи должно быть кратким, но информативным. Обращаем Ваше внимание на то, что журнал издается как на русском, так и на английском языке. В связи с этим, не следует использовать аббревиатуру в названии статьи.

Аннотация должна давать читателю сжатую информацию о содержании статьи. Аннотация должна быть информативной и отражать не только основные цели статьи, но и главные результаты и выводы работы. Аннотация не является частью текста и сама по себе должна являться законченным описанием.

Ключевые слова должны отражать основную проблематику статьи и должны приводиться на русском языке для русской и на английском для англоязычной версии статьи. Количество ключевых слов – не менее трех и не более семи.

Адрес для корреспонденции должен содержать фамилию автора для корреспонденции (не обязательно первого автора), его полный почтовый адрес, телефон, факс, e-mail.

При необходимости Редакция может потребовать представления Акта экспертизы.

Представление всех материалов осуществляется в электронном виде через личный кабинет ЭЛЕКТРОННОЙ РЕДАКЦИИ по адресу: <http://journals.spbstu.ru>

Статьи подаются в формате .docx (MS Word 2007–2010). Файл статьи, подаваемый через электронную редакцию, должен содержать только сам текст, без названия, списка литературы, фамилий и данных авторов. Список литературы, название статьи, вся информация об авторах задаются при подаче через электронную редакцию в отдельных полях. В тексте статьи должны быть ссылки на все источники из списка литературы. Порядковый номер источника в тексте статьи указывается в квадратных скобках.

2.2. Оформление материалов

2.2.1. Объем статей, как правило, 15–20 страниц формата А-4. Количество рисунков и фотографий (в том числе цветных) не должно превышать 4, таблиц – 3.

2.2.2. Число авторов — не более трех от одной организации и не более пяти от разных организаций. Статья должна быть подписана всеми авторами. Авторами являются лица, принимавшие участие во всей работе или ее главных разделах. Лица, участвовавшие в работе частично, указываются в сносках.

2.2.3. Статья должна содержать следующие разделы:
номер УДК в соответствии с классификатором;
фамилии авторов на русском и английском языках;
название на русском и английском языках;
аннотация — 3–5 предложений на русском и английском языках;
ключевые слова – не менее 2 и не более 7 на русском и английском языках;
введение (актуальность, краткое обоснование существующей проблемы) — 1,0–1,5 стр. ;
цель работы (краткая четкая формулировка поставленной задачи);
методика проведения исследований и расчетов, включая краткую информацию об использованных приборах, методах и точности экспериментальных измерений и теоретических расчетов и т. д.;